ASPECTS OF THE HIGH-PRESSURE BEHAVIOUR OF IRON OXIDES AND SULPHIDES

A thesis submitted for the degree of
DOCTOR OF PHILOSOPHY
of the
AUSTRALIAN NATIONAL UNIVERSITY
by

Catherine Ann McCammon

September 1983

This thesis is the result of research performed during the period March 1979 to September 1983 while I was a full-time student at the Research School of Earth Sciences, Australian National University. The work is entirely my own, unless otherwise acknowledged. This thesis has never been submitted to another University or similar institution.

.....

Catherine McCammon

September 1983

ACKNOWLEDGEMENTS

I thank my supervisors, A.E. Ringwood and I. Jackson, for their participation in what turned out to be a rewarding four years of research. A.E. Ringwood was a continual source of innovative ideas providing new lines of research to pursue. I am indebted to I. Jackson for countless hours of discussion, and for his careful and constructive criticism of my work. The infectious enthusiasm of both my supervisors always provided a source of excitement regarding experimental results, and their high academic standard undoubtedly improved mine. I am grateful to L. Liu for supervising the first two years of my research, and for numerous hours of instruction in the art of using the diamond anvil cell. The Mössbauer component of my research was made possible by D.C. Price (formerly at R.S.Phys.S., ANU) and J. Cashion (Dept. of Physics, Monash University), who permitted me access to their equipment. I am indebted to both of them for their interest in my work and their expertise in the subject which greatly extended my knowledge of the Mössbauer effect through numerous discussions. I am grateful to H. O'Neill who substantially contributed to my understanding of thermodynamics. Technical support was provided by K. Massey, N. Ware, H. Neisler, A. Major and W. Hibberson, and I am particularly indebted to the latter two for their generous assistance throughout the course of my research. Financial support was provided by an ANU Ph.D. scholarship, and I am grateful to RSES for providing monetary support to attend conferences and conduct Mössbauer experiments at Monash University. My greatest debt is to my parents who have unselfishly provided encouragement and financial support through all phases of my education. This thesis is a tribute to their confidence in my ability. Finally, I am especially indebted to Richard for our happy life together, and who never fails to restore my good humour after things go really wrong in the lab.

PREFACE

The research described in this thesis overlaps several scientific disciplines, and a number of concepts from different subjects are used to discuss the behaviour of compounds studied. While most readers will be familiar with these subjects at the levels that they are presented in this thesis, a list of suggested references is provided in the case that additional material is desired.

Thermodynamics: Kern, R. and Weisbrod, A. Thermodynamics for Geologists, Freeman, Cooper and Co., 1967.

Crystal field theory: Burns, R.G. Mineralogical Applications of Crystal Field Theory, Cambridge University Press, 1970.

Molecular Orbital Theory: Cotton, F.A. and Wilkinson, G. Advanced Inorganic Chemistry, Interscience, 1972.

Band theory and magnetism: Kittel, C. Introduction to Solid State Physics, John Wiley and Sons, 1976 (5th ed).

Behaviour of compounds in this thesis may be alternately described in terms of crystal field theory, molecular orbital theory and band theory, depending on which is the most convenient to describe the particular phenomena.

During the course of the research there have been opportunities to publish most of the work, and a list of these publications is given below.

McCammon, C.A. and Price, D.C. (1982). A Mössbauer effect investigation of the magnetic behaviour of $(Fe,Co)S_{1+x}$ solid solutions, J. Phys. Chem. Solids 43 431-437. (Chapter 3)

McCammon, C.A. and Cashion, J. A Mössbauer study of (Fe,Mn)S and (Fe,Mg)S solid solutions at 298 K and 4.2 K (in preparation). (Chapter 4)

McCammon, C.A., Jackson, I. and Ringwood, A.E. High-pressure phase relations in the systems FeS-MnS and FeS-MgS (in preparation). (Chapter 5)

McCammon, C.A. and Liu, L. (1983) The effects of pressure and temperature on nonstoichiometric wüstite, Fe_xO: The iron-rich phase boundary, Phys. Chem. Minerals, in press. (Chapter 6)

McCammon, C.A. and Price, D.C. A Mössbauer study of Fe_xO where $x > 0.95$ (in preparation). (Chapter 7)

McCammon, C.A., Ringwood, A.E. and Jackson, I. (1983). Thermodynamics of the system Fe-FeO-MgO at high pressure and temperature and a model for formation of the Earth's core, Geophys. J. R. astr. Soc. 72 577-595. (Chapter 8)

McCammon, C.A., Ringwood, A.E. and Jackson, I. (1983). A model for formation of the Earth's core, J. Geophys. Res. 88 (supplement) A501-A506. (Chapter 8)

In all but the latter two manuscripts, the coauthors' contributions were mainly of collaborating on original ideas of the first author. The latter two manuscripts were based on original ideas of A.E. Ringwood, which were developed by the first author using thermodynamic calculations and arguments in collaboration with A.E. Ringwood and I. Jackson. The manuscripts were written by the first author.

In this thesis standard deviations are generally given in terms of the last digit of the quantity, and follow in parentheses, e.g. 102.3(4) means 102.3 ± 0.4.

ABSTRACT

The complex and diverse behaviour exhibited by transition metal compounds is primarily attributed to the presence of d electrons in their outer bonding orbitals. The behaviour of FeO, FeS and some of their solid solutions is explored in the context of transitions at high pressure that have potential relevance to geophysics. The transitions studied are changes in spin state, magnetic transitions, changes in degree of electron delocalization, changes in oxidation state and B1/B8 (NaCl/NiAs) polymorphism. Mössbauer spectra recorded of a series of (Fe,Co)S solid solutions in the B8 structure imply increasing delocalization of electrons between Fe and S as the CoS endmember is approached, resulting in substantially decreased magnetic hyperfine interactions involving the Fe nuclei. Based on the similarities in Mössbauer parameters and interatomic distances between high-pressure phase FeS and ^{57}Fe:CoS, the degree of electron delocalization may be similar in the two compounds. Mössbauer spectra recorded of a series of (Fe,Mn)S and (Fe,Mg)S B1 solid solutions enables an assessment of the likely physical properties of the hypothetical phase FeS(B1) to be assessed. FeS(B1) is inferred to be more ionic than FeS(B8), and nonmetallic, and ΔV between the B1 and B8 polymorphs is calculated to be - 7.2%. The large negative ΔV should result in an exsolution of a B8 phase from (Fe,Mg)S and (Fe,Mn)S B1 solid solutions at high pressure, and this behaviour is confirmed experimentally. The low and pressure-independent solubilities observed for Mg and Mn in the B8 phase suggest that B8 polymorphism is unlikely for both MnS and MgS at high pressure. The change in stoichiometry (oxidation state) of Fe_xO in equilibrium with Fe is determined experimentally at high pressure and temperature, and correlation of the experimental results with theoretical calculations of the phase boundary suggests that the bulk modulus of Fe_xO does not vary significantly with composition for $x \lesssim 0.96$. One consequence of this conclusion is that changes in stoichiometry of Fe_xO at high pressure should result in only small changes in density. The nature of the defect structure of Fe_xO ($x = 0.95$ to 0.98) is explored using Mössbauer spectroscopy, and a physical model which behaves in a consistent manner according to the changing numbers of defects indicates that the relative populations of defect arrangements vary rapidly with composition. Shock wave data for MgO and $Fe_{0.94}O$ appearing in the literature suggest similar behaviour of (Fe,Mg)O and (Fe,Mg)S, namely

exsolution of essentially pure FeO(hpp) from (Fe,Mg)O B1 solid solutions at high pressure. Thermodynamic calculations of the phase boundary indicate that FeO(hpp) exsolution is not likely to be important in the present-day lower mantle, but may have been important in the formation of the Earth's core. Evidence for the miscibility of Fe and FeO in the liquid state is reviewed, and a series of schematic phase diagrams of the system Fe-FeO at high pressure is proposed where a low melting point alloy forms, analagous to the system Fe-FeS at low pressure. Exsolution of FeO(hpp) from (Fe,Mg)O(B1) and the low melting point Fe-FeO alloy provide a means of incorporating large amounts of oxygen into the Earth's core.

TABLE OF CONTENTS

CHAPTER 1 INTRODUCTION

Physical properties of the Earth's interior such as density, elasticity and electrical conductivity can be measured from the surface of the Earth using seismic, gravity and electromagnetic methods. A synthesis of information derived from these sources with temperature-pressure-depth profiles and results of detailed studies of relevant minerals at high P,T can provide models of the Earth in terms of mineralogy and chemical composition. This method has been relatively successful in constraining the composition and mineralogy of the upper mantle and transition zone because of access to the upper $\sim$ 200 km of the mantle through magmatic material, and the relatively large body of experimental data available regarding the behaviour of Na, Ca, Al, Mg and Fe silicates at high temperatures and pressures up to $\sim$ 30 GPa (corresponding to $\sim$ 800 km depth within the Earth). As a consequence of the more limited information available from experiments at higher pressures and the uncertainty concerning the nature of the 650 km discontinuity, the composition and mineralogy of the lower mantle and core are relatively less well constrained.

1.1 Composition and Mineralogy of the Lower Mantle and Core

1.1.1 Lower mantle

The lower mantle extends from 800 km to 2800 km depth within the Earth, and is characterized by a relatively uniform variation of seismic wave velocities with depth. Recent density models derived from inversion of gross Earth data (e.g. Dziewonski and Anderson, 1981) indicate that deviations (if present) from homogeneity must be minor, and they are not necessary to account for the bulk of the available observational evidence. There is, however, evidence from recent body wave studies of fine structure in the uppermost lower mantle to depths of $\sim$ 1200 km (Hendrajaya, 1981; Muirhead and Hales, 1980; Wright, 1983) and in the lowermost mantle below 2400 km depth (Wright and Lyons, 1981; Lay and Helmberger, 1983). The probable mineralogy of the lower mantle has been inferred on the basis of shock wave experiments and static phase transformation studies of upper mantle mineral assemblages at high P,T to be a mixture of $(Mg,Fe)SiO_3$ (perovskite), $(Mg,Fe)O$ (rocksalt), $Ca_2Al_2SiO_7$ (sodium titanate) and $NaAlSiO_7$ (calcium ferrite) (Liu, 1978; Liu, 1979; Ringwood, 1979).

Studies regarding the chemical composition of the lower mantle have involved either (1) relating seismic models to elasticity-density-pressure profiles of relevant minerals obtained from shock compression studies or equations of state based on low-pressure elasticity data, or (2) comparing experimentally measured incompressibilities and densities of the relevant mineral assemblages with the incompressibility and density of the lower mantle obtained by extrapolating lower mantle parameters to standard pressure-temperature conditions using adiabatic equations of state. There are several uncertainties, however, which constrain proposed models of lower mantle composition to be only consistent with available data, and by no means unique. These uncertainties include the nonuniqueness of seismic lower mantle density models (Worthington, 1973), differences in phase and temperature between the lower mantle and shock compression curves (e.g. Davies, 1974), and the wide trade-off between the composition and temperature of the lower mantle and the assumed properties of lower mantle phases (Davies, 1974; Jackson, 1983). A lower mantle composed of pyrolite (a widely accepted model of upper mantle composition; see Ringwood, 1975; Green et al., 1979) has been shown to be approximately consistent with available seismic and laboratory data in a wide variety of independent analyses (e.g. Ringwood, 1970; Davies, 1974; Mao, 1974; Ringwood, 1975; Graham and Dobrzykowski, 1976; Watt and O'Connell, 1978; Jackson and Ahrens, 1979; Jackson, 1983), and while not required, substantial enrichment in silica of the lower mantle relative to the upper mantle, possibly coupled with iron depletion, is equally consistent with the seismological and laboratory data.

1.1.2 Core

The outer core extends from 2900 km to 5080 km depth within the Earth, and is interpreted to be liquid by the absence of shear wave propagation. The inner core is inferred to be solid from free oscillation data which are best fit with finite rigidity ($V_s \sim 3.5$ km/sec) for the inner core.

Comparison of seismic pressure-density profiles with shock compression curves of various cosmochemically abundant materials has revealed that the core is composed predominantly of Fe, mixed with an uncertain, though probably small, amount of Ni. Seismic models indicate, however, that the core is $\sim$8-10% less dense than pure Fe at similar conditions, and therefore a light element (or elements) must be present to account for the discrepancy (first noted by Birch, 1952; supported by numerous later

studies; see Brett, 1976, and references therein for a review). It is generally believed that the light element is confined to the outer core, leaving an inner core of relatively pure Fe-Ni.

The nature of the light element, X, is important for a number of reasons. The temperature at the inner core-outer core boundary is related to the freezing of Fe-Ni from the liquid, and is determined by melting relations in the Fe-Ni-X system. Several models for the Earth's geodynamo (e.g. Gubbins, 1977; Loper, 1978) have proposed that the power comes from freezing of the outer core material; the dynamics of this process are influenced by the abundance and density of the light element in the outer core and melting relations in the relevant system. The electrical conductivity of the outer core is also likely to be sensitive to composition (Johnston and Strens, 1973), affecting the energetics of the core (Bullard and Gellman, 1954). The nature of the light element is important in constructing models of core formation which require knowledge of phase relations in the relevant systems (particularly Fe-X, but also Fe-X-MgO-SiO_2) at lower P,T conditions to describe the partitioning of the light element into the core.

1.2 Studying Iron Minerals at High P,T

The importance of iron mineral studies at high P,T to determining the composition of the lower mantle and core is evident from the above discussion, and emphasizes the need for more detailed studies at higher pressures and temperatures. Compared to Na, Ca, Mg and Al silicates, the behaviour of Fe compounds at high P,T is generally less well catalogued. This results partly from the structure of the cation outer electrons. Na^+ ($1s^2 2s^2 2p^6$), Mg^{2+} ($1s^2 2s^2 2p^6$), Al^{3+} ($1s^2 2s^2 2p^6$) and Ca^{2+} ($1s^2 2s^2 2p^6 3s^2 3p^6$) all have closed electron shell configurations, and behaviour of their oxides and silicates follows numerous empirical systematics which have been derived from experiments involving similar compounds over a number of years. It is generally observed, however, that transition metal compounds do not follow these systematics, because the outer electronic configuration of transition metal ions involves partially filled d electron orbitals, giving rise to a wide range of different phenomena.

1.2.1 Transition metal chemistry

Elements of the first transition series have the electronic configuration ($1s^2 2s^2 2p^6 3s^2 3p^6 3d^{10-n} 4s^{1 \text{ or } 2}$) where the 4s electrons and one or more 3d electrons are lost when forming ions. In an isolated transition metal ion, the five d orbitals are degenerate, but in a crystal lattice the effect of a nonspherical electrostatic field splits the five d orbitals according to the type, position and symmetry of the ligands surrounding the transition metal ion. Under several simplifying assumptions, the orbital energies can be calculated using crystal field theory; Fig. 1.1 illustrates the distribution of electrons in the 3d energy levels of a d^6 ion (e.g. Fe^{2+}) in tetrahedral and octahedral sites. The lower relative energy associated with d^6 ions in octahedral coordination explains the preference of Fe^{2+} for octahedral sites.

The presence of partially filled d orbitals increases the number of possible transitions which must be considered when interpreting data or predicting behaviour of transition metal compounds at high P,T. Several transitions are discussed below:

(1) High-spin → low-spin transitions

Distribution of the d electrons between orbitals is governed by two opposing tendencies: electrostatic repulsion between electrons favours the distribution of electrons in as many different orbitals as possible, while the crystal field effect favours spin pairing of electrons in the stabilized orbitals. At atmospheric pressure most Fe^{2+} compounds (oxides, silicates, some sulphides) are in the high-spin state, where there are four unpaired electrons (Fig. 1.2). The crystal field energy varies approximately inversely with the fifth power of the interatomic distance ($\Delta \sim \Delta_o (r_o/r)^5$) and the spin-pairing energy decreases with increasing covalency of the metal-ligand bond, so the low-spin state should be stable for Fe^{2+} at sufficiently high pressure. The decrease in the number of unpaired electrons (see Fig. 1.2) and the reduction in ionic radius of the low-spin state result in diamagnetic behaviour and a significantly increased density of the Fe^{2+} low-spin compound.

(2) Change of oxidation state

The relatively gradual increase of ionization potential with ionic charge leads to a range of possible oxidation states for most first-row transition metal ions. Formation of nonstoichiometric compounds, such as Fe_xO, in which vacancies are electrostatically balanced by oxidation of

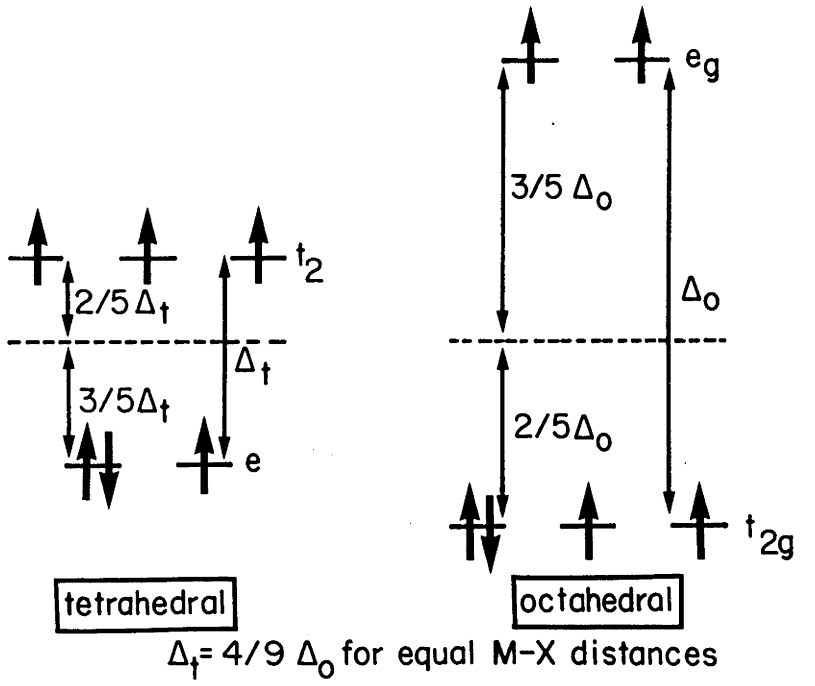

Fig. 1.1 Relative energy levels of d orbitals of a transition metal ion in tetrahedral and octahedral coordinations, showing the distribution of electrons for a high-spin d^6 ion (after Burns, 1970).

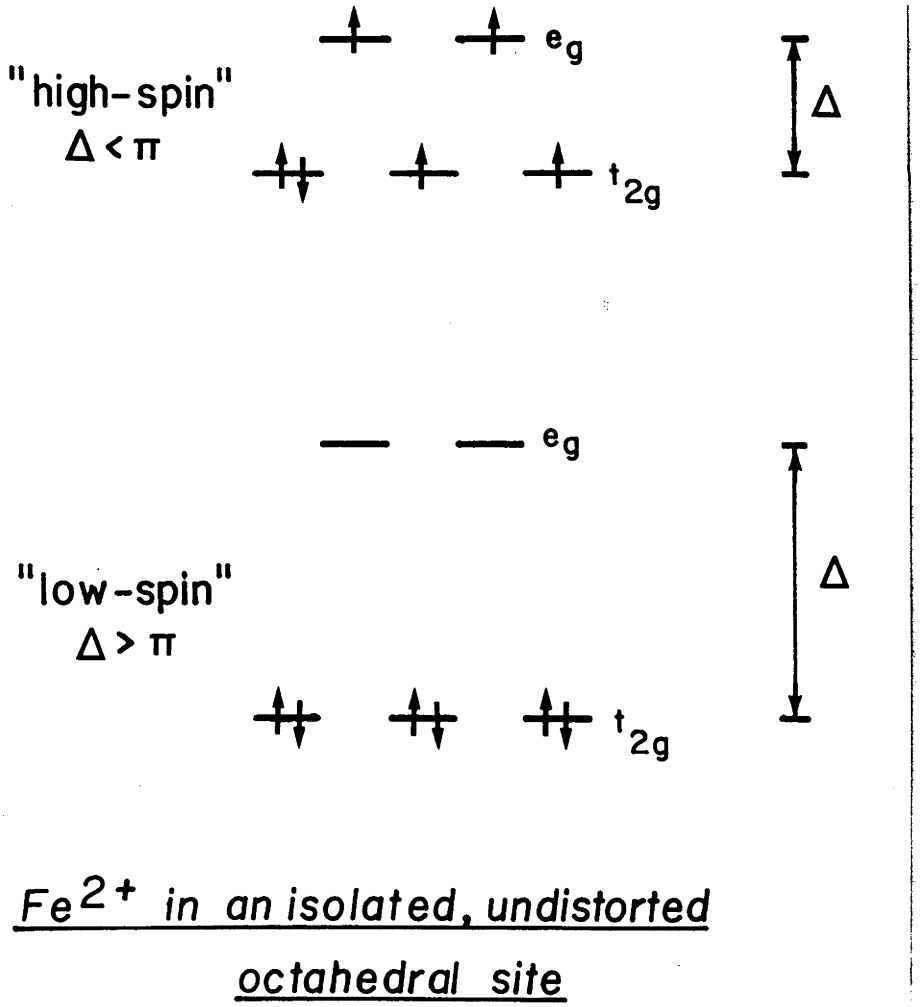

Fig. 1.2 Distribution of d electrons for high-spin Fe^{2+} and low-spin Fe^{2+}. Δ is the crystal field splitting and π is the spin pairing energy.

other cations, is energetically favoured in a number of transition metal systems (the monoxides, in particular). The equilibrium composition of a nonstoichiometric compound is sensitive to the partial pressure of the relevant constituents in the gaseous phase, and therefore varies as a function of pressure and temperature. Because molar volume and elastic properties may vary with composition, a nonstoichiometric compound can undergo a continuous transition at high pressure which changes its density.

(3) Metallic transitions

Although not restricted to transition metal compounds, metallic transitions are more likely to occur in Fe compounds (e.g. oxides and sulphides) at lower pressures than in Mg, Na, Ca and Al oxides and silicates because of d electrons. Metallic transitions are generally described in terms of band theory, which regards the electrons as occupying bands which are constructed by overlapping metal and ligand atomic orbitals (tight binding model). A solid is regarded as an insulator if all of the occupied bands are full of electrons, and as a metal if any bands are only partially full.

The d bands in transition metal compounds are constructed by mixing of metal d orbitals with ligand s and p orbitals, with the band width dependent on the degree of mixing. These compounds tend towards metallic behaviour as pressure is increased, because the enhanced overlap between metal and ligand atomic orbitals increases the degree of electron delocalization by broadening the bands. It is also possible to have discontinuous insulator-metal transitions at high pressure, and there are a number of proposed mechanisms (e.g. Van Zandt and Honig, 1974). All involve a drastic increase in the conducting properties of the solid, and usually a significant increase in density.

(4) Magnetic transitions (order-disorder)

The unpaired electrons of transition metal ions contribute to a net magnetic moment of each atom, which can interact with magnetic moments on other atoms to produce a bulk magnetization of the crystal. The magnetization varies as a function of pressure and temperature, and therefore transitions corresponding to ordering or disordering of atomic spins are possible. These transitions can involve changes in density because there may be coupling between elastic strain and magnetization direction, leading to a change in the unit cell on magnetization. Examples

are FeO, MnO and MnS which exhibit a progressive rhombohedral distortion on cooling below the Néel temperature at atmospheric pressure. Although density changes associated with magnetic transitions at high pressure are likely to be small, the drastic change in magnetic properties must be considered in determining the behaviour of the high-pressure phase.

1.2.2 Indirect experimental methods

It is often difficult to determine the crystal structure of a high-pressure phase if it cannot be quenched to atmospheric pressure, particularly if the high-pressure phase is of low symmetry since many x-ray diffraction lines are required to determine the structure unambiguously. If large transition pressures are involved, the relative uncertainties of the x-ray lines may be increased due to nonhydrostatic stress and pressure gradients on the sample. In addition, the change in crystal structure may be accompanied by one of the transitions discussed above, several of which are likely to be reversible with pressure (high-spin → low-spin, metallic and magnetic), and these may further impede unambiguous determination of the crystal structure. It is often convenient, therefore, to study transitions in analogue compounds at lower pressures.

The use of analogue compounds in studying systems which are experimentally difficult has been successful in a number of studies. The crystal chemical relationships between silicates and germanates have been exploited to predict silicate phase transformations at high pressure (Ringwood, 1970), and the elastic properties of many compounds can be predicted on the basis of their analogues (Liebermann, 1974; Jones and Liebermann, 1974; Davies, 1976). It is not surprising to learn, however, that transition metal oxides do not follow elastic systematics derived for other oxides such as MgO, CaO or SrO (Davies, 1976), and much of the discrepancy may be accounted for by crystal field contributions to the lattice energy (Ohnishi and Mizutani, 1978).

Analogues for transition metal compounds must be judged not only on the basis of similar crystal structure, but also on the basis of similar outer electron configuration; thus analogues should be chosen for the coordinating ligands, not the transition metal ion. One possibility is the use of transition metal chalcogenides (S, Se, Te) as analogues for transition metal oxides. Although little data is available to test the success or failure of the analogues, the substantial covalent bonding

involved in transition metal chalcogenides relative to transition metal oxides indicates that the greatest use of the analogues is probably in detailing already known transitions and identifying new transitions which may occur in the oxides at higher pressure, without necessarily expecting a one-to-one correlation between transitions in chalcogenides and oxides.

1.3 Outline of Thesis

This thesis presents work relating to the behaviour of FeO, FeS and some of their solid solutions at high pressure. Both O and S have been proposed as candidates for the light element in the core (Birch, 1952), and therefore studies of both FeO and FeS are important. FeS is also studied in this thesis as an oxide analogue, in the spirit of providing further ideas for transitions of FeO at high pressure. Chapter 2 describes the experimental apparatus, calibration and run procedures that were used in the experiments. Chapters 3 and 4 present studies that were undertaken of (Fe,Co)S, (Fe,Mn)S and (Fe,Mg)S solid solutions to study different aspects of the behaviour of Fe^{2+}, and to derive new knowledge about the FeS(B1) endmember. Chapter 5 describes studies of (Fe,Mn)S and (Fe,Mg)S that define the high-pressure phase relations, and their relevance to (Fe,Mg)O. The stoichiometry of Fe_xO is studied as a function of pressure and temperature in Chapter 6, and a thermodynamic model is developed to account for the observations; the analysis demonstrates that the observations tightly constrain the variation of elastic properties with composition. Chapter 7 explores the defect structure of Fe_xO (via the Mössbauer spectra) which might account for the proposed elastic properties. Chapter 8 presents calculations of the FeO-MgO phase diagram at high P,T, and implications for the lower mantle are discussed. A consideration of the Fe-FeO phase diagram at high P,T completes the framework of a model for core formation involving oxygen as the principal light element. Mössbauer spectroscopy is a prominent tool used in studying FeO, FeS and their solid solutions in this thesis; the appendix provides a brief introduction to the subject for the uninitiated.

CHAPTER 2 EXPERIMENTAL METHODS

2.1 Large-Volume High-Pressure Apparatus

Advantages of using this type of apparatus include well controlled and constrained P,T conditions and a relatively large sample volume. The major disadvantage is restriction to only moderate pressures (< 7 GPa).

2.1.1 Apparatus description and run procedure

a) Piston Cylinder - The single-stage piston cylinder apparatus was used (in the "piston-in" configuration described by Green et al., 1966) to generate pressures of up to 4.5 GPa. The sample is loaded into the assembly illustrated in Fig. 2.1a and placed inside a 0.5" (inner diameter) pressure vessel. Normal run procedure involves the application of an axial load of $\sim$ 180 tons (metric) to the pressure vessel via a hydraulic press, followed by the use of a second hydraulic press to drive a 0.5" piston which compresses the sample assembly. Current is applied to the graphite furnace until the run temperature is reached, and frequent corrections are made to the applied load during the course of a run to maintain the pressure to within $\pm$ 0.05 GPa. The run is quenched by terminating the flow of current to the furnace, causing the temperature to drop to 500 K within 10 seconds, and bleeding off the pressure over a period of about 5 minutes.

b) Girdle Apparatus - The high-pressure girdle apparatus described by Liebermann et al.(1974) and modified by Ringwood and Major (unpublished data) was used to generate pressures in the range 5-7 GPa. The sample is loaded into the assembly shown in Fig. 2.1b and placed inside a tungsten carbide die which opens out at either end with a 65° angle. The load is applied using tungsten carbide pistons which taper with 60° angles to a truncated face. Unfired pyrophyllite gaskets are placed between the walls of the die and the anvils. Normal run procedure consists of a gradual application of pressure until the run pressure is reached and then a controlled application of temperature. Only minor corrections to the pressure are necessary during a run. Quenching of the run is performed in an identical manner to the piston cylinder except that bleeding off of the pressure occurs overnight.

c) Bridgman Anvil Cell - A large-scale version of the apparatus described by Nishikawa and Akimoto (1971) was used to generate pressures in the range 5-7 GPa. The sample assembly is surrounded by a 1.5" diameter

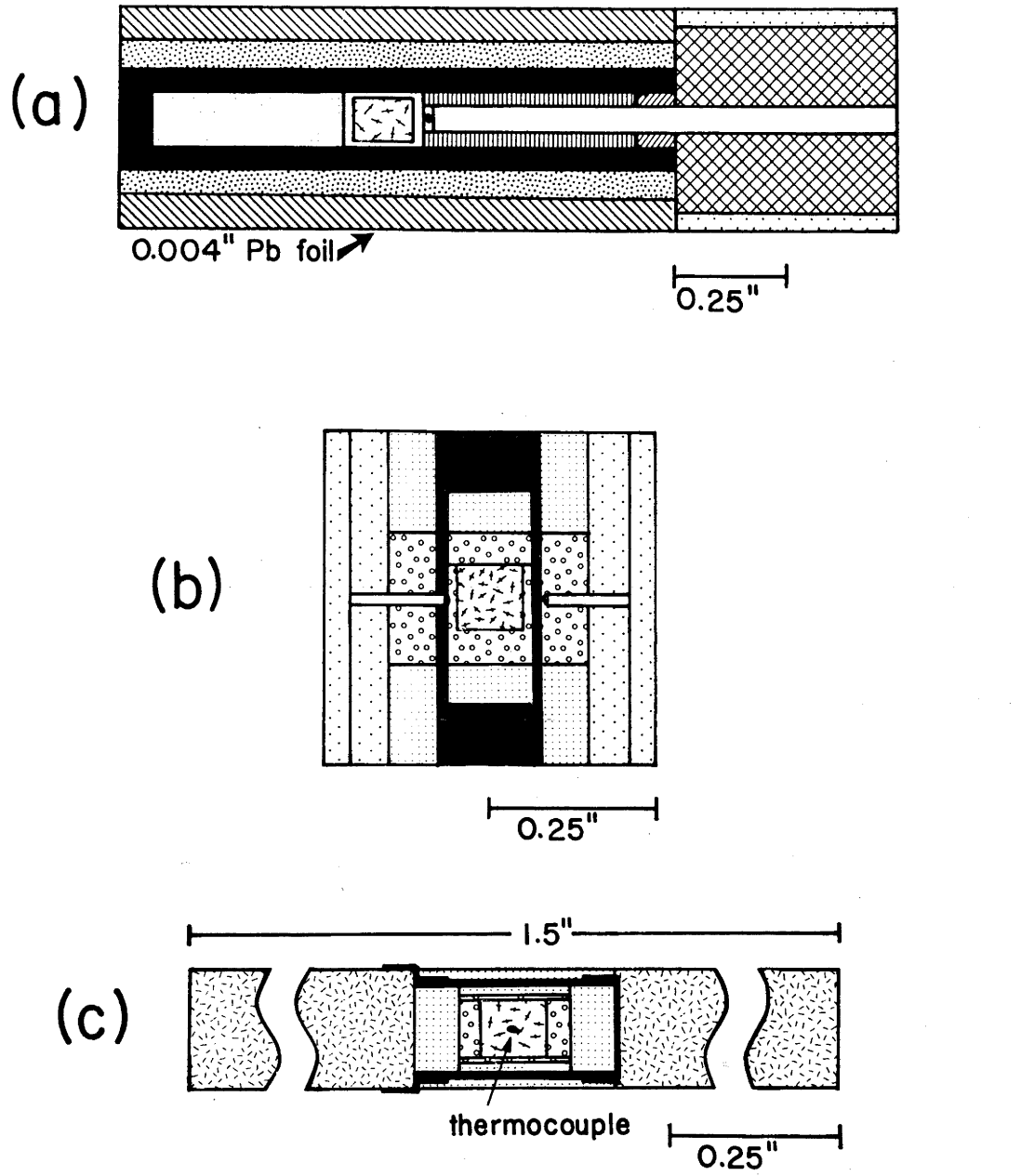

Fig. 2.1 Illustration of the sample assembly for the (a) piston cylinder apparatus, (b) girdle apparatus, (c) Bridgman anvil cell.

pyrophyllite ring which was prefired at 923 K for 1.5 hours (Fig. 2.1c). The assembly is placed between opposed tungsten carbide anvils, each with a 30^{o} taper ending at a truncated face of 1.5" diameter. The anvils are slowly loaded until the required pressure is reached and the subsequent run procedure and quenching process take place as described for the girdle apparatus.

2.1.2 Temperature measurement

Temperatures were measured with a $Pt/Pt_{90}Rh_{10}$ thermocouple, and are uncorrected for the effect of pressure on the e.m.f. Experiments by Getting and Kennedy (1970) indicate that run temperatures measured with $Pt/Pt_{90}Rh_{10}$ thermocouples near 1273 K at 3 GPa would be a maximum of 15 K higher than actually measured. Single thermocouples were used for runs in the piston cylinder and Bridgman anvil cell, whereas two thermocouples were employed with the girdle apparatus. Temperatures generally differed by 20 K - 25 K between the two thermocouples; the higher temperature of the two was always taken to be the run temperature.

2.1.3 Pressure calibration

a) Piston Cylinder - Experimental pressures in the piston cylinder are determined on the basis of the applied load and a 10% ($\pm$3%) downward correction for friction. The friction correction is the result of the work of several investigations, the most recent being a study by O'Neill and Hibberson (RSES Annual Report, 1981) who determined correction factors of 8-13% for talc cells in the piston cylinder on the basis of LiCl and AgCl melting points.

b) Girdle Apparatus - Experimental pressures were determined using the results of experiments by Ohtani (unpublished data) on the quartz-coesite and fayalite-spinel transitions (Fig. 2.2a). Pressures based on this calibration curve are thought to be accurate to within $\pm$ 0.5 GPa.

c) Bridgman Anvil Cell - Calibration curves for the Bridgman anvil cell are very sensitive to the firing temperature of the 1.5" pyrophyllite gasket. Previous room temperature (Ringwood and Major, unpublished data) and 1273 K (Sinclair, 1982) calibration curves for gaskets fired at 1123 K are illustrated in Fig. 2.2b. The pyrophyllite used in the calibrations was not available for the present work, however, and the new batch of pyrophyllite was fired at a temperature (923 K) where the behaviour of the new pyrophyllite most closely matched the old pyrophyllite under loading

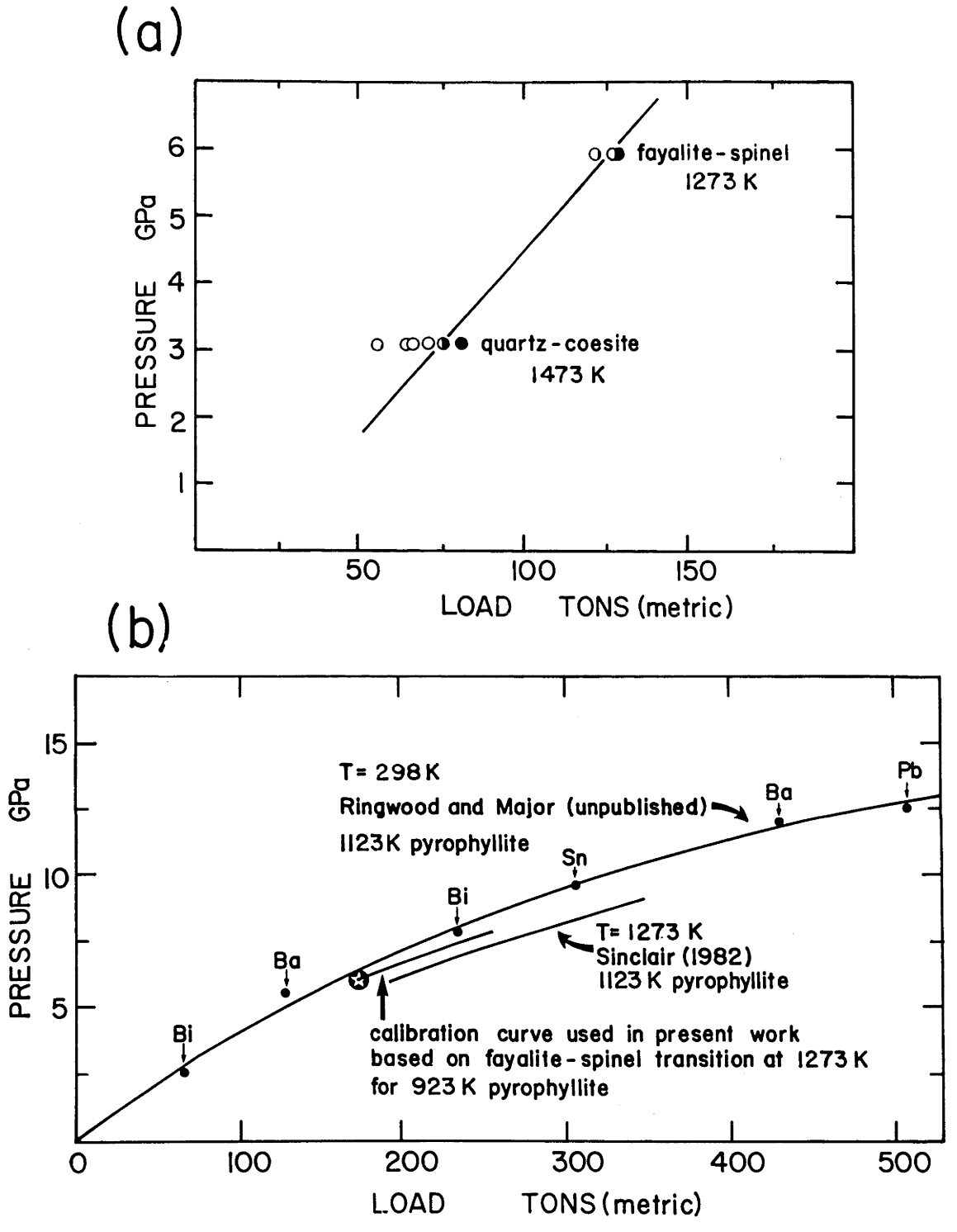

Fig. 2.2 (a) Calibration curve for the girdle apparatus based on data of Ohtani (unpublished). The solid circles indicate the presence of the high-pressure phase. (b) Calibration curve for the Bridgman anvil cell. The star represents the transition point determined between fayalite and spinel at 1273 K using the 923 K pyrophyllite.

stress. A set of calibration runs using the fayalite-spinel transition was performed at 1273 K, and the calibration curve for the new pyrophyllite was drawn through this point parallel to the old pyrophyllite calibration curve at 1273 K (Fig. 2.2b). Pressures based on the 923 K pyrophyllite calibration curve are thought to be accurate to within ± 0.5 GPa.

2.2 Diamond Anvil Cell

Advantages of using the diamond anvil cell include routine access to relatively high pressures and the ability to perform "in-situ" experiments (i.e. while the sample is under pressure) such as visual observation, laser heating and x-ray diffraction. Disadvantages include poorly constrained P,T conditions and a small sample volume which restricts the quality of techniques such as x-ray diffraction.

2.2.1 Quench experiments

Phase transformations that could be quenched were studied using an LD-type diamond anvil cell designed by Bassett and Takahashi (1965) which is capable of generating up to 30 GPa using 0.125 carat diamonds. The powdered sample is placed between the faces of two opposed gem-quality diamonds which are mounted on the ends of two pistons driven together by a lever and spring assembly. The size of the sample is 0.3 mm diameter and the region of highest pressure and minimum pressure gradient is at the centre and is approximately 0.1 mm in diameter. Once under pressure the sample is heated using a continuous Nd-doped YAG laser focussed on the sample. The pressure is then released and the sample is placed on the end of a 0.1 mm diameter collimator which is mounted in a conventional Debye-Scherrer camera (57.3 mm diameter) to record the x-ray diffraction pattern of the sample. Exposure times range from 100-200 hours using a Phillips x-ray generator operating at 800 W. NaCl is often mixed with the sample before the run to provide an internal standard with which to calibrate the x-ray film (assuming that NaCl does not react chemically with the sample during the run).

The applied pressure is determined on the basis of the length of the compressed spring, which was standardized using NaCl and the compression curve for NaCl reported by Weaver et al.(1971) (Liu, unpublished data). The estimated uncertainty is ± 10% of the measured pressure. The actual pressure (i.e. the pressure at high temperature) may differ from the pressure at room temperature, however. The temperature is estimated by eye from the brightness of incandescent light emitted by the sample during

heating. The uncertainty in temperature is generally ± 50% of the estimated temperature. Experimental problems such as variation in the amount of energy absorbed by the sample, non-uniform heating and variation in the emissivity of the sample have prevented a substantial improvement in the accuracy of temperature measurement.

2.2.2 Compression experiments

Room temperature compression curves were measured using a UP-type of diamond anvil cell designed by Bassett et al.(1967). The UP-type cell is similar to the LD-type cell, except that pressure is applied via a screw-in piston instead of a lever and spring assembly. Powdered sample is placed between the diamond faces and a small amount of pressure is applied. An x-ray diffraction pattern is taken of the sample using the diamond anvil cell as an x-ray camera. A 0.1 mm diameter collimator mounted on one side of the diamonds directs the x-ray beam onto the sample and a curved film cassette with a radius of 50 mm mounted on the other side of the diamonds records the diffraction pattern. Filtered Mo $K\bar{\alpha}$ radiation is used exclusively for these experiments due to the large amount of energy absorbed by the diamonds. Exposure times range from 24-36 hours using a Rigaku rotating anode x-ray generator operating at 11 kW. More pressure is applied to the diamond anvil cell and another x-ray diffraction pattern recorded. This process is repeated until a complete curve of unit cell volume versus pressure is obtained. Room temperature phase transitions can also be studied by this technique.

To calibrate the x-ray film a very thin platelet of NaCl is placed on the outside face of the diamond facing the film cassette (note that the NaCl is not under pressure). Measuring the position on the x-ray film of diffraction lines from the external NaCl standard enables the sample to film distance to be calculated. The internal pressure is calculated by measuring the diffraction lines produced by an internal NaCl standard which has been premixed with the sample in the ratio 1:2. By comparing the cell volume of the internal NaCl standard with the compression curve reported by Weaver et al.(1971) the sample pressure can be determined. The uncertainty is a function of the relative error in reading lines on the x-ray film and generally varies between 5-10% of the measured pressure.

2.3 Analytical Techniques

2.3.1 X-ray diffraction

Samples (excluding those from diamond anvil experiments) were x-rayed using a Debye-Scherrer camera (114.6 mm diameter) with a 0.9 mm diameter fine collimator. The samples were prepared by crushing in an agate mortar, mixing with clear nail polish and rolling to form a needle of 0.1-0.3 mm diameter. Fe $K\overline{\alpha}$, Co $K\overline{\alpha}$ or Cu $K\overline{\alpha}$ radiation was used depending on the composition of the sample. Exposure times varied from 2-24 hours using a Phillips x-ray generator operating at 800 W. X-ray films were calibrated using either NaCl(a = 564.01 $\pm$ 0.01 pm) or Si(a = 543.088 pm) as an internal standard.

2.3.2 Electron microprobe

Elemental compositions of samples were determined using an electron microprobe manufactured by Technisch Physische Dienst, Netherlands which was fitted with a Si(Li) detector (Reed and Ware, 1973; 1975). This system uses an energy-dispersive technique. Accelerating voltage was 20 kV, beam current 2.1 nA, beam size 1 μm and the counting interval 100 sec. Data was reduced by the computer program "METAL", written by N. Ware, RSES. An accuracy of approximately $\pm$ 2% is expected with the microprobe (Reed and Ware, 1975). Samples were prepared for the electron microprobe by Mr. K. Massey, RSES.

2.3.3 Mössbauer spectroscopy

Mössbauer spectra were recorded on two spectrometers, one located at Dept. Solid State Physics, ANU and the other at Dept. of Physics, Monash University, Victoria. The ANU spectrometer is based on a PDP 11/10 minicomputer which accumulates and stores eight spectra simultaneously (of 256 channels each), displays or outputs the data and generates the reference signal for the Mössbauer drives (Window et al., 1974). The reference waveform used by ANU consists of a constant acceleration signal (linear ramp) during data accumulation followed by a flyback of half the ramp period. No data is accumulated during the flyback period. Mössbauer data are punched onto paper tape to be used later for data reduction and analysis using a large computer. A 50-60 mCi ^{57}Co source diffused in a rhodium matrix was used, and counting times varied from roughly 12-36 hours, depending on the iron concentration of the sample. Mössbauer spectra were recorded at 77 K and 4.2 K using a liquid helium cryostat similar to one described by Cranshaw (1974). The Mössbauer spectrometer at

Monash University is similar to the one at ANU except that data are accumulated using a multichannel analyser in place of a minicomputer, and the reference waveform consists of two linear ramps joined together. This enables data accumulation during both sweeps of the transducer, producing a mirror-image spectrum. The final spectrum is obtained by folding the mirror-image spectrum into itself, removing any nonlinearity associated with the source-absorber geometry.

Mössbauer samples were prepared by crushing in an agate mortar, mixing with boron nitride to randomize the crystal grains and mounting in a 13 mm diameter sample holder. The concentration of iron in the samples was maintained below 5 mg/cm^2 to reduce saturation effects. The Mössbauer data were analysed by fitting the spectra to pseudo-lorentzian lineshapes (Price, 1981) using an iterative, nonlinear least squares method (Price, R.S.Phys.S. Research Report no. 7, ANU). The validity of computer fits was assessed on the basis of χ^2 values, consistency of parameters across samples and convergence of the fitting process. All Mössbauer spectra were calibrated with respect to metallic iron.

CHAPTER 3 THE SYSTEM FES-COS

3.1 Introduction

Fe_xS and Co_xS form a continuous solid solution at atmospheric pressure (Pearson, 1967, p. 789). $(Fe,Co)_xS$ crystallizes in the hexagonal NiAs (B8) structure with varying metal/sulphur ratios ranging from $x = 1$ to $x = \sim 0.87$. X-ray data for $(Fe,Co)_{0.99}S$ and $(Fe,Co)_{0.87}S$ have been reported in the literature (Vogel and Hillner, 1953; Perthel, 1960). The cell parameters of $(Fe,Co)_xS$ decrease smoothly from Fe_xS to Co_xS. The crystal lattice of Fe_xS thus contracts with the substitution of Co^{2+}.

The magnetic properties of the endmembers Fe_xS and Co_xS differ considerably. Co_xS is a Pauli paramagnet with an assumed magnetic moment of 1 μ_B per Co atom. The room temperature magnetic susceptibilities of $Co_{0.92}S$ and $Co_{0.88}S$ are 4.4×10^{-6} emu/g and 4.6×10^{-6} emu/g, respectively (Townsend et al., 1975). The magnetic properties of Fe_xS vary with stoichiometry. For $x \geq 0.92$ Fe_xS is antiferromagnetic with a Néel temperature of approximately 588-593 K, depending on the stoichiometry (Hirone et al., 1954). High-temperature magnetic susceptibility measurements indicate an effective magnetic moment of 5.24 μ_B per Fe atom (Vaughn and Craig, 1978). For $x \leq 0.92$ Fe_xS is ferrimagnetic with a Curie temperature which varies discontinuously from 473 K for $Fe_{0.92}S$ to 573 K for $Fe_{0.88}S$ (Schwartz and Vaughn, 1972).

The magnetic properties of $(Fe,Co)_{0.87}S$ have been studied as a function of composition (Perthel, 1960). At room temperature a ferrimagnetic-paramagnetic transition occurs at approximately $(Fe_{0.6}Co_{0.4})_{0.87}S$. The Curie temperature extrapolates to zero at the approximate composition $(Fe_{0.45}Co_{0.55})_{0.87}S$ (Fig. 3.1).

The mechanism of the magnetic transition which occurs as a function of composition in (Fe,Co)S is at present unknown. ((Fe,Co)S will be used henceforth to represent the general formula $(Fe,Co)_xS$.) Previous Mössbauer data from an experiment using ^{57}Co in CoS as the source and $K_4Fe(CN)_6.3H_2O$ as the absorber show no evidence of magnetic interaction in ^{57}Fe:CoS down to 80 K (Seregin et al., 1970). This suggests a change in the strength of the magnetic interaction involving the iron atoms as a function of composition.

One possible mechanism is a high-spin → low-spin transition of the

Fe^{2+} ions in (Fe,Co)S, which has also been proposed as being responsible for the high-pressure phase transition observed by Mössbauer spectroscopy in FeS (Vaughn and Craig, 1978). Fe^{2+} in FeS is in the high-spin (hs) state, whereas Co^{2+} in CoS is in the low-spin (ls) state (Townsend et al., 1975). The relative ionic radii for Fe^{2+}(ls) and Co^{2+}(ls) are 61 pm and 65 pm, respectively, compared with 78 pm for Fe^{2+}(hs) (Shannon, 1976). It is therefore possible that the decrease in interatomic distance produced by the substitution of Co^{2+} into FeS may cause a spin transition of Fe^{2+}. Observation of Fe^{2+}(ls) would provide an ideal opportunity to study the high-spin → low-spin transition in a chemically simple compound (previously studied compounds include phenanthroline, ferrocynanide and phthalocyanine complexes, among others), and may be relevant to transitions in Fe oxides at very high pressure. To investigate the magnetic transition and the possibility of Fe^{2+}(ls), the Mössbauer spectra of a suite of samples in the solid solution (Fe,Co)S were run at various temperatures.

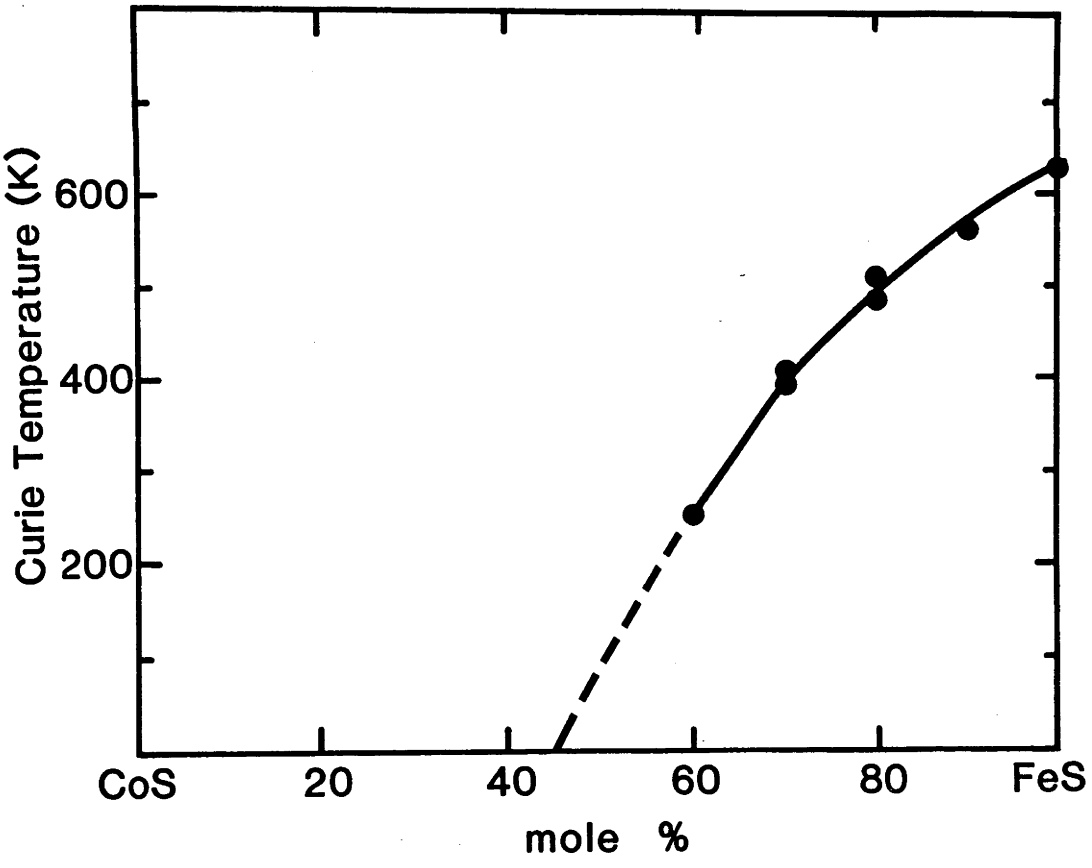

Fig. 3.1 Plot of the Curie temperature versus composition in $(Fe,Co)_{0.87}S$, taken from Perthel (1960).

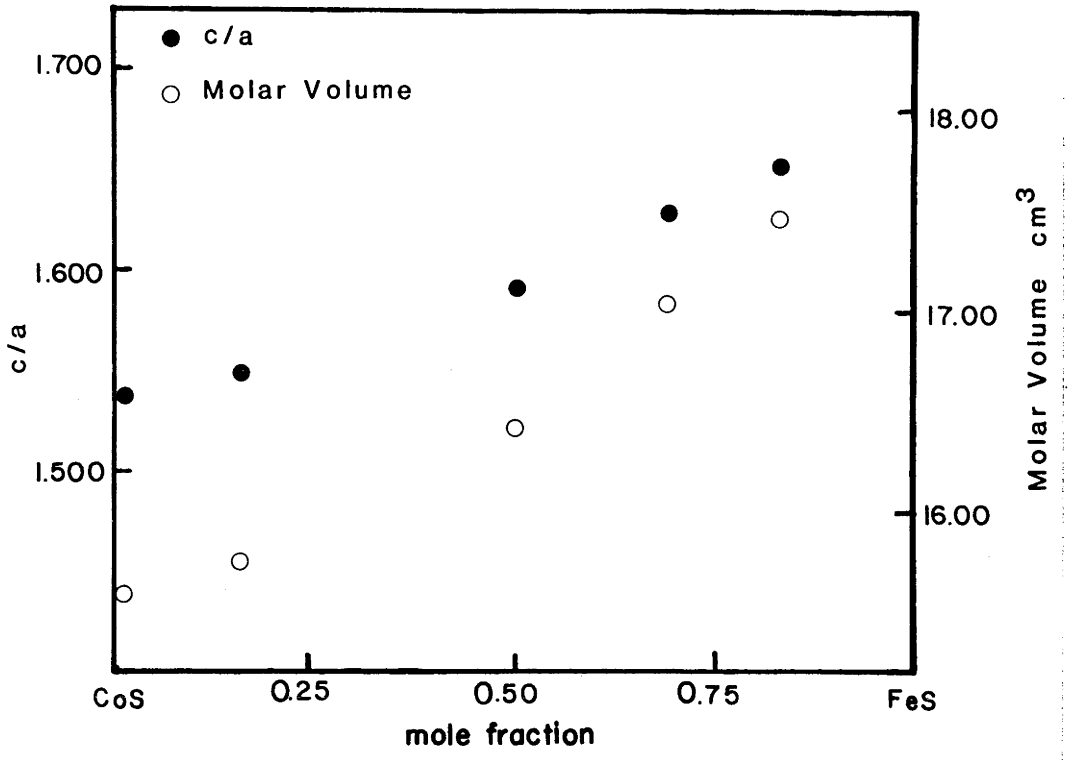

Fig. 3.2 Plot of the variation of molar volume and c/a ratio with composition in the system FeS-CoS.

Table 3.1 Composition and cell parameters for $(Fe_xCo_{1-x})_yS$

	^{57}Fe:CoS	16 mol % FeS	50 mol % FeS	69 mol % FeS	83 mol % FeS
Fe(x)	0.009(1)	0.156(3)	0.503(3)	0.692(4)	0.834(1)
Co (1-x)	0.991(1)	0.845(3)	0.497(3)	0.308(4)	0.166(1)
(Fe+Co)/S (y)	0.871(4)	0.919(7)	0.936(6)	0.958(2)	0.950(8)
a (pm)	338.8(1)	339.2(1)	340.7(1)	342.2(1)	343.5(1)
c (pm)	520.6(2)	525.0(2)	542.1(3)	557.5(12)	567.2(2)
c/a	1.537(1)	1.548(1)	1.591(1)	1.629(4)	1.651(1)
V (cm^3/mole)	15.58(1)	15.75(1)	16.41(1)	17.03(4)	17.45(1)

3.2 Experimental Procedures

Samples of varying composition of (Fe,Co)S were prepared in the following manner. Mixtures of the elements were finely ground, pelletized and sealed inside silica glass tubes evacuated to less than 10 mPa. The glass tubes were heated inside a temperature-controlled furnace at 823 K to allow the sulphur to react with the metal. After 2-3 hours the temperature was increased to 1273 K and the mixtures were sintered for 14-16 hours. The samples were quenched in water, reground, sealed inside new silica glass tubes and resintered at 1273 K. This process was repeated until x-ray diffraction patterns taken of the samples after each regrinding indicated no change in the composition of the mixture.

The x-ray diffraction patterns of all samples could be indexed according to the B8 structure; no evidence for the presence of a superstructure was observed. Small amounts (< 5%) of Fe_2O_3 were detected in some samples. The cell parameters of the samples are given in Table 3.1. There is a smooth increase in both molar volume and c/a ratio towards the FeS endmember (Fig. 3.2).

Compositions were determined using an electron microprobe and are listed in Table 3.1. The metal/sulphur ratio varies slightly from sample to sample, reflecting small variations in sample preparation. Excess sulphur was added to the starting mix of ^{57}Fe:CoS to prevent the formation of Co_9S_8 which was present in earlier runs with higher metal/sulphur ratios.

The Mössbauer spectra were recorded on a constant acceleration Mössbauer spectrometer located at Dept. Solid State Physics, R.S.Phys.S., ANU. Details of the apparatus and run procedure are given in Chapter 2.

3.3 Results

The Mössbauer spectra of the (Fe,Co)S samples are illustrated in Fig. 3.3. The nonmagnetically-split Mössbauer spectra were fitted to two quadrupole doublets with the half widths and line intensities of the components constrained to be equal. The Mössbauer parameters are listed in Table 3.2. A statistical F test was applied to determine if the reduction in χ^2 of a two doublet fit over a one doublet fit was statistically significant (Bevington, 1969). Although the results do not support the two doublet fit in all cases (see Table 3.2), the relatively large line widths indicate the likelihood of more than one doublet (an iron absorber gave a

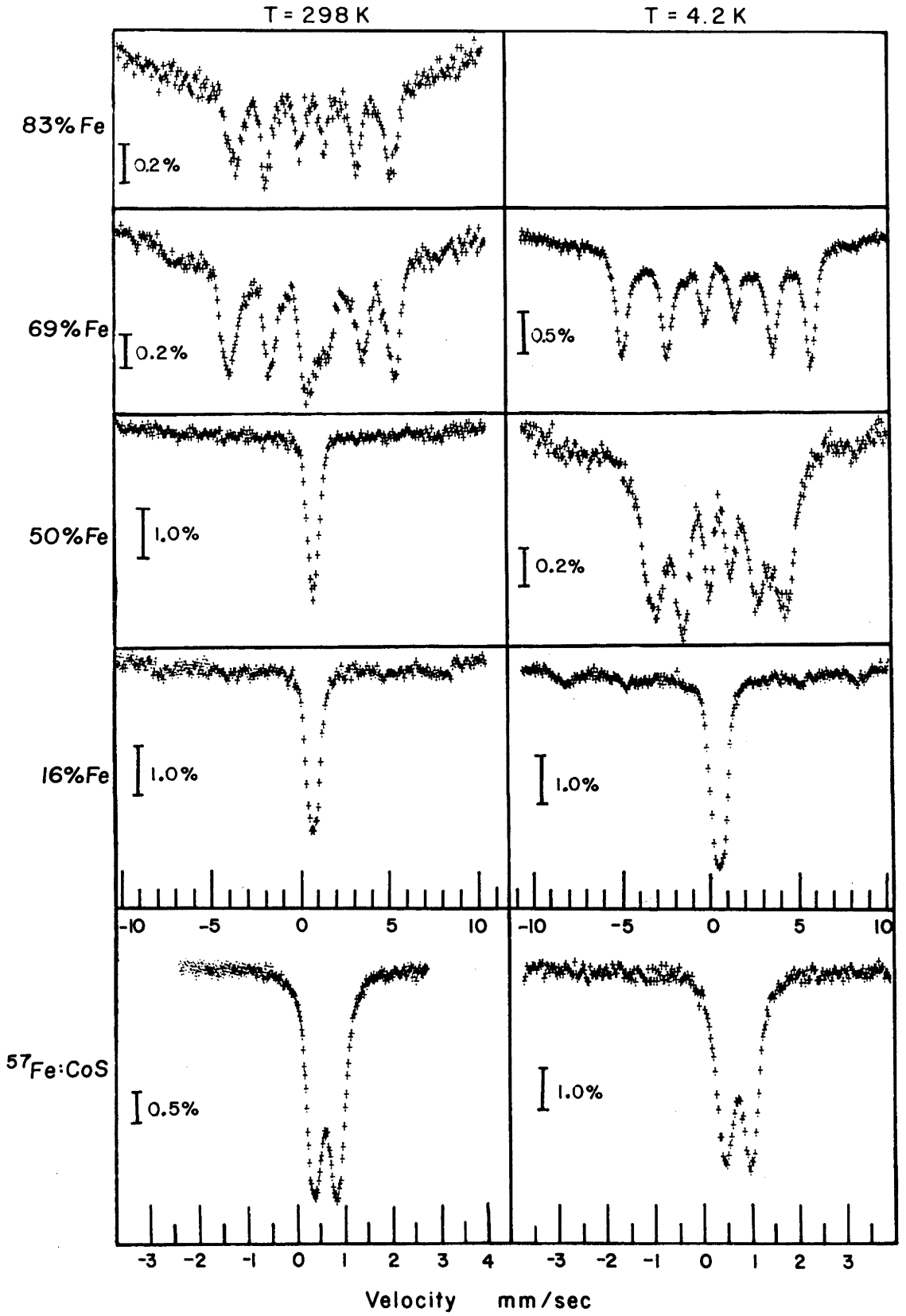

Fig. 3.3 Mössbauer spectra of (Fe,Co)S as a function of temperature and composition. The velocity scales are relative to Fe. The nonmagnetic spectra were also run on smaller velocity scales, but are not shown. Small absorption peaks corresponding to Fe_2O_3 can be observed in some spectra.

Table 3.2 Mössbauer parameters for the non-magnetic spectra of (Fe,Co)S

	50 mol % FeS T=298 K	16 mol % FeS T=298 K	^{57}Fe:CoS T=298 K	16 mol % FeS T=4.2 K	^{57}Fe:CoS T=4.2 K
δ[a] mm/sec	0.669(3)	0.594(3)	0.570(1)	0.740(4)	0.719(2)
ε mm/sec	0.330(4)	0.316(4)	0.326(2)	0.394(2)	0.338(4)
Γ mm/sec	0.314(7)	0.236(7)	0.228(3)	0.473(11)	0.303(6)
% Area	21	26	31	45	49
δ[a] mm/sec	0.683(1)	0.590(2)	0.573(1)	0.727(3)	0.730(3)
ε mm/sec	0.111(3)	0.175(2)	0.180(1)	0.143(5)	0.188(3)
Γ mm/sec	0.460(5)	0.348(6)	0.331(3)	0.471(16)	0.328(9)
% Area	79	74	69	55	51
χ^2	0.98	1.16	0.99	1.18	0.77
F_χ[b]	4.36	1.00	7.67	0.97	2.18

[a]relative to Fe metal

[b]To accept a two doublet fit over a one doublet fit at the 95% confidence level, the value of F_χ should be greater than or equal to 2.37.

Table 3.3 Mössbauer parameters for the magnetic spectra of (Fe,Co)S

	83 mol % FeS T=298 K	69 mol % FeS[b] T=298 K	69 mol % FeS T=4.2 K	50 mol % FeS T=4.2 K
δ[a] mm/sec	0.721(13)	0.759(11)	0.884(6)	0.860(10)
ε[c] mm/sec	0.03(1)	-0.15(1)	-0.09(1)	-0.03(1)
H kOe	293.0(12)	297.0(7)	338.4(5)	253.3(11)
% Area	31	40	45	32
δ[a] mm/sec	0.740(10)	0.726(14)	0.899(8)	0.849(10)
ε[c] mm/sec	0.06(1)	-0.12(1)	-0.08(1)	0.00(1)
H kOe	267.8(8)	269.1(13)	321.4(6)	218.8(8)
% Area	69	44	55	68
χ^2	0.87	1.46	2.00	1.50

[a]relative to Fe metal

[b]This spectrum also contained a quadrupole doublet with δ = 0.709(22) mm/sec, ε = 0.228(22) mm/sec, Γ = 0.717(49) mm/sec and occupied 16% of the total area.

[c]$\varepsilon = \frac{1}{4}(V_6 + V_1 - V_2 - V_5)$ where $V_{1,2,5,6}$ refer to 1st, 2nd, 5th and 6th peaks of the magnetic hyperfine spectrum arranged in order of increasing velocity.

line width of 0.25 mm/sec using the same Mössbauer source). The multiple doublets could originate from small crystallographic distortions due to metal defects or from distributional variations of cation nearest neighbours of the Fe^{2+} sites. In the latter case a set of broadened doublets corresponding to the predominant arrangements would be expected.

The magnetic Mössbauer spectra were fitted to two six-line hyperfine spectra and the data are listed in Table 3.3. The half widths and line intensities of corresponding peaks (i.e. peaks 1 and 6, peaks 2 and 5, etc.) were constrained to be equal. The multiple $^{57}Fe^{2+}$ environments seen in the magnetic Mössbauer spectra may correspond to those seen in the nonmagnetically-split spectra.

The onset of hyperfine splitting at 298 K occurs within the compositional range 50 mol % FeS to 83 mol % FeS. Although the 69 mol % FeS spectrum could be fitted to a combination of magnetically-split and nonmagnetically-split spectra, it is impossible to determine from the data if the spectrum represents two phases, one with zero hyperfine field, or one phase where some Fe^{2+} ions experience a very small exchange field not strong enough to cause hyperfine splitting. The 69 mol % FeS spectrum was therefore fitted on the basis of one phase being present since the uncertainties in the fitted parameters are large enough to encompass those which each component of a two-phase system would have.

Fig. 3.4a illustrates the variation of centre shift at 298 K as a function of composition. Only a small decrease in centre shift from the magnetic spectra to the nonmagnetic spectra is observed and the centre shift decreases as a function of decreasing Fe^{2+} concentration. It is difficult to ascertain if the centre shift varies continuously through the magnetic transition but it is clear that no large ($\gtrsim$ 0.03 mm/sec) discontinuity is involved.

The hyperfine magnetic field at the ^{57}Fe nucleus varies as a function of composition and the experimental values are illustrated in Fig. 3.4b. The field strength at 298 K of the 83 mol % FeS and 69 mol % FeS samples are identical within experimental error. The hyperfine field at 4.2 K of the 50 mol % FeS sample is substantially reduced, however. This sample was run at 100 K to determine if the hyperfine field at 4.2 K was saturated, or if the low value was merely due to the proximity of the ordering temperature to 4.2 K. The Mössbauer spectrum exhibited magnetic splitting

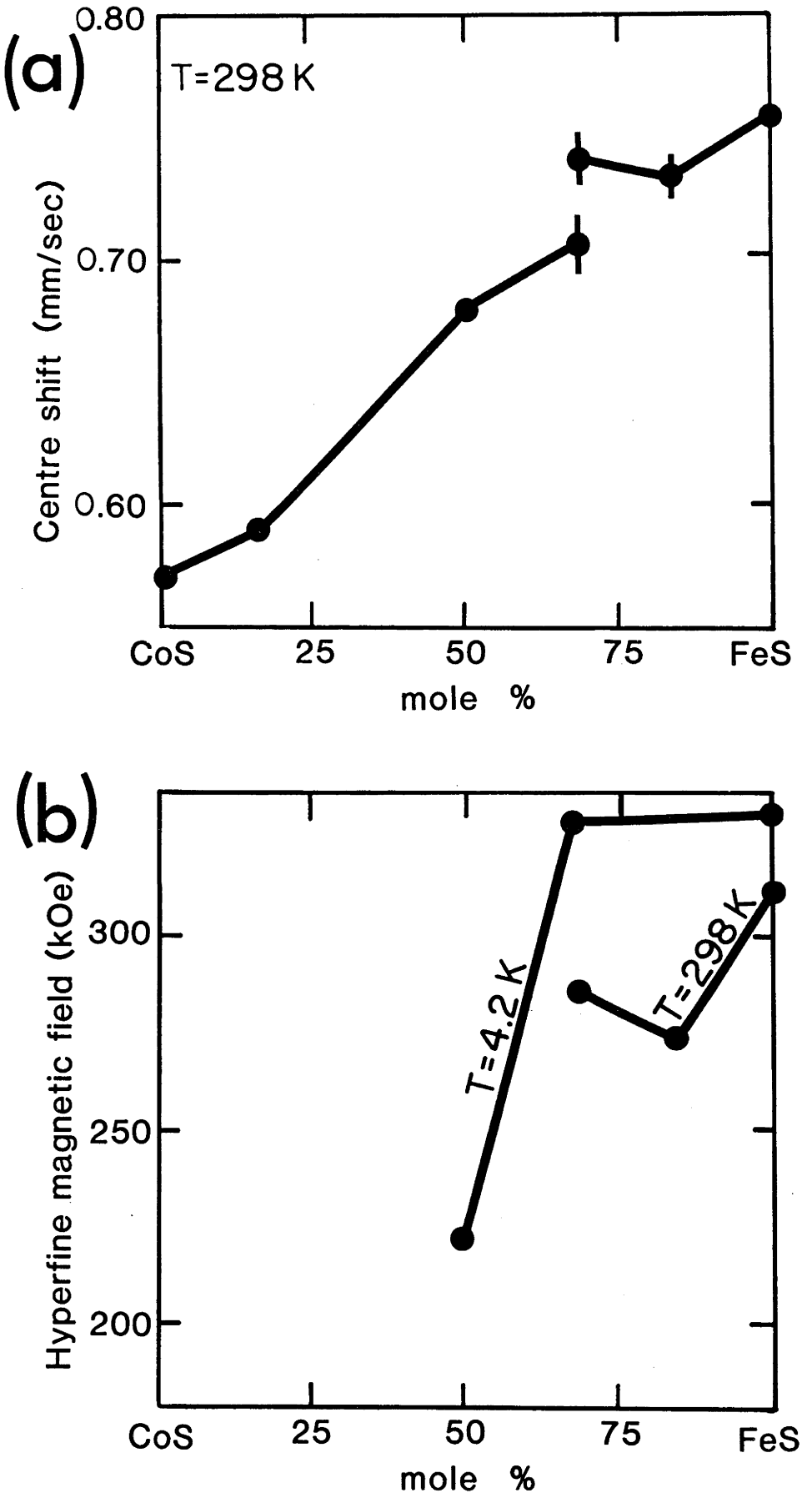

Fig. 3.4 Plot showing the variation with composition of (a) the room temperature centre shift and (b) the hyperfine field parameter. The values of δ and H were computed as a weighted average of the component spectra. The values for FeS were taken from Hafner and Kalvius (1966). The connecting lines have no significance, and are only intended as an aid to the eye.

with a hyperfine field smaller than the value at 4.2 K, indicating that the hyperfine field at 4.2 K is saturated; a nonsaturated field at 4.2 K would preclude the possibility of observing a magnetically-split spectrum at 100 K. The magnitude of the hyperfine field, then, decreases with decreasing Fe^{2+} concentration.

If only dilution effects were controlling the magnetic properties of the Mössbauer spectra the net result would be a steady decrease of the ordering temperature with the hyperfine field strength remaining constant. The decreasing magnitude of the field strength thus indicates a significant alteration to the factors which give rise to the hyperfine magnetic field. To study the problem further, the Mössbauer spectrum of ^{57}Fe:CoS was recorded in an external magnetic field of 25 kOe with the field axis parallel to the direction of γ-ray propagation (Fig. 3.5). The spectrum was recorded by Dr. P. Clark at Monash University, Victoria. The line width of the spectrum is broadened by approximately 0.6 mm/sec from the zero-field spectrum, and the splitting is nearly identical with the observed value for FeS_2 at 4.2 K in an external magnetic field of similar intensity (Montano and Seehra, 1976), indicating a zero contribution of the internal hyperfine field to the observed splitting.

3.4 Magnetic Transition in (Fe,Co)S

The room temperature centre shifts decrease almost continuously (Fig. 3.4a) from 0.76 mm/sec at FeS to 0.57 mm/sec at ^{57}Fe:CoS, although there may be a small discontinuity ($\sim$ 0.03 mm/sec) near 69 mol % FeS. At 4.2 K the hyperfine magnetic field at the ^{57}Fe nucleus decreases with decreasing Fe^{2+} concentration from 328 kOe at FeS to 230 kOe at 50 mol % FeS. The internal field contribution to the magnetic splitting of ^{57}Fe:CoS in an external magnetic field at 4.2 K is close to zero.

One possible mechanism for the observed decrease in the hyperfine magnetic field is a high-spin $\rightarrow$ low-spin transition of the Fe^{2+} ions, since Fe^{2+}(ls) has no unpaired electrons and cannot contribute significantly to the hyperfine magnetic field. Co^{2+} is probably in the low-spin state throughout the solid solution inferred on the basis of data presented in Fig. 3.1. Co^{2+}(hs) is most likely to occur near the FeS endmember, but the smooth decrease in ordering temperature with increasing Co^{2+} concentration is not consistent with a high-spin $\rightarrow$ low-spin transition in Co^{2+}.

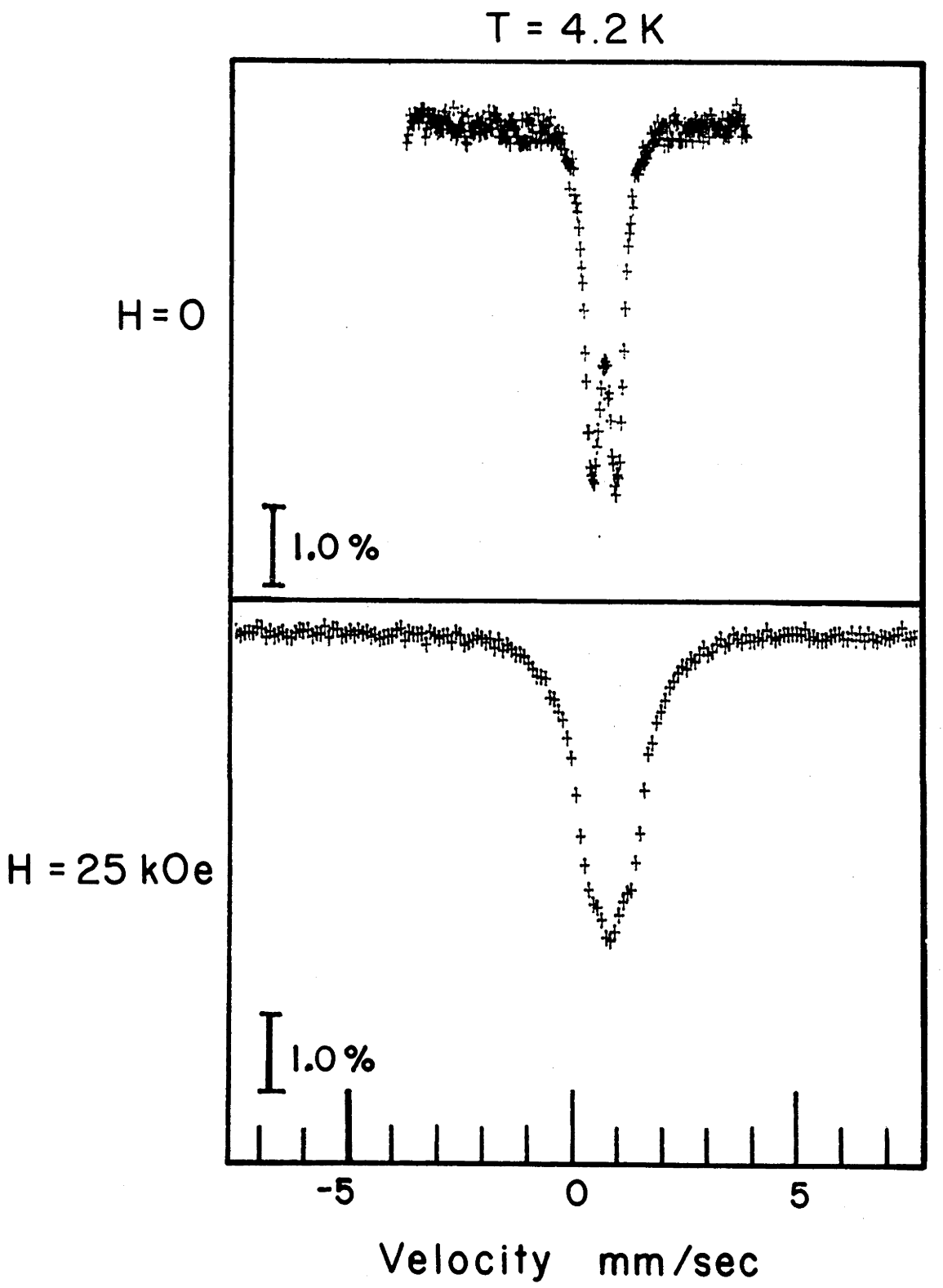

Fig. 3.5 Mössbauer spectrum of ^{57}Fe:CoS at 4.2 K with no external magnetic field (H=0) and an external magnetic field of 25 kOe. The velocity scale is relative to Fe.

The strongest evidence against the occurrence of an Fe^{2+} spin transition is the Mössbauer centre shift data of Fig. 3.4a. The Mössbauer isomer shift, which together with the second-order Doppler shift makes up the centre shift, depends to some extent on the degree of shielding of the Mössbauer nucleus from outer s electrons by the d electrons, and is therefore sensitive to the Fe^{2+} spin state. Isomer shifts for Fe^{2+}(ls) compounds are significantly lower than those for Fe^{2+}(hs) compounds due to the reduced shielding of the 3s electrons of Fe^{2+}(ls) by the highly delocalized 3d electrons. Isomer shift values for Fe^{2+}(hs) compounds range from typically 0.7 to 1.5 mm/sec at room temperature (relative to metallic iron), while room temperature values for Fe^{2+}(ls) compounds are in the approximate range -0.3 to +0.4 mm/sec (Gibb, 1976). The centre shifts of the (Fe,Co)S compounds measured in this work range from 0.57 to 0.76 mm/sec, and with second-order Doppler contributions of approximately -0.2 to -0.3 mm/sec, the isomer shifts would appear to be more typical of Fe^{2+}(hs) than of Fe^{2+}(ls).

More significant, perhaps, than the absolute values of the centre shifts is the composition dependence of the parameter, which is plotted in Fig. 3.4a. Two points should be considered here. First, a spin transition of Fe^{2+} should be accompanied by a large discontinuity in the centre shift. For example, the temperature-dependent high-spin → low-spin transitions of Fe^{2+} in $Fe(phen)_2(NCS)_2$ (Dezsi et al., 1967) and $[Fe(2\text{-pic})_3]Cl_2.C_2H_5OH$ (Sorai et al., 1976) are accompanied by centre shift changes of ∿ 0.5-0.6 mm/sec. The data of Fig. 3.4a show that no composition-dependent change of a comparable magnitude has occurred in this system. Consequently it is concluded that there is no concentration-dependent spin transition of the Fe^{2+} ions. Second, the large magnetic hyperfine interactions observed at ^{57}Fe in FeS and in the 50 mol % FeS sample at 4.2 K indicate strongly that the ferrous ions in both of these samples are in the high-spin state; Fe^{2+}(ls) is diamagnetic, so only weak transferred hyperfine interactions are expected.

It is therefore concluded that Fe^{2+} in (Fe,Co)S is in the high-spin state across the entire composition range of the solid solution, and a spin transition is not responsible for the observed composition dependence of the magnetic hyperfine interactions at the ^{57}Fe nuclei. This is consistent with calculations which indicate that FeS will not undergo a spin transition until the distance <Fe-S> is reduced to 228 pm (Tossell, 1977). (<M-S> in (Fe,Co)S decreases from 246 pm for FeS to 235 pm for

^{57}Fe:CoS.) However, it is difficult to reconcile the presence of Fe^{2+}(hs) with the absence of an internal magnetic field in ^{57}Fe:CoS at 4.2 K and 25 kOe so the factors contributing to the hyperfine field must be examined in more detail.

The internal hyperfine field arises from the vector sum of basically three components related to the orbital angular momentum of the atom (orbital term), the spin density of the electrons at the nucleus (Fermi contact term), and the dipolar interaction of the magnetic moment of the atom with the nucleus (dipolar term). The relative size of each term determines the sign and magnitude of the internal field.

In high-spin FeS the internal field is large and negative (Gosselin et al., 1976). The dominant contribution to the field, therefore, must be the Fermi contact term which is the only large negative term for Fe^{2+}(hs) compounds. The dipolar term and the lattice contribution to the quadrupole splitting involve the same lattice sum; hence the dipolar term is zero in cubic symmetry. The small values of the ^{57}Fe quadrupole splitting in (Fe,Co)S indicate that the dipolar term should be small, and thus adds only a small positive contribution to the internal field. The orbital term is also positive for Fe^{2+}(hs) compounds and its magnitude depends upon competing effects of the crystal field and the spin-orbit coupling. The magnitude of the orbital term in this case must be smaller than the Fermi contact term since the net internal field is negative.

In order to decrease the magnitude of the hyperfine field in (Fe,Co)S the relative magnitude of the various contributions must be altered. There are no plausible mechanisms which can be invoked to increase significantly the size of the dipolar and orbital terms. The Fermi contact term, however, which is a function of the electronic spin density at the nucleus, can be substantially reduced by an increase in electron delocalization (Gibb, 1976). The delocalization of 3d electrons would also lead to a reduction in the orbital and dipolar contributions. The suggestion is, therefore, that increased electron delocalization caused by the gradual shortening of the <M-S> distance with increasing Co^{2+} concentration in (Fe,Co)S reduces the Fermi contact term and the dipolar and orbital terms to a point where the net internal field becomes zero. The absence of an internal field in ^{57}Fe:CoS may be due to the almost negligible values of all contributions, or alternatively may be attributed to an almost exact cancellation of contributions which are small but

finite; either possibility is consistent with the experimental data, but the former would appear to be unlikely.

The variation of the room temperature centre shift data with composition is consistent with the above hypothesis. Delocalization of the 3d electrons decreases the value of the isomer shift (i.e. increases the charge density at the nucleus) due to the reduced shielding of the nucleus by 3d electrons (Gibb, 1976). The room temperature centre shift value for ^{57}Fe:CoS of 0.57 mm/sec is considerably below typical values for Fe^{2+}(hs) compounds, indicating the presence of an effect such as extensive electron delocalization.

A final note should be added concerning the effects of stoichiometry on the magnetic properties of (Fe,Co)S. In the preceding discussion the effects of the variable metal/sulphur ratio were not explicitly considered, but in reality the stoichiometry affects the cell parameters and dilution of metal atoms and hence the magnetic properties. The effect varies as a function of Co^{2+} composition. At the FeS endmember the <Fe-S> distance varies as a function of stoichiometry and the magnetic structure changes from antiferromagnetic to ferrimagnetic (Perthel, 1960). As the Co^{2+} concentration increases, however, the stoichiometry has considerably less effect on the magnetic properties. At 50 mol % FeS the <M-S> distance for $(Fe,Co)_{0.99}S$ is 236.7 pm whereas the equivalent distance in $(Fe,Co)_{0.87}S$ is 236.6 pm. At the CoS endmember the magnetic properties are virtually independent of stoichiometry (Townsend et al., 1975). The conclusion is, therefore, that stoichiometry affects the behaviour of (Fe,Co)S only near the FeS endmember. The overall discussion of the magnetic transition in (Fe,Co)S is not altered.

3.5 High-Pressure Phase of FeS

The decrease in cell parameters of FeS as Co^{2+} substitutes into the lattice raises the possibility that observations of ^{57}Fe:CoS may be relevant to FeS at high pressure. FeS undergoes two known phase transformations at high pressure and room temperature (Fig. 3.7). The first transition occurs at 3.4 GPa and has been interpreted as a transformation of FeS to an MnP (B31) structure (King and Prewitt, 1982). At 6.7 GPa there is a further structural transformation to a postulated distorted NaCl (B1) structure (Mao et al., 1981). An in-situ Mössbauer study using a diamond anvil cell has been performed to further characterize the 6.7 GPa transition (King et al., 1978). Below 6.7 GPa the

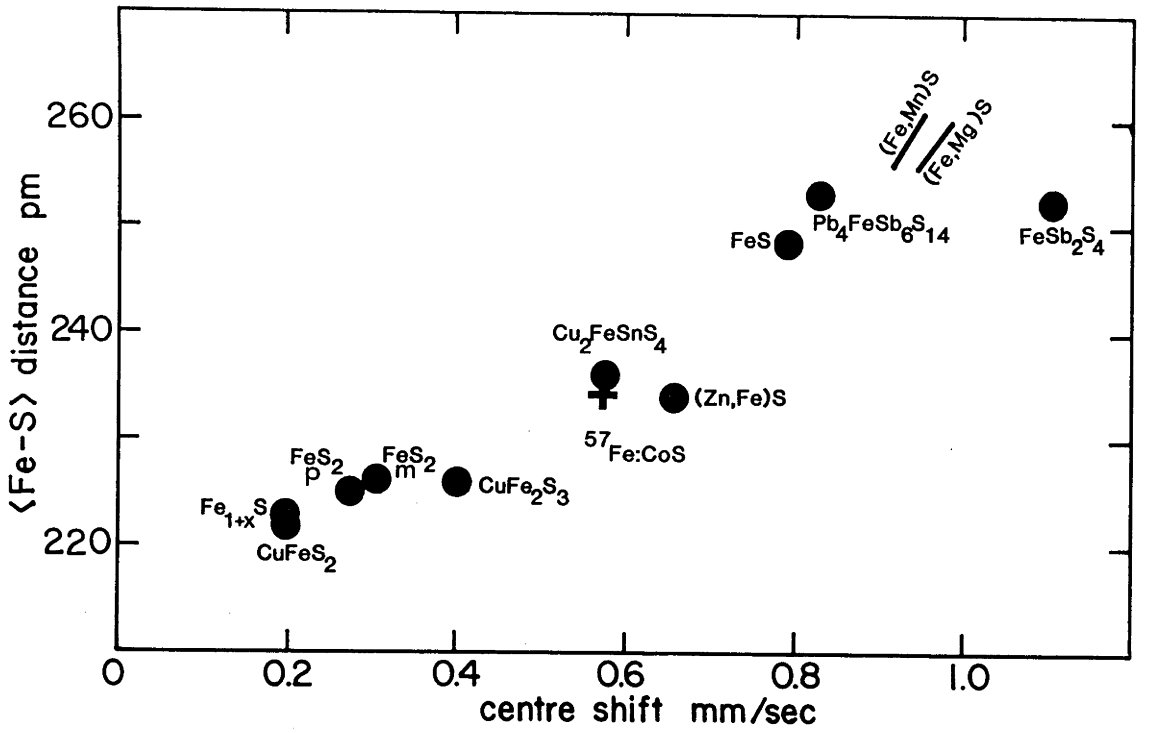

Fig. 3.6 Variation of the centre shift (relative to Fe) with ⟨Fe-S⟩ distance for some sulphide minerals (after Vaughn and Craig, 1978). Data for ^{57}Fe:CoS (represented by a cross) and (Fe,Mn)S and (Fe,Mg)S (represented by lines) were taken from the present thesis.

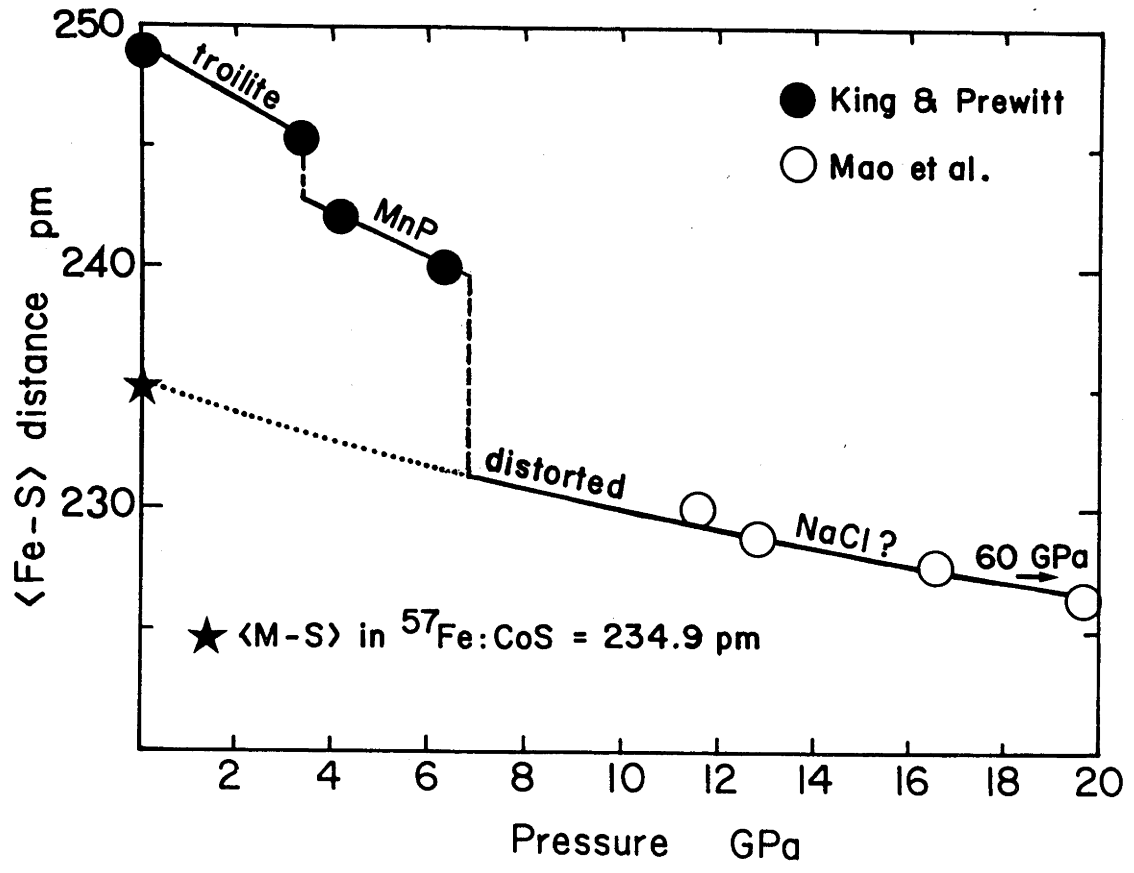

Fig. 3.7 Variation of the ⟨Fe-S⟩ distance with pressure at 298 K from the data of King and Prewitt (1982) and Mao et al.(1981). The data of Mao et al.(1981) extend to 60 GPa.

Mössbauer spectrum is magnetically split, but at 6.7 GPa the Mössbauer spectrum of FeS converts to a nonmagnetic spectrum with a small quadrupole splitting. The possibility of a high-spin → low-spin transition in Fe^{2+} was ruled out by King et al.(1978) on the basis of the centre shift data; at 298 K and 0.1 MPa the extrapolated value of the centre shift of the high-pressure phase is 0.53 ± 0.1 mm/sec relative to iron metal. To account for this value King et al.(1978) postulated the presence of a d^5 (Fe^{3+}) configuration for iron above the 6.7 GPa transition, with the extra electron being transferred to a conduction band, to an iron 4s orbital or to the sulphur atom.

The Mössbauer data of (Fe,Co)S may clarify the nature of the 6.7 GPa high-pressure phase (hpp) of FeS. It has been shown that the centre shifts of sulphide minerals increase approximately linearly with increasing <Fe-S> distance, reflecting the large dependence of the centre shift on metal-ligand interactions irrespective of crystal structure (Vaughn and Craig, 1978) (Fig. 3.6). The centre shift value of 0.57 mm/sec for ^{57}Fe:CoS in fact fits exactly with the linear trend for the observed <M-S> distance of 235 pm. Fig. 3.7 illustrates the variation of the <Fe-S> distance in FeS as a function of pressure, taken from the data of King and Prewitt (1982) and Mao et al.(1981). The <Fe-S> distance in FeS(hpp) above 6.7 GPa extrapolated to 0.1 MPa is calculated to be 235 ± 2 pm based on the postulated distorted B1 structure for the high-pressure phase (the extrapolation required is very modest since the compression data of Mao et al.(1981) extend to 60 GPa). The nearly identical values of both the centre shift and <M-S> distance of FeS(hpp) and ^{57}Fe:CoS strongly suggests extensive electron delocalization in Fe^{2+}(hs)-bearing FeS(hpp). The transition to high electron delocalization in (Fe,Co)S occurs as the <Fe-S> distance decreases continuously to 235 pm, but the transition to high electron delocalization in FeS occurs discontinuously with increasing pressure. The discontinuity is related to the change in crystal structure at 6.7 GPa which is simultaneous with a decrease of the <Fe-S> distance from 239 pm to 232 pm (Fig. 3.7).

Liu (1981) has compiled data on the relationship between bond length and molar volume for a number of elements, MX compounds and MX_2 compounds. He noted that the majority of structural phase transformations at high pressure involve an increase in the <M-M> or <M-X> bond length and a change to a more closely-packed structure. The few exceptions in which the bond length actually decreases are accompanied by either no change in

crystal structure or a change to a more open-packed structure. These transformations are always associated with substantial electronic transitions (e.g. Cs, Sr, Ti, EuO, SmS). Both of the high-pressure phase transformations in FeS involve a decrease in the <Fe-S> bond length and a change to either the same or a more open-packed structure (FeS in the B31 structure has the same "packing index" as FeS in the B8 structure, and the B1 structure is more open-packed than the B31 structure). The 3.5 GPa transition has already been shown to correspond to the semiconductor-metal transition observed at 420 K and 0.1 MPa (King and Prewitt, 1982); it is therefore very likely that the 6.7 GPa transition also involves a component of electronic change. This is consistent with the high degree of electron delocalization in FeS(hpp) relative to FeS(B8) suggested by the (Fe,Co)S data.

The outer electronic structure of FeS (B8) is commonly represented in terms of bands, with the six d electrons being accommodated in a spin-up t_{2g} band (three electrons), a spin-up e_g band (two electrons) and a spin-down t_{2g} band (one electron) (e.g. Goodenough, 1967; Wilson, 1972). The partially filled spin-down t_{2g} band gives rise to metallic conductivity in FeS above $\sim$ 420 K, but below this temperature a spontaneous distortion of the crystal structure is accompanied by a splitting of the band into two, resulting in a sharp decrease in electrical conductivity (Goodenough, 1967). The transition at 3.5 GPa and 298 K presumably removes the splitting of the spin-down band, resulting in metallic conductivity.

At high pressure Fe^{2+}(ls) has been thought to be more stable than Fe^{2+}(hs) because of the large effect of decreasing the <Fe-S> distance on the crystal field splitting. Fe^{2+} in FeS was interpreted to be in the high-spin state at 6.7 GPa, and no discontinuities in the room temperature compression data of Mao et al.(1981) are noted up to 60 GPa which are comparable to the density change expected for a spin transition (despite the fact that the <Fe-S> distance decreases well below 228 pm which was calculated by Tossell (1977) to be the minimum <Fe-S> distance for high-spin $^{VI}Fe^{2+}$). Additionally, the shock wave data of $Fe_{0.9}S$ show no further appreciable discontinuities up to 158 GPa (Ahrens, 1979). One possibility is that a high-spin $\rightarrow$ low-spin transition occurs in Fe^{2+} with a negligible volume change, or alternatively, Fe^{2+}(ls) is destabilized relative to Fe^{2+}(hs) at high pressure due to extensive electron delocalization; both possibilities represent significant departures from

current thinking regarding spin transitions in Fe^{2+} at high pressure.

3.6 Discussion of Fe^{2+} spin state in FeO

The observation of Fe^{2+}(hs) in FeS to very high pressure (or alternatively a negligible density change involved with a spin transition) raises the question of whether similar behaviour might occur in FeO at very high pressure. The behaviour of FeS is associated with a high degree of electron delocalization related to the short <Fe-S> distance. Can increasing pressure produce a similar effect in FeO?

The answer might come from considering the bonding in FeO and FeS in terms of the two types of covalency, central-field and symmetry-restricted (Jørgensen, 1962). Central-field covalency describes the radial expansion of the 3d orbitals due to interaction with the ligands, reducing the effective nuclear charge of the metal ion. Central-field covalency influences orbitals of different symmetry equally, and therefore both the t_{2g} and e_g electrons in Fe^{2+} become more delocalized. Symmetry-restricted covalency describes the radial expansion of the 3d orbitals due to σ and π bonding effects, and affects the 3d orbitals differently. The 3d e_g orbitals form σ bonds whereas the t_{2g} orbitals form π bonds, and the degree of delocalization of the 3d e_g and t_{2g} electrons depends on the relative stability of σ and π bonds, respectively.

FeO and FeS behave differently with respect to π bonding. If the ligand π orbitals are unoccupied and are less stable relative to the metal 3d t_{2g} orbitals, for example in FeS, the metal t_{2g} orbitals are stabilized by π bonding. If the ligand π orbitals are occupied and are more stable relative to the metal t_{2g} orbitals, however, for example in FeO, π bonding destabilizes the metal t_{2g} orbitals and no π bonds are formed (Burns, 1970). An increase in symmetry-restricted covalency with increasing pressure will have different effects on FeO and FeS, therefore; all of the 3d electrons (t_{2g} and e_g) will become more delocalized in FeS due to enhancement of both σ and π bonding as the interatomic distance decreases, but only the 3d t_{2g} electrons in FeO will become more delocalized with decreasing interatomic distance since π bonding is not favoured. In contrast, an increase in central-field covalency with increasing pressure will affect FeO and FeS similarly, increasing delocalization of both the t_{2g} and e_g 3d electrons.

The possibility of Fe^{2+} in FeO at very high pressure behaving

similarly to Fe^{2+} in FeS at lower pressure depends on whether the pressure-induced covalency increase of Fe-O bonds is dominated by symmetry-restricted or central-field covalency. Because π bonding is significant in sulphides and the effects observed in ^{57}Fe:CoS and FeS(hpp) are consistent with extensive delocalization of both the t_{2g} and e_g electrons, central-field covalency would be required to dominate in FeO with increasing pressure if FeO were to follow the behaviour of FeS. Huggins (1975), however, has determined that symmetry-restricted covalency dominates as pressure is increased in almandine (Fe-rich garnet) and $FeTiO_3$ using Mössbauer and optical absorption data which indicate that the t_{2g} 3d electrons remain relatively localized. If bonding in FeO is also dominated by symmetry-restricted covalency at high pressure, a high-spin → low-spin transition with a significant density increase is likely to occur in Fe^{2+} at high pressure as predicted widely in the literature.

Chapter 4 (Fe,Mn)S AND (Fe,Mg)S: THE B1 STRUCTURE

4.1 Introduction

FeS crystallizes in the B8 (NiAs) structure and is antiferromagnetic with a Néel temperature of roughly 590 K (Hirone et al., 1954). α-MnS and MgS both crystallize in the B1 (NaCl) structure, but α-MnS is antiferromagnetic with a Néel temperature of 148 K (Heikens et al., 1977) while MgS is diamagnetic (MnS will henceforth refer to α-MnS). Both FeS-MnS and FeS-MgS form extensive solid solutions with the B1 structure at atmospheric pressure, but only small amounts of MnS and no MgS are soluble in FeS(B8) (Skinner and Luce, 1971). The main purpose of this study of (Fe,Mn)S and (Fe,Mg)S B1 solid solutions is to determine the compositional variation of the cell size and the Mössbauer parameters as a basis for characterizing the behaviour of (Fe,Mn)S and (Fe,Mg)S at high pressure (see Chapter 5). A secondary aim is to study and compare the properties of Fe^{2+} in two different B1 hosts, and to determine how the magnetic properties of MnS and MgS are affected by the presence of Fe^{2+}. The results allow some speculation on the nature of the hypothetical phase FeS(B1), a phase which is important because of the proposed distorted B1 structure for FeS at high pressure (Mao et al., 1981).

A study was also undertaken of MnS at high pressure in order to identify the nature of the high-pressure phase transition (Clendenen and Drickamer, 1966). The Néel temperatures of MnO (118 K), CoO (289 K) and FeO (198 K) increase with pressure (FeO, CoO: Okamoto et al., 1967; MnO: Bloch et al., 1980), and therefore compression of these phases at 298 K should eventually result in a magnetically-ordered structure, probably accompanied by a distortion from cubic symmetry due to exchange interactions between transition-metal cations. MnS is expected to behave in a similar manner, and the continuous transition observed by Clendenen and Drickamer (1966) may reflect a change in magnetic structure. It is useful to determine the nature of the high-pressure distortion for comparison with the rhombohedral distortion observed at the Néel temperature (e.g. Morosin, 1970). FeO has been observed to undergo a rhombohedral distortion at $\sim$ 9 GPa and 298 K which occurs near the onset of magnetic ordering (Zou et al., 1980), and results from the study of MnS may be useful in understanding the nature of the FeO transition.

4.2 Experimental Procedure

A series of samples with varying iron compositions within the B1 single-phase region of (Fe,Mn)S and (Fe,Mg)S was prepared (see phase diagrams in Fig. 5.1, p. 54). The samples were synthesized by heating mixtures of the appropriate elements inside evacuated silica glass tubes (identical to preparation of (Fe,Co)S, see section 3.2). X-ray diffraction patterns of all samples were recorded using either Fe $K\overline{\alpha}$ or Co $K\overline{\alpha}$ radiation, and Si was used as an internal calibration standard. The cubic cell parameters of the samples were determined using a least-squares analysis of the x-ray reflections weighted according to the angular uncertainty. Compositions were determined using an electron microprobe (see section 2.3.2) and all samples probed were found to be stoichiometric (i.e. no metal defects) within experimental error. The variations of the cubic cell parameters of (Fe,Mn)S and (Fe,Mg)S are illustrated in Fig. 4.1. The results agree well with the data of Skinner and Luce (1971) (also illustrated). A linear least squares fit of the data gave the following results:

MgS–FeS $\quad a(pm) = 520.4 - 0.1299x \qquad (4.1)$

MnS–FeS $\quad a(pm) = 522.4 - 0.1653x \qquad (4.2)$

where x is mol % FeS.

The Mössbauer spectra of (Fe,Mn)S(B1) and (Fe,Mg)S(B1) were recorded at 298 K and 4.2 K using the spectrometers at Dept. Solid State Physics, ANU and Dept. of Physics, Monash University. Equipment description, sample preparation and run procedure are given in Chapter 2.

A sample of polycrystalline MnS (a = 522.45 $\pm$ 0.05 pm) was synthesized by J. Wilke (R.S.Chem., ANU) for the compression experiment. The compression curve of MnS was measured using the diamond anvil cell, and the procedure is described in Chapter 2.

4.3 Mössbauer Spectra at 298 K

4.3.1 Previous work

The Mössbauer spectra of (Fe,Mg)S have been recorded previously by Kurash et al.(1973) at 300 K and 78 K for samples with compositions ranging from 0 mol % FeS to 70 mol % FeS. The lattice parameters of their samples do not agree with the data presented in Fig. 4.1, however. This may be caused by too slow a quench rate from high temperature during sample synthesis; a slow quench is also implied by the observation of a

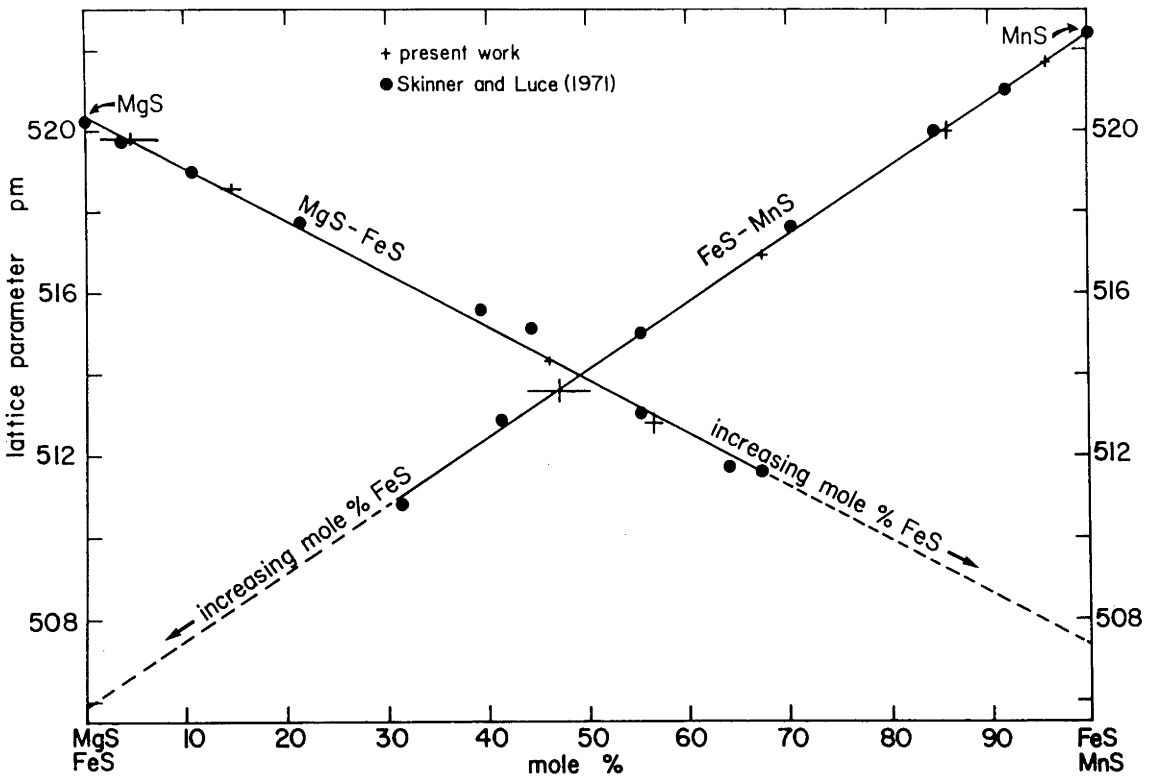

Fig. 4.1 Variation of the cubic cell parameter with composition for (Fe,Mg)S and (Fe,Mn)S B1 solid solutions.

TABLE 4.1 Mössbauer parameters for (Fe,Mn)S and (Fe,Mg)S at 298 K

Sample	% FeS[a]	δ[b] mm/sec	ε mm/sec	Γ mm/sec
(Fe,Mn)S:				
FMS 9	4.7(8)	0.953(2)	0.056(1)	0.345(1)
FMS 1	15.5(15)	0.948(4)	0.075(2)	0.304(4)
FMS 2[c]	35.1(8)	0.936(4)	0.095(2)	0.299(5)
FMS 8	54.6(15)	0.922(2)	0.116(1)	0.314(2)
FMS 7[d]	66.5(8)	0.922(7)	0.104(3)	0.357(8)
(Fe,Mg)S:				
FGS 7	3.1(8)	0.984(2)	0.056(2)	0.395(2)
FGS 10	13.3(8)	0.981(2)	0.067(1)	0.298(1)
FGS 9	35.4(8)	0.954(2)	0.102(1)	0.314(1)
FGS 8	48.4(8)	0.945(2)	0.105(1)	0.309(1)
FGS 2	58.9(15)	0.941(2)	0.109(1)	0.318(1)

[a] calculated from eqs. (4.1) and (4.2)

[b] relative to Fe metal

[c] this sample also contained a phase with δ = 0.19(2) mm/sec, ε = 0.48(2) mm/sec and occupied 5% of the area.

[d] this sample also contained a phase with δ = 0.14(2) mm/sec, ε = 0.50(2) mm/sec and occupied 16% of the area.

tetragonal phase in the x-ray patterns of their samples corresponding to an ordering of Fe and Mg in the rocksalt lattice. Their Mössbauer spectra at 300 K had an overall line width of $\sim$ 0.5 mm/sec which broadened at 78 K to $\sim$ 0.6 $\rightarrow$ 1.3 mm/sec (depending on the Fe concentration), but the resolution of their spectra was not sufficient to determine if magnetic interactions were present.

4.3.2 Experimental results and interpretation

The Mössbauer spectra of (Fe,Mn)S and (Fe,Mg)S recorded at 298 K are illustrated in Fig. 4.2, and consist of a single quadrupole doublet with a small splitting. The Mössbauer parameters of the doublet for each sample are listed in Table 4.1. (Fe,Mn)S samples containing 35 mol % (FMS 2) and 66 mol % FeS (FMS 7) were also found to contain small amounts of an impurity, perhaps corresponding to FeS_2 (see section 5.3.3). The impurity spectrum was fitted as a quadrupole doublet (parameters listed in Table 4.1), and was neglected in the following analysis because of its low relative proportion.

The variation of the centre shift and quadrupole splitting of (Fe,Mg)S and (Fe,Mn)S at 298 K are shown in Fig. 4.3. There are three trends to note:

(1) The centre shifts of (Fe,Mg)S are significantly higher than those of (Fe,Mn)S.
(2) The centre shifts of both (Fe,Mn)S and (Fe,Mg)S decrease as the Fe^{2+} concentration increases.
(3) The quadrupole splitting of both (Fe,Mn)S and (Fe,Mg)S increases as the Fe^{2+} concentration increases.

The centre shift is related to the s electron density at the ^{57}Fe nucleus, and depends to a certain extent on the amount of shielding of the outer s electrons by the d electrons. A high degree of shielding of the 3s electrons by the d electrons results in a lower s electron density at the nucleus and therefore a higher centre shift, whereas a low degree of shielding results in a higher s electron density at the nucleus and a lower centre shift. Delocalization of the 3d electrons reduces the degree of shielding, and therefore reduces the centre shift. The ionic radius of Mg^{2+} (65 pm) is considerably smaller than that of Mn^{2+} (80 pm), but the interatomic distances in MgS and MnS are nearly identical; hence the orbital overlap between Mn^{2+} and S^{2-} is likely to be greater than that in MgS. Because Fe^{2+} interacts with Mn^{2+} through the connecting sulphur

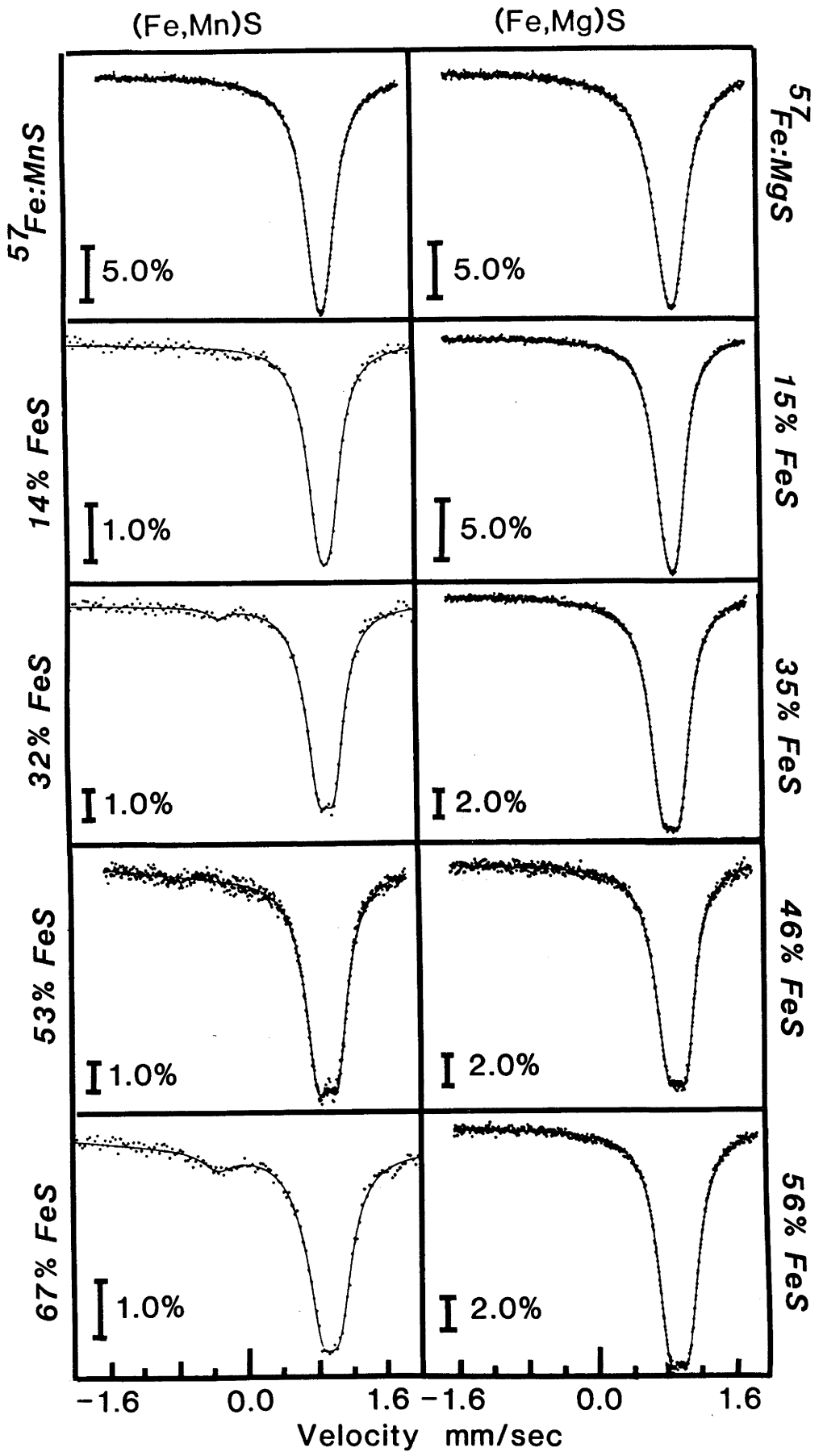

Fig. 4.2 Mössbauer spectra of (Fe,Mn)S(B1) and (Fe,Mg)S(B1) recorded at 298 K. The spectra were fitted to a single quadrupole doublet, with parameters given in Table 4.1. The velocity scales are relative to Fe.

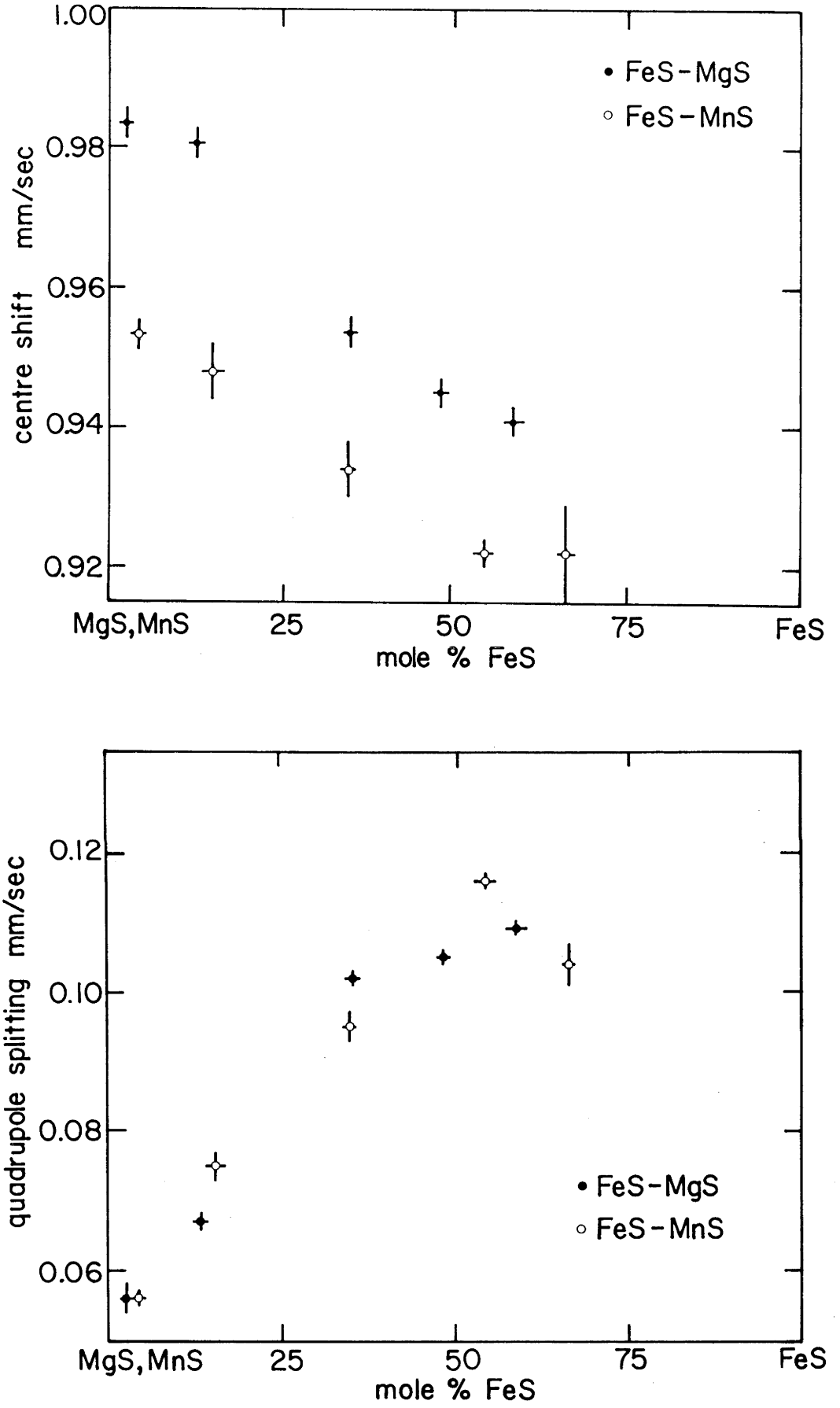

Fig. 4.3 Compositional variation of the centre shift and quadrupole splitting of (Fe,Mn)S(B1) and (Fe,Mg)S(B1) at 298 K.

ligands, it is reasonable to expect that the d electrons of Fe^{2+} in (Fe,Mn)S would spend more time away from the nucleus than those in (Fe,Mg)S. The shielding of the ^{57}Fe nucleus by the d electrons in (Fe,Mg)S would therefore be greater than in (Fe,Mn)S, and (Fe,Mg)S should have a larger centre shift. The decrease of the centre shift with increasing % Fe^{2+} in both (Fe,Mn)S and (Fe,Mg)S would then be due to the greater degree of d electron delocalization as the <Fe-S> interatomic distance decreases with increasing % Fe^{2+}.

In Fe^{2+} high-spin compounds the magnitude of the quadrupole splitting is usually dominated by the contribution from the electric field gradient (EFG) caused by the electrons of the Fe^{2+} ion. In a perfect octahedral site the EFG is zero, but a small distortion from cubic symmetry gives rise to a nonzero EFG at the Fe^{2+} nucleus due to nondegeneracy of the t_{2g} orbitals. One source of distortion is from the Jahn-Teller effect (Jahn and Teller, 1937), where the degeneracy of the ground state energy levels in $^{VI}Fe^{2+}$ (high spin) is removed because the t_{2g} orbitals are unequally populated. Such distortion is not possible for either Mg^{2+} or $^{VI}Mn^{2+}$ because Mg^{2+} has no d electrons and $^{VI}Mn^{2+}$ has equally populated t_{2g} and e_g orbitals. The quadrupole splitting in (Fe,Mn)S and (Fe,Mg)S is therefore small when Fe^{2+} is diluted by cubic MnS and MgS, but as the % Fe^{2+} increases the distortion of the sulphur ligands becomes greater. It should be noted that the magnitude of the distortion would be too small to be detected by the x-ray technique used in the present study.

4.4 Mössbauer Spectra at 4.2 K

4.4.1 Previous work

The Mössbauer spectrum of ^{57}Fe:MnS has been recorded previously by Pollard et al.(1983), who studied the magnetic structure of MnS over a range of temperatures. Below the Néel point an eight-line magnetic spectrum was obtained (principal axis of EFG not aligned with the magnetic field direction), but the Mössbauer parameters could not be determined unambiguously from the spectra (see below). Using a crystal field analysis of the Mössbauer data, the spins were determined to lie along the cubic <110> direction for $T_N > T > 131$ K. The linewidths became significantly broader below 117 K, however, and the Mössbauer spectra could not be fitted satisfactorily, which suggested a multiaxial spin arrangement.

4.4.2 Fitting the spectra

The Mössbauer spectra of (Fe,Mn)S and (Fe,Mg)S recorded at 4.2 K are shown in Fig. 4.4. The spectra were fitted with a model where the field direction is not parallel to the principal axis of the EFG. In this case there are six parameters to be fitted: the centre shift (δ), the quadrupole splitting (ε), the hyperfine field (H), the asymmetry of the EFG (η), and the angles specifying the direction of H with respect to the principal axis of the EFG (θ, ϕ). There are, however, only five experimental quantities which can be measured: the ground state splitting and the energies of the four excited nuclear energy levels. Only δ and H can be determined unambiguously from these quantities; in general ε, η, θ and ϕ vary within a range of values. The method used to determine the range of values in the present work was to fit the spectra with one set of parameters, and then systematically vary these parameters to determine all other valid solutions given the same nuclear eigenvalues, where valid solutions are given by $|\cos 2\phi| \leq 1$, $0 \leq \sin^2\theta \leq 1$ and $0 \leq \eta \leq 1$. The method of Kundig (1967) was used in fitting the Mössbauer spectra and a computer program written by D.C. Price was used to determine the range of parameters. The results of the analysis for (Fe,Mn)S and (Fe,Mg)S are listed in Table 4.2. The parameter ranges should not be regarded as formal uncertainties, but rather as ranges within which the true values of the parameters must lie. Often it is possible to obtain further data from another source to remove the ambiguity.

Both signs of the quadrupole splitting were considered in determining the allowed range of Mössbauer parameters, but in several cases (both (Fe,Mn)S and (Fe,Mg)S samples represented), only positive values resulted in allowed solutions. Assuming that the sign of the quadrupole splitting does not change within the solid solution, the Mössbauer spectra of both (Fe,Mn)S and (Fe,Mg)S are only consistent with positive values of ε.

4.4.3 Interpreting the spectra

The Mössbauer spectra of ^{57}Fe:MgS and ^{57}Fe:MnS are dramatically different at 4.2 K. There appears to be no evidence for magnetic ordering in ^{57}Fe:MgS and $Mg_{0.85}Fe_{0.15}S$, whose spectra were fitted to one quadrupole doublet each, but the large line widths indicate that at least two doublets (and possibly more) with slightly different parameters are present. The onset of magnetic ordering occurs between 15 mol % and 35 mol % FeS in (Fe,Mg)S at 4.2 K, and is likely to occur discontinuously. The magnitude of H does not vary appreciably with composition between

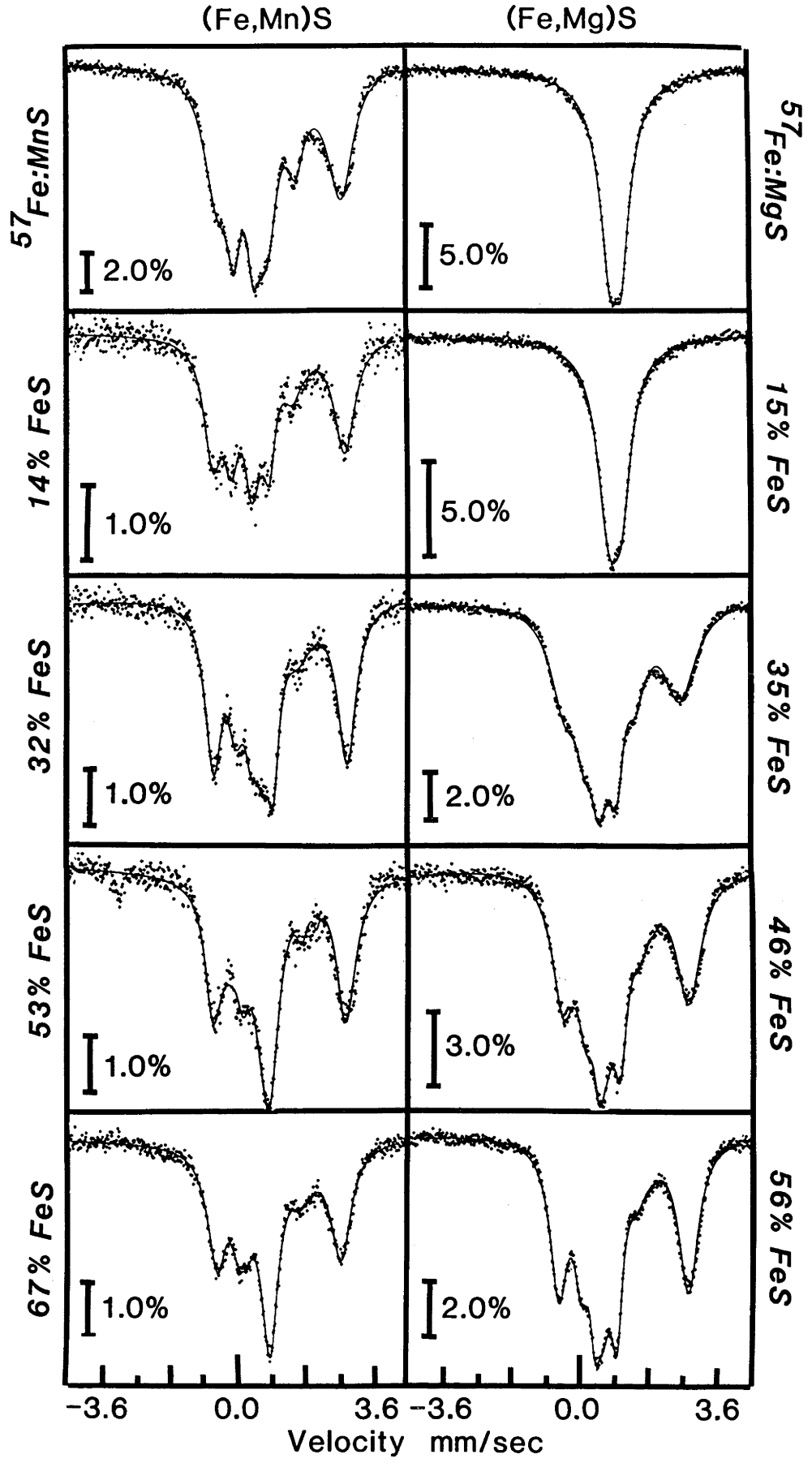

Fig. 4.4 Mössbauer spectra of (Fe,Mn)S(B1) and (Fe,Mg)S(B1) recorded at 4.2 K. The spectra were fitted to an eight-line magnetic spectrum, with parameters given in Table 4.2. The velocity scales are relative to Fe.

TABLE 4.2 Mössbauer parameters for (Fe,Mn)S and (Fe,Mg)S at 4.2 K

Sample	δ[a] mm/sec	H kOe	$\bar{\Gamma}$[b] mm/sec	ε mm/sec	η	θ^{o}	ϕ^{o}
FMS 9	1.024(4)	78.0(5)	0.66(19)	0.57-0.60	0.79-1.00	29.0-31.8	0.0-23.1
FMS 1	0.964(6)	84.5(7)	0.52(13)	0.58-0.62	0.69-1.00	20.7-26.6	0.0-40.4
FMS 2	0.967(4)	82.3(5)	0.56(13)	0.62-0.68	0.47-1.00	27.6-33.5	0.0-43.9
FMS 8	0.936(5)	66.7(7)	0.52(11)	0.79-0.87	0.46-0.96	17.6-26.6	0.0-78.5
FMS 7	0.952(3)	66.2(7)	0.54(13)	0.68-0.78	0.23-1.00	28.5-35.5	0.0-57.2
FGS 7[c]	1.002(2)	-	0.662(4)	0.154(2)	-	-	-
FGS 10[c]	0.972(2)	-	0.720(5)	0.164(3)	-	-	-
FGS 9	1.010(3)	70.5(3)	0.61(24)	0.52-0.59	0.38-1.00	21.8-30.4	0.0-65.5
FGS 8	0.985(4)	77.6(3)	0.57(16)	0.56-0.64	0.34-1.00	21.9-30.8	0.0-70.3
FGS 2	0.966(2)	78.7(2)	0.49(12)	0.62-0.68	0.33-0.93	19.8-28.5	0.0-84.0

[a] relative to Fe metal

[b] average component line width

[c] fitted to a quadrupole doublet

35 mol % and 56 mol % FeS in (Fe,Mg)S.

Below the Néel temperature atomic spins in MnS align in the plane perpendicular to [111] and adjacent planes are coupled antiferromagnetically (Corliss et al., 1956). Exchange interactions between Fe^{2+} and Mn^{2+} in ^{57}Fe:MnS contribute to a hyperfine internal magnetic field of similar magnitude to Fe-rich (Fe,Mg)S, and the magnitude of H does not vary appreciably with composition.

The quadrupole splitting at 4.2 K increases dramatically in (Fe,Mg)S with increasing Fe^{2+} concentration. This is consistent with a small rhombohedral distortion of the cubic lattice as Fe^{2+} exchange becomes significant in the solid solution. MnS undergoes a contraction of the cubic lattice along [111] below the Néel temperature (Morosin, 1970), which contributes to the observed quadrupole splitting of ^{57}Fe:MnS. The value of ε at 4.2 K does not vary significantly with Fe composition, and is similar in magnitude to ε for Fe-rich (Fe,Mg)S.

It is difficult to ascertain from the wide allowed ranges of θ and ϕ indicated in Table 4.2 if the Fe^{2+} spin orientation changes as a function of composition. Often it is possible to determine the spin orientation independently from a crystal field calculation (e.g. Price et al., 1974) combined with other information such as optical, electron paramagnetic resonance and magnetic susceptibility data, but the significant line broadening observed in all of the present spectra indicates that multiaxial spin arrangements are possible for (Fe,Mn)S and (Fe,Mg)S, and such an analysis would contribute no additional information. The Mössbauer spectra represent a sum of the spectra from the different ^{57}Fe sites, and therefore would average all of the different spin orientations. It is unlikely that solid solution effects contribute significantly to the observed line broadening since the average line width remains constant as a function of composition in both solid solutions (see Table 4.2).

4.5 The Hypothetical Phase FeS(B1)

FeS(B1) is the hypothetical endmember of (Fe,Mn)S and (Fe,Mg)S B1 solid solutions, and data derived from these solid solutions can be used to determine the likely properties of FeS(B1). The free energy difference between FeS(B1) and FeS(B8) at a given T can be calculated from the atmospheric pressure phase diagrams of (Fe,Mn)S and (Fe,Mg)S (Fig. 5.1, p. 54) by the following method (Ringwood, 1962a). Consider FeS as a

component of both the B1 and B8 solid solutions in equilibrium. The chemical potential of FeS in the B1 solid solution is given by

$$\mu_{B1}(T) = \mu^{o}_{B1}(T) + RT\ell n\ a_{B1}(T) \qquad (4.3)$$

where a_{B1} is the activity of FeS in the B1 solid solution. A similar expression can be written for the chemical potential of FeS in the B8 solid solution. At equilibrium $\mu_{B1}(T) = \mu_{B8}(T)$, and so

$$\mu^{o}_{B8}(T) - \mu^{o}_{B1}(T) = RT\ell n\ [a_{B1}(T)/a_{B8}(T)]. \qquad (4.4)$$

But the left-hand side of equation (4.4) is the free energy difference $\Delta G^{o}(T)$ between FeS(B1) and FeS(B8), and if both the B1 and B8 solid solutions are assumed to behave ideally,

$$\Delta G^{o}(T) = RT\ell n\ [N_{B1}(T)/N_{B8}(T)] \qquad (4.5)$$

where N_{B1} and N_{B8} are the mole fractions of FeS in the B1 and B8 solid solutions on the equilibrium phase boundaries. From the solubility data of Skinner and Luce (1971), the zero-pressure free energy difference between FeS(B1) and FeS(B8) at 1273 K is calculated to be -4.1 kJ/mole from FeS-MgS data and -2.4 kJ/mole from FeS-MnS data, indicating the near stability of FeS(B1) at 1273 K and atmospheric pressure (see also Jackson and Ringwood, 1981).

The lattice parameter of FeS(B1) can be determined from the cell parameter data of (Fe,Mg)S and (Fe,Mn)S (Jackson and Ringwood, 1981). A value of a = 506.5 $\pm$ 1.5 pm for FeS(B1) is obtained from an extrapolation of equations (4.1) and (4.2). The Mössbauer parameters of FeS(B1) at 298 K are determined by a rough linear extrapolation of the data in Fig. 4.3 to be $\delta \sim 0.90(4)$ mm/sec and $\varepsilon \sim 0.16(4)$ mm/sec. The bonding in FeS(B1) (<Fe-S> = 253 pm) is inferred to be more ionic than in FeS(B8) (<Fe-S> = 249 pm), and the octahedral Fe^{2+} site should show only small deviations from cubic symmetry.

The B1 $\rightarrow$ B8 transition has been of recent interest because of the proposed B8 high-pressure structure for FeO (Wang, 1970; Jackson and Ringwood, 1981; Navrotsky and Davies, 1981), but very little experimental data exists for B1 $\rightarrow$ B8 transitions in binary compounds. It is therefore worthwhile to determine parameters for the transition FeS(B1) $\rightarrow$ FeS(B8). The molar volume of FeS(B8) is 18.17 cm^3/mole, so ΔV for the transition is -7.2% at 298 K and 0.1 MPa (Jackson and Ringwood, 1981). On the basis of a correlation between bond lengths and molar volume, Liu (1981) has found that ΔV for B1 $\rightarrow$ B8 transitions should never be greater than 5% if the interatomic distances remain unchanged and c/a of the B8 phase does not exceed 2.18 (maximum known value). In the case of FeS there is a 1.8%

decrease of <Fe-S> in the transition from FeS(B1) to FeS(B8), which accounts for the larger ΔV. If a compound is known to undergo a B1 → B8 transition at high pressure with an accompanying large volume decrease (> 5%), there must be a significant reduction of the interatomic distance and/or an unusually large c/a value for the B8 phase (if c/a = 2.5 and B1 and B8 <M-X> distances are equal, ΔV = -12%; from Jackson and Ringwood, 1981). For Fe^{2+} compounds in which spin transitions might occur (for example, FeO; see discussion in section 3.6 comparing FeO and FeS), a high-spin → low-spin transition could provide a substantial reduction in interatomic distance, and might accompany a B1 → B8 transition.

FeS has been proposed by Mao et al.(1981) to transform to a distorted B1 structure above 7 GPa on the basis of a diamond anvil cell experiment (the high-pressure phase will be referred to as hpp). One of the greatest differences between FeS(B1) and FeS(hpp) is the mean <Fe-S> distance at 0.1 MPa; <Fe-S> is calculated to be 253 pm in FeS(B1) compared with 235 pm for FeS(hpp) based on the proposed distorted B1 structure, a decrease of 7%. This results in a volume reduction of nearly 20%, which probably is associated with a change in band structure. FeS(B1) is a good candidate for a Mott insulator (see Wilson, 1972 for a comprehensive discussion of Mott insulators); most first-row transition metal oxides and sulphides that crystallize in the B1 structure are Mott insulators (exceptions are VO and TiO) (Wilson, 1972), and the <Fe-S> distance in FeS(B1) is relatively large compared to other Fe sulphides (e.g. FeS in the troilite structure is a Mott insulator with <Fe-S> = 249 pm). In contrast, FeS(hpp) is likely to be metallic since its lower-pressure modification, FeS(B31), is also a metal, and the electrons in FeS(hpp) are more delocalized than in FeS(B31) (section 3.5).

4.6 Distortions of the B1 Structure at High Pressure

4.6.1 MnS - new results

Clendenen and Drickamer (1966) have reported a distortion of MnS from cubic symmetry occurring at ∿ 10 GPa and 298 K, but the origin and nature of the distortion is unknown. The present study was undertaken to characterize the symmetry and volume change at the transition, but no phase transformation was observed in MnS up to 21 GPa. The absence of a transformation is nevertheless significant, and the results are discussed in terms of observations of FeO at high pressure and 298 K.

The MnS compression data were fitted to a Birch-Murnaghan equation-of-state third-order Taylor expansion of energy in terms of the Eulerian finite strain (Birch, 1952; 1978)

$$P = 3f(1 + 2f)^{5/2} K_o[1 - 3f(4 - K_o')/2] \quad (4.6)$$

where the Eulerian finite strain is given by

$$f = [(V/V_o)^{-2/3} - 1]/2. \quad (4.7)$$

Equation (4.6) can be linearized using the normalized pressure (Birch, 1978; see also Jeanloz, 1981)

$$F = P/[3f(1 + 2f)^{5/2}]. \quad (4.8)$$

The compression data were fitted using both a weighted and unweighted least squares minimization procedure and each gave similar results (although standard deviations of K_o and K_o' were slightly higher in the weighted case), but the weighted results are quoted as giving a more accurate representation of the uncertainty (Bass et al., 1981). The weighting factor for each data point was determined by propagating the volume error into the pressure. The compression data are shown in Fig. 4.5 and results of the analysis are given in Table 4.3. The compression data of Clendenen and Drickamer (1966) and Wakabayashi et al.(1968) were also analysed by the same method for comparison.

The present MnS compression data are consistent with a single equation of state to 21 GPa; a fit of the data from 10 to 21 GPa is indistinguishable from a fit from 0 to 21 GPa. These results disagree with the data of Clendenen and Drickamer (1966), however. They noted that above $\sim$ 10 GPa the (220) x-ray reflection became substantially broader and the relative spacing between the (111) and (200) reflections changed, but no new lines appeared and the intensities of the old lines did not decrease, consistent with a distortion of the B1 phase. By assuming a tetragonal distortion, c/a at the transition was calculated by Clendenen and Drickamer (1966) to be 0.98 (assumed to be independent of pressure), and the resulting equation of state is indicated by the dotted line in Fig. 4.4 ($P > 10$ GPa). The zero-pressure elastic parameters of the distorted phase ($P > 10$ GPa) are identical within experimental error to the parameters of the undistorted B1 phase ($P < 10$ GPa).

Two points strongly suggest that MnS in the present work does not undergo the distortion observed by Clendenen and Drickamer (1966) above 10 GPa. Firstly, there was no significant variation in the broadness of the different x-ray reflections at high pressure in the present work to suggest splitting due to structure distortion, since any distortion is

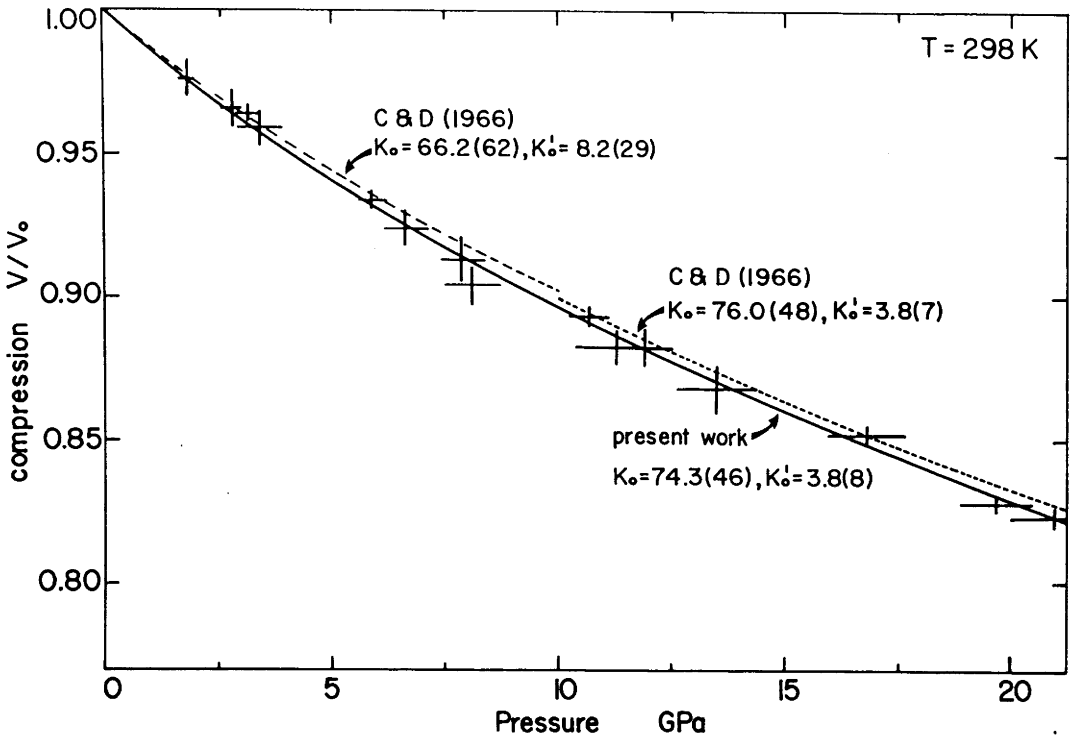

Fig. 4.5 Compression curve of cubic MnS at 298 K. The data were fitted to a third-order Birch-Murnaghan equation of state with the parameters indicated. The equations of state fitted to the data of Clendenen and Drickamer (1966) are also plotted, but note that above 10 GPa their data were fitted assuming a tetragonal cell with c/a = 0.98.

Table 4.3 Results of fitting MnS compression data to third-order Birch-Murnaghan equation of state

source	no. points	parameters	χ^2 [a]
present work 0 < P < 21 GPa	15	K_o=74.3(46) GPa K_o'=3.8(8)	0.2
present work 10 < P < 21 GPa	7	K_o=77.6(82) GPa K_o'=3.4(12)	0.2
C and D (1966) 0 < P < 10 GPa	18	K_o=66.6(62) GPa K_o'=8.2(29)	1.7
C and D (1966)[b] 10 < P < 22.2 GPa	28	K_o=76.0(48) GPa K_o'=3.8(7)	0.6
C and D (1966)[c] 10 < P < 22.2 GPa	28	K_o=101.7(55) GPa K_o'=2.4(6)	0.6
W et al.(1968) 0 < P < 6.5 GPa	28	K_o=77.9(131) GPa K_o'=7.1(66)	0.1

[a] reduced χ^2

[b] fitted assuming a tetragonal high-pressure phase with c/a=0.98 (independent of pressure)

[c] fitted assuming no phase transformation; volume calculated from (220) reflection assuming cubic symmetry

likely to split different reflections by different amounts (at least four reflections were measured at each pressure - (200), (220), (222) and (420)). Secondly, the compression curve reported by Clendenen and Drickamer (1966) is based on the volume calculated from the (220) reflection assuming cubic symmetry. If the structure of MnS is assumed to remain cubic above 10 GPa, K_o and K_o' are calculated from the data of Clendenen and Drickamer (1966) to be 101.7(55) GPa and 2.4(6), respectively. Significantly different values are obtained if the calculation is performed using the (220) reflections from the present work, where K_o and K_o' are similar to those determined using all x-ray reflections (K_o = 74.3(46) GPa, K_o' = 3.8(8)).

One explanation of the discrepancy between the present results and the previous data might be the presence of nonhydrostatic stress on the sample. Ostapenko (1971) has shown that for two polymorphs in hydrostatic equilibrium, the denser modification will become more stable if a uniaxial stress of significant magnitude is applied. A similar result has been shown to be true for second-order transitions where the more rigid form (higher bulk modulus and shear modulus) becomes the stable phase if a sufficiently large uniaxial stress is applied (Ostapenko, 1973). It follows, then, that under conditions of uniaxial nonhydrostatic stress a phase transformation (or distortion) could be observed to occur at a lower pressure than it would under hydrostatic conditions. This has been observed experimentally by Zou et al.(1981). Using solid helium as a pressure transmitting medium (hydrostatic conditions), they observed the $\alpha - \varepsilon$ transition in Fe to occur at a considerably higher pressure than had been previously recorded, which they attributed to the absence of nonhydrostatic stress in their sample compared to previous experiments. It should be noted that the concept of thermodynamic equilibrium is not valid under conditions of nonhydrostatic stress since local phase equilibria differ depending on the orientation of the phase interfaces to the stress, and therefore transformations occurring under nonhydrostatic stress cannot strictly be located on an equilibrium phase diagram. Although most phase transformations will still take place under hydrostatic conditions, Bridgman (1936) states that thermodynamics does not prevent a phase transformation occurring under nonhydrostatic stress that would never occur under hydrostatic conditions.

It is difficult to evaluate the possible differences in nonhydrostatic stress between the present experimental apparatus and the one of Clendenen

and Drickamer (1966); both used ungasketed samples with solid pressure-transmitting media, so both samples would be subject to nonhydrostatic stress. Clendenen and Drickamer (1966) used Al (μ = 2.6 GPa) as an x-ray standard, but the present work used NaCl (μ = 1.5 GPa). It is possible that the low shear strength of NaCl could create an environment closer to hydrostatic than in a sample mixed with Al, and result in the phase transformation occurring closer to the hydrostatic equilibrium pressure. Experiments on MnS in which the degree of nonhydrostatic stress were varied would provide a confirmation or refutation of the explanation of the discrepancy, and would also establish whether the distortion of the MnS crystal structure above 10 GPa could be observed under hydrostatic conditions.

4.6.2 FeO - relevance of MnS results

Zou et al.(1980) have reported a progressive rhombohedral distortion in FeO commencing at $\sim$ 9 GPa, but in a hydrostatic experiment (pressure-transmitting medium = neon) Hazen et al.(1981) report no deviation from cubic symmetry to at least 15 GPa, and suggest the absence of shearing forces to have caused the discrepancy. Results from the present work on MnS tend to support this suggestion. In previous nonhydrostatic experiments, however, compression data of FeO have been interpreted in terms of single equations of state all having similar parameters (Clendenen and Drickamer, 1966; Mao et al., 1969; Will et al., 1980); see Table 6.3 (p. 85) for specific values. The distortion may still have been present, however, but not observed. The distortion observed by Zou et al.(1980) was measured by the splitting of the (111) reflection; the (200) reflection remained unsplit. The previous analyses used only a small number of low-angle x-ray reflections, and would not indicate a distortion if the (200) reflection were given significant weight, and the splitting of the (111) reflection might have been obscured by broadening due to pressure gradients. The x-ray reflections used in the analyses were: Clendenen and Drickamer (1966) - (111) and (200); Mao et al.(1969) - (111), (200) and (220); Will et al.(1980) - (200).

Zou et al.(1980) have suggested that the rhombohedral distortion observed in FeO at high pressure and 298 K is similar to the one known to occur at low temperature, but data reported by Yagi and Akimoto (1981) indicate that the distortion involves more than a simple elongation along [111]. The Mössbauer data of Zou et al.(1980) indicate a magnetic hyperfine field in FeO existing from 5 GPa to at least 70 GPa, so some

rearrangement of atomic spins must take place near the onset of the distortion. Okamoto et al.(1967) have measured the Néel temperature of FeO as a function of pressure to 0.5 GPa, and a linear extrapolation of their results to 298 K gives a pressure of 15 GPa, which is reasonably consistent with the experimental results.

A detailed study of the structure of FeO at high pressure and 298 K has yet to be reported, but it is important to understanding the nature of FeO at high pressure. The progressive volume decrease of FeO beyond the extrapolated value of the cubic form may be important in the interpretation of the shock wave data for FeO of Jeanloz and Ahrens (1979) beyond 70 GPa; only a detailed knowledge of the 298 K transition will indicate if it lies in a region of the P-T phase diagram of FeO that extends to high temperature, or even if it occurs at all under hydrostatic (equilibrium) conditions.

CHAPTER 5 (Fe,Mn)S AND (Fe,Mg)S: HIGH-PRESSURE PHASE DIAGRAM

5.1 Introduction

At atmospheric pressure the phase diagrams for the binary systems FeS-MnS and FeS-MgS contain a large single-phase region (B1 structure), a two-phase region (B1 and B8 structures) and in FeS-MnS, a narrow single-phase region (B8 structure) (Skinner and Luce, 1971) (Fig. 5.1). The positions of the phase boundaries between regions can provide a measure of the relative stability of FeS (and also MgS and MnS) in the B1 and B8 structures, and vary as a function of pressure at constant temperature according to the size of the volume difference between the B1 and B8 phases. The properties of (Fe,Mg)S(B1) and (Fe,Mn)S(B1) have already been studied in detail, and the molar volume of the hypothetical phase FeS(B1) has been derived from these properties (Chapter 4, see also Jackson and Ringwood, 1981). The molar volume of the hypothetical FeS(B1) phase was calculated to be 7.2% greater than FeS(B8), and therefore increasing pressure in the FeS-MnS and FeS-MgS systems should result in exsolution of a B8-structured phase from the B1 solid solution due to the displacement of the B1 phase boundary towards the B1-structured endmember.

The purpose of the present study is to determine experimentally the phase diagrams of FeS-MgS and FeS-MnS at high pressure, firstly to determine if the predicted exsolution of the B8 phase takes place, and secondly to correlate the results with thermodynamic calculations of the phase boundaries. The latter provides further data regarding B1 → B8 transitions at high pressure, and allows the likelihood of B8 polymorphism in MgS and MnS to be assessed. The observation of a high-pressure phase of FeO above 70 GPa by Jeanloz and Ahrens (1980) raises the possibility of (Fe,Mg)O(B1) behaving in an analogous manner to (Fe,Mg)S(B1), and results from the study of FeS-MgS at high pressure may be relevant to calculation of the high-pressure FeO-MgO phase diagram.

5.2 Experimental Procedure

The phase diagrams of FeS-MgS and FeS-MnS were determined at high pressure using samples of (Fe,Mg)S and (Fe,Mn)S with compositions close to the phase boundary between the single-phase B1 region and the two-phase B1/B8 region in order to obtain a run product within the two-phase B1/B8 region. The compositions of the B1 and B8 phase boundaries were taken to be equal to the compositions of the B1 and B8 phases in the run product quenched from high pressure and high temperature.

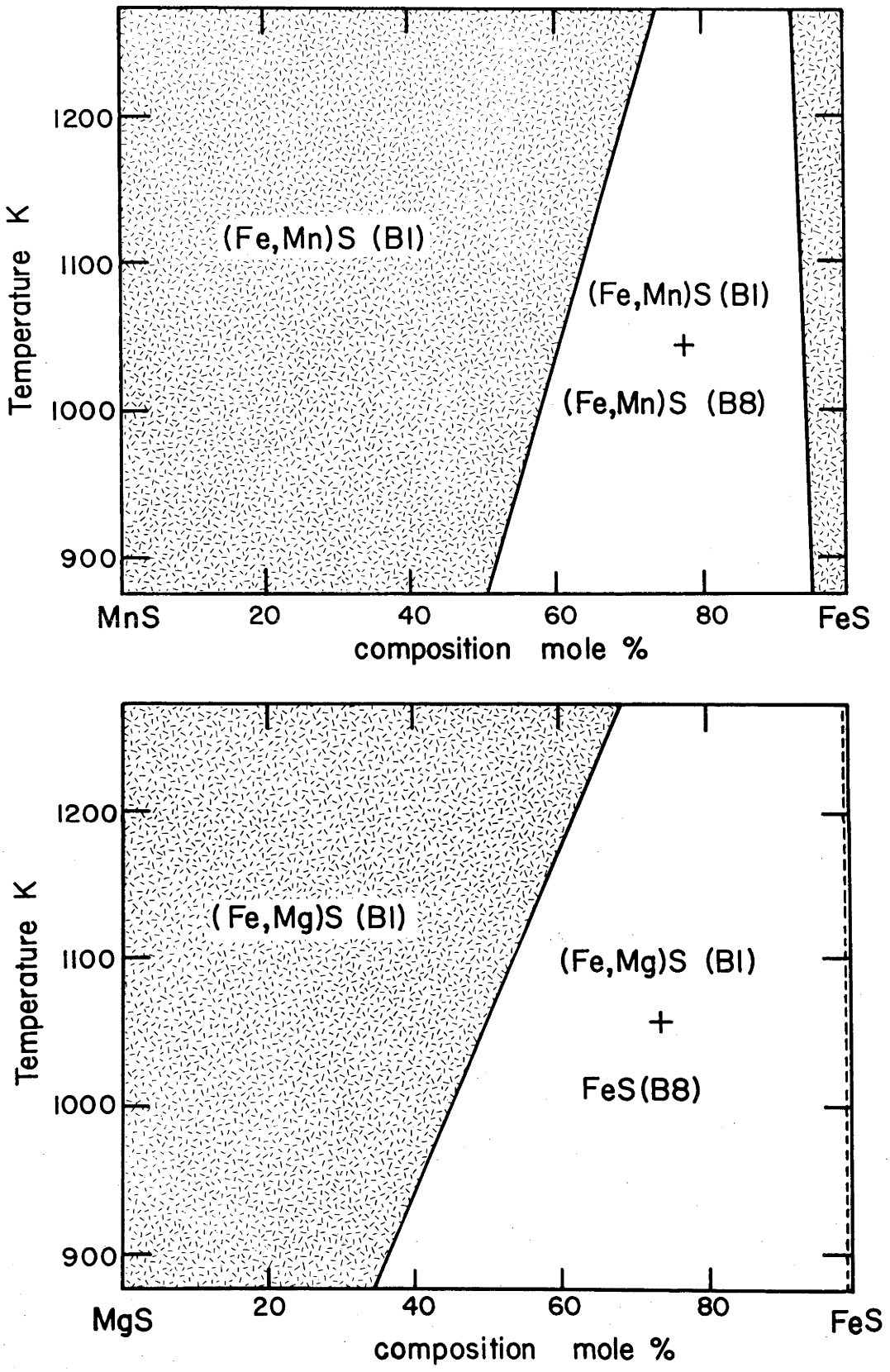

Fig. 5.1 Phase diagrams of the systems FeS-MnS and FeS-MgS at atmospheric pressure. The shaded areas correspond to single-phase regions (after Skinner and Luce, 1971).

Three samples were used in the experiments: Fe-rich (Fe,Mn)S (66 mol % FeS) (FMS 7) and (Fe,Mg)S (59 mol % FeS) (FGS 2) from the single-phase B1 region, and Fe-rich (Fe,Mg)S (80 mol % FeS) (FGS 1) from the two-phase B1/B8 region. Samples FMS 7 and FGS 2 were taken from the study described in the previous chapter (method of preparation described in section 4.2), and sample FGS 1 was prepared for the present study using an identical technique.

The samples were run at high pressure using a solid-media piston cylinder apparatus (Boyd and England, 1960), a Bridgman anvil squeezer (modified after Ringwood and Major, 1968) and a girdle apparatus (Liebermann et al., 1974). The sample was contained within a capsule which consisted of either graphite or spectroscopically-pure Fe. All runs were performed at 1273 K. Descriptions of the apparatus, calibration curves and run procedures are given in Chapter 2.

X-ray diffraction patterns of the quenched run products were recorded using Fe $K\bar{\alpha}$ and Co $K\bar{\alpha}$ radiation to determine the lattice parameters which were calculated on the basis of a least-squares analysis of the x-ray reflections weighted according to the angular uncertainty. Si was used as a calibration standard. The composition of the B1 phase was determined using either equation (4.1) or (4.2) (p. 36) relating the lattice parameter of the cubic cell to the iron composition. The composition of the B8 phase was determined from the (102) reflection of the hexagonal cell, using data of Skinner and Luce (1971) who found that the d_{102} spacing increased smoothly from 209.3 pm for FeS(B8) to 210.2 pm for $Fe_{0.92}Mn_{0.08}S$(B8). There were additional x-ray lines in several patterns corresponding to a superstructure of the hexagonal B8 phase, but in general the lines were not sufficiently well resolved to determine unambiguously the lattice parameters of the superstructure; for consistency all lattice parameters of the Fe-rich phase were calculated assuming a hexagonal B8 structure. This assumption would not affect the determination of the Fe-rich phase composition, since a similar method using the d_{102} spacing has been successfully used to determine the iron composition of nonstoichiometric Fe_xS (Arnold and Reichen, 1962).

There is no data available regarding the variation of the d_{102} spacing with % MgS in (Fe,Mg)S(B8) since it is reported (Skinner and Luce, 1971) that MgS is insoluble in FeS(B8) at atmospheric pressure. It is reasonable

to assume, however, that the increase in d_{102} spacing with MgS composition will be comparable to the increase for (Fe,Mn)S since variations of the lattice parameters of (Fe,Mg)S(B1) and (Fe,Mn)S(B1) are almost identical. Also there is a strong correlation of the cation/anion electronegativity difference ($\Delta\chi$) with the c/a ratio of the B8 structure (e.g. Jackson and Ringwood, 1981), such that the greater electronegativity difference between Mg^{2+} and S^{2-} ($\Delta\chi$ = 1.3 cf. 1.0 and 0.7 for (Mn^{2+},S^{2-}) and (Fe^{2+},S^{2-}), respectively) should result in greater lattice distortion (larger c/a, and therefore larger d_{102} for similar <M-X> distance) for (Fe,Mg)S(B8) than for (Fe,Mn)S(B8).

Mössbauer spectra of the run products were recorded at 298 K using the spectrometers at Dept. Solid State Physics, ANU and Dept. of Physics, Monash University. Equipment description, sample preparation and run procedure are given in Chapter 2.

5.3 Experimental Results

5.3.1 X-ray diffraction: the phase diagram

Twenty-six high-pressure runs were performed on (Fe,Mn)S and (Fe,Mg)S samples to determine the phase diagrams. The results of the runs are listed in Table 5.1 and 5.2. Two different starting materials were used in the (Fe,Mg)S runs, and the absence of any difference in phase composition between run products produced from a single-phase B1 starting material and a two-phase B1/B8 starting material confirms that thermodynamic equilibrium has been achieved.

Relatively large uncertainties were recorded for the phase boundaries due to the broadness of x-ray lines in the B1 and B8 phases. X-ray lines corresponding to the Si standard are very sharp, so geometrical errors from x-ray diffraction can be ruled out. The nonattainment of equilibrium at high P,T can also be ruled out; several runs were repeated with significantly longer run times, and no change was noted in the broadness of lines or the compositions of the B1 and B8 phases. Some of the broadening may be attributed to minor variation in temperature across the sample, but the most likely source of broadening is from poor crystallization of the B1 and B8 phases, perhaps but not necessarily due to the quenching rate.

Mann and Van Vlack (1976) have observed differences in the stoichiometry of the B8 phase between phase diagrams of FeS-MnS (iron

TABLE 5.1 Results of (Fe,Mg)S high-pressure runs at T = 1273 K

Run #	P GPa	Capsule	Starting[a] Material	B1 phase a(pm)	B8 phase a(pm)	B8 phase c(pm)	d_{102}(pm)	phase boundary compositions B1(mol % FeS)	B8(mol % MgS)
9261	0.5(1)	Fe	B1/B8	511.9(2)	-[b]	-[b]	210(5)	65.4(15)	
9257	1.0(1)	Fe	B1/B8	512.4(4)	344.7(5)	588(1)	209.3(1)	61.6(31)	nil
9266	1.5(1)	Fe	B1/B8	513.7(4)	344.9(5)	587(1)	209.5(1)	51.6(31)	<1%[c]
9295	1.5(1)	C	B1	514.1(2)	345.3(5)	580(1)	208.1(1)	48.5(15)	
9259	2.0(1)	Fe	B1/B8	514.2(4)	344.8(5)	588(1)	209.6(1)	47.7(31)	<2%[c]
9288	2.2(1)	C	B1	514.5(2)	344.7(5)	586(2)	209.2(2)	45.4(15)	
9265	2.5(1)	Fe	B1/B8	515.6(4)	344.7(5)	588(1)	209.4(1)	37.0(31)	<1%[c]
9260	3.0(1)	Fe	B1/B8	515.6(4)	344.5(5)	588(1)	209.2(1)	37.0(31)	nil
9273	3.5(1)	C	B1	515.3(4)	344.3(5)	589(1)	209.6(1)	39.3(31)	
9196	3.7(1)	C	B1/B8	515.7(4)	344.7(5)	588(1)	209.4(1)	36.2(31)	
9296	4.5(2)	C	B1	516.1(3)	344.9(3)	586(1)	209.2(1)	33.1(23)	
G2-112	5.3(5)	C	B1	516.2(2)	345.4(5)	581(1)	208.3(1)	32.3(15)	
G2-99	6.0(5)	C	B1	516.6(4)	344.7(5)	588(1)	209.5(1)	29.3(31)	

[a] indicates whether starting material was single phase (B1) or two phase (B1 + B8)

[b] only the strongest reflection of the B8 phase (102) was present; the lattice parameters could not therefore be determined

[c] maximum allowed composition, assuming d_{102} in (Fe,Mg)S (B8) varies in a similar manner to d_{102} in (Fe,Mn)S (B8)

TABLE 5.2 Results of (Fe,Mn)S high-pressure runs at T = 1273 K[a]

Run #	P GPa	Capsule	B1 phase a(pm)	B8 phase a(pm)	B8 phase c(pm)	d_{102}(pm)	phase boundary compositions B1 (mol % FeS)	B8 (mol % MnS)
9303	0.5(1)	C	511.2(3)	-	-	-	>67.8(18)[b]	
9305	1.0(1)	C	511.4(2)	-	-	-	>66.5(12)[b]	
9306	1.5(1)	C	511.3(3)	-	-	-	>67.2(18)[b]	
9304	2.0(1)	C	512.1(3)	343.5(8)	591(5)	209.5(3)	62.3(18)	
9302	2.5(1)	C	513.5(3)	346.8(5)	579(3)	208.5(2)	53.8(18)	
9298	3.0(1)	C	513.5(3)	345.4(5)	589(2)	209.8(1)	53.8(18)	
8807	3.5(1)	C	513.7(3)	345.2(5)	587(1)	209.5(1)	52.6(18)	
8811	3.5(1)	Fe	513.7(3)	346.2(5)	589(2)	209.9(1)	52.6(18)	5.4(11)
9297	4.5(2)	C	514.2(2)	345.4(5)	591(2)	210.2(1)	49.6(12)	
9311	5.0(2)	Fe	514.4(3)	345.7(5)	588(2)	209.9(1)	48.4(18)	5.4(11)
G2-113	5.7(5)	C	514.5(2)	345.7(5)	585(1)	209.2(1)	47.8(12)	
G2-114	6.0(5)	C	514.6(2)	346.1(5)	584(2)	209.1(1)	47.2(12)	
S286	7.0(5)	Fe	516.9(3)	345.5(5)	589(2)	209.9(1)	33.3(18)	5.4(11)

[a] all runs performed with single-phase (Fe,Mn)S (B1) as a starting material

[b] no B8 phase was observed to be present in the run product; the B1 - B1/B8 phase boundary must therefore lie at a higher FeS composition

saturated) and FeS-MnS (no excess iron) at atmospheric pressure, so two types of sample capsule were used in the experiments to determine if the phase boundaries were affected by the presence or absence of metallic iron at high pressure. No change was noted in the composition of the B1 phase boundary regardless of whether a graphite capsule (no excess iron) or iron capsule (iron saturated) was used. There was a decrease, however, in the spacing of the (102) reflection of the B8 phase when the system was undersaturated with respect to iron, caused by nonstoichiometry of the B8 phase. The amount of MgS or MnS present in the B8 phase could not then be reliably determined, and therefore the composition of the B8 phase boundary was determined only from those runs which used iron capsules.

The phase diagrams of FeS-MnS and FeS-MgS determined from the high-pressure experiments are illustrated in Fig. 5.2. The most notable feature of the phase diagrams is the considerable displacement of the B1 phase boundary towards the B1 endmember at high pressure, confirming earlier predictions based on the relative molar volumes of FeS in the B1 and B8 structures. A further feature of the phase diagrams is the pressure insensitivity of the composition of the B8 phase. In FeS-MnS the maximum concentration of MnS in FeS(B8) decreases from 7.4 mol % at 0.1 MPa to 5.4(11) mol % at 3.5 GPa, and remains relatively constant to at least 7 GPa. The results from FeS-MgS are consistent with less than 1 mol % MgS dissolved in FeS(B8) to at least 3 GPa. Although the experiments on (Fe,Mg)S at higher pressure were performed with graphite capsules, there is no evidence to suggest a substantial increase in the amount of MgS in FeS(B8) to at least 6 GPa.

The limiting composition for the (Mn,Fe)S B1 solid solutions appears to change dramatically between 6 GPa and 7 GPa. It is likely that the discontinuity is caused by the high-pressure phase transition (Fe,Mn)S(B8) → (Fe,Mn)S(hpp) where the high-pressure phase is similar to the one reported by Mao et al.(1981) for FeS.

5.3.2 Optical examination of exsolution textures

Several of the high-pressure run products were examined using the electron microprobe to determine the compositions of the B1 and B8 phases, but in all cases only the bulk composition of the sample could be obtained, suggesting a grain size of the exsolved B8 phase smaller than 1 μm. The high-pressure run products were then examined using a polarizing optical microscope to determine the textures of the exsolved B8 phase.

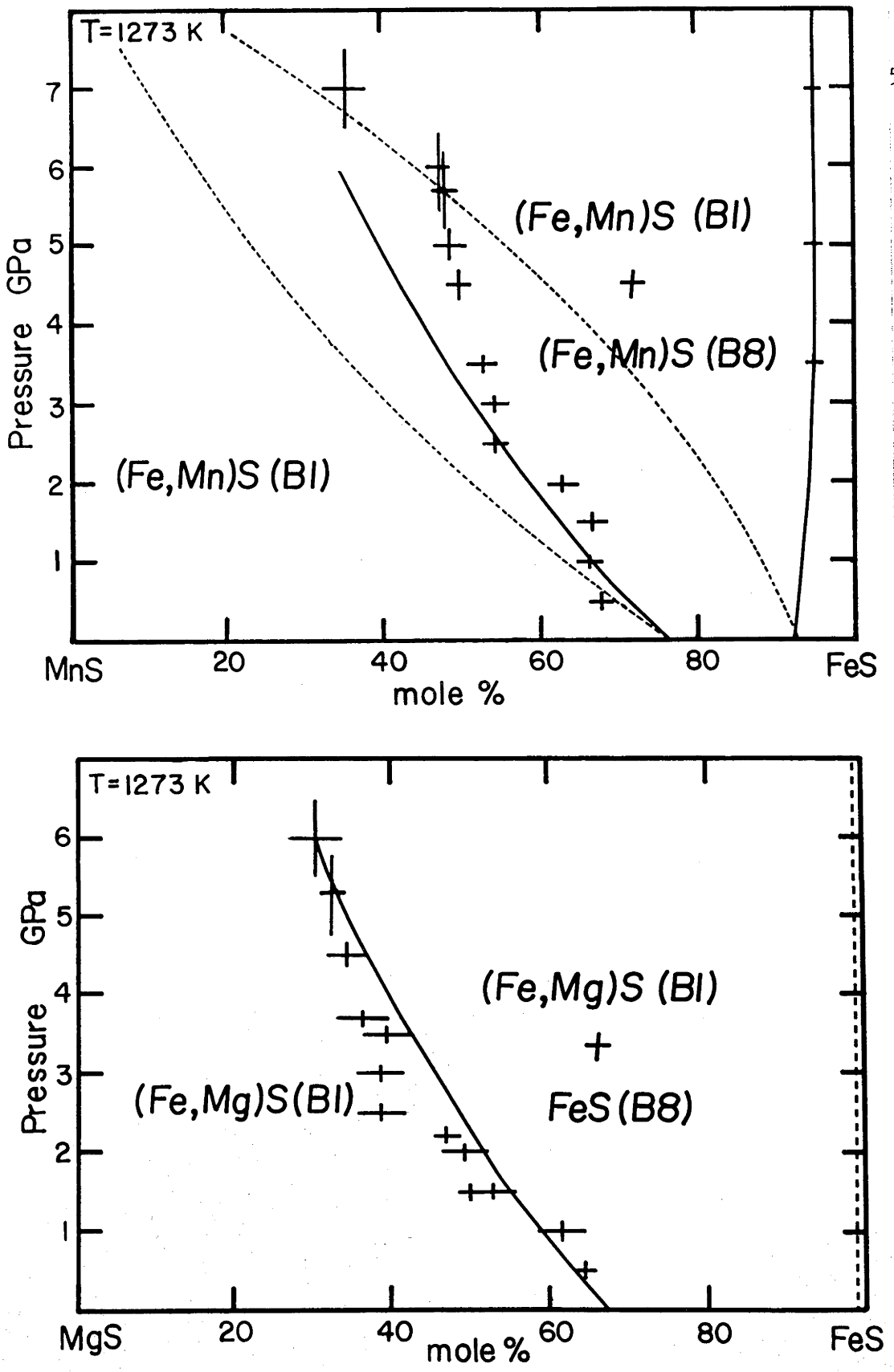

Fig. 5.2 Phase diagrams of the systems FeS-MnS and FeS-MgS determined from high-pressure runs at 1273 K. The solid curves correspond to the phase boundaries calculated assuming that only the B1 solid solutions behave ideally (see section 5.4). For FeS-MnS the activity coefficient of the B8 solid solution ($\neq 1$) was assumed to remain constant with pressure. The dashed lines correspond to the phase boundaries calculated assuming that both the B1 and B8 (Fe,Mn)S solid solutions behave ideally.

Only the products of runs with starting materials from the single-phase B1 region were studied to avoid confusion of the exsolved B8 phase with a B8 phase which was present initially.

The photographs that were taken of the (Fe,Mn)S and (Fe,Mg)S high-pressure run products in polarized light are shown in Plate 5.1. The dark grey areas correspond to the B1 phase, the light grey areas to the B8 phase, the black areas to either graphite or epoxy resin (mounting compound), and the white area in (f) to metallic iron from the sample capsule. The B1 and B8 phases could not be distinguished in unpolarized light.

The photographs in Plate 5.1 confirm that the grain size of the B8 phase is less than 1 μm, but the exsolution textures vary from sample to sample. The classic lamellar form is illustrated by (i), where the grains form octahedral nets (four preferred directions) typical of a hexagonal guest phase (B8) in a cubic host phase (B1) (Ramdohr, 1980, p. 173). The exsolution boundaries in the remaining (Fe,Mg)S samples show varying degrees of rounding, with almost spheroidal grains in (g). The grains of the exsolved B8 phase in the (Fe,Mn)S samples are nearly all spheroidal, with only remnants of a lamellar texture in (e) and (f).

The variation in exsolution textures can probably be attributed to differences in their time of formation. Ramdohr (1980, p. 172) has observed the lamellar texture of chalcopyrite in bornite formed by rapid cooling from 873 K to be obliterated and replaced by spheroidal grains when the sample was cooled slowly. Slow cooling increases the time available for diffusion of the cations through the sample and hence causes rounding of sharp-cornered exsolution boundaries, merging of fine bodies into larger inclusions and flowing out of lamellae into irregular rows of dots (Ramdohr, 1980, p. 169). In (Fe,Mg)S and (Fe,Mn)S exsolution of the B8 phase is not caused by cooling below a critical temperature, but by destabilizing the solid solution at high pressure; here the equivalent of a slow cooling rate is a run of long duration at high P,T. The exsolution textures of (Fe,Mg)S samples are qualitatively accounted for by the run duration, because the deterioration of the lamellar texture corresponds to increasing run time: (i), (k) - 30 min, (j) - 45 min, (h) - 2 hr, (g) - 6 hr. The absence of lamellar textures in the (Fe,Mn)S samples does not correspond to long run times (all less than 2 hr), and probably indicates a higher diffusion rate of Mn^{2+} compared to Mg^{2+}.

Plate 5.1 Photographs taken of products from (Fe,Mg)S and (Fe,Mn)S high-pressure runs. The white scale bar corresponds to 1 μm. The key below indicates the run number, the pressure of the run, and the duration of the run.

Key to phases.: dark grey - B1 phase
light grey - B8 phase
black - graphite or epoxy

(Fe,Mn)S	(Fe,Mg)S
(a) Run 9306 - 1.5 GPa, 2 hrs	(g) Run 9295 - 1.5 GPa, 6 hrs
(b) Run 9302 - 2.5 GPa, 1.5 hrs	(h) Run 9288 - 2.2 GPa, 2 hrs
(c) Run 9298 - 3.0 GPa, 0.67 hr	(i) Run 9296 - 4.5 GPa, 0.5 hr
(d) Run 9297 - 4.5 GPa, 0.5 hr	(j) Run G2-112 - 5.3 GPa, 0.8 hr
(e) Run G2-113 - 5.7 GPa, 0.5 hr	(k) Run G2-99 - 6.0 GPa, 0.5 hr
(f) Run S286 - 7.0 GPa, 1.0 hr -the white areas correspond to metallic Fe	

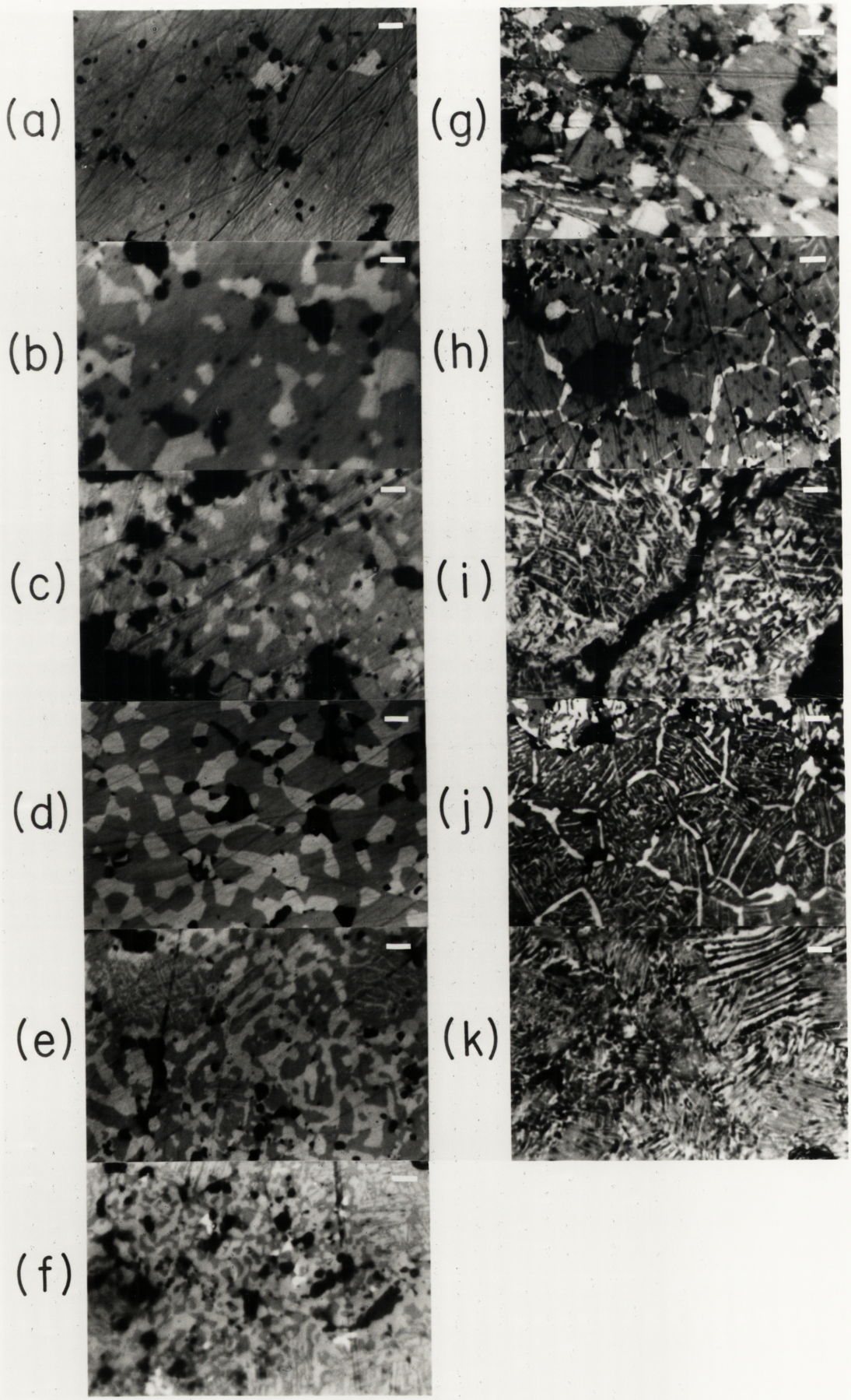
(a)
(b)
(c)
(d)
(e)
(f)
(g)
(h)
(i)
(j)
(k)

The relative amounts of the B8 phase and the B1 phase are constrained by the final composition of the B1 phase and the metal/sulphur ratio of the B8 phase

$$Fe_{0.59}Mg_{0.41}S(B1) \rightarrow (1-a)Fe_xMg_{1-x}S(B1) + aFe_yS(B8) \quad (5.1)$$

$$Fe_{0.66}Mn_{0.34}S(B1) \rightarrow (1-a)Fe_xMn_{1-x}S(B1) + a(Fe_{0.95}Mn_{0.05})_yS(B8) \quad (5.2)$$

where y should fall between the values 1.0 and 0.88 (Fe_7S_8). The B8/B1 ratio is sensitive to the stoichiometry of the B8 phase, and an independent determination of the B8/B1 ratio would constrain the metal/sulphur ratio. In theory the B8/B1 ratio could be determined by point counting the phases from photographs such as those in Plate 5.1, but the large uncertainty involved would preclude a meaningful interpretation. A rough count of the area covered by the B8 phase in Plate 5.1, however, indicates that the relative proportions of the B1 and B8 phases are at least consistent with the final compositions of the B1 and B8 phases listed in Tables 5.1 and 5.2, assuming that y lies between the values 1.0 and 0.88.

TABLE 5.3 Mössbauer parameters for (Fe,Mg)S and (Fe,Mn)S high-pressure run products

Run #	P GPa	% FeS[a]	B1 phase δ mm/sec	B1 phase ε mm/sec	B8 phase[b] δ mm/sec	B8 phase[b] H kOe	area ratio B8/B1 calculated[c]	area ratio B8/B1 observed[d]
(Fe,Mn)S:								
9306	1.5(1)	67.2(3)	0.925(3)	0.117(3)	-	-	-	-
9302	2.5(1)	53.8(3)	0.926(3)	0.115(3)	0.74(5)	287(1)	0.74-1.1	1.2(1)
8811	3.5(1)	52.6(3)	0.940(6)	0.132(6)	0.78(4)	310(1)	0.83-1.2	1.4(2)
9297	4.5(2)	49.6(2)	0.915(6)	0.119(7)	0.78(1)	310(1)	1.1 -1.5	1.4(2)
G2-114	6.0(5)	47.2(2)	0.920(3)	0.119(3)	0.76(1)	312(1)	1.3 -1.8	2.0(1)
S286[e]	7.0(5)	33.3(3)	0.965(12)	0.106(14)	0.75(4)	312(1)	3.2 -4.6	3.2(2)
(Fe,Mg)S:								
9295	1.5(1)	50.2(2)	0.920(19)	0.095(26)	0.67(8)	309(1)	0.43-0.53	1.2(1)
9288	2.2(1)	47.8(2)	0.952(3)	0.114(3)	0.80(5)	295(2)	0.57-0.71	1.2(1)
9273	3.5(1)	43.0(3)	0.950(6)	0.112(6)	0.81(3)	314(1)	0.91-1.1	1.9(1)
9296	4.5(2)	38.1(3)	0.958(4)	0.095(5)	0.76(1)	311(1)	1.3 -1.7	2.3(1)
G2-99	6.0(5)	35.1(3)	0.972(7)	0.095(9)	0.75(1)	312(1)	1.7 -2.1	2.8(1)

[a] composition of the B1 phase determined from the cell parameter data using eqs. (4.1) and (4.2)

[b] based on a fit of the B8 phase to three doublets

[c] calculated assuming reactions (5.1) and (5.2) with a metal/sulphur ratio of 1.0 and 0.88 (lower and upper bounds, respectively)

[d] based on the area under the Mössbauer spectrum of the B8 phase relative to the spectrum of the B1 phase

[e] this sample also contained ~60% metallic iron (present as a six-line magnetic spectrum)

5.3.3 Mössbauer spectra of high-pressure runs

The Mössbauer spectra were recorded at 298 K of a series of (Fe,Mn)S and (Fe,Mg)S samples quenched from high pressure (Fig. 5.3), selected from runs with a starting composition in the single-phase B1 region of the phase diagram. The spectra indicate that the run products consist of at least two phases: a quadrupole doublet corresponding to the B1 phase, and a six-line magnetic spectrum corresponding to the B8 phase. The relative spacings of the spectral lines corresponding to the B8 phase indicate that the magnetic field direction and the principal axis of the electric field gradient in the B8 phase are not parallel, and a simple six-line fit to the spectrum is not appropriate. This has been previously observed by Ono et al.(1962) and Hafner and Kalvius (1966) to be true for Fe_xS (x = 1.00, 0.95, 0.93, 0.88). For computational simplicity the B8 phase spectrum was fitted to three sets of doublets, with the centre shift being calculated from the weighted average of the centres and the hyperfine field from the splitting of the outermost doublet.

The Mössbauer parameters of the spectra are listed in Table 5.3. The centre shift and quadrupole splitting of the B1 phase quenched from high pressure should agree with the values determined for single-phase (Fe,Mn)S(B1) and (Fe,Mg)S(B1) samples as a function of composition in Chapter 4. The present values of δ and ε are plotted in Fig. 5.4 along with lines indicating the variation of δ and ε with composition taken from Fig. 4.3 (p. 40). The agreement between δ and ε and previously measured values is satisfactory, given the poor resolution of the large velocity scale and the presence of a third phase (discussed below).

The centre shift and hyperfine field of the B8 phase do not vary appreciably with either pressure or composition, and the values are identical within experimental error to those recorded for $Fe_{1.0}S$ (e.g. Ono et al., 1962; Hafner and Kalvius, 1966); the small amount of Mn present in FeS cannot be measured, therefore, in the present work. The few odd values of δ and H are probably due to effects from the small particle size of the B8 phase (e.g. Schroeer, 1970). Evidence for these effects is provided by the unusually broad line widths of the B8 phase, consistent with a partial relaxation of the spin domains due to their small volume (e.g. Collins et al., 1967).

There is evidence from the Mössbauer spectra in Fig. 5.3 for a third Fe-bearing phase, present as a quadrupole doublet with parameters

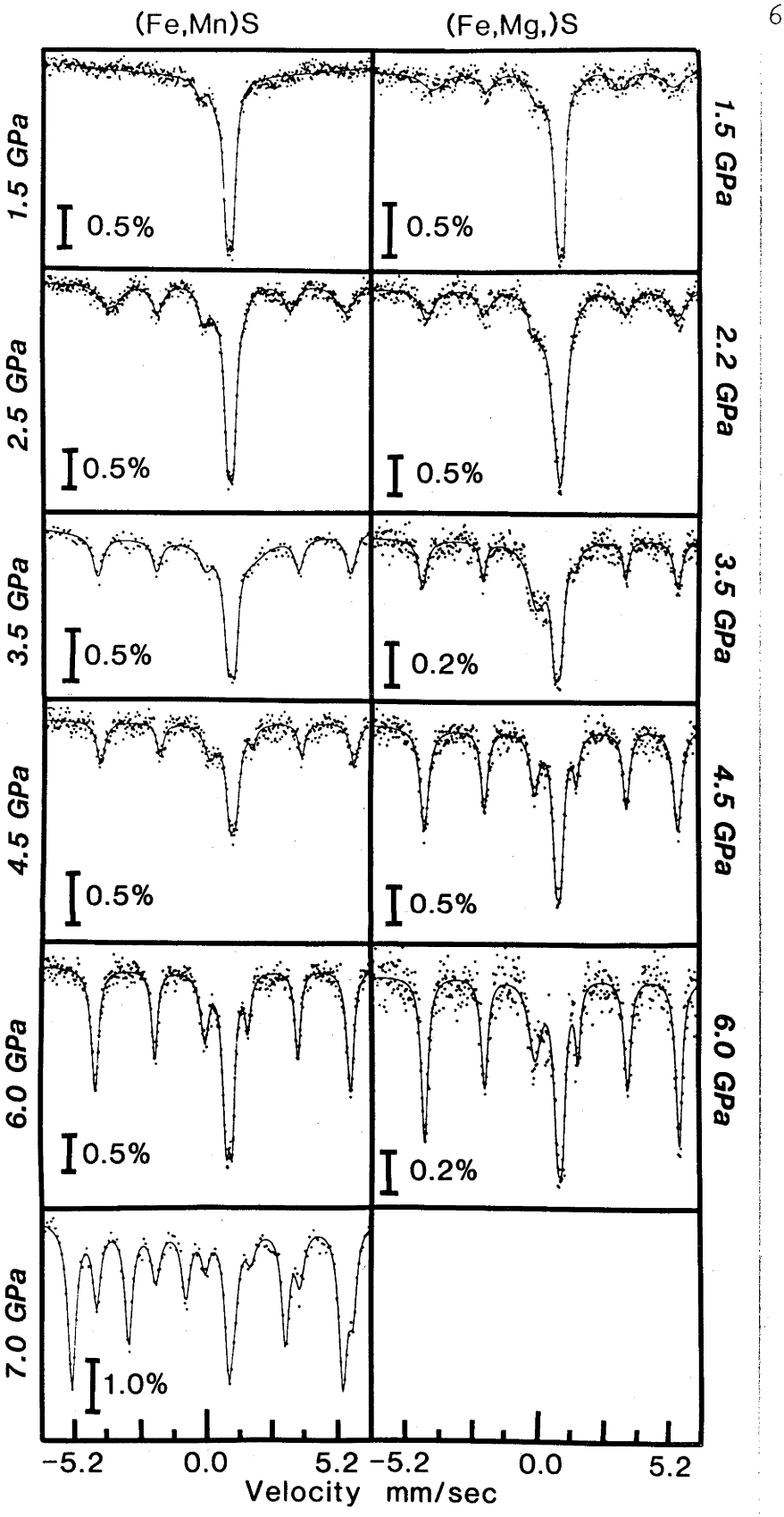

Fig. 5.3 Mössbauer spectra of (Fe,Mn)S and (Fe,Mg)S run products quenched from high pressure, recorded at 298 K. The velocity scales are relative to Fe.

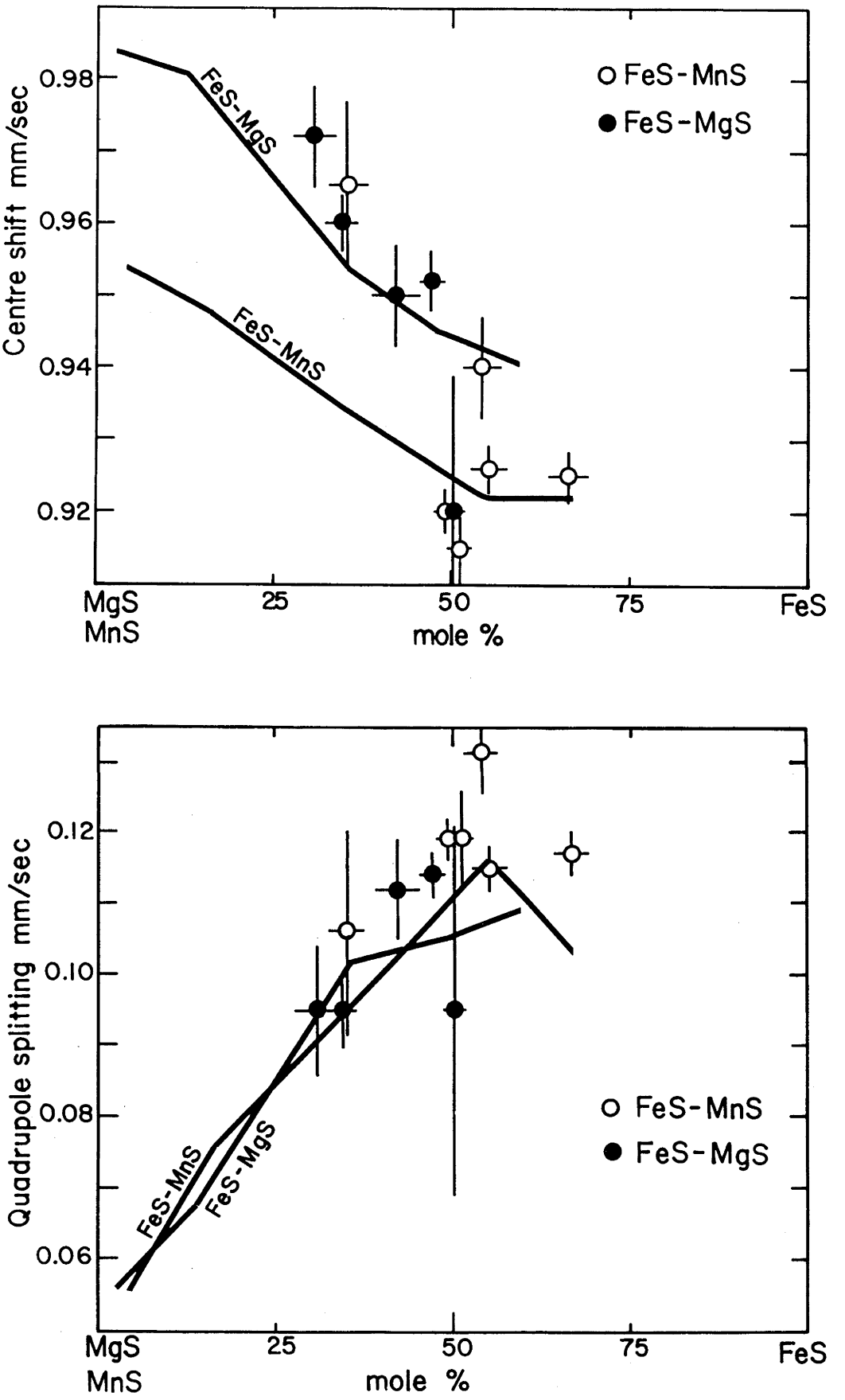

Fig. 5.4 Variation of the centre shift and quadrupole splitting with composition of the spectra shown in Fig. 5.3. The bold lines indicate the variation of the parameters observed for single-phase (Fe,Mn)S(B1) and (Fe,Mg)S(B1) (section 4.4).

$\delta \sim 0.2$ mm/sec, $\varepsilon \sim 0.6$ mm/sec and very broad line widths (~ 0.5 - 1.0 mm/sec). Small amounts of a similar phase were also observed in two spectra of (Fe,Mn)S(B1) at 298 K (section 4.3.2). The high-pressure spectra could not be successfully fitted with a quadrupole doublet corresponding to the third phase because of its relatively small proportion and the large velocity scale of the spectra; to accommodate the additional intensity the widths and areas of the inner doublet of the B8 phase were permitted to vary, and the remaining area of the impurity doublet was taken up by the B1 phase doublet. The fit introduces small errors into the measured parameters for the B1 phase, and might account for the deviations of the centre shift and quadrupole splitting data in Fig. 5.4.

The third phase might correspond to iron-rich FeS_2 (C2-structured phase), whose Mössbauer parameters are nearly identical to those observed here (e.g. Temperley and Lefevre, 1966). There are two points which suggest that the particle size of the C2 phase is very small (< 100 nm). Firstly, there was no evidence for large grains of an additional phase noted in the mounts illustrated in Plate 5.1, and FeS_2 should be easily distinguished by its metallic lustre. Secondly, the Mössbauer lines of the spectrum are excessively broad, consistent with wide ranges of the Mössbauer parameters (δ , ε) caused by stress and strain effects from the large number of crystallite surfaces, and coupling of large numbers of atoms to the environment at crystallite interfaces (Schroeer, 1970).

The relative amounts of Fe in the B1 and B8 phases can be roughly determined from the areas of the corresponding spectra, and are listed in the last column of Table 5.3. The area ratio B8/B1 can also be calculated on the basis of reactions (5.1) and (5.2); B8/B1 = ay/(x(1-a)) for (Fe,Mg)S and B8/B1 = 0.95ay/(x(1-a)) for (Fe,Mn)S, where x is the Fe composition of the B1 phase in the run product and y is the metal/sulphur ratio of the B8 phase (the Mössbauer effect sees only the Fe atoms, not Mg or Mn). The range of values that are obtained for the area ratio B8/B1 when y is varied from 1.0 to 0.88 are listed in Table 5.3.

For the runs performed in Fe capsules, the value of y is already known to be 1.0 (Mann and Van Vlack, 1976), and therefore the area ratios from spectra of runs 8811 and S286 should correspond to the lower bound of the calculated range. The observed and calculated values agree within 30%, which is consistent with the magnitude of additional errors in the area

ratio that were not accounted for due to uncertainty regarding the magnitude of their contributions. These errors include differences in recoil-free fraction between phases, the poor resolution of the large velocity scale, the presence of Fe^{3+}, and the effect of the impurity phase, which taken together, could probably affect the area ratio by $\sim$ 30 - 40%.

From the d_{102} spacing data, the metal/sulphur ratios of the B8 phase in runs performed in graphite capsules are already known to be less than 1.0 (section 5.3.1). This is confirmed by the observed area ratios of these runs which exceed the calculated range (y = 1.0 to 0.88) in all cases. Bearing in mind the large error associated with the area ratio measured from the Mössbauer spectra and that it probably overestimates rather than underestimates the true value, the metal/sulphur ratios of the B8 phase in runs performed in graphite capsules probably fall within the range 1.0 to 0.88, although it is likely that they lie closer to 0.88 than to 1.0.

5.4 Theoretical Calculation of High-Pressure Phase Diagrams

5.4.1 FeS-MgS

The phase diagram of FeS-MgS can be calculated at high pressure from thermodynamic data derived from the solid solution. Experimentally the phase FeS(B8) is observed to dissolve negligible MgS to at least 3 GPa, so FeS(B8) will be assumed to be a pure phase in the calculation. Nonstoichiometry of FeS is also neglected; this was shown in section 5.3.1 not to affect the composition of the B1 - B1/B8 phase boundary. FeS(B8) is assumed to be stable at 1273 K from 0.1 MPa to 6 GPa. King and Prewitt (1982) have identified a phase with the orthorhombic MnP structure (B31) above 3.5 GPa at 298 K, but the location of the phase boundary between the B31 and B8 structures at high P,T is unknown. The transition FeS(B31) $\rightarrow$ FeS(B8) is observed to be second order at 0.1 MPa and occurs from $\sim$ 360 K - 490 K (King and Prewitt, 1982), so any reasonable estimate of the slope of the B31/B8 phase boundary would support the assumption that FeS(B8) is stable at 1273 K from 0.1 MPa to 6 GPa.

At the P,T conditions where $Fe_xMg_{1-x}S$(B1) exists in equilibrium with the mixture $Fe_xMg_{1-x}S$(B1) + FeS(B8), the chemical potentials of FeS in each phase are equal. The chemical potential of FeS in the B1 phase is given by

$$\mu_{FeS}^{B1}(P,T) = \mu_{FeS}^{B1,o}(P,T) + RT\ell n\ a_{FeS}^{B1} \quad (5.3)$$

where the zero subscript refers to pure FeS and a is the activity of FeS in the (Fe,Mg)S B1 solid solution. If the B1 solid solution is assumed to behave ideally, the activity of FeS is equal to its mole fraction, x. The chemical potential of FeS in the B8 phase is given by

$$\mu_{FeS}^{B8}(P,T) = \mu_{FeS}^{B8,o}(P,T). \quad (5.4)$$

At equilibrium

$$\mu_{FeS}^{B1}(P,T) = \mu_{FeS}^{B8}(P,T) \quad (5.5)$$

so

$$\mu_{FeS}^{B8,o}(P,T) - \mu_{FeS}^{B1,o}(P,T) = RT\ell n\ x. \quad (5.6)$$

But the left-hand side of equation (5.6) is the free energy change $\Delta G^o(P,T)$ for the reaction

$$FeS(B1) \rightarrow FeS(B8) \quad (5.7)$$

which is related to $\Delta G^o(0,T)$ by

$$\Delta G^o(P,T) = \Delta G^o(0,T) + \int \Delta V(P,T)\, dP \quad (5.8)$$

where $\Delta V(P,T)$ refers to reaction (5.7). If the effects of thermal expansion and compression are assumed to be equal in FeS(B1) and FeS(B8), the value of x is given by

$$x = \exp\{[\Delta G^o(0,T) + P\Delta V(0,298\ K)]/RT\}. \quad (5.9)$$

The values for $\Delta G^o(0,\ 1273\ K)$ and $\Delta V(0,\ 298\ K)$ have been determined from FeS–MgS solid solution data to be −4.1 kJ/mole and −1.4 cm^3/mole, respectively (Jackson and Ringwood, 1981; section 4.5, this thesis).

The composition of the B1 - B1/B8 phase boundary in the system FeS–MgS has been calculated using equation (5.9) at T = 1273 K, and is plotted in Fig. 5.2 (p. 59). The close agreement between the experimental results and the calculated curve confirms that the analysis which predicts exsolution of FeS(B8) at high pressure from (Fe,Mg)S(B1) is valid.

The solubility of a given compound (e.g. MgS) in solid solution with another compound having a denser structure (e.g. FeS(B8)) is a function of the free energy difference between structures, and is thus related to the pressure at which the former compound (MgS) transforms to the denser structure (Ringwood, 1962a). The negligible solubility of MgS in FeS(B8) to at least 6 GPa is therefore not consistent with B8 polymorphism of MgS at moderate pressures, and indicates that an alternative structure might be a more likely candidate for MgS at high pressure, for example the B2 structure which is more favoured among Group IIA compounds.

5.4.2 FeS-MnS

The method of calculating the FeS-MnS phase diagram at high pressure is similar to FeS-MgS, except that the B8 phase composition must be considered variable. There are two phase boundaries to be calculated, one between $Fe_xMn_{1-x}S$(B1) and the two-phase region, and the other between the two-phase region and $Fe_yMn_{1-y}S$(B8). The chemical potentials of both FeS and MnS in the B1 and B8 solid solutions must be considered to obtain two equations expressed in (P,T,x,y). These are

$$\Delta G^{o}_{FeS}(0,T) + P\Delta V_{FeS} = RT\ell n\ (x/y) \qquad (5.10)$$

$$\Delta G^{o}_{MnS}(0,T) + P\Delta V_{MnS} = RT\ell n\ [(1-x)/(1-y)] \qquad (5.11)$$

where thermal expansion and compression effects have been neglected, ΔV refers to the B1 → B8 transition, and both the B1 and B8 solid solutions are assumed to behave ideally. ΔG^{o}_{MnS}(0, 1273 K) can be obtained from the solubility data of Skinner and Luce (1971), and is equal to 13.4 kJ/mol (Jackson and Ringwood, 1981). ΔV_{MnS}(B1 → B8) can be calculated if the <Mn-S> distance and the c/a ratio of the B8 polymorph are known. If the % reduction in <Mn-S> distance from B1 to B8 is assumed to be identical to that in FeS, and c/a is determined from the correlation with the electronegativity difference, ΔV_{MnS} is calculated to be -1.5 cm^3/mol (Jackson and Ringwood, 1981). The resulting phase boundaries calculated from equations (5.10) and (5.11) are indicated by the dashed curves in Fig. 5.2 (p. 59). The calculations indicate that the two-phase region closes at 9 GPa where MnS undergoes a B1 → B8 transition; this directly contradicts the experimental results which show a solubility of only 5 mol % MnS in FeS(B8) to at least 7 GPa.

The most likely source of error in the calculation is the assumption that the B8 solid solution behaves ideally. A measure of the nonideality of the (Fe,Mn)S(B8) solid solution is provided by the determinations of ΔG^{o}_{FeS}(B1 → B8) calculated in section 4.5. Assuming the value of ΔG^{o}_{FeS}(1273 K) calculated from FeS-MgS data to be correct, the discrepancy caused when FeS-MnS data are used is attributed to nonideal behaviour of the (Fe,Mn)S(B8) solid solution. If the B1 solid solution is assumed to behave ideally and the B8 solid solution is not, the zero-pressure free energy difference between FeS(B1) and FeS(B8) is given by

$$\Delta G^{o}_{FeS}(0,T) = RT\ell n\ (x/\gamma y) \qquad (5.12)$$

where x is the maximum solubility of FeS in the B1 phase, y is the minimum solubility of FeS in the B8 phase, and γ is the activity coefficient of the B8 solid solution (γ = 1 for ideal solutions). Using the value

-4.1 kJ/mole for ΔG^{o}_{FeS}(1273 K) determined from FeS-MgS data, γ is calculated to be 1.2 at 1273 K and 0.1 MPa.

The calculation of the FeS-MnS phase diagram at high pressure now closely follows the method for FeS-MgS. The chemical potential of FeS in the B8 phase is taken to be

$$\mu^{B8}_{FeS}(P,T) = \mu^{B8,o}_{FeS}(P,T) + RT\ln(0.95\gamma) \qquad (5.13)$$

where the composition of the B8 phase is assumed to remain constant at 95 mol % FeS up to 6 GPa as indicated by the experimental data. Assuming that the (Fe,Mn)S(B1) solid solution behaves ideally at high pressure, the composition of the B1 - B1/B8 phase boundary in FeS-MnS is given by

$$x = 0.95\gamma \exp\left(\frac{\Delta G^{o}(0,T) + P\Delta V(0,298\ K)}{RT}\right). \qquad (5.14)$$

If γ is assumed to remain constant as a function of pressure, the B1 phase boundary does not coincide with the experimental data at 1273 K (see curve plotted on Fig. 5.2, p. 59). To achieve coincidence of the phase boundary with the experimental results, the value of γ must increase from 1.2 at 0.1 MPa to 1.6 at 6 GPa. Such an increase is consistent with a greater departure from ideal behaviour as cohesive forces between atoms become greater at high pressure.

Above 6 GPa at 1273 K FeS(B8) is assumed to transform to the dense high-pressure phase (hpp) observed by Mao et al.(1981) at 298 K, and the equilibrium between (Fe,Mn)S(B1) and (Fe,Mn)S(B1) + (Fe,Mn)S(hpp) must now be considered. Note that the Fe/Mn ratio in (Fe,Mn)S(hpp) must be similar to (Fe,Mn)S(B8) since the sample quenched from 7 GPa indicates a composition of 95 mol % FeS (Table 5.3). The B1 phase boundary can be calculated using equation (5.14), with $\Delta G^{o}(0,T)$ and $\Delta V(0,298\ K)$ referring to the reaction

$$FeS(B1) \rightarrow FeS(hpp). \qquad (5.15)$$

Since both the values of ΔG and ΔV are significantly more negative for reaction (5.15) than for reaction (5.7), the iron composition of the B1 phase boundary should become substantially lower, exactly the trend shown by the experimental results. A similar discontinuity should be observed in the FeS-MgS system above 6 GPa.

The low solubility of MnS in the B8 phase to at least 6 GPa indicates that MnS is not likely to transform to the B8 structure at moderate pressures, similar to MgS (section 5.4.1). A B1 $\rightarrow$ B8 transition has been observed to occur at 9 GPa and 298 K in MnSe (Cemic and Neuhaus, 1972),

but no evidence for a similar transition was noted in MnS up to 20 GPa (section 4.6.1). B8 polymorphism in MnS cannot be completely ruled out, but other candidates, such as the B2 structure, should also be considered as likely for MnS at high pressure.

5.5 Implications for FeO-MgO at High P,T

The phase diagram of FeS-MgS at moderate pressure (P < 6 GPa) may provide a model for the system FeO-MgO at high pressure (P > 70 GPa). At atmospheric pressure the B1 solid solutions FeO-MgO and FeS-MgS are similar; the lattice parameter varies linearly with composition and both are assumed to deviate negligibly from ideal behaviour. One important difference between the solid solutions, however, is that the molar volume of (Fe,Mg)O increases with increasing % FeO whereas the molar volume of (Fe,Mg)S decreases with increasing % FeS, probably related to the strong covalent bonding in FeS relative to FeO.

At high pressure both systems contain a dense Fe-rich phase which competes with the B1 phase for stability. In FeS-MgS the dense phase is FeS(B8) (and above 6-7 GPa, FeS(hpp)), which is observed to contain negligible MgS to at least 6 GPa. In the case of MgO-FeO, the shock wave experiments of Jeanloz and Ahrens (1980) provide evidence for the transformation of $Fe_{0.94}O$ to a dense high-pressure phase (hpp) above $\sim$ 70 GPa. Shock wave data for MgO to 200 GPa can be fitted to a single Hugoniot equation of state, consistent with the assumption that no phase transformation occurs up to that pressure (Vassiliou and Ahrens, 1981). The absence of a phase transformation in MgO to 200 GPa is therefore consistent with a negligible solubility of MgO in FeO(hpp) to at least 100 - 150 GPa, because of the implied large free energy difference between MgO(B1) and MgO(hpp) (similar to arguments concerning B8 polymorphism in MgS and MnS).

Above 70 GPa a two-phase region forms in the system FeO-MgO consisting of (Fe,Mg)O(B1) and FeO(hpp), and increasing pressure should cause exsolution of FeO(hpp) from (Fe,Mg)O(B1) analogous to the exsolution of FeS(B8) from (Fe,Mg)S(B1) at low pressure (0 - 6 GPa). Since experimental data of (Fe,Mg)O are not available at high pressure (P > 70 GPa), the B1 phase boundary must be calculated from thermodynamics. The validity of such an analysis has already been demonstrated by the close agreement between the calculated phase boundaries and the experimental results of FeS-MnS and FeS-MgS. The effect of pressure on the B1 solid solutions does

not appear to produce any gross deviations from ideal behaviour, which strengthens an assumption of ideal behaviour of (Fe,Mg)O(B1) above 70 GPa since the oxide solid solution should approximate the ideal solution model of zero cohesive forces at least as well as the sulphide solid solution, even allowing for the difference in pressure.

CHAPTER 6 NONSTOICHIOMETRY OF FeO AT HIGH PRESSURE

6.1 Introduction

An important ingredient in constructing models of the Earth's interior is knowledge of how the relevant minerals behave at high pressure and temperature. FeO differs from other simple oxides studied in connection with the Earth's interior such as MgO, CaO, SiO_2 and Al_2O_3 in that it displays considerable nonstoichiometry within its stability field at atmospheric pressure. Iron defects in the FeO lattice give rise to complexities in the crystal structure and wide ranges of variation have been reported for physical properties such as elasticity, electrical conductivity and magnetic structure. The addition of pressure and temperature as variables in measuring physical properties of FeO adds unwanted complexity, for the physical properties are modified not only by the applied pressure, but also by the variation of the nonstoichiometry of FeO with pressure and temperature. The purpose of this study is to quantify and understand the variation of the nonstoichiometry of FeO with pressure and temperature through experiment and thermodynamic calculations, in order to better evaluate the likely nature and properties of FeO at pressures and temperatures found within the Earth's interior.

FeO is commonly assigned the chemical formula Fe_xO, where $x < 1$. Fe_xO is thermodynamically stable only at temperatures above 843 K at atmospheric pressure; below 843 K it disproportionates into Fe_3O_4 + Fe (Darken and Gurry, 1945). At high temperature Fe_xO crystallizes in a defect NaCl structure throughout the range of composition, although several thermodynamic studies have suggested that multiple phase regions exist within the single-phase Fe_xO field which are separated by second (or higher) order transitions (e.g. Vallet and Racah, 1965; Carel, 1967; Fender and Riley, 1969). Fe_xO can be successfully quenched in the defect NaCl structure to room temperature, and the lattice parameter of the quenched phase varies linearly with x over the entire compositional range (e.g. Jette and Foote, 1933). The composition of Fe_xO varies from $x \sim 0.95$ to $x \sim 0.88$ at atmospheric pressure, the specific boundary values of x being temperature dependent (Darken and Gurry, 1945). The value of x on the iron-rich boundary of Fe_xO varies at atmospheric pressure from 0.945 at 835 K to 0.953 at 1573 K (Giddings and Gordon, 1973).

6.2 Previous Work

The effect of pressure and temperature on the composition of Fe_xO in equilibrium with Fe has been studied experimentally. Mao and Bell (1971) and Bassett and Ming (1972) have found that Fe_2SiO_4 disproportionates to SiO_2 + Fe + Fe_xO, with x = 0.91 to 0.95 at 25 GPa and 1073 K. Katsura et al.(1967) and Simons and Seifert (1979) have studied Fe_xO in the temperature range 873 K - 1473 K to 5.3 GPa, and found that x increases as a function of pressure and that the rate of increase is greater at lower temperatures. Sawamoto et al.(1974) and Liu (1976) have observed that Fe_xO becomes less iron-rich above 10 GPa at high temperature, and Liu (1976) suggests that x then decreases with increasing pressure. This result has been confirmed in a diamond anvil experiment using a gasket which minimizes the nonhydrostatic stress on the sample (Shen et al., 1983).

Mao (1974) has calculated the phase boundary between Fe_xO + Fe and $Fe_{1.00}O$ at high pressure. His calculations demonstrate that the increase and subsequent decrease of x with pressure is due to the variation of the bulk modulus of Fe_xO with x. His calculations cannot be directly compared with the experimental data, however, because the values of x at high pressure were not explicitly calculated. Kurepin (1975) has calculated the phase diagram for the system Fe-Fe_xO-Fe_3O_4-Fe_2O_3 at high pressure where x was considered to be variable and his results agree with experimental data to $\sim$ 5 GPa. The neglect of the effect of pressure on volume in the calculations, however, fails to reproduce the experimentally observed decrease in x at pressures greater than 10 GPa. In this study both the composition and the bulk modulus of Fe_xO are considered to be variable at high pressure.

6.3 Experimental Procedure

The samples of Fe_xO used in the high-pressure experiments were prepared by sintering stoichiometric amounts of powdered Fe_2O_3 and reduced Fe powder in an Fe bucket which was sealed inside a silica glass tube evacuated to less than 10 mPa. The tube was heated in a furnace at 1173 K for 18 hours and then rapidly quenched in air. After grinding and x-raying the sample the process was repeated until the x-ray diffraction pattern indicated a pure and homogeneous sample of Fe_xO. The samples of Fe_2SiO_4 and $FeAl_2O_4$ were prepared in a similar manner. Excess metallic Fe present in all starting materials was removed by magnetic separation.

The high-pressure experiments were performed using three different

types of apparatus. Experiments at pressures below 7 GPa were performed using a solid-media piston cylinder apparatus (Boyd and England, 1960) and a Bridgman anvil squeezer (modified after Ringwood and Major, 1968) (see Chapter 2 for full descriptions). The sample cell consisted of an intimate mixture of Fe_xO and reduced Fe powder in the molar ratio 10:1 packed into an Fe capsule.

Experiments at pressures above 6 GPa were performed using a diamond anvil cell in the ungasketed configuration as described by Bassett and Takahashi (1965). The technique is described in Chapter 2. The starting material of Fe_xO for the diamond anvil experiments was prepared from the product of a piston cylinder run to ensure maximum homogeneity of Fe_xO and Fe in the sample. Because of the difficulty in heating Fe_xO at pressures above 20 GPa in the diamond anvil cell due to low absorption at the laser wavelength, samples of Fe_2SiO_4 and $FeAl_2O_4$ were also used as starting materials. These decompose at high pressure into mixtures of Fe_xO+Fe+SiO_2 and Fe_xO+Fe+Al_2O_3, respectively. The stoichiometry of Fe_xO in the product quenched from these runs represents the equilibrium composition at the P,T conditions where the decomposition reaction took place.

The compositions of all run products of Fe_xO were determined using the lattice parameters of the samples measured by x-ray diffraction. NaCl (a = 564.01 $\pm$ 0.01 pm) was mixed with the samples as a calibration standard. The relationship

$$a\ (pm) = 385.6 + 47.8x \qquad (6.1)$$

(Section 6.5) was used to calculate the composition x of Fe_xO from a, the lattice parameter.

6.4 Experimental Results

The results of the high-pressure runs are compiled in Table 6.1. The starting material for each run is given along with the pressure and temperature of the run and their estimated uncertainties. The uncertainties in the lattice parameters of the products Fe_xO from each run were assigned on the basis of a weighted least-squares fit to the x-ray reflections, and on the basis of the reproducibility of the lattice parameter on subsequent readings of the same x-ray film, with uncertainties being increased in the latter circumstance for the case of broad x-ray reflections. The variation of composition with pressure of the present experimental data is illustrated in Fig. 6.1, with the estimated temperatures noted beside each data point. The error bars do not include

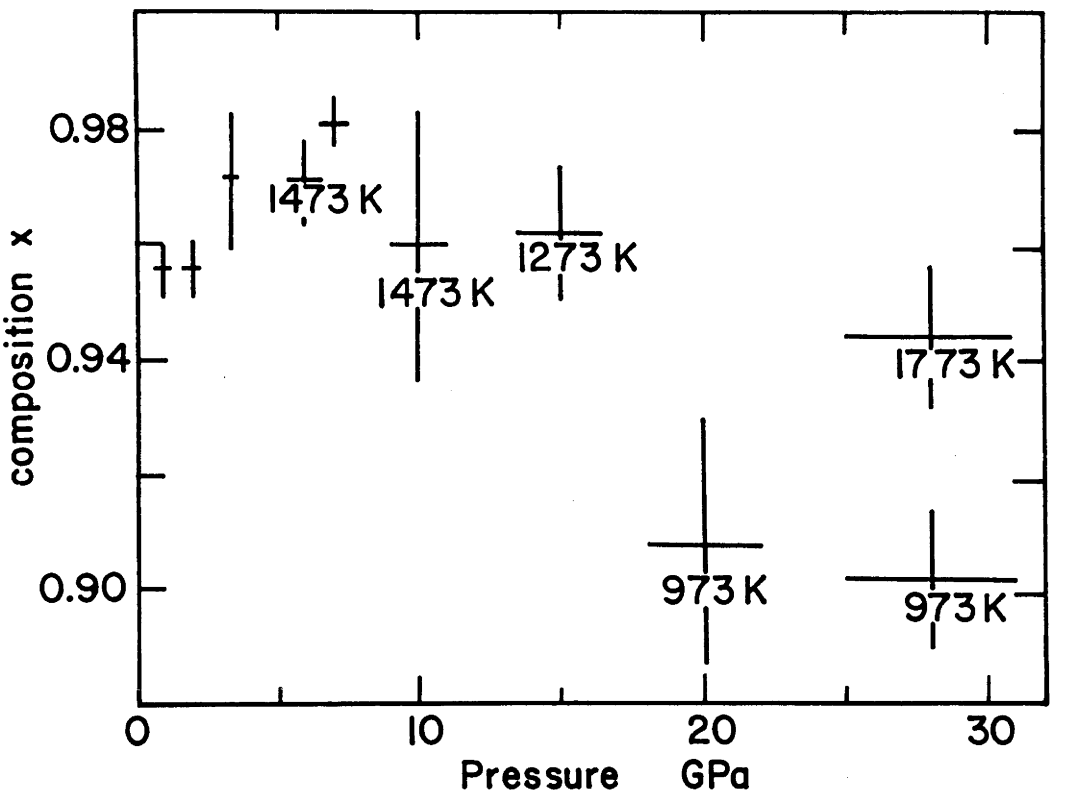

Fig. 6.1 Plot of experimental results. The value of x was determined from the lattice parameter using equation (6.1). The estimated temperatures of the diamond anvil runs are noted beside the data points; all other runs were performed at 1273 K.

TABLE 6.1 Results of high-pressure experimental runs

Run No.	Starting Material	P GPa	T K	Run Products	a(Fe_xO) pm	Technique
FeO-1	Fe + Fe_2O_3	-	1273(5)	Fe_xO + Fe	431.1(1)	Evac. Silica Tube
7479	FeO-1	1.0(2)	1273(10)	Fe_xO + Fe	431.3(2)	Piston Cylinder
8294	FeO-1	2.0(2)	1273(10)	Fe_xO + Fe	431.3(2)	Piston Cylinder
7474	FeO-1	3.5(2)	1273(10)	Fe_xO + Fe	432.0(5)	Piston Cylinder
S270	FeO-4	7.0(5)	1273(15)	Fe_xO + Fe	432.5(2)	Bridgman Anvil
DS119	FeO(#8294)	6.0(6)	1473(300)	Fe_xO + Fe	432.0(3)	Diamond Anvil
DS117	FeO(#8294)	10.0(10)	1473(300)	Fe_xO + Fe	431.5(10)	Diamond Anvil
DS121	FeO(#8294)	15.0(15)	1273(300)	Fe_xO + Fe	431.6(5)	Diamond Anvil
DS118	FeO(#8294)	20.0(20)	973(250)	Fe_xO = Fe	429.0(10)	Diamond Anvil
DS100	Fe_2SiO_4	28.0(30)	1773(300)	Fe_xO(+Fe+SiO_2)[a]	430.7(5)	Diamond Anvil
SDII83	$FeAl_2O_4$	28.0(30)	973(250)	Fe_xO+Al_2O_3(+Fe)[a]	428.7(5)	Diamond Anvil

[a]Not observed in x-ray diffraction pattern, but inferred to be present

the temperature uncertainty. The data below 10 GPa are in excellent agreement with the data of Katsura et al.(1967) and Simons and Seifert (1979), illustrating the increase of x with pressure. Above 10 GPa x decreases with increasing pressure, supporting the observation of Liu (1976).

Mao (1974) has shown that the increase and subsequent decrease of x with pressure is related to the change in sign between the partial molar volume of Fe in Fe_xO ($\overline{V}_{Fe\ in\ Fe_xO}$) and the molar volume of Fe at high pressure. The rate at which $\overline{V}_{Fe\ in\ Fe_xO}$ increases with pressure is directly related to the steepness of the variation of the bulk modulus of Fe_xO with x, and determines the pressure at which the two volume curves cross. If a steep variation of K with x is assumed the Fe compression curve and the $\overline{V}_{Fe\ in\ Fe_{0.94}O}$ cross near 10 GPa at 1273 K (see Fig. 6.2) (thermal expansion is assumed to be constant with both pressure and composition). If a less steep variation of K with x is assumed, such as that which approximates the majority of the available data (see shaded region, Fig. 6.4, p. 85), the curves do not cross below 20 GPa. Finally, compression data of Hazen (1981) indicate that K varies only slightly with x in the range x = 0.90 to x = 0.947. In this case $\overline{V}_{Fe\ in\ Fe_{0.94}O}$ actually decreases with pressure and the volume curves never cross, indicating that x continues to increase at high pressure instead of decreasing, contradicting the results presented in Fig. 6.1. To reconcile the variation of K versus x with the high-pressure experimental data it is necessary to perform a rigorous calculation of the variation of x with pressure and temperature.

6.5 Theoretical Calculation of x at High P,T

6.5.1 General method

To calculate the variation of x, the composition of Fe_xO in equilibrium with Fe, as a function of pressure and temperature it is useful to consider the thermodynamics of a solution between $Fe_{1.00}O$ and O_2. Darken and Gurry (1953) provide a good treatment of the thermodynamics of solutions.

The equilibrium reaction is given by

$$Fe + (1/2x)\ O_2 = (1/x)\ Fe_xO \qquad (6.2)$$

and Fe_xO is treated as $(FeO)_x(O_2)_{(1-x)/2}$. At atmospheric pressure (0.1 MPa) the free energy change of reaction (6.2) is given by

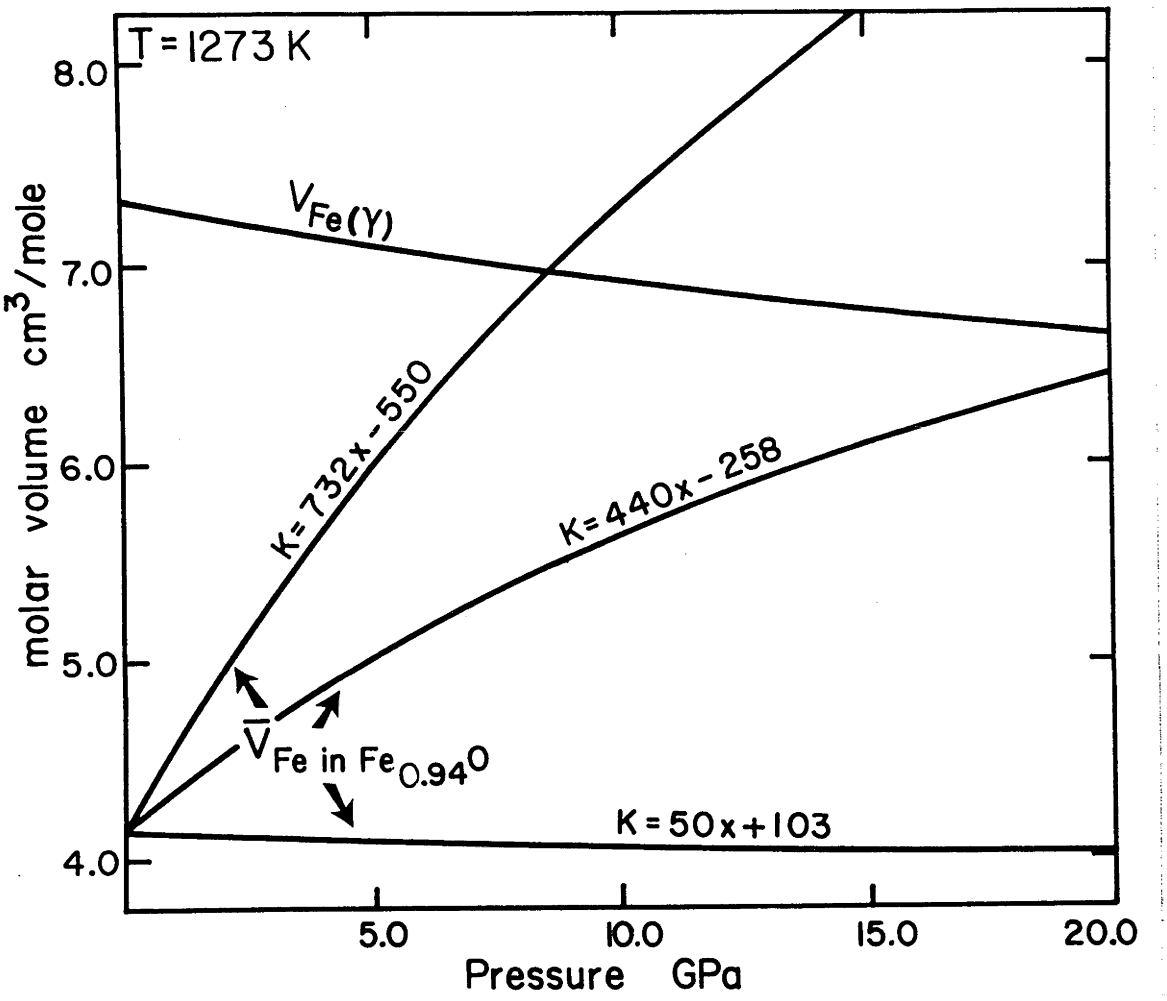

Fig. 6.2 The effect of various relationships between K and x of Fe_xO on the variation of the partial molar volume of Fe in $Fe_{0.94}O$ with pressure. The compression curve for γ-Fe is also illustrated.

$$\Delta G(1,T,X) = 0 = \Delta G^{\circ}_{f\ FeO}(1,T,X) + RT\ell n\ a_{FeO}(1,T,X) - \tfrac{1}{2}RT\ell n\ f_{O_2}(1,T,X) \qquad (6.3)$$

where X refers to the equilibrium composition at 0.1 MPa and temperature T. At high pressure the free energy change becomes

$$\Delta G(P,T,x) = \Delta G(1,T,x) + \int(\overline{V}_{FeO} - \tfrac{1}{2}\overline{V}_{O_2} - V_{Fe})\ dP \qquad (6.4)$$

where x is a variable and $\overline{V}_{FeO}$ and $\overline{V}_{O_2}$ refer to the respective partial molar volumes of FeO and O_2 in Fe_xO. From equation (6.3) the first term on the right-hand side of equation (6.4) is given by

$$\Delta G(1,T,x) = RT\ell n \frac{a_{FeO}(1,T,x)}{a_{FeO}(1,T,X)} - \tfrac{1}{2}RT\ell n \frac{f_{O_2}(1,T,x)}{f_{O_2}(1,T,X)}\ . \qquad (6.5)$$

From the definition of partial molar volumes, the second term on the right-hand side of equation (6.4) becomes

$$\int(\overline{V}_{FeO} - \tfrac{1}{2}\overline{V}_{O_2} - V_{Fe})\ dP = \int \frac{\partial V_{Fe_xO}}{\partial x}\ dP \qquad (6.6)$$

$$= \int(\overline{V}_{Fe\ in\ Fe_xO} - V_{Fe})\ dP. \qquad (6.7)$$

At equilibrium the free energy change of reaction (6.2) is zero, so from equation (6.4) the equilibrium value of x occurs at the P,T where the integrated volume difference between $\overline{V}_{Fe\ in\ Fe_xO}$ and V_{Fe} exactly balances the free energy of formation of Fe_xO at atmospheric pressure.

6.5.2 Thermodynamic parameters

To evaluate equation (6.5) the equilibrium value of f_{O_2} in Fe_xO must be known as a function of temperature. From a compilation of Giddings and Gordon (1973)

$$\log f_{O_2}(T,x) = M(T)\ x^{-1} + B(T) \qquad (6.8)$$

where the coefficients M(T) and B(T) are given in Table 2 of Giddings and Gordon (1973) and x varies between the values on the Fe,Fe_xO and the Fe_xO,Fe_3O_4 boundaries. To calculate $f_{O_2}(T,x)$ where $x > X$ several constraints have been used. In an infinitely dilute solution, the activity of FeO should follow Raoult's Law ($a_{FeO} = N_{FeO} = 2x/(x+1)$) and f_{O_2} should follow Henry's Law ($f_{O_2} = kN_{O_2} = k(1-x)/(1+x)$). Such behaviour has been observed near stoichiometric MnO (Davies and Richardson, 1959). To join the regions of linear and logarithmic behaviour, a quadratic form of $\ln f_{O_2}$ was used in which the fugacities and the first derivatives were matched at the boundaries. The fugacity relations used were

$$x < X \qquad \ell n\ f_{O_2} = \ell n\ (10)\ (Mx^{-1} + B) \qquad (6.9)$$

$$0.9995 < x < X \qquad \ell n\ f_{O_2} = ax^{-2} + bx^{-1} + c \qquad (6.10)$$

$$x > 0.9995 \qquad \ell n\ f_{O_2} = \ell n\left(\frac{1-x}{1+x}\right) + k \qquad (6.11)$$

The corresponding values for the activity of FeO in Fe_xO were calculated using a Gibbs-Duhem integration

$$x < X \qquad \ln a_{FeO} = - \frac{\ln (10)\, M(1-x)^2}{4x^2} \qquad (6.12)$$

$$0.9995 > x > X \qquad \ln a_{FeO} = - \frac{a}{3} x^{-3} + \frac{a}{2} x^{-2} - \frac{b}{4}\left(\frac{1-x}{x}\right)^2 - \frac{a}{6} \qquad (6.13)$$

$$x > 0.9995 \qquad \ln a_{FeO} = \ln \left(\frac{2x}{1-x}\right) \quad . \qquad (6.14)$$

To calculate the volume integrals in equation (6.6) a Murnaghan equation of state was used (Murnaghan, 1951)

$$V(P,T) = V(T)\ (1 + K'P/K)^{-1/K'} \quad . \qquad (6.15)$$

Values of the physical parameters of Fe_xO and Fe required are listed in Table 6.2. Fe was considered as α-Fe below 1189 K and as ε-Fe above 1189 K. For computational simplicity no transformations to ε-Fe were considered, but the neglect of Fe(ε) has only a minor effect on the results.

6.5.3 Variation of a with x in Fe_xO

To calculate the molar volume of Fe_xO, a knowledge of the variation of a, the unit cell lattice parameter, with x is required. Observations by several investigators suggest that a judicious selection of data in the literature must be made when compiling the data to yield the best fit to a versus x. Foster and Welch (1956) have observed that the lattice parameter of a given composition of Fe_xO increases dramatically as the quenching rate from high temperature is reduced. Greenwood and Howe (1972a,b) have observed that the kinetics of the disproportionation sequence which occurs below 843 K

$$Fe_xO \rightarrow Fe_zO + Fe_3O_4 \rightarrow Fe + Fe_3O_4 \qquad z > x \qquad (6.16)$$

are directly related to both the quench rate and the temperature from which quenching took place. During a slow quench the composition of Fe_xO becomes gradually more iron-rich, with an accompanying production of Fe_3O_4; the lattice parameter of Fe_xO therefore appears to increase although the bulk composition of the sample remains unchanged, consistent with the observations of Foster and Welch (1956). The presence of Fe_3O_4 may not necessarily be detected in the final sample as only small amounts are produced (e.g. $Fe_{0.90}O = 0.88\ Fe_{0.92}O + 0.03\ Fe_3O_4$).

In selecting data for the compilation of a versus x, data which appeared to be affected by quenching effects discussed above were

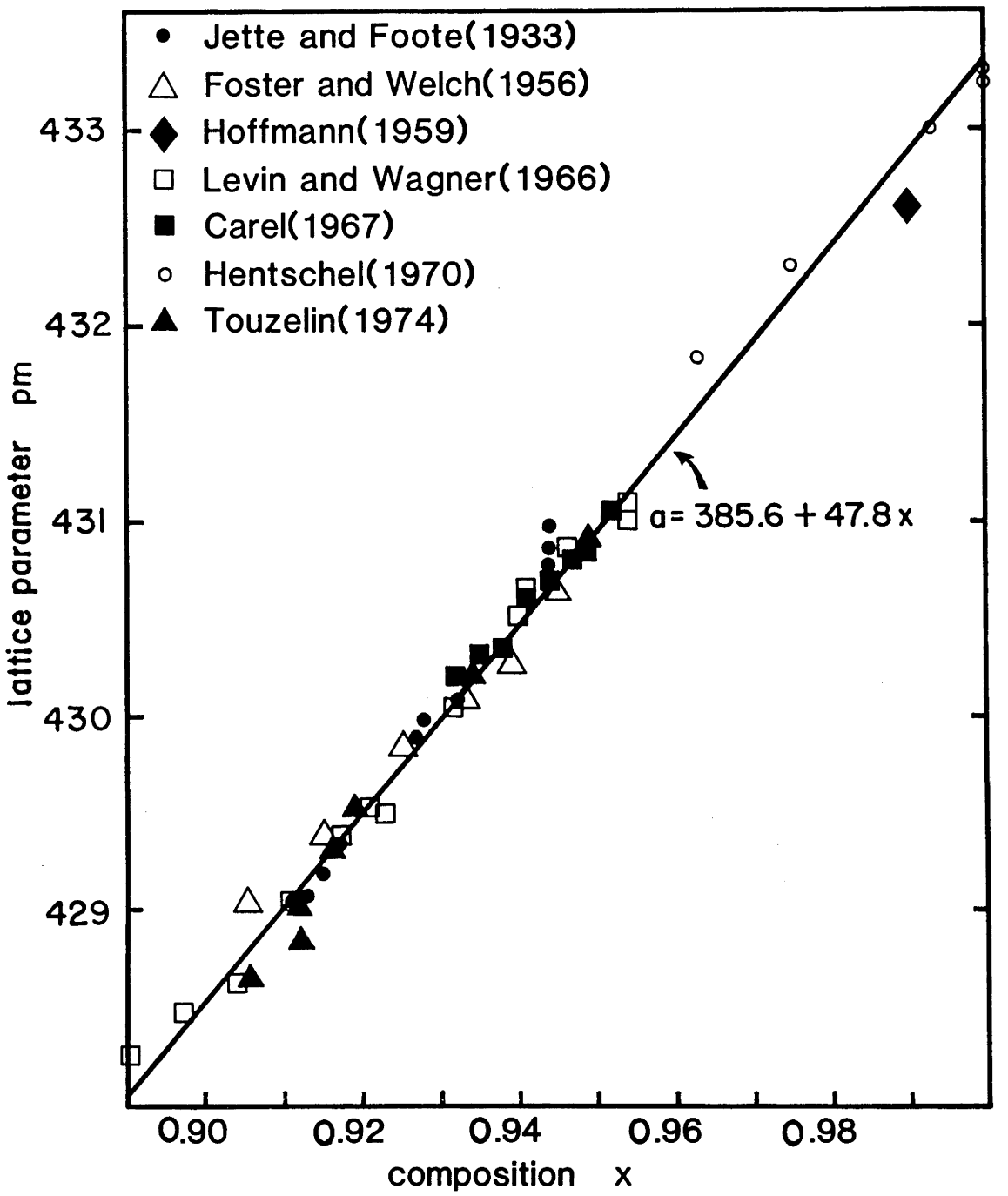

Fig. 6.3 Compilation of values from the literature of a, the unit cell lattice parameter, versus x. The straight line represents the least squares fit to the data.

TABLE 6.2 Physical parameters for Fe and Fe_xO

		Fe	Fe_xO
molar volume (cm^3)		7.0924[a]	see Fig. 6.3
298 K 0.1 MPa			
thermal expansion coefficients	T<1189 K	a= -1.610×10^{-3} [b,c]	a= -3.780×10^{-3} [b,d]
		b= 4.578×10^{-5}	b= 4.529×10^{-5}
	T>1189 K	a= -3.723×10^{-2} [b,c]	
		b= 7.310×10^{-5}	
bulk modulus (GPa)		166.4[e]	see Fig. 6.4
$\frac{dK}{dP}$		5.29[e]	4.0[f]
$\frac{dK}{dT}$ (GPa K^{-1})		-0.43[g]	-0.23[h]

[a] Swanson et al. (1955)

[b] coefficients of best fit to $V(T) = V_o(1 + a + bT)$

[c] Basinski et al. (1955)

[d] by analogy with MgO, MnO; from Suzuki et al. (1979)

[e] Guinan and Beshers (1968)

[f] third and higher order terms neglected in Birch-Murnaghan equation state

[g] Dever (1972)

[h] by analogy with MgO; from Sumino and Anderson (1980)

discarded, i.e. if the lattice parameter for a given value of x was unusually high. Fig. 6.3 illustrates the data which were used to determine the variation of a versus x for Fe_xO and the least-squares line which describes the best fit. The determination gives a slightly steeper slope than the compilation of Simons (1980), because Simons used the data of Hentschel (1970); the data of Hentschel was rejected because it gave unusually high values of a near x = 0.90. It was necessary to use Hentschel's data for x = 0.96-1.00, however, because no other data were available for that range.

6.5.4 Variation of K with x in Fe_xO

A significant number of values for K, the bulk modulus, have been reported in the literature for different compositions of Fe_xO. The values of K reported by different investigators using static compression methods are derived from fits to various equations of state with different values of K'. To create a more uniform basis for comparison of the values of K derived from compression data, the data have been refitted to the Birch-Murnaghan equation of state (Birch, 1952)

$$P = {}^3/_2 K (x^{-7/3} - x^{-5/3}) [1 - {}^3/_4(4-K') (x^{-2/3} - 1)] \quad x = V/V_o \qquad (6.17)$$

using a least squares analysis. In general the compression data were not sufficiently well resolved to determine values for K'; K' was therefore set equal to 4.0. Table 6.3 lists all the available data for K of Fe_xO from the literature and gives the revised fits to the compression data. The data are plotted in Fig. 6.4.

The determination of Sumino et al.(1980) is clearly discrepant with respect to all other data points. Their value appears to imply that there is a substantial (and almost discontinuous) increase in K at $x \sim 0.90$, or that all of the other experimental data are in error and there is a negligible variation of K with x; neither possibility seems satisfactory. Jeanloz and Sato-Sorenson (1982) have suggested that Fe_xO exhibits a finite bulk viscosity, resulting in a reduction of K in compression experiments where the time scale is long. The relatively low values of K measured by Berger et al.(1981) and Bonczar and Graham (1982) using ultrasonic techniques, however, appear to contradict this interpretation. The value of K determined by Sumino et al.(1980) was neglected in the subsequent analysis; further investigation as to the cause of the discrepancy between the Sumino et al. datum and the other data is clearly needed.

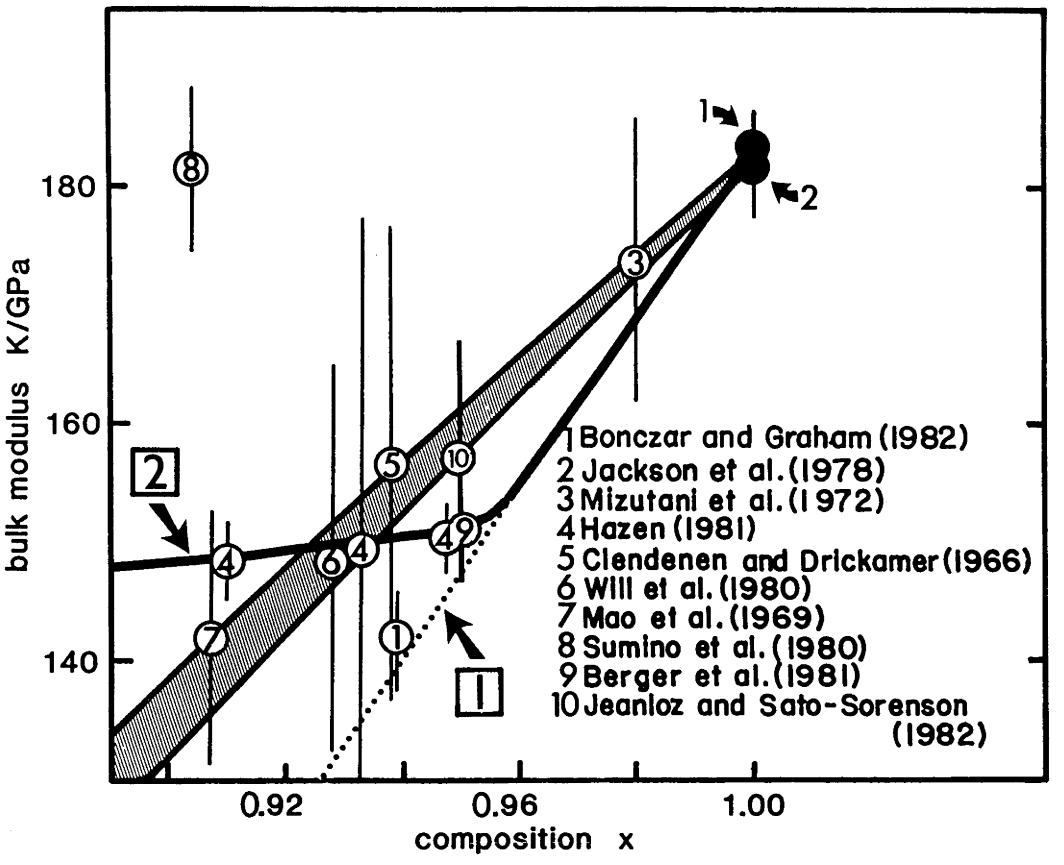

Fig. 6.4 Plot of the bulk modulus of Fe_xO as a function of x, compiled from data in the literature. Compression data were fit to a Birch-Murnaghan equation of state with K' = 4 (see Table 6.3). The shaded region represents the range of linear relationships used to calculate the phase boundary between Fe and Fe_xO at high P,T. The Sumino et al.(1980) datum was omitted from the analysis. The open circles refer to experimental data and the shaded circles to inferred values. The curves marked 1 and 2 are considered as alternate fits to the experimental data.

TABLE 6.3 Literature values for bulk modulus of Fe_xO

Study	Method	x[a]	K_o (GPa)	K_o'	K_o[b] (GPa)
Clendenen and Drickamer (1966)	compression	0.938	154(15)	3.2	157(20)
Mao et al. (1969)	compression	0.907	142(10)	4.0[c]	142(11)
Mizutani et al. (1972)	ultrasonic	0.98	174(12)	-	-
Jackson et al. (1978)	inferred[d]	1.00	182(5)	-	-
Sumino et al. (1980)	resonance	0.904	181.4(7)	-	-
Will et al. (1980)	compression	0.928	154(5)	4.0[c]	149(16)
Hazen (1981)	compression	0.910	151.9(1)	2.1	148.5(3)
Hazen (1981)	compression	0.933	153.1(1)	2.1	149.5(28)
Hazen (1981)	compression	0.947	154.0(1)	2.1	150.6(3)
Bonczar and Graham (1982)	ultrasonic	0.939	141.5(4)	-	-
Bonczar and Graham (1982)	inferred[d]	1.00	183.5(3)	-	-
Berger et al. (1981)	ultrasonic	0.950	1.5	-	-
Jeanloz and Sato-Sorenson (1982)	compression	0.946	157(12)	4.0[c]	157(12)

[a] values of x have been readjusted where necessary using equation (6.1)

[b] based on fit to the Birch-Murnaghan equation with $K_o' = 4$

[c] $K_o' = 4$ assumed in fit to equation of state

[d] inferred from ultrasonic data for $(Mg_{1-y}\ Fe_y)_xO$ solid solutions

From Fig. 6.4 it is clear that the value of K generally decreases as a function of decreasing x, but no smooth variation is indicated. As a first approximation straight lines have been fitted which attempt to incorporate the majority of the data points, indicated by the shaded region in Fig. 6.4.

6.6 Results

Using numerical methods equation (6.4) has been solved using the parameters given in Table 6.2 and the relationships plotted in Fig. 6.3 and Fig. 6.4 (shaded region), thus calculating the phase boundary between Fe + Fe_xO and Fe_xO at high pressure and temperature. The results of the calculation for 973 K and 1473 K are plotted in Fig. 6.5. The value of x increases with pressure in the range 0-30 GPa, asymptotically approaching the stoichiometric composition $Fe_{1.00}O$. This contradicts the high-pressure experimental data which indicate that x decreases above 10 GPa. As indicated in section 6.4, a steeper variation of K versus x must be chosen to ensure a decrease in x at high pressure. If K is assumed to vary

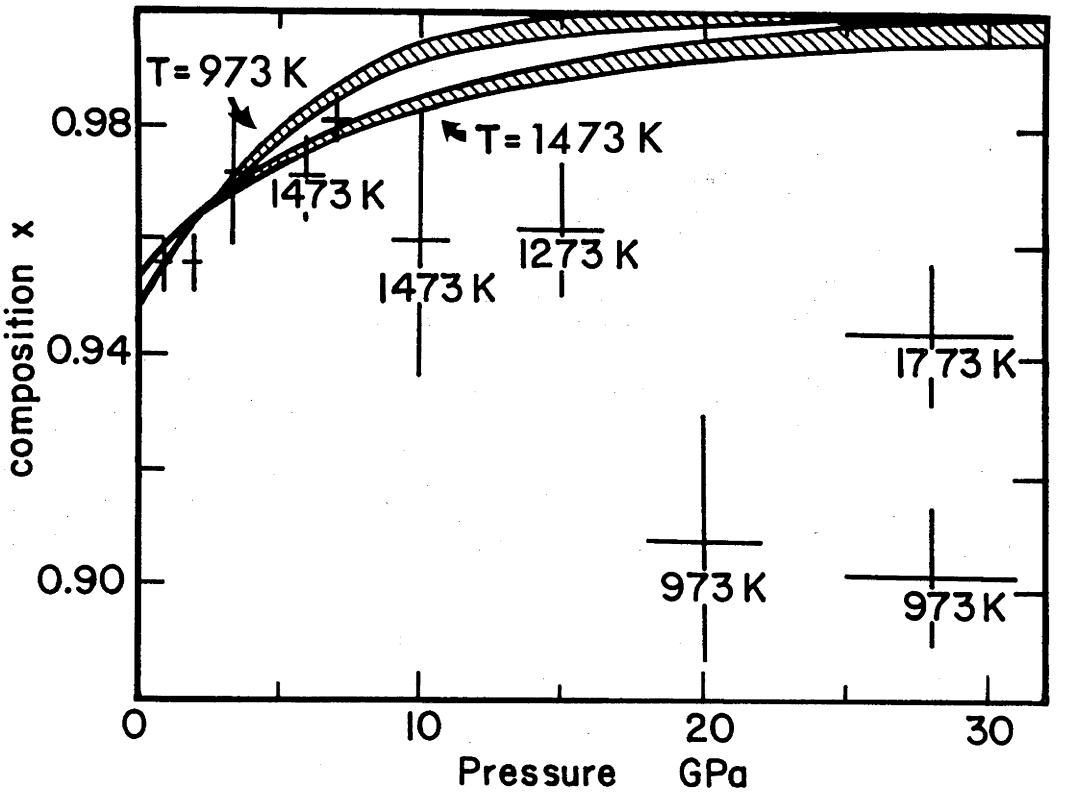

Fig. 6.5 Plot of the calculated phase boundary between Fe and Fe_xO at 973 K and 1473 K. The shaded region indicates the variation of the phase boundary for the range of relationships between K and x as illustrated by the shaded region in Fig. 6.4.

steeply over the entire range of Fe_xO, however, an absurdity is encountered at high pressure and therefore an alternative variation of K with x must be chosen. Strong constraints are imposed by the compression data of Hazen (1981) who measured the differential compression of three Fe_xO single crystals with differing stoichiometries to a relative accuracy of less than 0.5%. These data indicate only a minor variation of K with x between x = 0.90 and x = 0.947. The variation of K with x that is most consistent with both the data of Hazen (1981) and the high-pressure experimental data is the solid line (marked 2) shown in Fig. 6.4 where K varies steeply from x = $\sim$ 0.95 to 1.00, and only slightly from x = 0.90 to x = $\sim$ 0.95. To understand why the solid line provides the most consistent fit, we must take a closer look at the factors governing equilibrium at high pressure.

The point (P,T,x) at which Fe_xO and Fe are in equilibrium is given by

$$\Delta G(P,T,x) = 0 = \Delta G(1,T,x) + \int(\overline{V}_{Fe \text{ in } Fe_xO} - V_{Fe})\, dP. \qquad (6.18)$$

$\Delta G(P,T,x)$ is plotted in Fig. 6.6 as a function of x at three different pressures (T = 1273 K) for two different variations of K with x (curves marked 1 and 2 on Fig. 6.4). Fe and Fe_xO are in equilibrium at the point where $\Delta G(P,T,x) = 0$. It is evident that serious problems are encountered at high pressure if curve 1 (K versus x) is used to calculate $\Delta G(P,T,x)$ (shown by solid line with dotted line extension for x > 0.96). There is one solution if P = 0.1 MPa, two solutions if P = 15 GPa and no solutions if P = 30 GPa. Neither of the latter two scenarios is consistent with experiment which clearly indicates one and only one composition of Fe_xO in equilibrium with Fe up to 30 GPa. A means of avoiding the inconsistency is to adopt curve 2 (K versus x) when x < 0.96 (revised $\Delta G(P,T,x)$ is indicated by continuous solid lines). $\Delta G(P,T,x)$ is reduced from being very positive at small x to negative, thus crossing $\Delta G(P,T,x) = 0$ only <u>once</u> (see inset, Fig. 6.6). The dramatic decrease in $\Delta G(P,T,x)$ is due to a change in the manner with which V_{Fe_xO} varies with x at high pressure. It should be noted that the discontinuities in $\Delta G(P,T,x)$ are associated with the discontinuities in $\Delta V(P,T,x)$, and arise from the use of a K versus x relationship which has a discontinuity in dK/dx. The latter is not physically realistic, and the discontinuity in $\Delta G(P,T,x)$ is only an artifact of the oversimplified relationship between K and x.

Fig. 6.7a illustrates the variation of V_{Fe_xO} versus mole fraction using the K versus x curves labelled 1 and 2 in Fig. 6.4 at various pressures (Fe_xO is considered here as a solution between Fe and O_2).

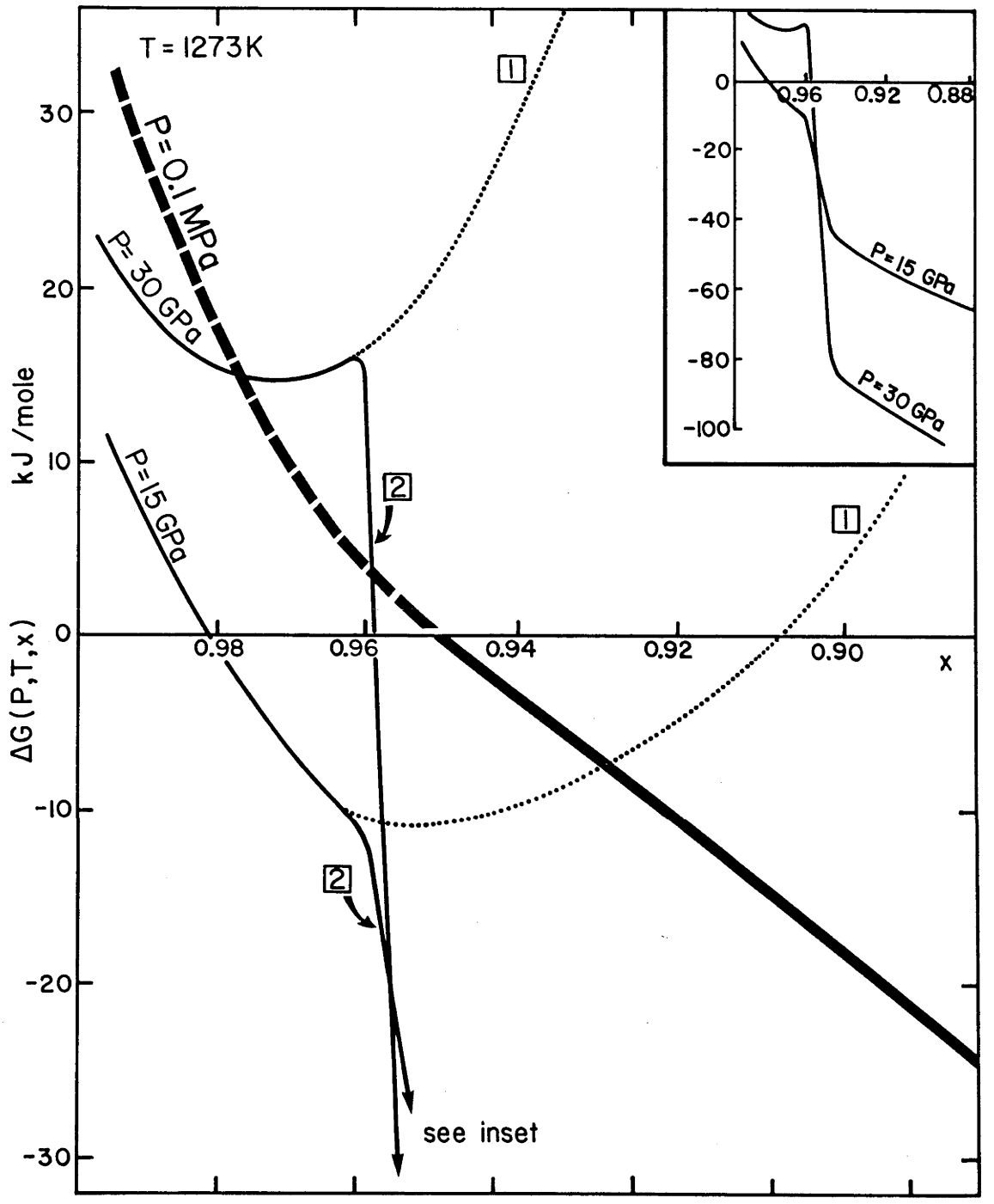

Fig. 6.6 Variation of $\Delta G(P,T,x)$ with x at various pressures. The thick solid line represents $\Delta G(1,T,x)$ and is dashed outside the stability field for Fe_xO at 0.1 MPa. The thin solid lines represent $\Delta G(P,T,x)$ calculated using curve 2 of Fig. 6.4 and the dotted extensions were calculated using curve 1. Note that the abscissa is linear in x^{-1}.

$\overline{V}_{Fe \text{ in } Fe_xO}$ is considered as the intercept of the tangent to the V_{Fe_xO} curve at $N_{O_2} = 0$ (i.e. Fe). A small change in slope of V_{Fe_xO} therefore has a large effect on the value of $\overline{V}_{Fe \text{ in } Fe_xO}$. Fig. 6.7b illustrates the determination of $\overline{V}_{Fe \text{ in } Fe_{0.96}O}$ at 0.1 MPa, 15 GPa and 30 GPa. The rapid increase in $\overline{V}_{Fe \text{ in } Fe_xO}$ with pressure is evident. Note, however, the difference between the choice of curve 1 and curve 2 (K versus x) in constructing V_{Fe_xO} when x is small (e.g. x = 0.91). For curve 1 where K decreases dramatically with x, V_{Fe_xO} decreases to ridiculously low values at high pressure and $\overline{V}_{Fe \text{ in } Fe_xO}$ increases to enormous values; consequently equation (6.18) has no solution. To fully illustrate the consequences of using curve 1 of K versus x, V_{Fe_xO} at 30 GPa has been extended to $Fe_{0.83}O$ on Fig. 6.7b; in fact V_{Fe_xO} reaches zero well before the composition isochemical with magnetite, $Fe_{0.75}O$, is reached.

The revised version of the variation of x with P and T is shown in Fig. 6.8 (where curve 2 has been used in the calculation). The fit to the experimental data is good below 10 GPa, but does not reproduce the lower values of x at high pressure. Consideration of the ε-phase of Fe has a negligible effect on these results. The point where the value of x levels off in Fig. 6.8 at high pressure is directly related to the abrupt change in slope at $x \sim 0.96$ of K versus x (curve 2). To reproduce the value of x at high pressure, parameters such as K', K" and dK/dT could be varied as a function of x (all assumed to be constant in the present calculations) in order to change the variation of V_{Fe_xO} with x at high pressure and to either smooth out or alter the position of the abrupt discontinuity in Fig. 6.6 between $+\Delta G$ and $-\Delta G$ at high pressure (curve 2). Variation of other parameters with x also affects the results. For example, if thermal expansion is assumed to vary inversely with bulk modulus in Fe_xO, higher temperature favours higher values of x. This is inconsistent with the experimental data, however, so thermal expansion is not assumed to vary dramatically with x in Fe_xO. To reproduce the experimental results exactly, the values of all parameters could be systematically varied until the desired fit were obtained. Such a set of "best-fit" parameters, however, would be essentially ad hoc, in view of the large numbers of parameters involved and their significant uncertainties, and would likely have no physical significance. In addition, the large uncertainties associated with the experimental data would significantly multiply the number of acceptable fits. It is clear that more detailed calculations of the phase boundary between Fe and Fe_xO must await further experimental

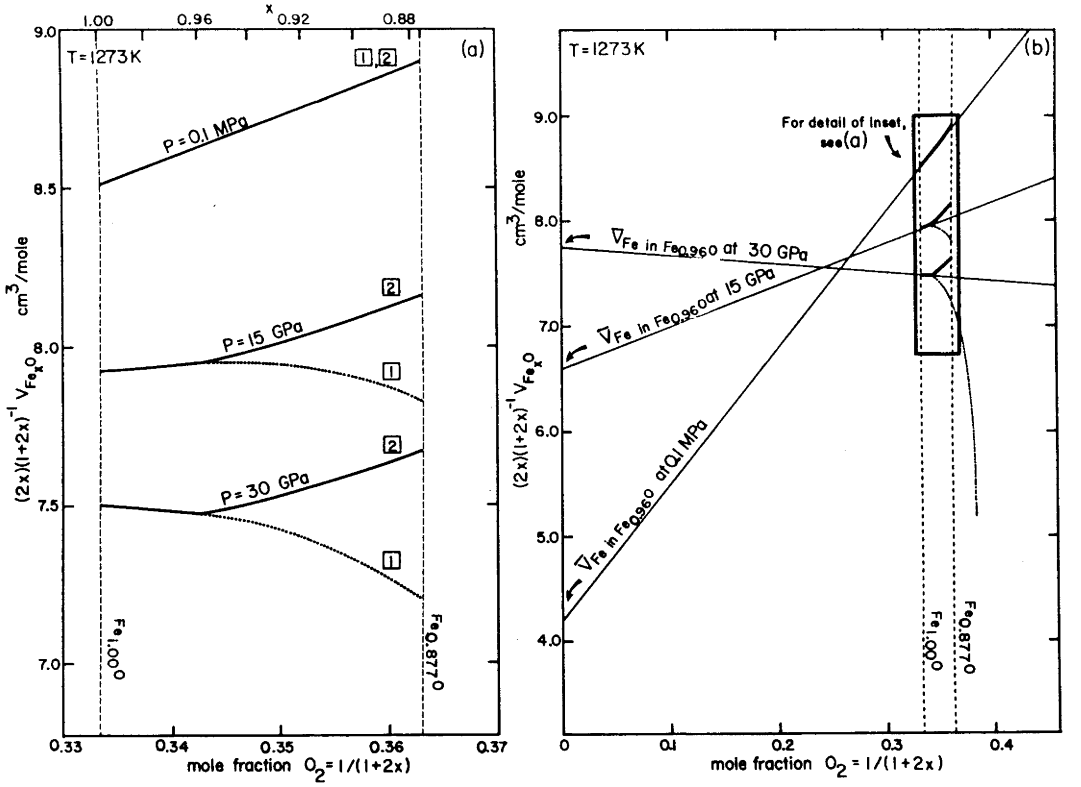

Fig. 6.7 (a) Variation of the volume of Fe_xO versus composition at various pressures. The solid lines were calculated using curve 2 of Fig. 6.4 and the dotted lines using curve 1. (b) Similar plot to (a) but showing the tangent to the volume curves at x = 0.96 which defines the partial molar volume of Fe in $Fe_{0.96}O$ at the point where the tangent intersects the ordinate. The volume curve of Fe_xO has been extended to $Fe_{0.83}O$ to indicate the rapid decrease of $V(Fe_xO)$ if curve 1 in Fig. 6.4 is used to calculate the volume.

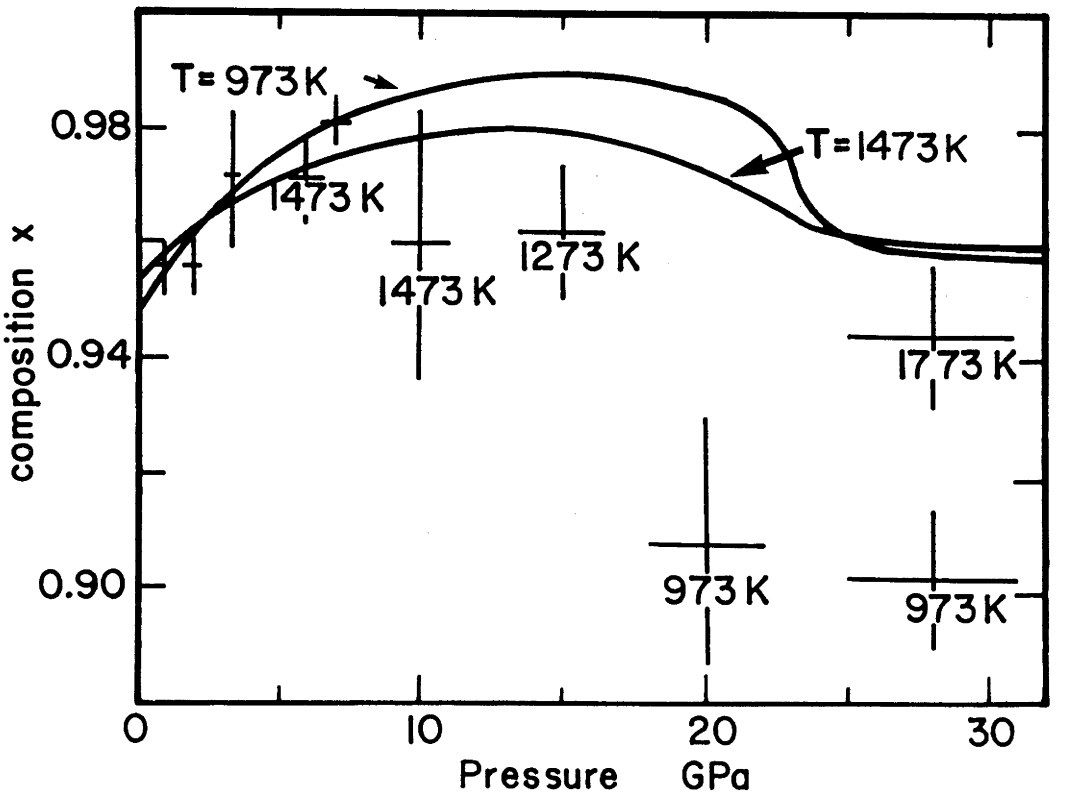

Fig. 6.8 Revised plot of the phase boundary between Fe and Fe_xO at 973 K and 1473 K, calculated using the K versus x relationship represented by curve 2 in Fig. 6.4.

determination of the physical properties of Fe_xO. The following projects are suggested as having the highest priority:

1) Determination of the variation in bulk modulus of Fe_xO with composition using a suite of carefully characterized samples prepared under similar conditions.
2) Determination of the variation in thermal expansion of Fe_xO with composition using samples as above.
3) Determination of the pressure derivatives K' and K" and dK/dT of Fe_xO with composition; investigating the reliability of the value of K' = 19 for $Fe_{0.939}O$ measured by Bonczar and Graham (1982).

6.7 Interpretation of the Shock Wave Data of Fe_xO

Using shock wave techniques, Jeanloz and Ahrens (1980) have obtained evidence for a phase transformation in $Fe_{0.94}O$ occurring at approximately 70 GPa. An alternative interpretation has been proposed by Liu et al.(1982) who suggest that the density increase observed in the Hugoniot data can be explained by a large decrease in the stoichiometry of Fe_xO at high pressure and temperature (reaching $Fe_{0.75}O$ at 228 GPa), without requiring a first-order phase transformation. Results from the present work can be used to assess the validity of the Liu et al.(1982) interpretation.

The conclusions of Liu et al.(1982) are based on a calculation of the density increase associated with the reaction

$$Fe_xO = Fe_yO + (x - y)\ Fe \qquad x > y \qquad (6.19)$$

at high pressure. The bulk modulus of Fe_xO is assumed to vary steeply and linearly with x, resulting in a large density increase. If the bulk modulus versus composition relationship used by Liu et al.(1982) is used in the present work to calculate x as a function of P and T (equation 6.4), two solutions for x are found at 15 GPa and none are found at 30 GPa. As discussed in section 6.6 this result is inconsistent with existing experimental data. If the K versus x relationship illustrated in Fig. 6.4 (curve 2) is used in the Liu et al.(1982) calculations, the Fe_xO + Fe mixture of $Fe_{0.94}O$ bulk composition (i.e. Fe_xO + (0.94-x) Fe with $x < 0.94$) remains less dense than $Fe_{0.94}O$ throughout the pressure range represented by the shock wave data. For example, at 0.1 MPa and 298 K the density of $Fe_{0.94}O$ is 4½% greater than the density of the mixture $Fe_{0.75}O$ + 0.19 Fe(ε). At 200 GPa and 298 K, comparison of the Murnaghan isotherms indicates that $Fe_{0.94}O$ is still 4% denser than the mixture $Fe_{0.75}O$ + 0.19 Fe(ε). The interpretation of Liu et al.(1982)

requires a large increase in density of the mixture Fe_xO + (0.94-x) Fe(ε) relative to $Fe_{0.94}O$ in order to account for the large densities observed in the shock wave data; their interpretation is therefore not consistent with the small sensitivity of K with x for x < 0.94 as proposed by the present work and demonstrated experimentally by Hazen (1981).

Further evidence questioning the validity of the Liu et al.(1982) interpretation is provided by the shock wave data for Fe_3O_4 (Jackson et al., 1983). There is an enormous discrepancy between the experimental data for Fe_3O_4 compared with the calculated Hugoniot for the hypothetical $Fe_{0.75}O$ phase based on the equation-of-state parameters used by Liu et al.(1982).

In conclusion, the shock wave data of $Fe_{0.94}O$ appear to be best described by a first-order phase transformation occurring at ∿ 70 GPa. While the stoichiometry of Fe_xO is expected to change in the pressure range preceding the transformation, it is not expected to affect the overall density significantly. Depending on the nature of the high-pressure phase, a change in the Fe:O ratio of the stable phase could be involved, but would contribute only a small amount to the overall density change of the phase transformation.

CHAPTER 7 DEFECT STRUCTURE OF FeO

7.1 Introduction

Fe_xO crystallizes in the NaCl structure where the crystal lattice is modified by the presence of Fe^{3+} cations and vacant Fe^{2+} sites. The specific arrangement of these defects has been studied extensively using x-ray and electron diffraction (e.g. Roth, 1960; Koch and Cohen, 1969; Andersson and Sletnes, 1977; Bauer and Pianelli, 1980; Yamamoto, 1982). It is generally agreed that these defects are arranged into clusters of interstitial Fe^{3+} cations each surrounded by a tetrahedron of vacant $^{VI}Fe^{2+}$ sites, although the size and shape of the stable equilibrium clusters are expected to vary with pressure, temperature and composition.

One of the main conclusions from the work presented in Chapter 6 is that the variation of the bulk modulus of Fe_xO with composition does not follow a simple linear relation, but displays at least two distinct slopes. The physical basis for such a variation is likely to be related to the defect structure of Fe_xO, and how it varies with composition.

Mössbauer spectroscopy is a useful tool for studying the defect structure of Fe_xO because the Mössbauer effect can distinguish between Fe^{2+} and Fe^{3+}, and between Fe^{2+} in different environments. The number of potential contributions to the Mössbauer spectrum of Fe_xO where $x < 1$ is large, however, due to the many variations of defect nearest-neighbour coordinations possible for Fe^{2+} cations in the crystal lattice. The Mössbauer spectrum of Fe_xO where $x \leq 0.95$ has been recorded by a number of investigators and is extremely complex. In contrast, Hentschel (1970) recorded the Mössbauer spectrum of $Fe_{1.00}O$ at 298 K, and the spectrum was observed to consist only of one singlet. In this study attention is focussed on the Mössbauer spectra of a series of Fe_xO samples where $1.00 > x > 0.95$. The lower density of defects in these samples reduces the complexity of the spectra, and enables a physically realistic fitting model to be applied.

7.2 Experimental Procedure

Mössbauer spectra were recorded at 298 K and 4.2 K for the samples quenched from experiments using the large-volume high-pressure apparatus (Chapter 6; see Table 6.1). The Mössbauer spectrometer at ANU (Solid State Physics, R.S.Phys.S.) was used exclusively in the experiments. Details of the apparatus and run procedure are given in Chapter 2.

7.3 Mössbauer Spectra of Fe_xO at 298 K

The Mössbauer spectra of Fe_xO at 298 K are shown in the right column of Fig. 7.1. The main feature of the spectra is a poorly resolved doublet, and the splitting of the doublet decreases as x increases, with the lines no longer being resolvable at x = 0.981. A number of different fitting methods have been applied to series of Fe_xO spectra, three of the most successful being Johnson (1969)(two doublets, one singlet), Greenwood and Howe (1972a)(five singlets) and Checherskaya et al.(1973)(five singlets). None of the above methods was able to successfully reproduce the $Fe^{3+}/\Sigma Fe$ ratio closer than a factor of $\sim$ 2, however. A slightly different method of fitting was used in the present work. Two singlets were fitted corresponding to Fe^{3+} and the Fe^{2+} cations that are in undistorted sites. The remainder of the spectrum was fitted by adding quadrupole doublets corresponding to Fe^{2+} in noncubic sites until a reasonable fit was achieved; two doublets were sufficient in the present case to fit the data. The small amount of free Fe metal present in the Fe_xO samples was represented by a quadrupole doublet (on the small velocity scale used only the two inner peaks of the six-line magnetic spectrum of Fe appear).

All spectra of Fe_xO run at 298 K were fitted by the above method. The spectra for $Fe_{0.952}O$, $Fe_{0.956}O$ and $Fe_{0.981}O$ are illustrated in Fig. 7.2 and parameters are listed in Table 7.1. There are several features to note about the fits. The position of the Fe^{2+} singlet (Fe^{2+}_A) remains roughly constant as x decreases, and agrees well with the value 1.1 mm/sec (relative to Fe) reported by Hentschel (1970) for the single line of the $Fe_{1.00}O$ spectrum. The area of the singlet (Fe^{2+}_A) decreases as x decreases, consistent with the increasing proportion of defects. The relative area of the Fe^{3+} singlet agrees well with the % Fe^{3+} calculated to be present by electrostatically balancing the Fe^{2+} vacancies with Fe^{3+} (total Fe composition determined from unit cell lattice parameter, equation 6.1). The weighted average centre shift of the Fe_xO spectrum increases as x increases, approaching the value 1.1 mm/sec observed for $Fe_{1.00}O$ by Hentschel (1970). The ratio of the outer doublet (Fe^{2+}_C) to the inner doublet (Fe^{2+}_B) increases as x decreases, consistent with the increasing number of Fe^{2+} atoms in more distorted environments.

Previously reported fitting methods which were successful in fitting series of Fe_xO spectra were applied to the present data to compare results. The spectrum of $Fe_{0.952}O$ was chosen as being closest to the

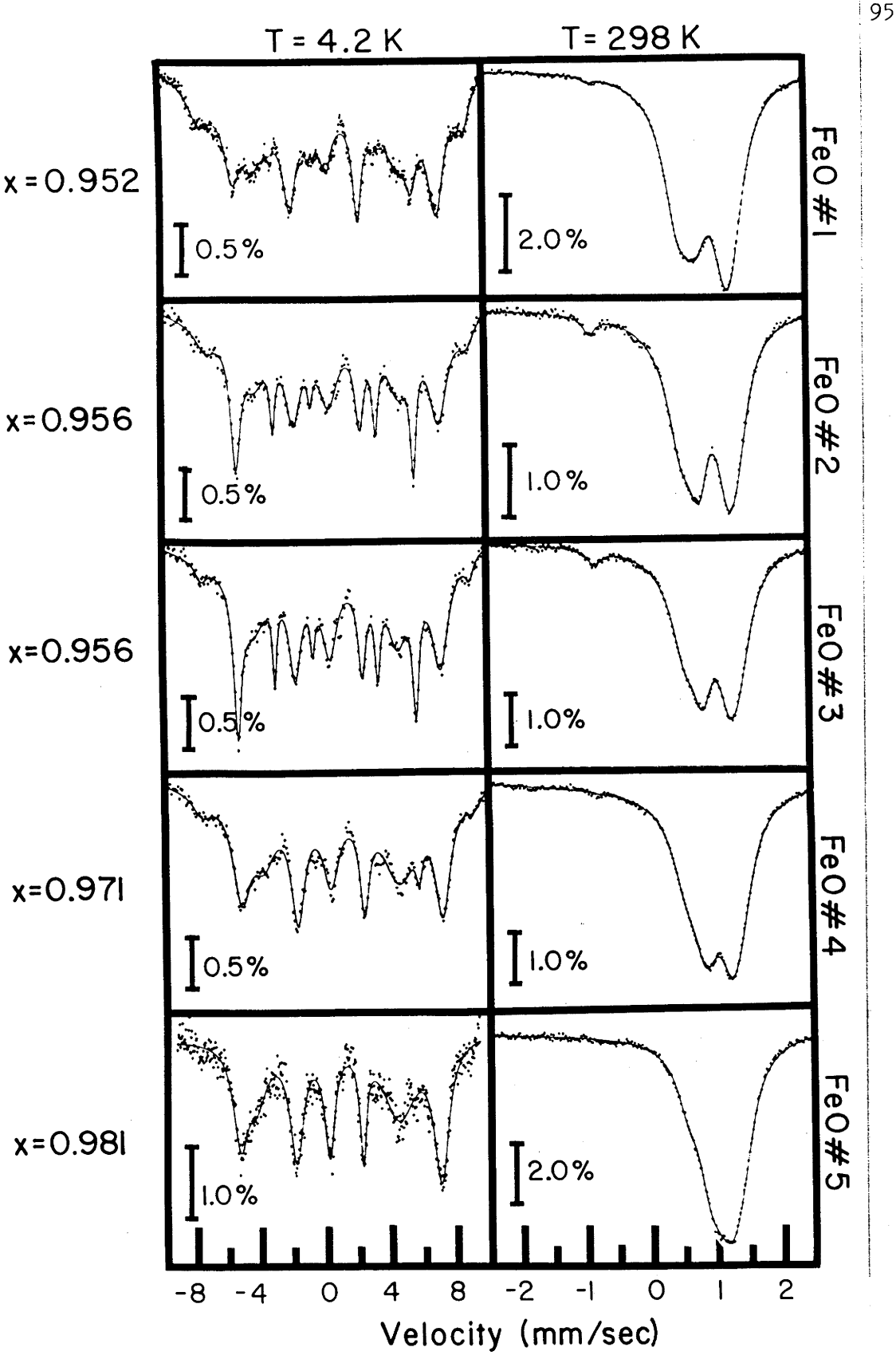

Fig. 7.1 Mössbauer spectra of Fe_xO samples recorded at 4.2 K (left column) and 298 K (right column). The parameters of the fitted lines for the 298 K and 4.2 K spectra are given in Tables 7.1 and 7.3, respectively. The velocity scales are relative to Fe.

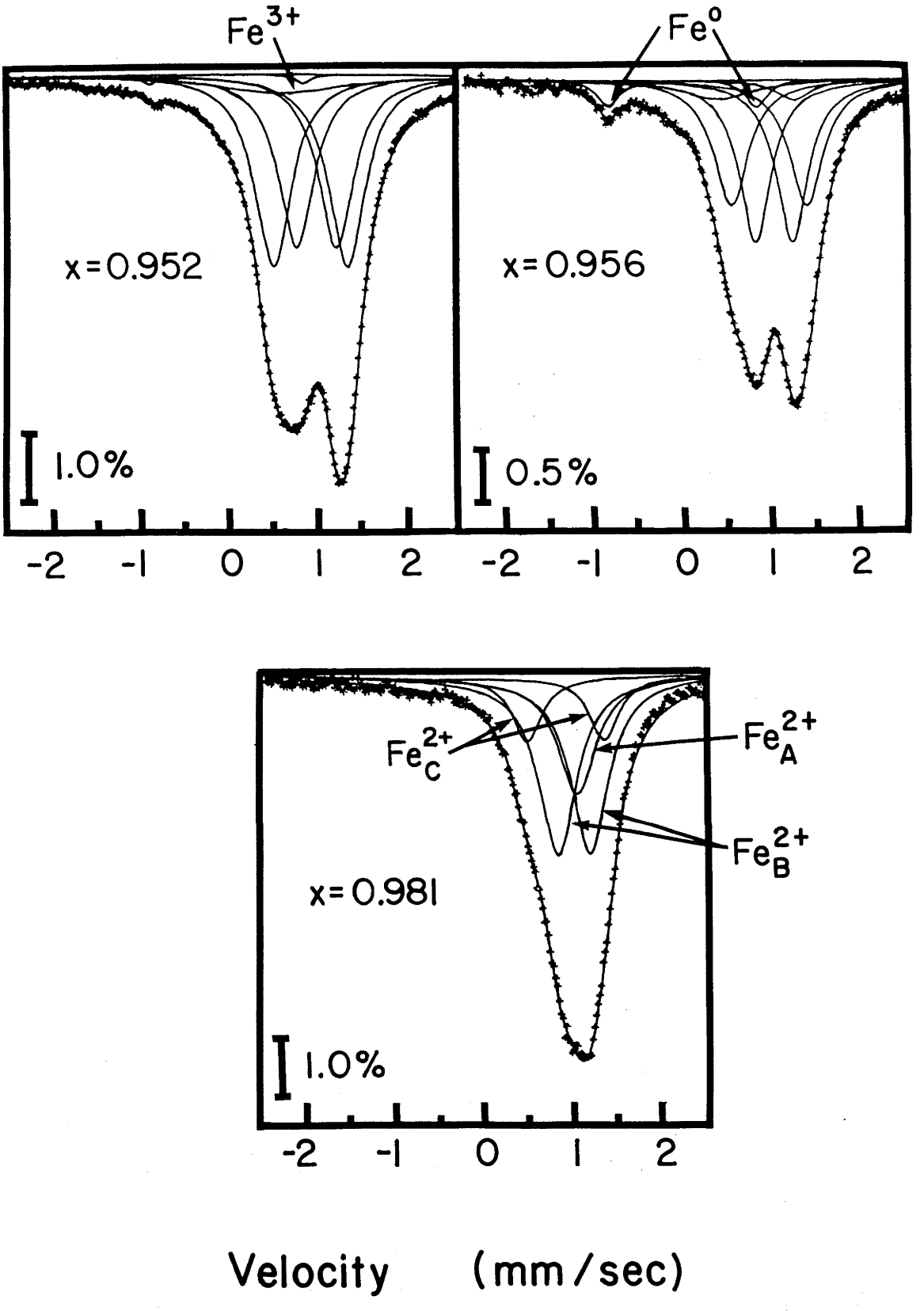

Fig. 7.2 The components fitted to the Mössbauer spectra of Fe_xO. The two singlets correspond to Fe^{2+}_A and Fe^{3+} and the two sets of doublets to Fe^{2+}_B and Fe^{2+}_C. There is also a small doublet corresponding to Fe^0 in some spectra.

TABLE 7.1 Mössbauer parameters for Fe_xO spectra at 298 K

	FeO #1	FeO #2	FeO # 3	FeO #4	FeO #5
x[a]	0.952(a)	0.956(4)	0.956(4)	0.971(10)	0.981(4)
Fe_A^{2+} δ[b] mm/sec	-	-	1.25(37)	1.11(8)	1.07(1)
% area	-	-	3.3(6)	5.7(22)	20.8(9)
Fe_B^{2+} δ[b] mm/sec	1.005(3)	1.014(3)	1.027(20)	1.042(4)	1.028(3)
ε mm/sec	0.224(2)	0.232(3)	0.211(20)	0.198(4)	0.181(7)
% area	42.2(3)	45.5(4)	46.6(7)	63.7(10)	62.0(11)
Fe_C^{2+} δ[b] mm/sec	0.933(2)	0.963(3)	0.973(6)	0.975(10)	0.944(5)
ε mm/sec	0.419(3)	0.435(4)	0.430(7)	0.431(9)	0.437(6)
% area	48.0(3)	43.1(6)	38.9(6)	26.7(6)	17.2(4)
Fe^{3+} δ[b] mm/sec	0.60(5)	0.34(4)	0.39(5)	0.45(8)	-
% area	8.7(8)	7.3(6)	6.0(7)	3.7(3)	-
Fe^{o} δ[b,f] mm/sec	0.0	0.0	0.0	0.0	-
ε mm/sec	0.87(1)	0.86(1)	0.83(1)	0.72(7)	-
% area	1.0(2)	4.0(3)	5.1(4)	0.3(2)	-
% Fe^{3+}[c]	8.8(10)	7.6(9)	6.3(10)	3.7(4)	-
% Fe^{3+}[d]	9.6(4)	8.8(8)	8.8(8)	5.9(21)	3.8(8)
$\%Fe_B^{2+}/\%Fe_C^{2+}$	0.88(1)	1.06(2)	1.20(3)	2.39(6)	3.60(5)
$\bar{\delta}$[b,e]	0.934(5)	0.939(5)	0.971(18)	1.007(10)	1.022(5)

[a] calculated from lattice parameter using a(pm) = 385.6 + 47.8x

[b] relative to Fe metal

[c] calculated from Mössbauer data

[d] calculated from x-ray data

[e] mean centre shift of entire spectrum

[f] centre shift of Fe metal constrained to be 0.0; splitting should be 0.84 mm/sec (Violet and Pipkorn, 1971)

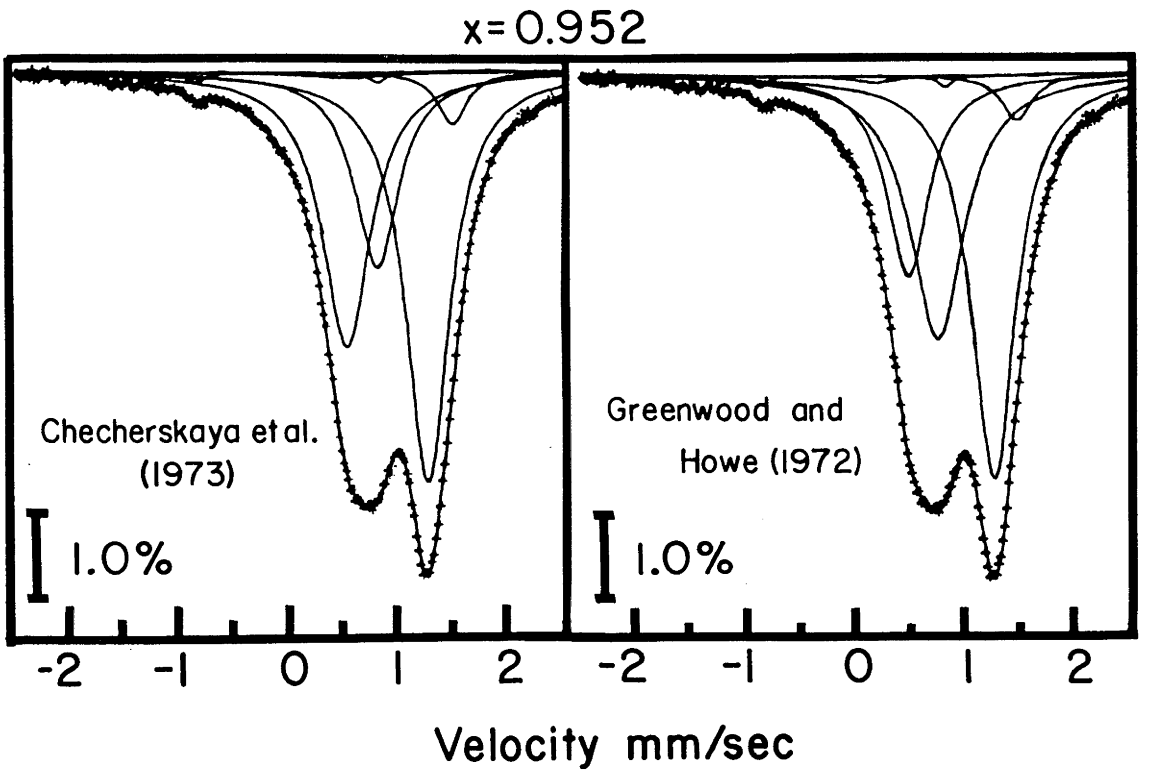

Fig. 7.3 Some previously reported fitting methods for Fe_xO spectra applied to the spectrum of $Fe_{0.952}O$.

TABLE 7.2 Comparison of fits to $Fe_{0.952}O$ spectrum

Source	Johnson (1969)	Greenwood and Howe (1972)	Checherskaya et al. (1973)	this work
fitting model	2 quadrupole doublets, 1 singlet	5 singlets	5 singlets	2 singlets, 2 quadrupole doublets
No. of adjustable parameters	14	18	18	14-17
reduced χ^2	?[a]	1.3	1.3	1.6
physical model	2 distinct noncubic Fe^{2+} sites, $\%Fe^{2+}_A = \%Fe^{2+}$ at x = 0.92	2 predominant noncubic Fe^{2+} sites (1 and 2 defect nearest neighbours) with other coordinations in smaller proportion	3 nonequivalent noncubic Fe^{2+} sites, electronic exchange between $VI_{Fe^{2+}}$ and $VI_{Fe^{3+}}$	1 cubic Fe^{2+} site, 2 distinct noncubic Fe^{2+} sites $\%Fe^{2+}_A = \%Fe^{2+}_B$ at x = 0.95
composition range (x)	0.91 → 0.93	0.910 → 0.947	0.917 → 0.954	0.952 → 0.981

[a]The parameters of the Johnson (1969) fit could not be successfully fitted to the $Fe_{0.952}O$ data set.

compositions previously studied. A summary of the fitting methods is given in Table 7.2, and the results are illustrated in Fig. 7.3. It is interesting to note that although the peak positions and widths of the previous fits could be reproduced in the present data, the peak areas could not. This is due to the manner in which the individual computer programs treat the area variables, and sounds a caution against considering a particular fit to Fe_xO Mössbauer spectra as unique. The present fitting model is probably a more physically realistic method than fitting five singlets, because the subspectra correspond to different Fe environments whose proportions vary in a manner consistent with the changing numbers of defects in the structure.

TABLE 7.3 Some Mossbauer parameters for Fe_xO spectra at 4.2 K

	FeO #1	FeO #2	FeO #3	FeO #4	FeO #5
x[a]	0.952(2)	0.956(4)	0.956(4)	0.971(10)	0.981(4)
Fe^{2+} $\bar{H}$ kOe	390(3)	388(3)	387(3)	385(3)	383(3)
$\bar{\delta}^b$ mm/sec	1.38(3)	1.20(2)	1.00(2)	1.13(4)	1.20(4)
Fe^{3+} $\bar{H}^c$ kOe	504(4)	501(3)	514(3)	519(4)	-
$\bar{\delta}^{b,c}$ mm/sec	0.69(3)	0.85(5)	0.68(5)	0.71(7)	-
$\%Fe^{3+c}$	26(2)	18(2)	7(2)	12(2)	-
$\%Fe^{3+d}$	9.6(4)	8.8(8)	8.8(8)	5.9(21)	3.8(8)

[a] calculated from lattice parameter using a(pm) = 385.6 + 47.8x

[b] relative to Fe metal

[c] calculated from peaks 1 and 6 of Fe^{3+} Mössbauer spectrum

[d] calculated from x-ray data

7.4 Mössbauer Spectra of Fe_xO at 4.2 K

Below ~ 198 K at atmospheric pressure Fe_xO becomes antiferromagnetic (Roth, 1960) and the crystal lattice undergoes a progressive rhombohedral distortion (Willis and Rooksby, 1953). The Mössbauer spectrum of the defect antiferromagnetic phase for $x \leq 0.95$ has been previously studied by Kurash et al.(1972), Romanov and Checherskaya (1972) and Greenwood and Howe (1972a), and reveals a complex set of magnetic subspectra. Romanov and Checherskaya (1972) recorded the Mössbauer spectrum for $Fe_{1.00}O$ at 85 K, which was a single magnetic six-line spectrum. They concluded that the complexity in the Mössbauer spectrum of Fe_xO was due to defects and not to the rhombohedral distortion.

The spectra recorded for the five samples of Fe_xO where $x = 0.952$ to 0.981 are shown in the left column of Fig. 7.1. The spectra consist of a number of poorly resolved lines and a rough estimate indicates that at least three sets of magnetic six-line spectra of Fe^{2+} are present. The decreasing complexity of the spectra as x increases supports the conclusion of Romanov and Checherskaya (1972) that the complexity is due to defects in the rhombohedral lattice.

A fit of the present Mössbauer data was attempted using sets of six-line magnetic spectra, but it failed due to the poor resolution of the lines. A more empirical approach was therefore taken. The resolvable lines were fitted to singlets, and the broad shoulders at the high- and low-velocity ends of the spectrum (representing Fe^{3+}) were fitted to a doublet (component areas constrained to be equal). By accounting for all of the area in the spectrum in this manner, it was possible to calculate several quantities from the fitted parameters. These quantities are listed in Table 7.3.

The amount of Fe^{3+} present was calculated on the basis of twice the area of the doublet relative to the area of the entire spectrum. It is evident from a comparison of the calculated % Fe^{3+} and the % Fe^{3+} available from x-ray analysis that the fitting procedure has overestimated the amount of Fe^{3+}, either by underestimating the total area of the spectrum or by overestimating the width of the outer Fe^{3+} peaks. The parameters for Fe^{3+} were calculated assuming the doublet to represent peaks 1 and 6 of the magnetic subspectrum. The average internal hyperfine field for Fe^{3+} is 510 ± 8 kOe and the average centre shift for Fe^{3+} is 0.73 ± 0.08 mm/sec at 4.2 K (relative to Fe) (assuming zero EFG). The

parameters for Fe^{2+} are 1.18 ± 0.14 mm/sec for the average centre shift and 386 ± 3 kOe for the average hyperfine magnetic field. There appears to be no systematic variation of these parameters with composition outside of experimental uncertainty. The values of these parameters are all in agreement with those reported by Kurash et al.(1972) at 80 K for $Fe_{0.95}O$ and Greenwood and Howe (1972a) at 77 K for $Fe_{0.947}O$ (allowing for temperature corrections) (H and δ both generally decrease with increasing temperature). The values reported for the centre shift and hyperfine field of Fe^{2+} in $Fe_{1.00}O$ at 85 K by Romanov and Checherskaya (1972), however, are greater than those observed for Fe_xO where x = 0.952 to 0.981, again allowing for the temperature difference (δ = 1.36(8) mm/sec (relative to Fe), H = 370(5) kOe at 85 K for $Fe_{1.00}O$).

7.5 The Physical Model

The physical model suggested by the fit to the 298 K Mössbauer data is of three dominant Fe^{2+} environments, one cubic (Fe_A^{2+}), and two noncubic (Fe_B^{2+} and Fe_C^{2+}). The cubic site is identical to the one Fe^{2+} site in $Fe_{1.00}O$, but is only observed in samples where x > 0.95. The proportion of Fe^{2+} atoms in the more distorted environment (Fe_C^{2+}) becomes greater than the number in the less distorted environment (Fe_B^{2+}) at x ∿ 0.95. The linewidths of the Fe^{2+} doublets are broad, indicating that more than one site with slightly different parameters is represented by each doublet. It is impossible to determine the likely arrangement of defects around each Fe^{2+} atom directly from the data. It does not seem likely that the doublets only correspond to Fe^{2+} atoms with 1 and 2 defect (Fe^{3+} or vacant Fe^{2+} site) nearest neighbours as suggested by Greenwood and Howe (1972a), because they calculate the ratio $Fe^{2+}(1):Fe^{2+}(2)$ to be ∿ 3 for x = 0.947 (assuming only single $^{IV}Fe^{3+}(^{VI}\square)_4$ clusters to be present). The large line width of the singlet corresponding to Fe^{3+} indicates that there is more than one Fe^{3+} site, probably at least one being noncubic. It seems unlikely that the Fe^{3+} peak could ever be resolved into its individual components due to the low proportion of Fe^{3+} in Fe_xO. There is no evidence for any absorption peak in the 298 K spectrum of Fe_xO corresponding to Fe^{2+}/Fe^{3+} interactions as reported by Elias and Linnett (1969) and Checherskaya et al.(1973). Greenwood and Howe (1972a) reached a similar conclusion.

The physical model corresponding to the 4.2 K Mössbauer data is not well defined. The positions of the strongest peaks of Fe^{2+} in the x = 0.981 spectrum indicate that the hyperfine field is probably not

aligned with the principal axis of the electric field gradient, and the large line widths of Fe^{2+} peaks in all spectra indicate a probable range of magnetic and quadrupole interactions. The possibility of fitting magnetic subspectra to Fe_xO data at 4.2 K, therefore, does not seem likely. The parameters deduced from the empirical fit can only provide rough information on the statistically averaged environment of Fe^{2+} and Fe^{3+} in Fe_xO. It is interesting, however, to compare this data with the Mössbauer parameters of Fe_3O_4. The Mössbauer spectrum of Fe_3O_4 is quite different to Fe_xO at 4.2 K (e.g. Srivastava et al., 1981) and the crystal structure is believed to be monoclinic (Chiba and Chikazumi, 1982), but the local Fe^{3+} environments in Fe_3O_4 and Fe_xO could be similar. The hyperfine field of $^{IV}Fe^{3+}$, $^{VI}Fe^{3+}$(I) and $^{VI}Fe^{3+}$(II) in Fe_3O_4 at 4.2 K are 512 kOe, 532 kOe and 505 kOe, respectively (Srivastava et al., 1981), compared with the average value of 510 $\pm$ 10 kOe for Fe^{3+} in Fe_xO ($x > 0.95$). The centre shifts are considerably different, however. Srivastava et al.(1981) measured the centre shift for $^{IV}Fe^{3+}$ to be 0.20 mm/sec at 4.2 K (relative to Fe) and $^{VI}Fe^{3+}$ to be 0.43 and 0.55 mm/sec. The average centre shift measured from the outer two lines corresponding to Fe^{3+} in Fe_xO is observed to be 0.73 $\pm$ 0.08 mm/sec, considerably higher than the values for Fe_3O_4. This might indicate that the crystallographic sites of Fe^{3+} in rhombohedral Fe_xO are different to those in low-temperature Fe_3O_4, or alternatively, that there is a large EFG in Fe_xO which renders the method of calculating δ from the outer two lines of the spectrum invalid.

The analysis of Fe_xO ($x = 0.952$ to 0.981) Mössbauer spectra in the present work has suggested a physical model where there are three dominant Fe^{2+} environments whose proportions vary in a manner consistent with the defect concentration. Although the fits to the Mössbauer spectra are probably not unique, they indicate a trend which is likely to be common to any fitting method which attempts to model realistically the actual Fe^{2+} crystallographic sites, namely that the defect arrangements around Fe^{2+} in Fe_xO ($x = 0.95$ to 1.0) vary rapidly with composition. Physical properties which are sensitive to the defect structure may therefore vary in a complicated manner with composition, reflecting changes in the population of certain defect arrangements relative to others. These properties may include the bulk modulus, which was concluded in Chapter 6 to display different sensitivity to compositional variation in the ranges $x > 0.96$ and $x < 0.96$.

CHAPTER 8 PHASE RELATIONS IN THE SYSTEMS FeO-MgO AND Fe-FeO

8.1 Introduction

A number of models for core formation has been proposed involving oxygen as the principal light element in the core (Dubrovskiy and Pan'kov, 1972; Bullen, 1973; Larionov, 1977; Ringwood, 1977; 1979). The specific details of a process by which sufficient amounts of oxygen can be incorporated into the core to satisfy present density constraints must be consistent with the known behaviour of relevant minerals at high pressure and temperature, the systems FeO-MgO and Fe-FeO being particularly important. The observation of a phase transformation in FeO at high pressure has significant implications for both these systems. The purpose of this work is to redetermine the phase diagrams of FeO-MgO and Fe-FeO in view of the FeO high-pressure phase, and discuss the results in terms of formation of the Earth's core if oxygen is considered to be the principal light alloying element.

8.2 The System FeO-MgO

8.2.1 The high-pressure phase of FeO

Various mechanisms have been proposed for the density increase observed by Jeanloz and Ahrens (1980) in the shock wave data of $Fe_{0.94}O$ at $\sim$ 70 GPa:

(a) A B1 $\rightarrow$ B8 structural transition (Wang, 1970; Jackson and Ringwood, 1981; Navrotsky and Davies, 1981);

(b) A B1 $\rightarrow$ B2 structural transition (Jeanloz and Ahrens, 1980; Navrotsky and Davies, 1981);

(c) A high-spin $\rightarrow$ low-spin electronic transition in FeO (e.g. Jackson and Ringwood, 1981 and references therein);

(d) Disproportionation of FeO to yield a mixture of Fe and either Fe_3O_4 or Fe_2O_3 high-pressure phases (Bell and Mao, 1975; Jeanloz and Ahrens, 1980). The structure of the Fe_3O_4 high-pressure phase is unknown (Mao et al., 1974), whereas the work of Yagi and Akimoto (1983) suggests spin-pairing in corrundum-structured Fe_2O_3 at about 60 GPa;

(e) A progressive change in Fe_xO stoichiometry resulting from exsolution of Fe (Liu et al., 1982; see, however, section 6.7, this thesis);

(f) A progressive rhombohedral distortion of the B1 phase (Zou et al., 1980; see also section 4.6.2, this thesis).

The zero-pressure density increase involved in the phase transformation was calculated by Jeanloz and Ahrens (1980) to be at least 4%. While conceding the possibility of alternative interpretations, Jeanloz and Ahrens (1980) based their analysis of the Hugoniot data upon predicted physical properties for a B2-structured high-pressure phase. An empirical correlation (Jamieson, 1977) between B1/B2 volume contraction and ionic radius ratio suggests that B1/B2 polymorphism in FeO would be accompanied by a volume reduction of about 4%. With the zero-pressure density of the high-pressure phase thus constrained, Jeanloz and Ahrens (1980) required a fourth-order Eulerian isentrope characterized by absolutely minimal K_o and K_o' and positive K_o'' for a satisfactory fit of the resulting calculated Hugoniot to the data. This treatment, while perhaps demonstrating marginal viability for the B1/B2 model, does not constitute an objective assessment of the high-pressure phase. An alternative procedure was adopted by Jackson and Ringwood (1981) in which the key parameters of the theoretical Hugoniot were allowed wider variation. It was concluded that the zero-pressure density difference between the low- and high-pressure phases was at least 10-16%, and possibly significantly larger.

The large magnitude of the density increase raises the possibility that the transition involves significant shortening of Fe-O and/or Fe-Fe bond lengths, in conjunction with a possible change of crystal structure. Jackson and Ringwood (1981) argue that Fe-O bonds in the B8 structure are likely to be more covalent than in the B1 structure, and thus a shortening of Fe-O bond lengths is implied. Conclusions from section 4.5 regarding the hypothetical phase FeS(B1) indicate that B1 → B8 transitions must be accompanied by significant shortening of M-X bond lengths and/or unusually large c/a ratios in the B8 phase (although the latter is probably less likely for FeO since c/a appears to be correlated with the cation/anion electronegativity difference (Jackson and Ringwood, 1981)). More generally, data presented by Liu (1981) indicate that the volume changes involved in transitions of FeO to all other common structures are small ($\lesssim$ 5%), unless there is a substantial shortening of bond lengths. For the purposes of the following discussion, it is assumed only that the phase transformation in FeO involves a change in crystal structure, but is probably accompanied by a substantial change in electronic properties associated with significant shortening of bond lengths.

8.2.2 Calculation of the FeO-MgO phase diagram

Above the transformation pressure of FeO a two-phase region consisting of a Mg-rich B1 phase and an Fe-rich high-pressure phase (hpp) forms. The formation of such a region has been recognized previously by Jeanloz and Ahrens (1980), Navrotsky and Davies (1981) and Vassiliou and Ahrens (1982). The absence of evidence for a phase transformation in MgO to at least 200 GPa is consistent with a negligible solubility of MgO in FeO(hpp) to at least $\sim$ 100 - 150 GPa (section 5.5). Because of the large negative volume difference between FeO(B1) and FeO(hpp), an increase of pressure in the system FeO-MgO should result in a gradual exsolution of an almost pure FeO(hpp) phase, leaving an Fe-depleted (Fe,Mg)O(B1) phase. This behaviour is analagous to that observed experimentally in the system FeS-MgS (Chapter 5).

The degree to which FeO(hpp) exsolves with increasing pressure is a function of the trade-off between the decrease in free energy obtained by the volume reduction from the formation of FeO(hpp) and the increase in free energy associated with the loss of configurational entropy of the B1 solid solution. The calculation is similar to determining the phase boundary in the system FeS-MgS (section 5.4.1). The chemical potentials of FeO in the $Fe_xMg_{1-x}O$(B1) and FeO(hpp) phases are equal at equilibrium, and if ideal behaviour of the B1 solid solution is assumed

$$\mu_{FeO}^{hpp,o}(P,T) - \mu_{FeO}^{Bl,o}(P,T) = RT\ln x \qquad (8.1)$$

where the left-hand side of equation (8.1) is $\Delta G^o(P,T)$ for the reaction

$$FeO(B1) \rightarrow FeO(hpp). \qquad (8.2)$$

$\Delta G^o(P,T)$ can be calculated from the following equation where P_{tr} and T_{tr} are the respective pressure and temperature of transformation ($\Delta G^o(P_{tr},T_{tr}) = 0$)

$$\Delta G^o(P,T) = \Delta G^o(P_{tr},T_{tr}) + \int_{P_{tr}}^{P} \Delta V(T_{tr})\, dP - \int_{T_{tr}}^{T} \Delta S(P_{tr})\, dT \qquad (8.3)$$

where ΔV and ΔS refer to reaction (8.2). If variations of ΔV and ΔS with pressure and temperature are ignored, the phase boundary between FeO(hpp) and $Fe_xMg_{1-x}O$(B1) is given by

$$RT\ln x - (P - P_{tr})\Delta V + (T - T_{tr})\Delta S = 0. \qquad (8.4)$$

Equation (8.4) assumes that no MgO is soluble in FeO(hpp) which gives an infinite pressure for the phase transformation of MgO. The general shape of the phase boundary is not altered, however, if a transformation pressure of 200 GPa for MgO is used, and the conclusions remain unchanged. Nonstoichiometry of FeO has been neglected since it is probably important

only close to the FeO endmember in the B1 solid solution (Jackson et al., 1978; Bonczar and Graham, 1982).

Determination of the phase boundary between FeO(hpp) and $Fe_xMg_{1-x}O$(B1) requires an estimate of ΔV and ΔS. To calculate the range for ΔV the parameters describing the extremal Hugoniots for the shock wave data of FeO(hpp) calculated by Jackson and Ringwood (1981) were used to determine $\Delta V(B1 \rightarrow hpp)$ at 70 GPa using a Birch-Murnaghan equation of state. The maximum allowed range for ΔV at 70 GPa is -0.54 to -0.99 cm^3/mol (7-11% volume decrease). Since ΔV is expected to decrease with increasing pressure, this range probably represents an overestimate of the true uncertainty. Estimates of ΔS are more difficult because of the lack of data concerning the temperature effect on the phase transformation. Accordingly, ΔS was varied between the limits +5 and -5 $JK^{-1}mol^{-1}$ which represent the range within which the majority of values for phase transformations fall.

8.2.3 Results

The calculated phase diagram for the system FeO-MgO is illustrated in Fig. 8.1 for T = 1000 K, 2000 K and 3000 K. Estimates of P_{tr} and T_{tr} of 70 GPa and 1300 K, respectively, were taken from the shock wave data of Jeanloz and Ahrens (1980). The value 70 GPa probably represents a maximum estimate of P_{tr} since shock experiments tend to overestimate equilibrium transformation pressures. The shaded region represents the range in which the phase boundary between $Fe_xMg_{1-x}O$(B1) and $Fe_xMg_{1-x}O$(B1) + FeO(hpp) will lie for the variation of ΔV and ΔS between the limits given above. The effect of increasing temperature is generally to increase the pressure at which a given composition $Fe_xMg_{1-x}O$(B1) exsolves FeO(hpp).

The calculations are consistent with the results of a recent shock wave experiment on $Fe_{0.4}Mg_{0.6}O$ to 200 GPa (Vassiliou and Ahrens, 1982). The shock wave data are adequately explained without first-order phase transitions, although there is marginal evidence for a transition of no more than 3% density increase near 120 GPa. The increase in density associated with the exsolution of FeO(hpp) from $Fe_{0.4}Mg_{0.6}O$ might occur gradually as a function of pressure and no significant discontinuity in the shock data would then be predicted. Moreover the overall density increase involved with exsolution is calculated to be small. Using a Birch-Murnaghan equation of state, the maximum density contrast between $Fe_{0.4}Mg_{0.6}O$(B1) and the mixture 0.6 MgO(B1) + 0.4 FeO(hpp) (the extreme

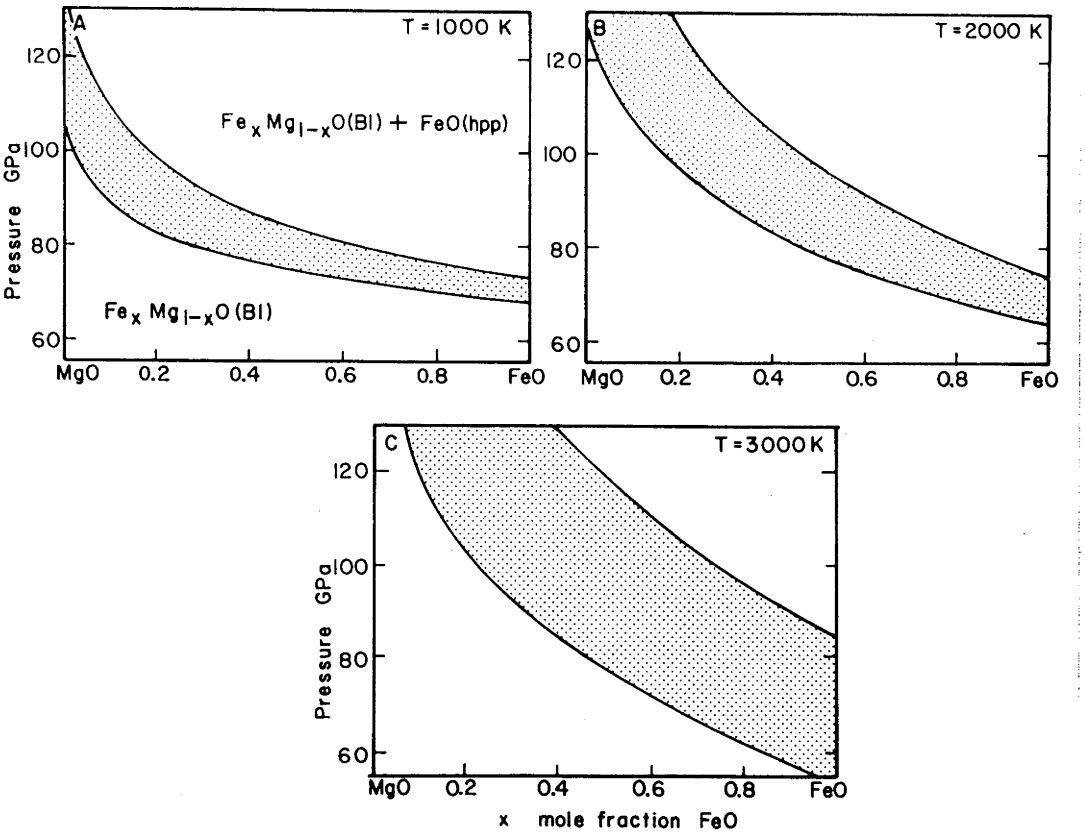

Fig. 8.1 Pressure-composition phase diagrams for the system FeO–MgO at temperatures of 1000 K (A), 2000 K (B) and 3000 K (C). The shaded region represents the range where the phase boundary between $Fe_xMg_{1-x}O$ and FeO(hpp) falls for variation of ΔV and ΔS between the limits given in the text.

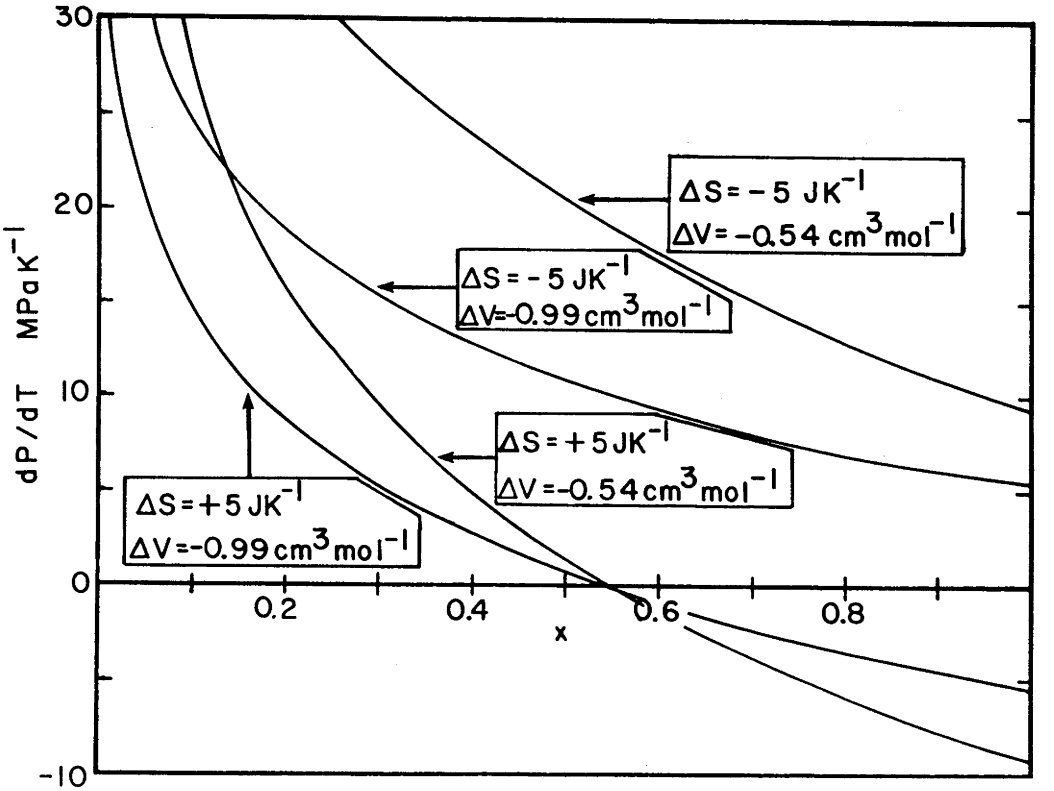

Fig. 8.2 Clapeyron slope dP/dT as a function of composition for the phase boundaries shown in Fig. 8.1. Curves corresponding to different choices of the parameters ΔS and ΔV are plotted to indicate their effect on the slope. Note that the slope of dP/dT changes sign as a function of composition for all positive values of ΔS.

case) is calculated to be less than 2.% at 200 GPa and 298 K. The Hugoniot for the mixture would therefore be within the limit of error of the $Fe_{0.4}Mg_{0.6}O$(B1) Hugoniot.

The slope dP/dT of the exsolution phase boundary may be determined from equation (8.4) and is approximately given by

$$\frac{dP}{dT} = \frac{R\ell n\ x}{\Delta V} + \frac{\Delta S}{\Delta V} \quad . \qquad (8.5)$$

The two contributions to the slope dP/dT are clearly shown. The first term represents the configurational entropy contribution arising from the disorder of Fe atoms among Mg atoms in the B1 phase, and is positive throughout the range $0 < x < 1$. The second term is the contribution from the change of entropy between the low- and high-pressure phases of FeO. This term is either negative or positive, depending on the sign of ΔS. In the case where ΔS is positive, since the right-hand side of equation (8.5) is dominated by the second term at high values of x, dP/dT assumes a negative value. As x decreases, however, the magnitude of the first term increases and eventually dominates the value of dP/dT. When ΔS is negative, dP/dT is positive for all values of x. Fig. 8.2 illustrates the variation of dP/dT as a function of x. A decrease of ΔS from +5 to $-5\ JK^{-1}mol^{-1}$ displaces dP/dT to higher values, whereas increasing the magnitude of ΔV from -0.54 to $-0.99\ cm^3/mol$ decreases dP/dT by a factor of two.

8.2.4 Implications for the Earth

In the following the present-day lower mantle is assumed to have a pyrolite bulk composition (Ringwood, 1975; Green et al., 1979) with a Mg/(Mg + Fe) ratio of approximately 0.90. That such a model is approximately consistent with available seismic and laboratory data has been demonstrated in a wide variety of independent analyses (see section 1.1). The dominant phases in such a lower mantle are believed to be $(Mg,Si)O_3$ (perovskite), (Mg,Fe)O (rocksalt), $Ca_2Al_2SiO_7$ (sodium titanate) and $NaAlSiO_7$ (calcium ferrite) (Liu, 1978; 1979; Ringwood, 1979) with partitioning of Fe between the rocksalt and perovskite phases predicted to yield the phases $Fe_{0.18}Mg_{0.82}O$(B1) and $(Fe_{0.02}Mg_{0.98})SiO_3$(pv) (Bell et al., 1979). Recent experiments by Ito and Yamada (1982) and Ito et al.(1983) have redetermined the partitioning coefficient for Fe and Mg between perovskite and magnesiowüstite, but the Fe content of the rocksalt phase is not changed by more than $\sim$ 2 atom %.

To determine the depth at which exsolution of FeO(hpp) from the B1 phase might occur in the lower mantle, the region in which the phase boundary between $Fe_{0.2}Mg_{0.8}O$(B1) and $Fe_{0.2}Mg_{0.8}O$(B1) + FeO(hpp) would lie has been plotted as a function of temperature and depth within the lower mantle (Fig. 8.3). A typical geotherm is also plotted. Exsolution, if it did occur in the lower mantle, would take place only in the region immediately overlying the core and would not be a significant factor in the chemistry of the present-day lower mantle.

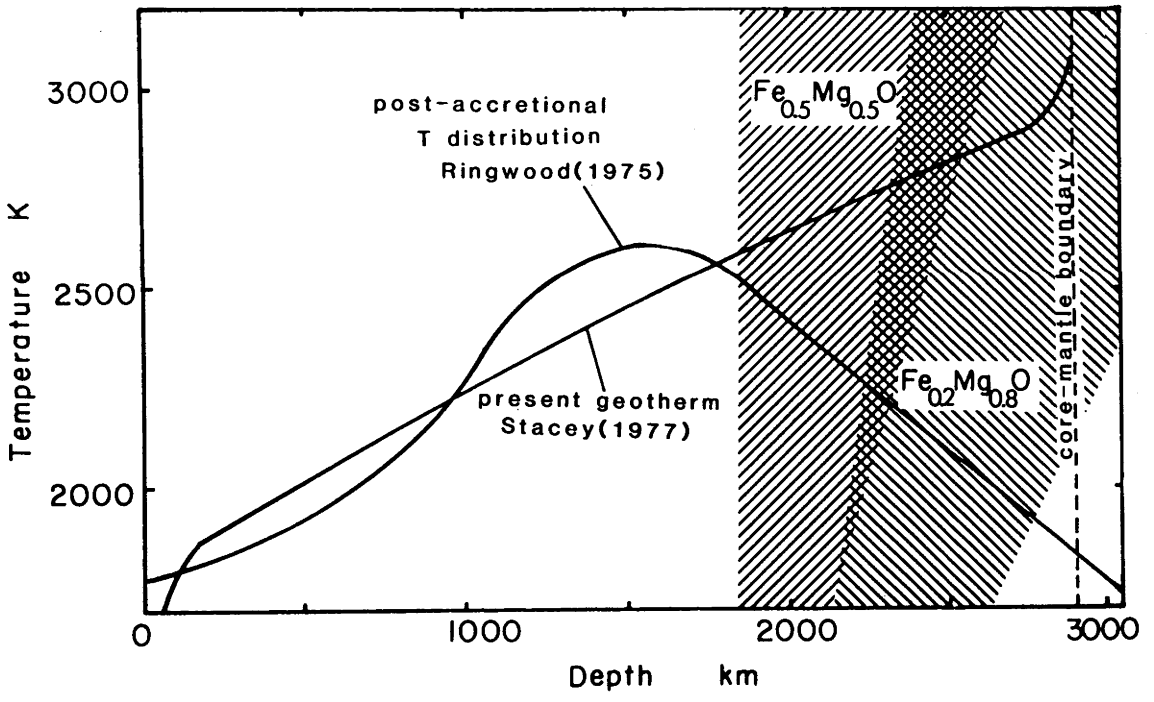

Fig. 8.3 Temperature-depth profile illustrating the region (shaded) where exsolution of FeO(hpp) from two B1 compositions begins, where ΔV and ΔS have been varied between the limits given in the text. A present-day geotherm (Stacey, 1977) and an estimate of the post-accretional temperature distribution (Ringwood, 1975) are also plotted.

Exsolution of FeO(hpp) from (Fe,Mg)O may, however, have played a significant role in the development of the early Earth. Assuming oxygen to be the light alloying element, the composition of the core can be estimated by comparison of shock compression data of Fe and Fe oxides with density profiles of the core (e.g. Dubrovskiy and Pan'kov, 1972; Ringwood, 1977; Jeanloz and Ahrens, 1980). The recent shock wave data of Jeanloz and Ahrens (1980) indicate a composition for the outer core of 45% (wt) FeO and 55% Fe. Thus the simplified bulk composition of the Earth (Fe/FeO core + pyrolite mantle), and by inference of the material from which the Earth was accreted, is 20% (wt) metallic Fe, 32% SiO_2, 28% MgO and 20% FeO. The bulk Mg/(Fe + Mg) ratio of the primordial nonmetallic component is thus approximately 0.7 with partitioning of Fe and Mg between the coexisting perovskite and magnesiowüstite phases at pressures in excess of 23 GPa (Bell et al., 1979) resulting in the rocksalt phase composition $Fe_{0.5}Mg_{0.5}O$. Fig. 8.3 illustrates the region in which the phase boundary between $Fe_{0.5}Mg_{0.5}O$(B1) and $Fe_{0.5}Mg_{0.5}O$(B1) + FeO(hpp) will lie plotted as a function of temperature and depth. The horizontal axis is based on the current density distribution; the exsolution region of $Fe_{0.5}Mg_{0.5}O$(B1) will therefore lie at slightly shallower depths than indicated since pressure will have increased more rapidly with depth in the mantle of the early Earth. One estimate of the post-accretional temperature distribution within the Earth is also plotted. It is clear, therefore, that exsolution of FeO(hpp) from (Fe,Mg)O could occur at the P,T conditions within the accreting Earth.

The formation of a dense FeO(hpp) phase early in the Earth's history raises the possibility of gravitational separation of the high-pressure phase from the surrounding silicate material. Mao et al.(1979) have proposed a model for the differentiation and subsequent formation of the core based on the separation of Fe-rich and Mg-rich phases due to partitioning of Fe between the perovskite and rocksalt structures. Additional partitioning of Fe caused by exsolution of FeO(hpp) would greatly enhance such a differentiation process and place additional compositional constraints on the system. The time required for gravitational separation can be estimated using Stokes' law. Given the density difference between phases, $\Delta\rho$, and the viscosity of the surrounding material, η, a spherical particle with a radius r will fall with a velocity given by

$$V = \frac{2gr^2\Delta\rho}{9\eta} \qquad (8.6)$$

where g is the gravitational acceleration (Batchelor, 1970, p. 234). Given a lower mantle viscosity of 10^{16} P (Stevenson, 1981), an FeO(hpp) blob of several cm diameter would fall with a velocity of $\sim 10^{-13}$ cm/s, requiring $\sim 10^{13}$ yr to fall through the lower mantle to the core. To reduce the time to be compatible with Earth history, e.g. 10^{8} yr, the size of the individual FeO(hpp) blobs in the lower mantle would have to exceed 10 m in diameter. Solid-state diffusion processes required for the growth of FeO(hpp) into such large blobs might require prohibitively long periods of time and therefore gravitational separation in the solid state does not seem a likely mechanism for differentiation of the Earth with respect to Fe. Watt and Ahrens (1982) have reached an identical conclusion based on a similar Stokes' Law calculation. If FeO were molten, however, gravity could effectively separate the dense liquid from less dense unmelted silicate phases. Using a modification of Darcy's law (e.g. Walker et al., 1978) the velocity with which a melt of viscosity η will percolate through an aggregate of crystals with radius R is given by

$$V = \frac{g\Delta\rho R^2 f^2}{73.5\eta} \qquad (8.7)$$

where f is the fraction of melt present. For a melt viscosity of 1 P (by analogy with Fe_2SiO_4, see Bottinga and Weill, 1972) and a silicate grain size of 0.1 cm, the FeO melt would sink at a rate of $\sim 10^{-3}$ cm/s, a velocity large enough to ensure an effective segregation of Fe into the core within the Earth's history. One means of producing an FeO-rich melt would be the formation of a low-melting point alloy between Fe and FeO(hpp) in the primordial Fe-silicate mixture, as proposed by Ringwood (1977; 1979).

8.3 The System Fe-FeO

8.3.1 The Fe-FeO phase diagram at 0.1 MPa

At atmospheric pressure the phase diagram of Fe-FeO contains a large liquid immiscibility region (LIR). The solubility of oxygen in molten Fe has been studied as a function of temperature to 2319 K (Taylor and Chipman, 1943; Distin et al., 1971; Fischer and Schumacher (1978), and the data are illustrated in Fig. 8.4. Recent data of Fischer and Schumacher (1978) have provided a more accurate determination of the solubility of oxygen in Fe due to the use of a sophisticated levitation and heating technique which allows an in-situ determination of the solubility temperatures, and the results are both reversible and reproducible. A linear extrapolation of the data of Fischer and Schumacher (1978) indicates that the

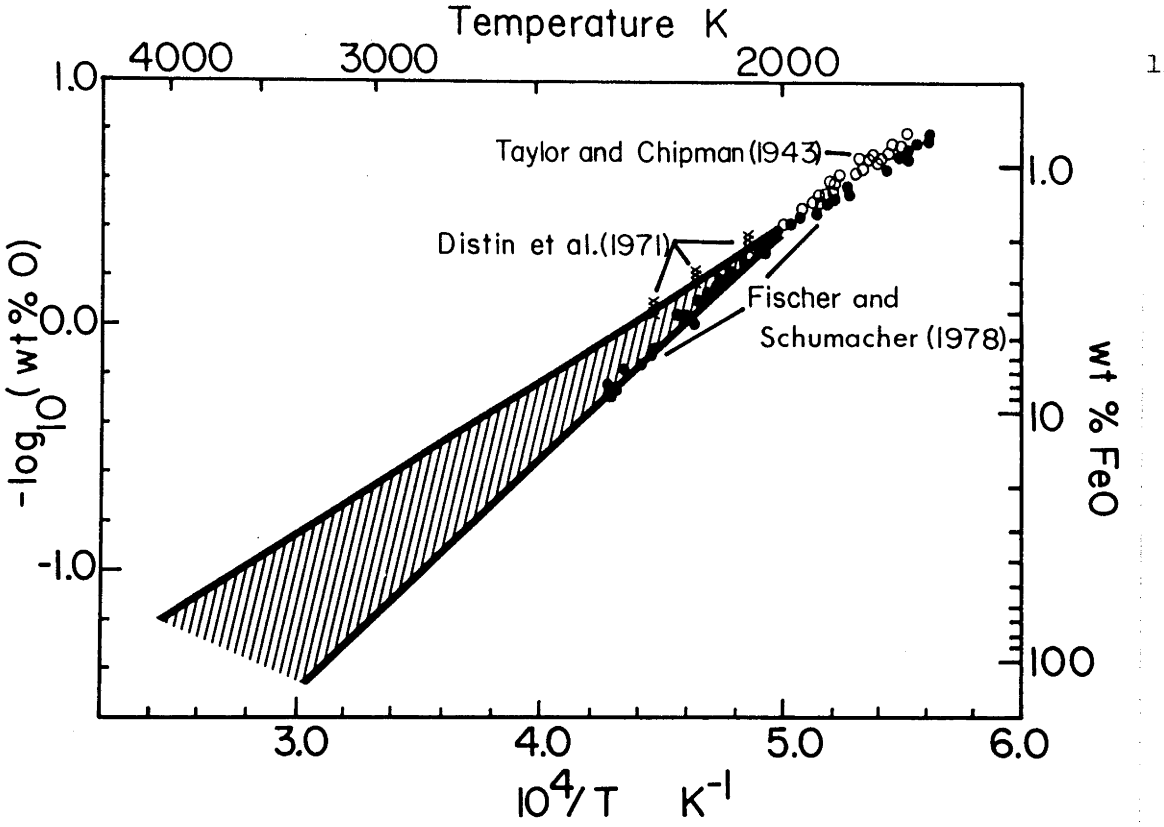

Fig. 8.4 Solubility of oxygen in liquid Fe as a function of inverse temperature. The open circles refer to data of Taylor and Chipman (1943), the crosses to data of Distin et al.(1971) and the closed circles to data of Fischer and Schumacher (1978). The shaded region indicates the uncertainty allowed in extrapolating the data to high temperature.

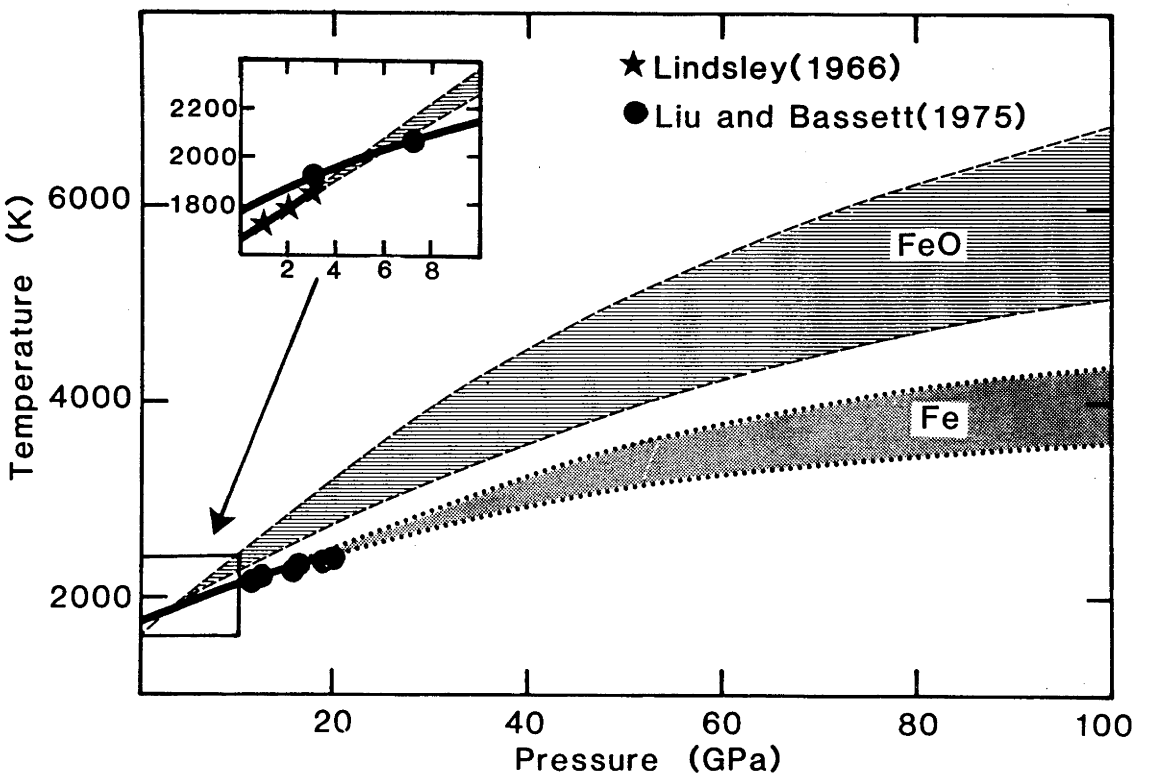

Fig. 8.5 Melting temperature versus pressure for Fe and FeO. The solid lines indicate experimentally determined curves and the shaded areas are an extrapolation of the Lindsley (1966) data for FeO based on the Kraut-Kennedy relation, and a calculation of the Fe melting curve based on the Lindemann law. The bounds of the shaded region reflect the magnitude of uncertainties in the input parameters.

miscibility gap closes at approximately 3000 K. Because of the length of extrapolation required, a somewhat larger uncertainty has been assumed for the solubility of oxygen in Fe at high temperature, and is indicated by the shaded region in Fig. 8.4. The extrapolated phase diagram for the system Fe-FeO at 0.1 MPa is illustrated in Fig. 8.6 (Box A) (see also Ringwood, 1977). The error bars attached to the temperature at which the miscibility gap closes are $\pm$ 500 K, based on the allowed range of solubilities in Fig. 8.4. It should be noted, however, that Fig. 8.6(A) probably overestimates the temperature of closure of the miscibility gap in view of the high accuracy attributed to the Fischer and Schumacher (1978) dataset, which strengthens considerably the arguments presented in the following sections.

8.3.2 Melting curves for Fe and FeO

The effect of pressure on the melting point of Fe can be calculated using Lindemann's rule (e.g. Alder, 1966; Boschi, 1974; Stacey and Irvine, 1977). If $\rho\gamma$ = constant is assumed to be valid for Fe, where γ represents the solid state Grüneisen parameter and ρ is the density, the variation of the melting point as a function of pressure for Fe according to Lindemann's rule (see Stacey and Irvine, 1977) can be written as

$$T_m = T_{m_o}\left(\frac{\rho_o}{\rho}\right)^{2/3} \exp[2\gamma_o\,(\rho - \rho_o)/\rho] \qquad (8.8)$$

where the zero subscript refers to atmospheric pressure and temperature is expressed in Kelvin. Using the Hugoniot data of McQueen et al.(1970) to constrain the density and the analysis of Jeanloz (1979) based on the McQueen et al.(1970) data to constrain the Grüneisen parameter, the bounds for the melting curve of Fe to 100 GPa were determined (Fig. 8.5). The melting curve is consistent with recent evidence from shock wave data of Brown and McQueen (1980) that Fe melts between 5000 K and 6000 K at 250 GPa (Brown and McQueen, 1982); equation (8.8) predicts a melting temperature for Fe at 250 GPa of between 4665 K and 6080 K. The experimental data of Liu and Bassett (1975) to 20 GPa also lie within the bounds of the melting curve illustrated in Fig. 8.5.

Experimental data of the melting of FeO at high pressure are only available to 3 GPa (Lindsley, 1966), and therefore the melting curve of FeO is not well constrained. It can be demonstrated, however, that the melting curve of FeO lies above the melting curve of Fe at high pressure. The initial melting slope for FeO measured by Lindsley (1966) is approximately 70 K/GPa, compared with 35 K/GPa for Fe. A modest

extrapolation of the FeO melting data indicates that the melting curves of FeO and Fe cross at approximately 5 GPa (see inset, Fig. 8.5). Consideration of the uncertainty in the FeO melting data does not alter the crossover point by more than 2 GPa. Assuming that the melting temperature of FeO ascends uniformly with pressure and does not display a maximum, the melting curve of FeO must lie above the melting curve of Fe above $\sim$ 5 GPa. To estimate the effect of pressure on the melting temperature of FeO, the Lindsley (1966) data were first extrapolated using the Lindemann criterion as for Fe, but it was found that the calculated melting curve deviated more 100 K at 3 GPa from the Lindsley (1966) melting data for all reasonable values of γ. As a first approximation, therefore, the Kraut-Kennedy extrapolation formula was used instead, where the melting temperature is given by

$$T_m = T_{m_o} \left(1 + \frac{C\Delta\rho}{\rho}\right) \qquad (8.9)$$

where $\Delta\rho/\rho$ is the isothermal (298 K) compression and C is a constant (Kraut and Kennedy, 1966). Using a Birch-Murnaghan equation of state with $K_o = 150 \pm 10$ GPa and $K_o' = 3.5 \pm 0.5$ to calculate $\Delta\rho/\rho$, C was calculated to be 10 ± 2 from the Lindsley (1966) data. Using the isothermal compression data calculated from the Hugoniot data for FeO of Jeanloz and Ahrens (1980), the melting curve for FeO was calculated using equation (8.9) (Fig. 8.5). The effect of the phase transformation in FeO at $\sim$ 70 GPa is to increase dT_m/dP at the B1-hpp-ℓ triple point according to the general argument of Schreinemakers (1916), and thus increase the discrepancy between the melting temperatures of Fe and FeO.

8.3.3 The effect of pressure on liquid immiscibility

The effect of pressure on the LIR is to reduce the temperature at which the miscibility gap closes, if the partial molar volume of FeO (FeO*, Ringwood, 1977) dissolved in the metallic Fe-rich liquid is assumed to be less than that of FeO in the nonmetallic FeO-rich liquid (Ringwood, 1977). Substantial reductions in M-O bond lengths have been observed in metallic oxides of Mo, Tc, Ru, Rh, W, Re, Os and Ir relative to insulating compounds containing the same cations (Shannon, 1976). In the first-row transition metal series, the M-O bond lengths of metallic VO and TiO are substantially shorter than would be predicted from their ionic radii, whereas the M-O bond lengths in nonmetallic MnO, FeO, CoO and NiO are very close to those calculated from their ionic radii. The substantial shortening of Fe-O bond lengths associated with a metallic transition of FeO supports the assumption that the partial molar volume of FeO in the

metallic Fe-rich liquid is less than that of FeO in the nonmetallic FeO-rich liquid. The degree to which the LIR is reduced with pressure depends on the magnitude of the difference between the partial molar volumes of FeO in the two melts. In view of the large uncertainty associated with the volume difference, it is assumed only that pressure does not increase the extent of the LIR; thus the temperature at the top of the LIR remains constant with increasing pressure.

In a general sense Fe-FeO liquid immiscibility reflects an incompatibility in bond character between the endmember melts, and perhaps indirectly a similar disparity in bond type between the corresponding crystalline phases. The phase transformation FeO(B1) → FeO(hpp) could have a significant effect on the high-pressure phase diagram of Fe-FeO if the bonding in FeO(hpp) were metallic. The melt formed from FeO(hpp) might become more structurally compatible with liquid Fe with increasing pressure, resulting in a depression or even closing of the liquid miscibility gap. The observation of very low electrical resitivity (Endo and Ito, 1980) for the high-pressure phase of Fe_2O_3 (Yagi and Akimoto, 1982) supports the possibility of metallic behaviour in Fe-O compounds at high pressure.

8.3.4 The effect of pressure on eutectics of Fe-FeO

The variation of eutectics in the system Fe-FeO can be assessed on the basis of thermodynamic considerations. In a discussion by Ringwood (1962b), it is pointed out that the variation with pressure of the eutectic temperature may be substantially less than the melting point gradients of the pure phases because of the increase in $\Delta S_{melting}$ for an intermediate composition due to the entropy of mixing in the liquid phase. Newton et al.(1962) have explicitly calculated the slope dT_m/dP for a binary eutectic, and demonstrate its reduction over dT_m/dP of the pure endmembers due to a term representing the entropy of mixing. Experimentally a substantial depression of the eutectic with respect to the liquidi of the endmembers has been observed in the binary systems Na-K (Newton et al., 1962), NaF-NaCl and CsCl-NaCl (Kim et al., 1972) and Fe-FeS (Usselman, 1975a).

The eutectic may also be affected by the solid-state phase transition in FeO. If FeO liquid were to become more compatible with Fe liquid discontinuously in the pressure range of the transition (60-90 GPa), there might be an abrupt shift of the eutectic to more FeO-rich compositions and

hence an abrupt lowering of the eutectic according to the increased proportion of the alloying species.

8.3.5 The Fe-FeO phase diagram at high pressure

Although the considerations presented above are largely qualitative, they provide useful constraints on the topology of the phase diagram of Fe-FeO at high pressure. A series of schematic phase diagrams has been constructed based on these considerations (Fig. 8.6). With increasing pressure the melting point of FeO rises above the melting point of Fe and a new phase region consisting of FeO(B1) + metallic liquid forms. The temperature of the Fe-rich eutectic increases more slowly with pressure than the melting point of Fe, which causes a more pronounced lowering of the melting temperature of Fe by solution of oxygen. The Fe-rich eutectic is displaced towards more FeO-rich compositions and the eutectic near FeO is correspondingly displaced towards less FeO-rich compositions because a eutectic tends to be displaced towards the endmember whose melting point varies least with pressure (Bridgman, 1931, p.221) (here the top of the LIR is considered an endmember and its invariance with pressure displaces both the Fe-rich and the O-rich eutectics). As pressure increases, several factors contribute to a contraction of the liquid immiscibility field:

(1) an upwards displacement of the melting points of Fe and FeO relative to the top of the liquid immiscibility region which is assumed to remain fixed on the basis of earlier discussion;
(2) a more rapid increase with pressure of the melting points of Fe and FeO relative to the eutectic temperatures;
(3) a progressive displacement of the eutectic compositions towards the LIR.

At the point where complete liquid immiscibility occurs, the Fe-FeO phase diagram becomes qualitatively similar to that of Fe-FeS at atmospheric pressure.

8.4 Formation of the Earth's Core

A prospective candidate for the light alloying element in the Earth's core must satisfy at least three criteria (Stevenson, 1981):

(1) it must be present in sufficient cosmic quantities;
(2) it should be capable of forming a high-pressure alloy with Fe and significantly depressing the Fe melting point;
(3) it should partition into the core-forming Fe liquid in sufficient amounts.

The need for a low-temperature eutectic between Fe and the light element

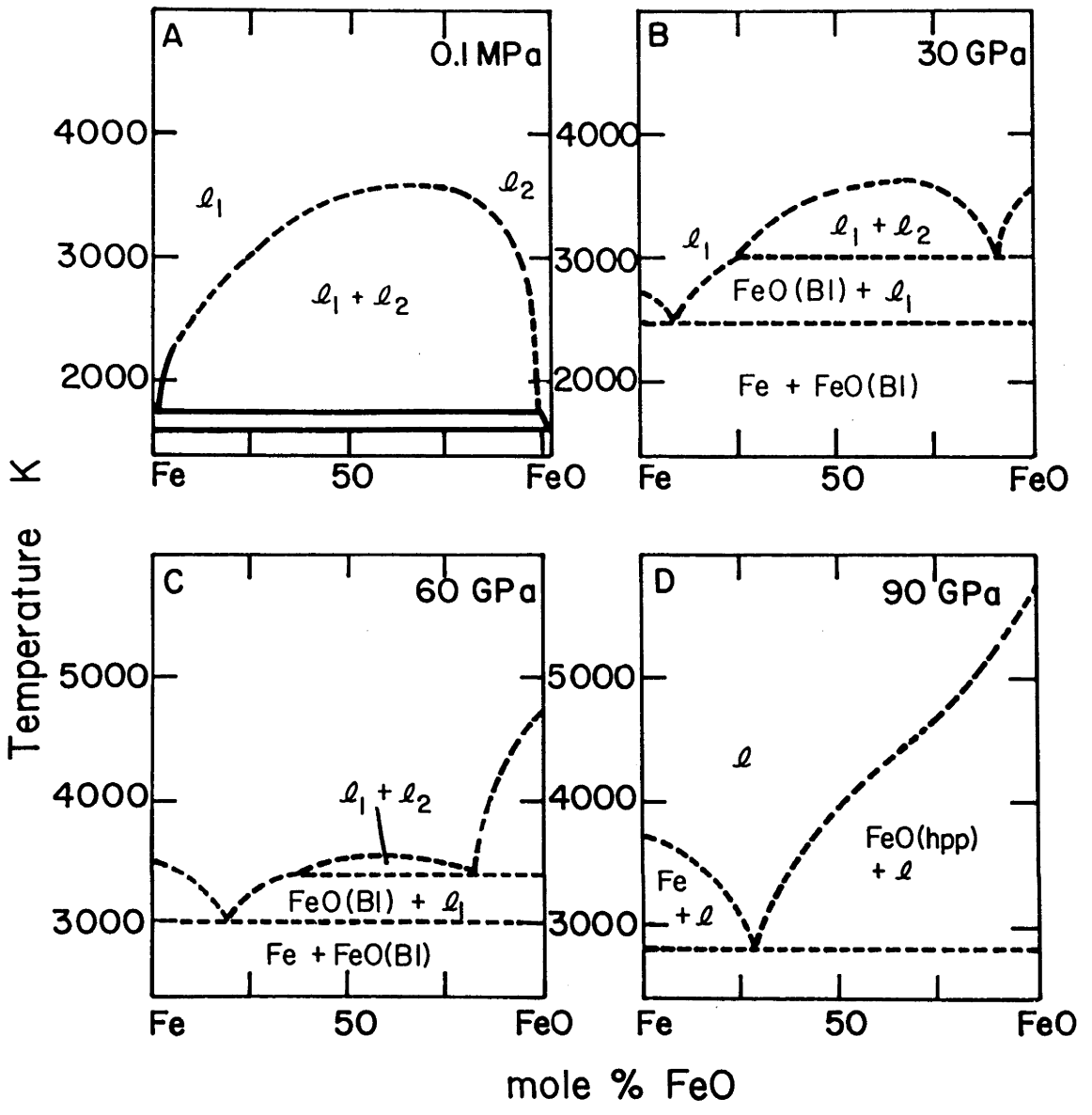

Fig. 8.6 Sequence of proposed schematic phase diagrams of Fe-FeO at high pressure. The dashed lines indicate that no experimental data are available. The phase diagram at atmospheric pressure is shown in box A. As pressure increases, T_m(FeO) > T_m(Fe) and the extent of the liquid immiscibility region decreases as the temperature at the top of the region remains constant (B). The rate of increase of the eutectic temperatures with pressure is retarded with respect to the increase of the endmember melting points, and the eutectic compositions move towards the liquid miscibility gap (C). Above the solid-state transformation in FeO the liquid miscibility gap closes and the phase diagram is qualitatively similar to that of Fe-FeS (D).

arises from a reconciliation of the proposed low-temperature accretion of the Earth and the inferred rapid formation of the core (e.g. Murthy and Hall, 1972). Sulphur is regarded as one of the more likely light elements because of its cosmic abundance, the deep eutectic in the Fe-S system and the limited amounts of sulphur needed to satisfy core density constraints. Usselman (1975b) has estimated the increase of the Fe-S eutectic with pressure based on an extrapolation of experimental data. Fig. 8.7 illustrates Usselman's extrapolated curve with the melting curve derived for pure Fe; the eutectic lies well below the melting curve at all pressures. In models of core formation involving sulphur, the solidus of the system Fe-S is generally assumed to be exceeded first in the surface region of the accreting Earth because of heat concentration near the surface due to the dissipation of gravitational energy of infalling planetesimals. The Fe-rich liquid coalesces into large bodies which sink

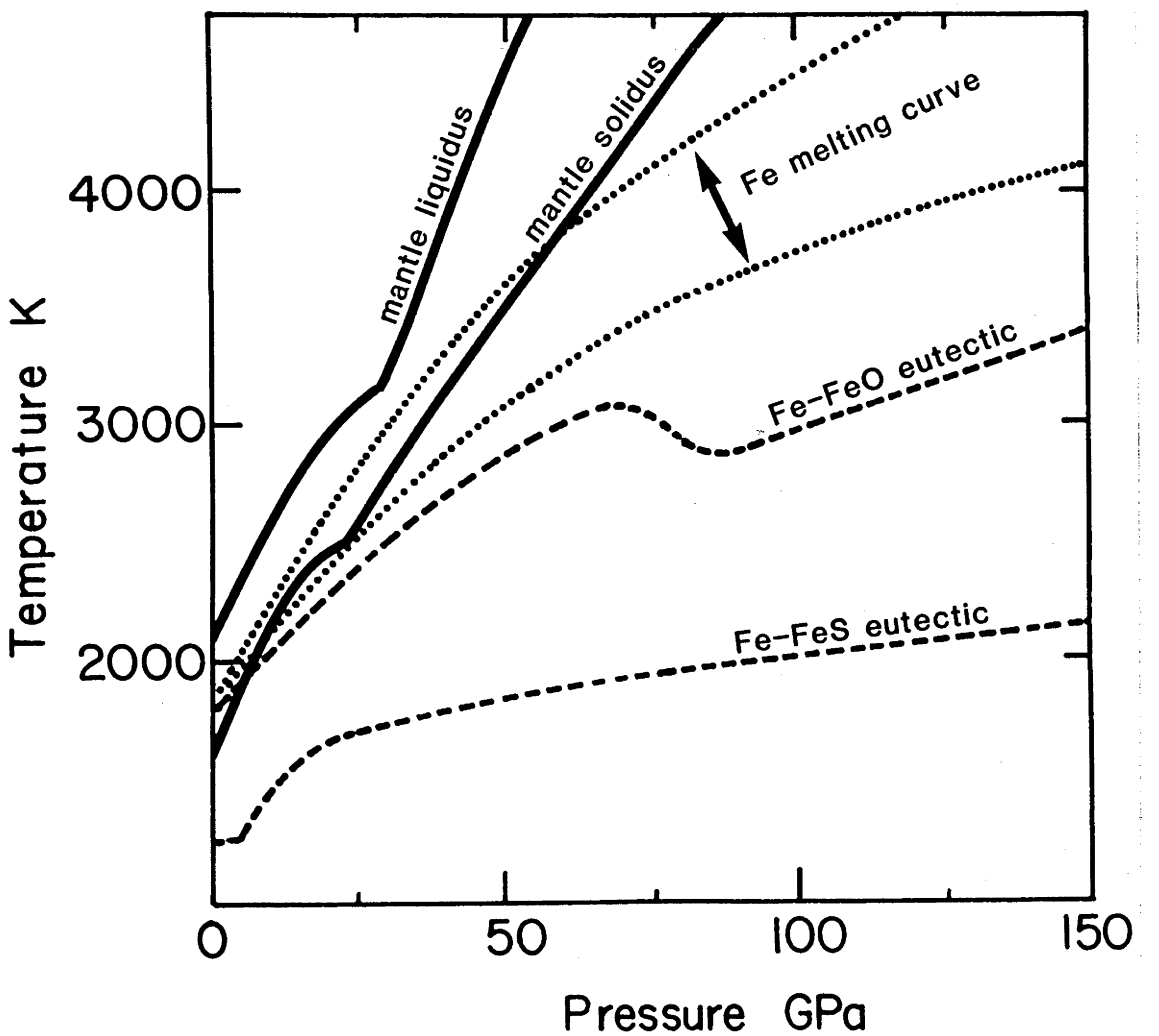

Fig. 8.7 Estimates of the melting interval of the mantle (Ohtani, 1983) and the melting curve of Fe (see Fig. 8.5). Also plotted are the estimated variation with pressure of the Fe-FeS eutectic (Usselman, 1975b) and the purely schematic curve corresponding to the Fe-FeO eutectic (see Fig. 8.6).

through the viscous but solid mantle (e.g. Elsasser, 1963; Vityasev and Mayeva, 1976; Stevenson, 1981); core formation is therefore governed by the essentially vertical movement of large bodies of contrasting density in the Earth's gravitational field.

Ringwood (1977; 1979) has suggested that oxygen can participate in core formation models in a similar manner to sulphur, forming a low-temperature Fe-rich melt which sinks to form the core. In this work it has been argued that (a) a dense FeO(hpp) phase exsolves from the (Fe,Mg)O(B1) phase above 70 Gpa, and (b) above $\sim$ 70-80 GPa at high temperature ($T > 2000$ K) FeO and Fe are presumed to be completely miscible in the liquid state. The variation of the Fe-FeO eutectic with pressure has been determined by crudely estimating the position of the eutectic from Fig. 8.6 (Fig. 8.7). An estimate of the mantle melting interval has also been plotted (Ohtani, 1983). Since the estimated Fe-FeO eutectic lies considerably below the mantle solidus (whereas the melting curve of Fe does not), it is possible that production of an Fe-FeO melt within the accreting Earth can occur without extensive melting of the silicate-oxide phases. This is consistent with geochemical evidence that suggests a lack of gross chemical fractionation, combined with the lack of evidence for a thick primordial crust, which would be indicative of extensive melting of the mantle (e.g. Urey, 1952; Ringwood, 1979).

Ringwood (1977; 1979) has proposed a model for the formation of the Earth's core in which molten blobs of a low-melting point alloy of Fe-O sink through unmelted silicate material to form the core and the unmelted silicate material coalesces to form diapirs which rise upwards to form the mantle. The revised phase diagrams of FeO-MgO and Fe-FeO presented in sections 8.2 and 8.3 add important input to Ringwood's model, and allow the core formation process to be developed in greater detail. The following model is taken from McCammon et al.(1983):

(1) The Earth accretes in the primordial solar nebula as an intimate and homogeneous mixture of metallic Fe particles and (Mg,Fe) silicates and oxides. The gravitational energy of infalling planetesimals liberated as heat warms the surface of the accreting Earth, but temperatures are low with respect to the relevant silicate and metal melting points (Fig. 8.8a).

(2) The Earth continues to accrete and interior temperatures rise as

adiabatic compression becomes significant. Pressure becomes sufficiently high to allow exsolution of FeO(hpp) from the (Mg,Fe)O component of the primordial mixture. Temperatures remain below all relevant melting points (Fig.8.8b).

(3) FeO(hpp) continues to exsolve and remains intimately mixed with the Fe metal-silicate mixture (Stokes' law, section 8.2.4) until temperatures within the Earth exceed the Fe-FeO eutectic temperature (region DE, Fig. 8.8c). The metallic melt sinks through the region of unmelted Fe metal-silicate + FeO(hpp) mixture in accordance with Darcy's law (section 8.2.4) to begin formation of the core. The residual Fe-depleted silicate in region DE which is now less dense than the primordial Fe metal-silicate

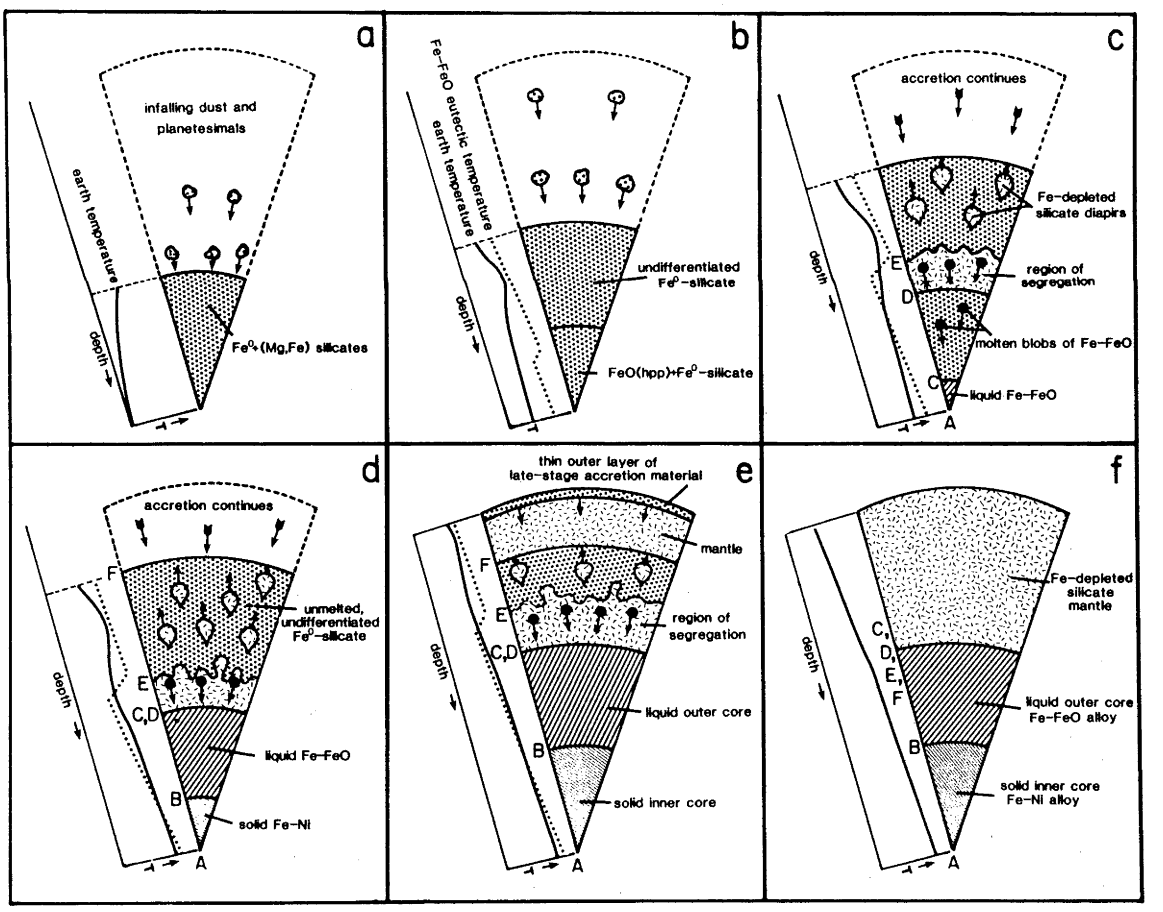

Fig. 8.8 Proposed sequence of events leading to core formation (from McCammon et al., 1983).

coalesces in the absence of the melt to form large diapirs of perhaps several km in diameter which rise upwards through the primordial Fe metal-silicate to form the mantle. The large diameter of these bodies ensures an upwards migration timescale of relatively short duration in accordance with Stokes' law.

(4) Accretion continues. The rise of interior temperatures and the displacement of material from region CD into the zone of melting (region DE) contribute to the overall reduction and eventual elimination of region CD. The overall temperature distribution within the Earth approaches an adiabatic gradient due to vigorous convection. Solidification of an inner core from the Fe-FeO melt begins as pressure raises the Fe-FeO liquidus above the prevailing temperature at the centre of the core (Fig. 8.8d). Present models for core dynamics and the geodynamo (e.g. Gubbins, 1977; Fearn et al., 1981) require the composition of the inner core to be predominantly Fe, but the estimate of outer core composition (45 wt % FeO) combined with the schematic phase diagram (Fig. 8.6) implies that inner-core crystallization would take place on the FeO-rich side of the eutectic. This inconsistency might be resolved by invoking the presence of other light elements in the core liquid. The requirement would then be that the liquid composition lie on the Fe-rich side of the eutectoid in the relevant multicomponent system, for example, Fe-S-O.

(5) Accretion of the Earth is almost complete. Melting and segregation continues in region DE and the metallic core and silicate mantle continue to grow in size. The thin outer layer of dense material resulting from the final stages of accretion is subducted into the mantle and vigorous convection assists in homogenization of material comprising the mantle (Fig. 8.8e).

(6) Core segregation is complete and the Earth has separated into the present-day mantle and core (Fig. 8.8f). In accordance with uranium/lead isotopic studies (Oversby and Ringwood, 1971; Gancarz and Wasserburg, 1977; Pidgeon, 1978), this stage would be reached within $\sim 10^8$ yr of the Earth's accretion.

CHAPTER 9 CONCLUSION

9.1 Summary

The behaviour of transition metal compounds is both diverse and complex, and is attributed primarily to the presence of d electrons in the outer bonding orbitals. This thesis has explored the behaviour of Fe oxides and sulphides in terms of some potentially important transitions related to their electronic structure. These transitions include changes in spin state, electron delocalization and magnetic properties. Changes in stoichiometry (oxidation state) and crystal structure were also studied. The main conclusions from this work are summarized in a series of phase diagrams (Figs. 9.1 - 9.3) which are marked with circled numbers corresponding to the chapters from which the information was drawn.

Fig. 9.1 illustrates the phase diagram of FeS at high pressure and high temperature. The plotted liquidus corresponds to the eutectic between Fe and FeS determined by Usselman (1975a). Fe^{2+} in high-pressure phase FeS has been inferred to be in the high-spin state from the study of FeS-CoS solid solutions in Chapter 3. The probable nature of the hypothetical phase FeS(B1) has been determined from the study of FeS-MnS and FeS-MgS B1

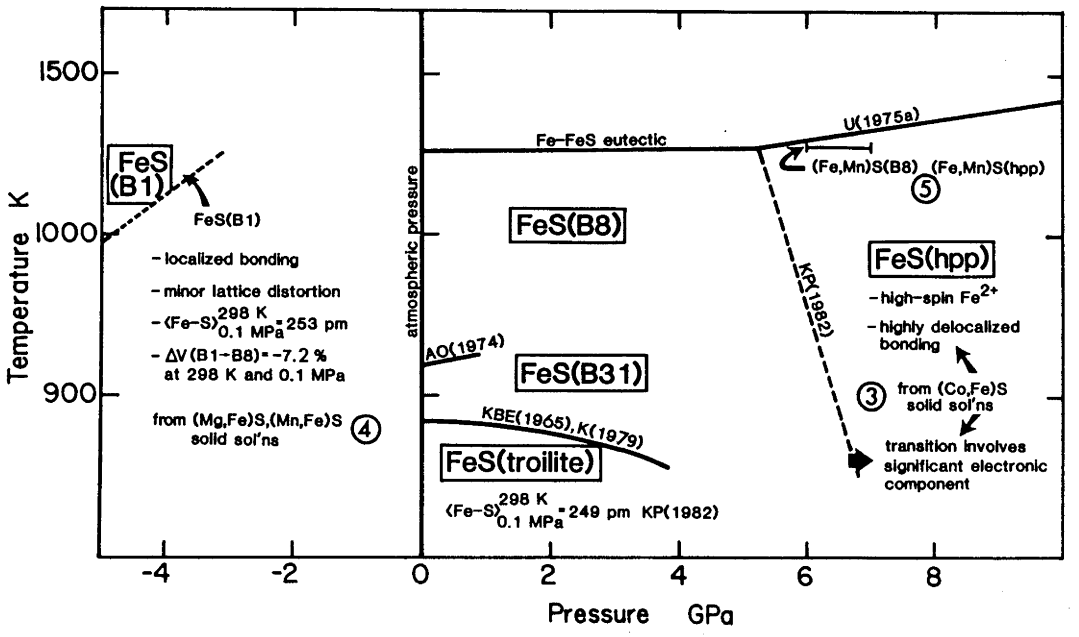

Fig. 9.1 Phase diagram of FeS based on conclusions from Chapters 3, 4 and 5. Some phase boundaries from the literature are shown; the notations refer to Anzai and Ozawa (1974), King (1979), King and Prewitt (1982), Kullerud et al.(1965) and Usselman (1975a). The slope of the FeS(B1) phase boundary was determined using $P = \Delta G^{o}_{FeS}(0,T)\Delta V_{FeS}$ (from equation (5.8)), where $\Delta G^{o}_{FeS}(0,T)$ was calculated as a function of temperature from Fig. 5.1 (see equation (4.5)).

solid solutions in Chapter 4. The stability field of FeS(B1) is indicated at negative pressures in Fig. 9.1, and while the phase diagram is not physically realistic for $P < 0$, it indicates the position of the FeS(B1) stability field relative to other stable phases in the system. The transition (Fe,Mn)S(B8) → (Fe,Mn)S(hpp) has been observed to occur between 6 and 7 GPa at 1273 K (Chapter 5), and is consistent with the phase boundary between FeS(B8) and FeS(hpp) proposed by King and Prewitt (1982), since the presence of Mn is likely to raise the transition pressure of the B8 phase.

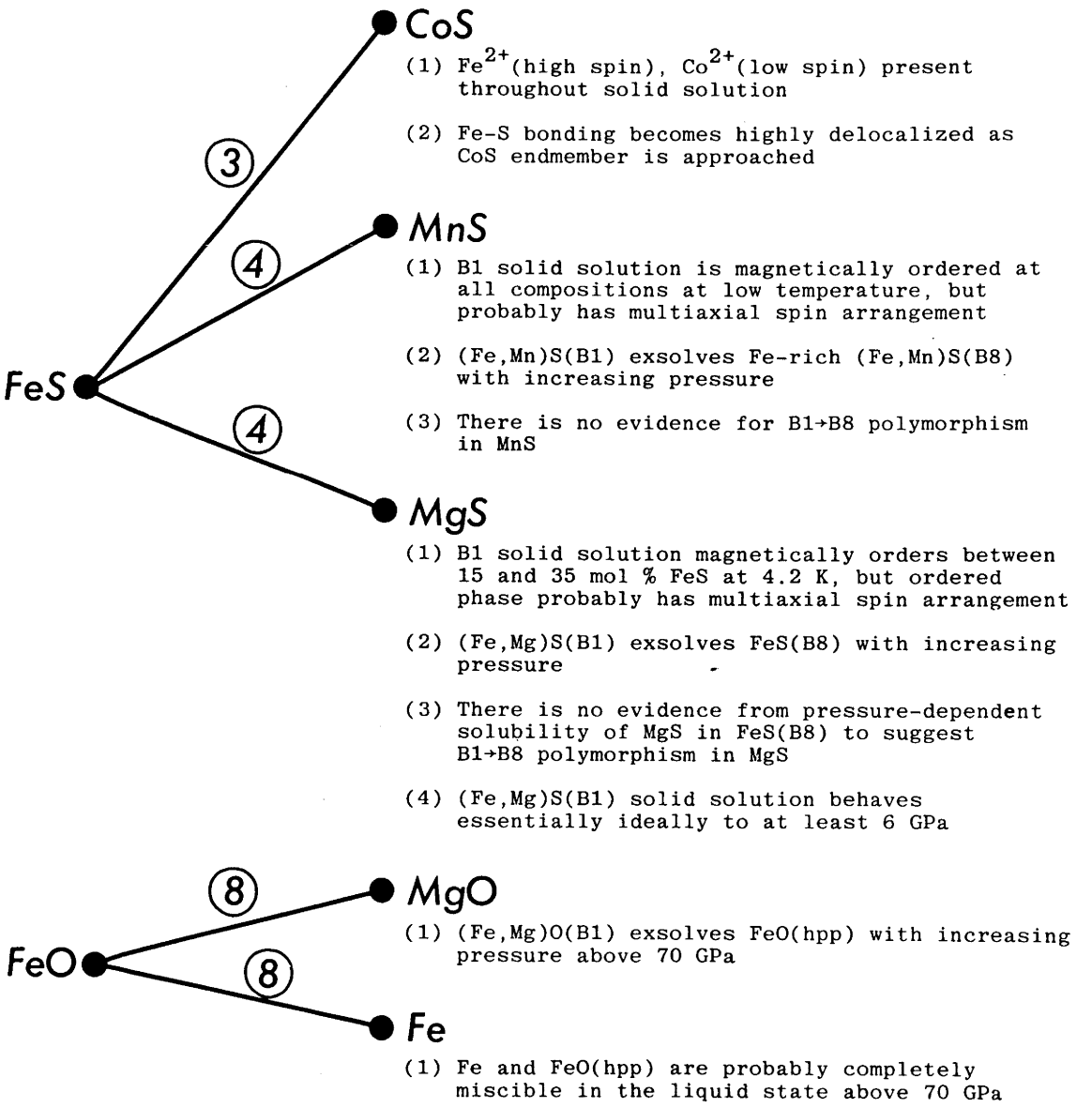

Fig. 9.2 Schematic diagram listing conclusions regarding FeS and FeO solid solutions from Chapters 3, 4 and 8.

Fig. 9.2 lists the major conclusions from studies of oxide and sulphide solid solutions. The studies involving sulphide solid solutions have been mainly experimental, while the studies involving oxide solid solutions have been largely theoretical, although several results from the sulphides are relevant to the oxides. The experimentally observed exsolution of FeS(B8) from both (Mg,Fe)S and (Mn,Fe)S B1 solid solutions at high pressure confirms calculations based on estimates of the volume and free energy differences between the B1 and B8 phases of FeS derived from atmospheric pressure data. However, the absence of an increase in solubility of Mg and Mn in the B8 phase suggests that any polymorphism in MnS and MgS at high pressure is unlikely to involve the B8 phase. Shock wave data for MgO and $Fe_{0.94}O$ reported in the literature suggest similar behaviour in the system FeO–MgO at high pressure, namely exsolution of essentially pure FeO(hpp) from (Fe,Mg)O B1 solid solutions. The observation that the behaviour of (Fe,Mg)S and (Fe,Mn)S B1 solid solutions is close to ideal at high pressure supports a similar assumption for (Fe,Mg)O B1 solid solutions.

Fig. 9.3 illustrates the phase diagram of FeO at high pressure and high temperature. The isopleths were derived from the experimental data presented in Chapter 6 (not the theoretical calculations), and show a gradual decrease of x above 20 GPa. As demonstrated by the theoretical calculations, the experimental data, combined with compression data of Hazen (1981) for Fe_xO, require the bulk modulus of Fe_xO to vary only slightly with composition when $x < 0.96$, and the rate of decrease of x above 30 GPa must slow dramatically to avoid anomalies in the partial molar volume of Fe in Fe_xO. One implication of the slow decrease of x at high P,T is that the density change involved in the transition FeO(B1) → FeO(hpp) is dominated by changes in the electronic and crystal structure, not by decreasing stoichiometry of the B1 phase as suggested by Liu et al.(1982). The melting curve of FeO(B1) was calculated in Chapter 8 by extrapolating low-pressure melting data. The phase boundary between FeO(B1) and FeO(hpp) is taken from estimates of ΔS and ΔV in Chapter 8 for the reaction FeO(B1) → FeO(hpp), and the shaded area in Fig. 9.3 illustrates where the phase boundary should lie if ΔS is assumed to be positive. It should be noted, however, that either sign of ΔS is possible.

Fig. 9.3 is based on the stable phases of FeO at high P,T and does not include the rhombohedral distortion observed in the metastable FeO phase at $\sim$ 9 GPa by Zou et al.(1980). The transition is likely influenced by the

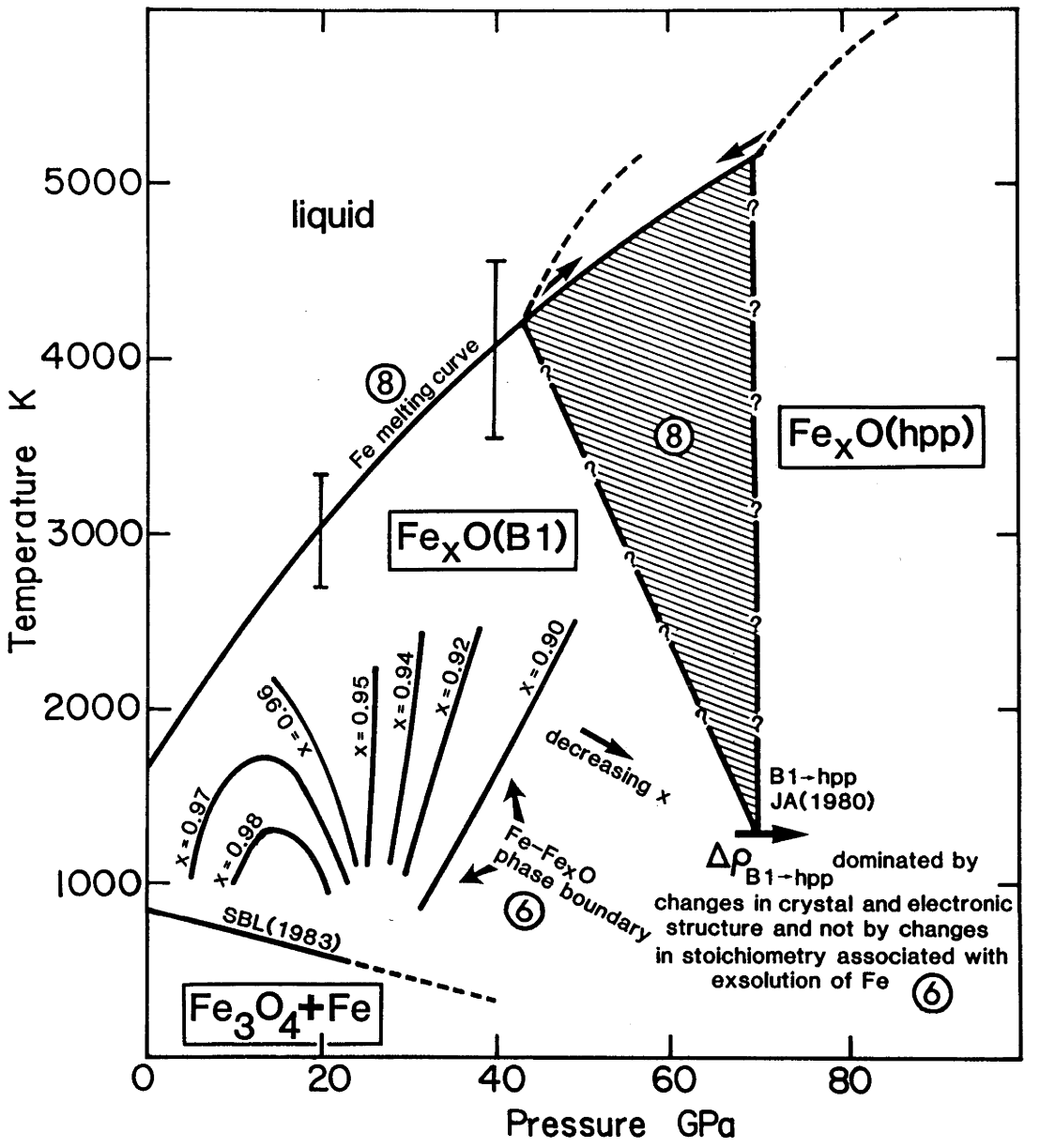

Fig. 9.3 Phase diagram of FeO based on conclusions from Chapters 6 and 8. The annotations referring to previous work correspond to Jeanloz and Ahrens (1980) and Shen et al.(1983).

presence of nonhydrostatic stress, and has not been demonstrated yet to occur under hydrostatic conditions (Chapter 4); more work is needed before the transition can be located (or determined not to occur) on the equilibrium phase diagram of FeO at high P,T.

9.2 Future work

This thesis has answered many important questions concerning the behaviour of FeO and FeS at high pressure, and has presented a model for formation of the Earth's core involving FeO based on some of the answers, but there are still many outstanding questions regarding FeO and FeS whose answers are important to further development of lower mantle models and scenarios of core formation. Some of the answers might be easily obtained using current techniques, and a list of ideas for potential projects that relate to work presented in this thesis are given below:

(1) Determine the structure of FeO(hpp). This structure might be determined by laser-heated diamond anvil cell experiments using either FeO or Fe_2SiO_4 as a starting material. If FeO(hpp) were not quenchable, the structure could be determined by in-situ x-ray diffraction after laser heating. Mössbauer spectra recorded both at high pressure and of the quenched phase (if quenchable) would be able to answer the following important questions:
   a) Does FeO(hpp) contain low spin Fe^{2+}?
   b) Is there evidence for highly delocalized bonding between Fe and O as in FeS(hpp) above 7 GPa?
   c) Are the magnetic interactions present that have been observed by Zou et al.(1980) in FeO at 298 K between 5 GPa and 80 GPa?

(2) Determine the structure of FeS(hpp). Although Mao et al.(1981) have determined the structure to be distorted B1 above 7 GPa, there is some doubt concerning the results (C.T. Prewitt, personal communication). Single-crystal x-ray diffraction of FeS at high pressure has failed to provide a refinement of the high-pressure phase due to twinning of the crystal and splitting of the reflections (King and Prewitt, 1982), so a study of FeS containing small amounts of Co^{2+}, Ni^{2+} or Mn^{2+} might provide a means of obtaining a refinement. Another possibility is a study of FeSe, which crystallizes in the B8 structure at 0.1 MPa, and might undergo a similar transition at high pressure. Another important study would be to record the Mössbauer spectrum of FeS to very high pressure ($\sim$ 80 GPa) to determine if any dramatic changes occur involving Fe-S interactions. A study of the Mössbauer spectrum above 7 GPa over a range of temperatures below 298 K would clarify the nature of magnetic interactions involving Fe^{2+}(high spin) (i.e. how close does FeS(hpp) follow the behaviour of ^{57}Fe:CoS at 0.1 MPa?).

(3) Determine partitioning of Fe^{2+} and Mg^{2+} between high-pressure phases in the system FeO-MgO-SiO_2 above 70 GPa. Chapter 8 has presented calculations concerning the phase diagram of FeO-MgO at high pressure, but the conclusions remain to be confirmed experimentally. A study of a series of $(Fe,Mg)_2SiO_4$ solid solutions using a laser-heated diamond anvil cell would enable the compositions of the (Fe,Mg)O(B1) phase, the FeO(hpp) phase, and the $(Fe,Mg)SiO_3$ phase (if present) to be determined using x-ray diffraction, and perhaps also electron diffraction techniques which are being developed (Fitzgerald, Liu and Willis, RSES Annual Report 1981; Fitzgerald and Liu, RSES Annual Report 1982).

APPENDIX AN INTRODUCTION TO MÖSSBAUER SPECTROSCOPY

This appendix presents a brief introduction to the theory and measurement of Mössbauer spectra. Some suggested references for further reading are listed at the end of the Appendix.

A.1 Theory

An atomic nucleus possesses a discrete set of energy levels which can be excited by γ-radiation ($E = 10^4 - 10^7$ eV). When a nucleus decays from an excited state to its ground state, a photon with a frequency corresponding to the energy difference between states is emitted, but because the lifetime of the excited state is finite, the frequency of the emitted radiation is broadened over an energy corresponding to the natural linewidth. The shape of the resulting intensity distribution as a function of energy (frequency) can be derived from the quantum theory of radiation as being Lorentzian

$$I(E) \propto [(E - E_o)^2 + \Gamma_o^2/4]^{-1} \qquad (A.1)$$

where Γ_o is the natural linewidth. The shape of the absorption cross-section for a nucleus absorbing a γ-ray is also Lorentzian with natural linewidth Γ_o. Γ_o can be determined from the Heisenberg uncertainty principle; if the mean lifetime of the excited state is τ, the natural linewidth is calculated from $\tau\Gamma_o = h/2\pi$. ^{57}Fe is a convenient isotope since it has an excited state 14.4 keV above the ground state with a mean lifetime of 0.14 μsec, resulting in a very narrow line with $\Gamma_o/E_o = 3 \times 10^{-13}$.

When an excited nucleus decays and emits a photon of energy E_o, the momentum of the photon and recoiling nucleus must be equal and opposite due to momentum conservation (Fig. A.1a). The energy of the photon is given by

$$E_\gamma = E_o - E_R = E_o - E_o^2/(2Mc^2) \qquad (A.2)$$

where E_R is the recoil energy and M is the mass of the nucleus. Similarly, when a nucleus absorbs a photon, nuclear recoil causes the nucleus to "see" a photon of energy $E_o + E_R$ (Fig. A.1a). For a ^{57}Fe nucleus, E_R is approximately 3.6×10^{-3} eV, about 10^6 larger than the natural linewidth. The relative energies are illustrated in Fig. A.1b; note that the Lorentzian shape of the emission and absorption lines cannot be represented on this scale since Γ_o is trivial relative to the recoil energy. No resonance is possible since there is no overlap of the emission and absorption peaks.

In most physical systems the total linewidth is significantly greater than Γ_o due to constant thermal motion of the emitting and absorbing nuclei. If the source and absorber nuclei are assumed to obey Maxwell-Boltzman statistics, the thermal linewidth is given by

$$\Gamma_T = \frac{E_o}{c}\sqrt{\frac{4kT}{M}} \quad . \qquad (A.3)$$

In most cases the thermal linewidth is much greater than the natural linewidth, so $\Gamma \sim \Gamma_T$. At room temperature Γ_T for the 14.4 keV transition in ^{57}Fe is 2.7×10^{-2} eV, comparable with the recoil energy. Fig. A.1c illustrates the effect of Doppler (thermal) broadening on the emission and absorption linewidths; there is a small overlap (shaded region) which makes nuclear resonance fluorescence experiments possible.

In theory there should be less resonance at lower temperature where the overlap is less due to smaller linewidths, but the discovery which made Rudolf Mössbauer famous was that the resonance became in fact larger at lower temperature if the nuclei were embedded in a crystal lattice. What Mössbauer observed was that in a certain fraction of occurrences, there was no recoil when a nucleus in a crystal lattice emitted, absorbed or scattered radiation, and this recoil-free fraction increased as the temperature of the system was lowered. This is illustrated in Fig. A.1d where emission and absorption of the recoil-free fraction are each centred about E_o with a linewidth Γ_o, and the remainder of the nuclei still experience recoil and Doppler broadening. At room temperature the recoil-free fraction for ^{57}Fe is approximately 70%.

The explanation of the Mössbauer effect lies in quantum theory, and can be considered naively in the following manner. If the solid is approximated by the Einstein model (all elastic waves have the same frequency), vibrations within the solid are quantized, and the smallest amount of energy that can be given to the solid is equal to $E = h\omega_E/2\pi = k\theta_E$, where θ_E is the Einstein temperature of the solid. If the recoil energy of a nucleus is small compared to this excitation energy, the probability of phonon emission will be small, the lattice will not be excited, and none of the γ-ray energy will be lost.

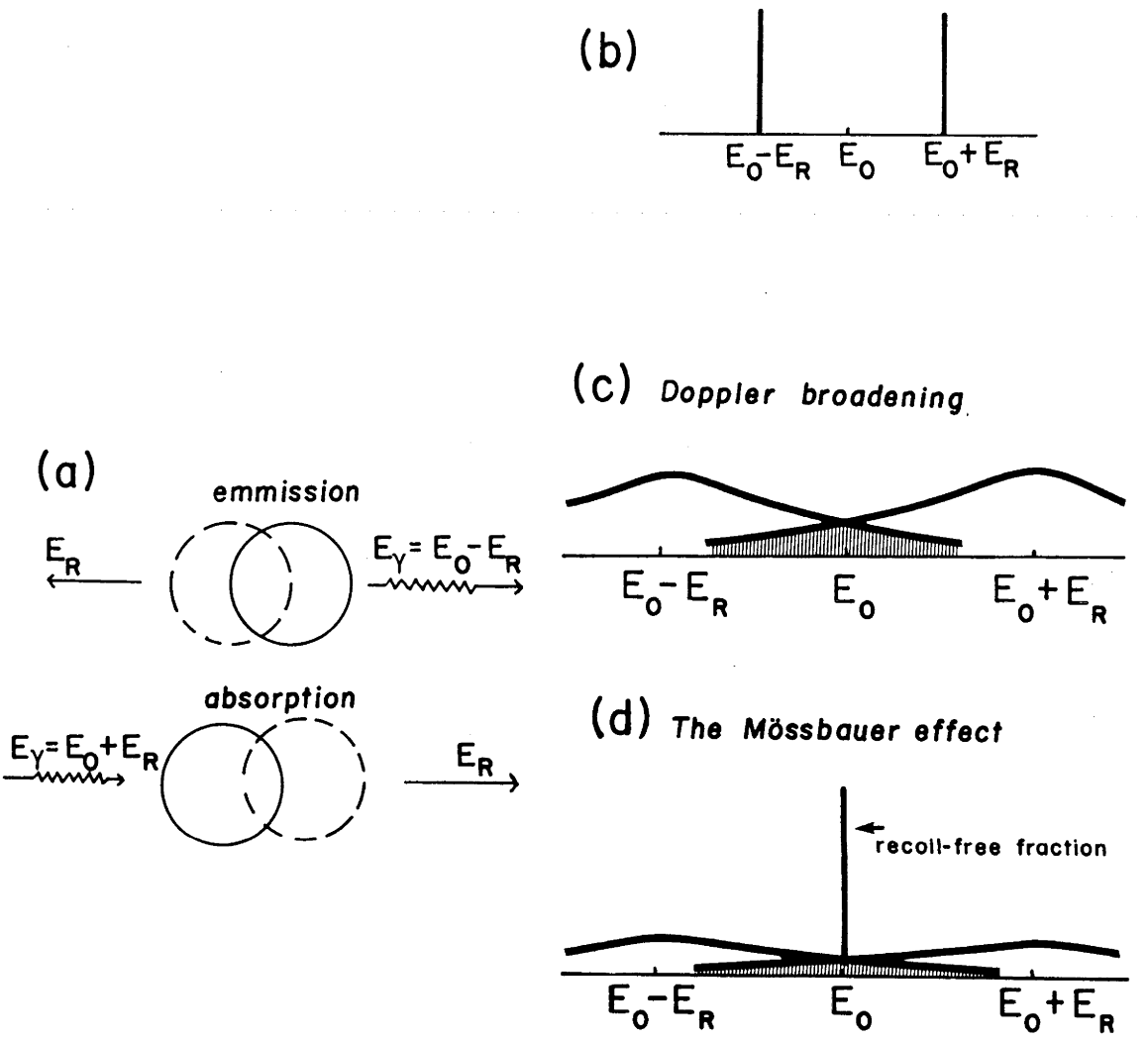

Fig. A.1 (a) Both emitting and absorbing nuclei experience nuclear recoil, either increasing or decreasing the energy of the γ-ray. (b) Energy-intensity profile corresponding to (a). There is no overlap of emission and absorption peaks, and therefore no resonance. (c) If doppler (thermal) broadening is considered, there is a small amount of overlap (shaded region), and resonance occurs. (d) If the nuclei are embedded in a crystal lattice, a certain fraction of nuclei experience no recoil, and emission and absorption peaks are centred at E_o. A small fraction of nuclei still experience thermal broadening and nuclear recoil.

A.2 Experiment

A Mössbauer experiment consists of a source of γ-rays, an absorber (the sample being studied) and a means of recording the amount of radiation passing through the absorber. Generally the source is given a velocity relative to the absorber, thus shifting the energy spectrum of the source by an amount $\delta E = vE_o/c$, where v needs only to be varied on the order of mm/sec to study nuclear energy levels. The resulting absorption spectrum measured by the recording apparatus is a plot of % absorption versus velocity (energy). The shape of the absorption spectrum will be Lorentzian, derived by taking the convolution of the intensity spectrum of the emitter with the cross-section absorption spectrum of the absorber (both Lorentzian). A typical Mössbauer setup is illustrated in Fig. A.2.

To perform Mössbauer experiments on Fe compounds, a ^{57}Co source is used which decays to an excited state of ^{57}Fe, and then emits a 14.4 keV γ-ray in decaying to stable ^{57}Fe. Only ^{57}Fe nuclei in the absorber will be excited by the 14.4 keV γ-ray, but the concentration of ^{57}Fe in the absorber required to produce a good absorption spectrum is small ($\sim$ 0.1 mg $^{57}Fe/cm^2$); if the concentration of Fe is less, a sample can be prepared using Fe enriched in ^{57}Fe.

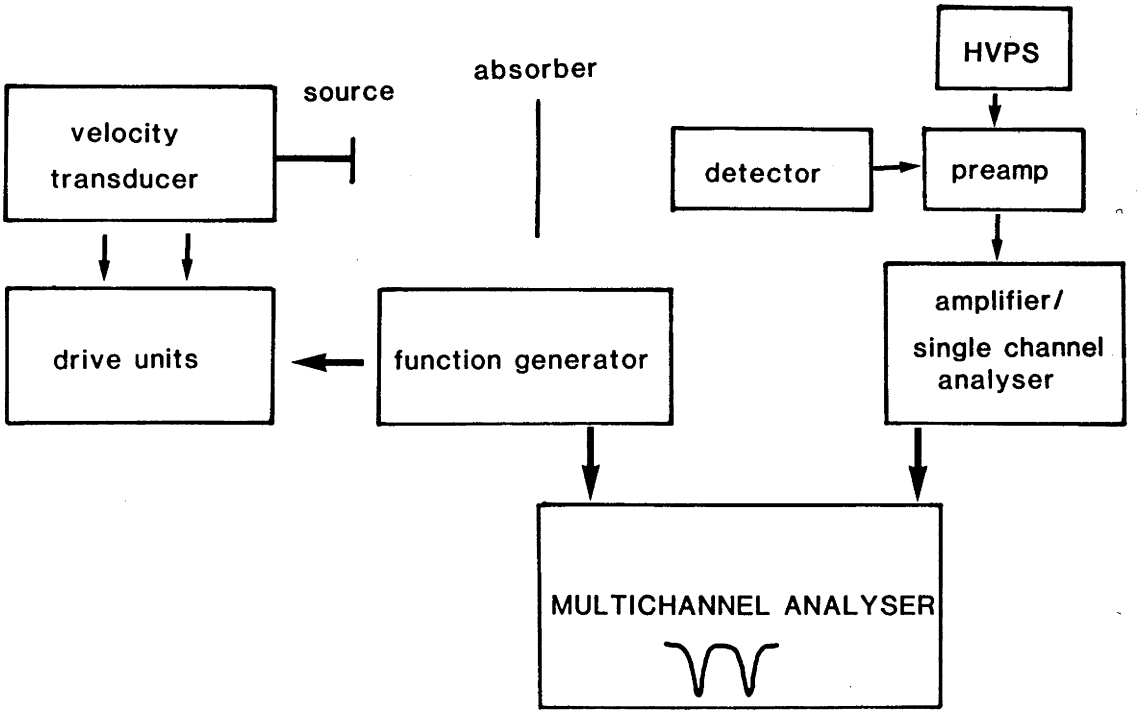

Fig. A.2 Schematic diagram of a typical Mössbauer spectrometer.

A.3 Mössbauer Parameters

The linewidth of the Mössbauer absorption spectrum is trivial compared to the energy between the ground and excited states of the nucleus, so that Mössbauer spectroscopy provides a very sensitive probe to study very small changes in the nuclear environment. There are several parameters which can be measured from Mössbauer spectra, and they are related to the properties of the absorbing nucleus and its chemical environment. The parameters are discussed below assuming ^{57}Fe to be the absorbing nucleus.

Isomer shift

The isomer shift, δ, is related to the interaction of the nuclear charge distribution with the electron charge density at the nucleus (s electrons), and the latter is usually different between the source and absorber nuclei because each are in different chemical environments. This difference results in a shift of the γ-ray energy from E_o, and is seen in the Mössbauer spectrum as a displacement of the absorption peak from zero velocity (Fig. A.3). Because the isomer shift is only a relative quantity, it is important when reporting isomer shifts to specify the material that zero velocity on the absorber spectrum corresponds to (metallic Fe is frequently used).

An increase in s electron density at the absorber nucleus results in a more negative isomer shift for ^{57}Fe compounds. In Fe compounds the 1s and 2s electrons are close to the nucleus and contribute a relatively fixed amount to the s-electron density, regardless of the chemical environment of the nucleus. The 3s electron density, however, is sensitive to both the number and radial extent of the 3d electrons, which vary with oxidation state, coordination number and spin state of the Fe atom. For example, high-spin (hs) Fe^{2+} has one more 3d electron than Fe^{3+} (hs), and therefore Fe^{2+} (hs) compounds have greater isomer shifts than Fe^{3+} (hs) compounds because the extra 3d electron increases the shielding of the 3s electrons by the 3d electrons, and hence decreases the s electron density at the nucleus. If the population of the 4s orbitals is increased, for example in highly covalent bonds, the s electron density at the nucleus is increased. Delocalization of the 3d electrons (for example, Fe^{2+} (ls)) also increases the s electron density at the nucleus because the shielding of the 3s electrons by the 3d electrons is reduced.

The second-order Doppler shift, caused by vibrations of atoms in the solid, also adds a small contribution to the shift of the absorption

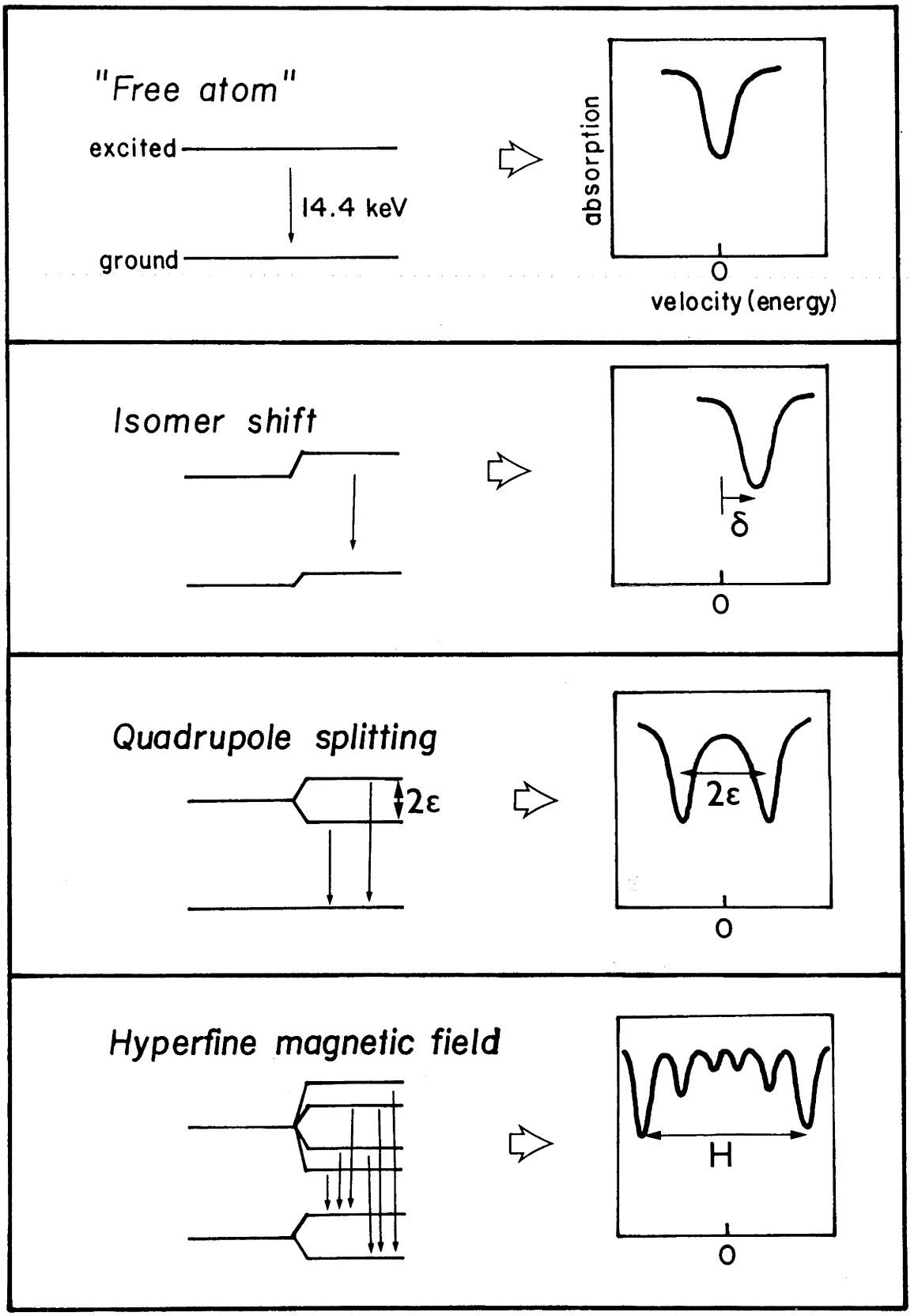

Fig. A.3 Diagram showing the Mössbauer parameters which can be measured from a Mössbauer spectrum and the relative energies of the nuclear levels associated with a particular type of spectrum.

spectrum from zero velocity, and varies as a function of temperature. Mössbauer experiments thus measure the centre shift which is a combination of the isomer shift and the second-order Doppler shift. The latter is similar for different compounds, however, and therefore centre shifts compared at the same temperature give the same information as the isomer shifts.

Quadrupole splitting

If the ligands are not distributed symmetrically about the absorbing nucleus, the nuclear electric quadrupole moment interacts with the resulting electric field gradient (EFG) to split the excited state into two energy levels. The resulting Mössbauer absorption spectrum has two lines which correspond to the two possible transitions between the excited and ground state of the nucleus (Fig. A.3). The quadrupole splitting is given by

$$\varepsilon = \pm \tfrac{1}{4} eQV_{zz}(1 + \eta^2/3)^{1/2} \qquad (A.4)$$

where eQ is the nuclear electric quadrupole moment, V_{zz} is the principal component of the diagonalized EFG tensor, and η is the asymmetry parameter of the EFG ($\eta = (V_{xx}-V_{yy})/V_{zz}$).

There are two contributions to the EFG, one from the ligand charges surrounding the atom (lattice contribution), and one from the valence electrons (valence contribution). The valence contribution can be subdivided into a crystal field term which considers the atoms as point charges, and a molecular orbital term which considers bonding between metal and ligands. The quadrupole splitting is therefore sensitive to the oxidation state, spin state and coordination number of the Fe atom, and the distortion of the crystal lattice around it. For example, octahedrally coordinated Fe^{2+} (hs) compounds tend to have large quadrupole splittings because of the large crystal field term due to unequal population of the t_{2g} (or e_g) orbitals, while octahedrally coordinated Fe^{2+} (ls) compounds have low quadrupole splittings because the crystal field term is zero since the t_{2g} orbitals are equally populated.

Magnetic hyperfine splitting

The ^{57}Fe nucleus has a magnetic dipole moment which interacts with any local or applied magnetic fields present at the nucleus to remove completely the degeneracy of the nuclear energy levels, resulting in a Mössbauer absorption spectrum with six lines corresponding to the six allowed transitions. In a randomly oriented absorber, the intensities of

the peaks will be 3:2:1:1:2:3 (Fig. A.3).

Often there are combined magnetic dipole and electric quadrupole interactions, and the intensities and positions of the Mössbauer lines may change. If the principal axis of an axially symmetric ($\eta = 0$) EFG and the direction of the magnetic field at the nucleus are parallel, and the magnetic interaction is much greater than the electric quadrupole interaction, the spacing between the excited levels is altered, but the basic six-line shape of the Mössbauer spectrum is retained. In the general case, however, the magnetic field direction and the principal axis of the EFG are not parallel, and two additional "forbidden" transitions occur, resulting in an eight-line Mössbauer spectrum. The intensities and positions of the lines for a randomly oriented absorber are dependent on the values of H, ε, η, θ and ϕ, where θ and ϕ are the angles of the magnetic field direction with respect to the principal axis of the EFG.

There are three principal contributions to the internal hyperfine magnetic field, a term from the unbalanced spin density of the electrons at the nucleus (Fermi contact term), a term from the orbital momentum of the atom (orbital term), and a term from the interaction of the atomic magnetic moment with the nucleus (dipolar term). In Fe^{3+} (hs) compounds the internal magnetic field is large, with the dominant contribution to the field being the Fermi contact term; the orbital term is zero because Fe^{3+} has zero angular momentum. In Fe^{2+} (hs) compounds the internal magnetic field tends to be smaller because the significant orbital term, which is opposite in sign to the Fermi contact term, reduces the magnitude of the net hyperfine field. In Fe^{2+} (ls) compounds there should be no hyperfine magnetic field because Fe^{2+} (ls) has a zero net atomic moment (no unpaired electrons).

Suggested references for further reading:

Bancroft, G.M., Mössbauer Spectroscopy, McGraw-Hill, England, 1973. 252 pp.

Frauenfelder, H. The Mössbauer Effect, W.A. Benjamin, New York, 1962. 336 pp.

Gonser, U. (ed.), Mössbauer Spectroscopy, Topics in Applied Physics Vol. 5, Springer-Verlag, Berlin, 1975. 241 pp.

REFERENCES

Ahrens, T.J. (1979). Equations of state of iron sulphide and constraints on the sulphur content of the Earth, J. Geophys. Res. 84 985-998.

Alder, B.J. (1966). Is the mantle soluble in the core? J. Geophys. Res. 71 4973-4979.

Andersson, B. and Sletnes, J.O. (1977). Decomposition and ordering in $Fe_{1-x}O$, Acta Cryst. A33 268-276.

Anzai, S. and Ozawa, K. (1974). Effect of pressure on the Néel and the ferrimagnetic Curie temperatures of $FeS_{1+\delta}$, Phys. Stat. Solidi 24 K31-K34.

Arnold, R.G. and Reichen, L.E. (1962). Measurement of the metal content of naturally occurring metal-deficient, hexagonal pyrrhotite by an X-ray spacing method, Am. Mineral. 47 105-111.

Basinski, Z.S., Hume-Rothery, W. and Sutton, A.L. (1955). The lattice expansion of iron, Proc. Roy. Soc. A229 459-467.

Bass, J.D., Liebermann, R.C., Weidner, D.J. and Finch, S.J. (1981). Elastic properties from acoustic and volume compression experiments, Phys. Earth Planet. Int. 25 140-158.

Bassett, W.A. and Ming, L.C. (1972). Disproportionation of Fe_2SiO_4 to $2FeO + SiO_2$ at pressures up to 250 kbar and temperatures up to 3000°C, Phys. Earth. Planet. Int. 6 154-160.

Bassett, W.A. and Takahashi, T. (1965). Silver iodide polymorphs, Am. Mineral. 50 1576-1594.

Bassett, W.A., Takahashi, T. and Stook, P. (1967). X-ray diffraction and optical observations of crystalline solids up to 300 kilobars, Rev. Sci. Instr. 38 37-42.

Batchelor, G.K. (1970). An Introduction to Fluid Dynamics, Cambridge Univ. Press, London. 615pp.

Bauer, E. and Pianelli, A. (1980). Mise au point sur la structure lacunaire de la wüstite et necessite de nouvelles recherches experimentales, Mat. Res. Bull. 15 177-188.

Bell, P.M. and Mao, H.K. (1975). Preliminary evidence of disproportionation of ferrous iron in silicates at high pressures and temperatures, Ann. Rept. Geophys. Lab. 74 557-559.

Bell, P.M., Yagi, T. and Mao, H.K. (1979). Iron-magnesium distribution coefficients between spinel [$(Mg,Fe)_2SiO_4$], magnesiowüstite [(Mg,Fe)O] and perovskite [$(Mg,Fe)SiO_3$], Ann. Rept. Geophys. Lab. 78 618-621.

Berger, J., Berthon, J., Revcolevschi, A. and Jolles, E. (1981). Elastic constants of $Fe_{1-x}O$ single crystals, J. Am. Ceram. Soc. 64 C153-C154.

Bevington, P.R. (1969). Data Reduction and Error Analysis for the Physical Sciences, McGraw-Hill, N.Y. 336pp.

Birch, F. (1952). Elasticity and constitution of the Earth's interior, J. Geophys. Res. 57 227-286.

Birch, F. (1978). Finite strain isotherm and velocities for single-crystal and polycrystalline NaCl at high pressures and 300K, J. Geophys. Res. 83 1257-1268.

Bloch, D., Vettier, C. and Burlet, P. (1980). Phase transition in manganese oxide at high pressure, Phys. Lett. 75A 301-303.

Bonczar, L.J. and Graham, E.K. (1982). The pressure and temperature dependence of the elastic properties of polycrystal magnesiowüstite, J. Geophys. Res. 87 1061-1078.

Boshi, E. (1974). Melting of iron, Geophys. J.R. astr. Soc. 38 327-334.

Bottinga, Y. and Weill, D.F. (1972). The viscosity of magmatic silicate liquids: A model for calculation, Amer. J. Sci. 272 438-475.

Boyd, F.R. and England, J.L. (1960). Apparatus for phase-equilibrium measurements at pressures up to 50 kilobars and temperatures up to 1750°C, J. Geophys. Res. 65 741-748.

Brett, R. (1976). The current status of speculations on the composition of the core of the Earth, Rev. Geophys. Space Phys. 14 375-383.

Bridgman, P.W. (1931). The Physics of High Pressure, G. Bell and Sons, Ltd., London, 398pp.

Bridgman, P.W. (1936). Shearing phenomena at high pressure of possible importance for geology, J. Geol. 44 653-659.

Brown, J.M. and McQueen, R.G. (1980). Melting of iron under core conditions, Geophys. Res. Lett. 7 533-536.

Brown, J.M. and McQueen, R.G. (1983). The equation of state for iron and the Earth's core, in High-Pressure Research in Geophysics, Adv. Earth Planet. Sci. vol. 12, eds. S. Akimoto and M. Manghnani, Centre for Academic Publications, Tokyo, pp611-623.

Bullard, E.C. and Gellman, H. (1954). Homogeneous dynamos and terrestrial magnetism, Phil. Trans. R. Soc. A247 213-278.

Bullen, K.E. (1973). On planetary cores, The Moon 7 384-395.

Burns, R.G. (1970). Mineralogical Applications of Crystal Field Theory, Cambridge Univ. Press, 224pp.

Carel, C. (1967). Recherches expérimentales et théoriques sur le diagramme d'état de la wüstite solide au-dessus de 910°C, Mem. Sci. Rev. Met. 64 821-836.

Cemic, L. and Neuhaus, A. (1972). New high-pressure modification of manganese selenide of the nickel arsenide type and miscibility of manganese selenide-manganese telluride, High Temp.-High Pres. 4 97-99.

Checherskaya, L.F., Romanov, V.P. and Tatsienko, P.A. (1973). Mössbauer effect in wüstite, Phys. Stat. Sol. 19A K177-K182.

Chiba, K. and Chikazumi, S. (1982). Low-temperature structure of magnetite as deduced from diffuse electron scattering, Ferrites, Proc. ICF, 3rd 1980, pp96-100.

Clendenen, R.L. and Drickamer, H.G. (1966). Lattice parameters of nine oxides and sulfides as a function of pressure, J. Chem. Phys. 44 4223-4228.

Collins, D.W., Dehn, J.T. and Mulay, L.N. (1967). Superparamagnetism and Mössbauer spectroscopy: A review and new results on iron dispersion, Mössbauer Effect Methodology, vol. 3, (ed. Gruverman), Plenum Press, N.Y. pp103-122.

Corliss, L., Elliott, N. and Hastings, J. (1956). Magnetic structures of the polymorphic forms of manganous sulphide, Phys. Rev. 104 924-928.

Cranshaw, T.E. (1974). Mössbauer spectroscopy, J. Physics E 7 497-505.

Darken, L.S. and Gurry, R.W. (1945). The system iron-oxygen. I. The wüstite field and related equilibria, J. Amer. Chem. Soc. 67 1398-1412.

Darken, L.S. and Gurry, R.W. (1953). Physical Chemistry of Metals, McGraw Hill, N.Y. 535pp.

Davies, G.F. (1974). Limits on the constitution of the lower mantle, Geophys. J.R. astr. Soc. 38 479-504.

Davies, G.F. (1976). The estimation of elastic properties from analogue compounds, Geophys. J.R. astr. Soc. 44 625-647.

Davies, M.W. and Richardson, F.D. (1959). The non-stoichiometry of manganous oxide, Trans. Faraday Soc. 55 604-610.

Dever, D.J. (1972). Temperature dependence of the elastic constants in α-iron single crystals: relationship to spin order and diffusion anomalies, J. Appl. Phys. 43 3293-3301.

Dézsi, I., Molnar, B., Tarnozci, T. and Tompy, K. (1967). Magnetic behaviour of bis-(1,10-phenanthroline)-iron(II) thiocyanate between -190° and 30°, J. Inorg. Nuclear Chem. 29 2486-2490.

Distin, P.A., Whiteway, S. and Masson, C. (1971). Solubility of oxygen in liquid iron from 1785° to 1960°. A new technique for the study of slag-metal equilibria, Canad. Metallurg. Quart. 10 13-18.

Dubrovskiy, V.A. and Pan'kov, V.L. (1972). On the composition of the Earth's core, Izvestia, Phys. Solid Earth 7 48-54.

Dziewonski, A.M. and Anderson, D.L. (1981). Preliminary reference Earth model, Phys. Earth Planet. Int. 25 297-356.

Elias, D.J. and Linnett, J.W. (1969). Oxidation of metals and alloys. III. Mössbauer spectrum and structure of wüstite, Trans. Faraday Soc. 65 2673-2677.

Elsasser, W.M. (1963). Early history of the Earth, in Earth Science and Meteorites, J. Geiss and E. Goldberg (eds.) North Holland, Amsterdam, pp1-30.

Endo, S. and Ito, K. (1980). Electrical resistance of αFe_2O_3 under ultra-high static pressure, Solid State Comm. 36 189-190.

Fearn, D.R., Loper, D.E. and Roberts, P.H. (1981). Structure of the Earth's inner core, Nature 292 232-233.

Fender, B.E.F. and Riley, F.D. (1969). Thermodynamic properties of $Fe_{1-x}O$ transitions in the single phase region, J. Phys. Chem. Solids 30 793-798.

Fischer, W.A. and Schumacher, J.F. (1978). Die Sättigungslöslichkeit von Reineisen au Sauerstoff vom Schmelzpunkt bis 2046°C, ermittelt mit dem Schwebeschmelzverfahren, Arch. Eisen. 49 431-435.

Foster, P.K. and Welch, A.J.E. (1956). Metal-oxide solid solutions. I. Lattice constant and phase relationships in ferrous oxide (wüstite) and in solid solutions of ferrous oxide and manganous oxide, Trans. Faraday Soc. 52 1626-1635.

Gancarz, A.J. and Wasserburg, G.J. (1977). Initial Pb of the Amitsoq gneiss, West Greenland and implications for the age of the Earth, Geochim. Cosmochim. Acta 41 1283-1301.

Getting, I.C. and Kennedy, G.C. (1970). Effect of pressure on the emf of chromel-alumel and platinum-platinum 10% rhodium thermocouples, J. Appl. Phys. 41 4552-4562.

Gibb, T.C. (1976). Principles of Mössbauer Spectroscopy, Chapman and Hall, London, 254pp.

Giddings, R.A. and Gordon, R.S. (1973). Review of oxygen activities and phase boundaries in wüstite as determined by electromotive-force and gravimetric methods, J. Am. Ceram. Soc. 56 111-116.

Goodenough, J.B. (1967). Description of transition metal compounds: Application to several sulphides, In Propriétés Thermodynamiques Physiques et Structurales des Dérivés Semi-metalliques, Centre National de la Recherche Scientifique, Paris, pp263-292.

Gosselin, J.R., Townsend, M.G., Tremblay, R.J. and Webster, H.H. (1976). Mössbauer effect in single crystal $Fe_{1-x}S$, J. Solid State Chem. 17 43-48.

Graham, E.K. and Dobrzykowski, D. (1976). Temperatures in the mantle as inferred from simple compositional models, Am. Mineral. 61 549-559.

Green, D.H., Hibberson, W.O. and Jaques, A.L. (1979). Petrogenesis of mid-ocean ridge basalts, In The Earth, It's Origin, Structure and Evolution, edited by M.W. McElhinny, Academic Press, London. pp265-299.

Green, T.H., Ringwood, A.E. and Major, A. (1966). Friction effects and pressure calibration in a piston-cylinder apparatus at high pressure and temperature, J. Geophys. Res. 71 3589-3594.

Greenwood, N.N. and Howe, A.T. (1972a). Mössbauer studies of $Fe_{1-x}O$. Part 1. The defect structure of quenched samples, J. Chem. Soc. Dalton Trans. 110-116.

Greenwood, N.N. and Howe, A.T. (1972b). Mössbauer studies of $Fe_{1-x}O$. Part 11. Disproportionation between 300K and 700K, J. Chem. Soc. Dalton Trans. 116-121.

Gubbins, D. (1977). Energetics of the Earth's core, J. Geophys. 43 453-464.

Guinan, M.W. and Beshers, D.N. (1968). Pressure derivatives of the elastic constants of α-iron to 10 kilobars, J. Phys. Chem. Solids 29 541-549.

Hafner, S. and Kalvius, M. (1966). The Mössbauer resonance of Fe^{57} in troilite (FeS) and pyrrhotite ($Fe_{.88}S$), Zeit. Krist. 123 443-458.

Hazen, R.M. (1981). Systematic variation of bulk modulus of wüstite with stoichiometry, Ann. Rept. Geophys. Lab. 80 277-280.

Hazen, R.M., Mao, H.K., Finger, L.W. and Bell, P.M. (1981). Irreversible unit-cell volume changes of wüstite single crystals quenched from high pressure, Ann. Rept. Geophys. Lab. 80 274-277.

Heikens, H.H., Wiegers, G.A. and van Bruggen, C.F. (1977). On the nature of a new phase transition in α-MnS, Solid. State Comm. 24 205-209.

Hendrajaya, L. (1981). The Shear-Wave Velocity Structure in the Mantle to 1100km Depth, Determined Using the Warramunga Seismic Array, Ph.D. thesis, Australian National University, 295pp.

Hentschel, B. (1970). Stoichiometric FeO as metastable intermediate of the decomposition of wüstite at 225°C, Zeit. Natur. 25 1996-1997.

Hirone, T., Maeda, S., Chiba, S. and Tsuya, N. (1954). Thermal analysis of iron sulphides at the temperature range of the β-transformation, J. Phys. Soc. Japan 9 500-502.

Hoffman, A. (1959). Der Zerfallsmechanismus des Wüstits $Fe_{1-x}O$ unterhalb 570°C, Z. Electrochem. 33 207-213.

Huggins, F.E. (1975). The effect of pressure on the covalency of Fe^{2+}-oxygen bonds, Ann. Rept. Geophys. Lab. 74 551-555.

Ito, E., Takahashi, E. and Matsui, Y. (1983). The mineralogy and chemistry of the lower mantle: An implication of the ultrahigh-pressure phase relations in the system MgO-FeO-SiO_2, Earth Plan. Sci. Lett., submitted.

Ito, E. and Yamada, H. (1983). Stability relations of silicate spinels, ilmenites and perovskites, in High-Pressure Research in Geophysics Adv. Earth Planet. Sci. vol.12., eds. S. Akimoto and M. Manghnani, Centre for Academic Publications, Tokyo, pp405-419.

Jackson, I. (1983). Some geophysical constraints on the composition of the lower mantle, Earth Planet. Sci. Lett. 62 91-103.

Jackson, I. and Ahrens, T.J. (1979). Shock wave compression of single crystal forsterite, J. Geophys. Res. 84 3039-3048.

Jackson, I., Liebermann, R.C. and Ringwood, A.E. (1978). The elastic properties of $(Mg_xFe_{1-x})O$ solid solutions, Phys. Chem. Minerals 3 11-31.

Jackson, I. and Ringwood, A.E. (1981). High-pressure polymorphism of the iron oxides, Geophys. J.R. astr. Soc. 64 767-783.

Jackson, I., Ringwood, A.E. and McCammon, C.A. (1983). Comment on 'High-pressure polymorphism of FeO? An alternative interpretation and its implications for the Earth's core' by L. Liu, P. Shen and W.A. Bassett, Geophys. J.R. astr. Soc., in press.

Jahn, H.A. and Teller, E. (1937). Stability of polyatomic molecules in degenerate electronic states. I. Orbital degeneracy. Proc. Roy. Soc. (London) A161 220-235.

Jamieson, J.C. (1977). Phase transitions in rutile-type structures, in High Pressure Research, Application to Geophysics, edited by M.H. Manghnani and S. Akimoto, Academic Press, New York. pp209-218.

Jeanloz, R. (1979). Properties of iron at high pressures and the state of the core, J. Geophys. Res. 84 6059-6070.

Jeanloz, R. (1981). Finite-strain equation of state for high-pressure phases, Geophys. Res. Lett. 8 1219-1222.

Jeanloz, R. and Ahrens, T. (1980). Equations of state of FeO and CaO, Geophys. J.R. astr. Soc. 62 505-528.

Jeanloz, R. and Sato-Sorenson, Y. (1982). Wüstite (Fe_xO): Compression, nonstoichiometry and bulk viscosity (abstract), Trans. Am. Geophys. Union 63 1097-1098.

Jette, E.R. and Foote, F. (1933). An X-ray study of the wüstite (FeO) solid solutions, J. Chem. Phys. 1 29-36.

Johnson, D.P. (1969). Mössbauer study of the local environments of ^{57}Fe in FeO, Solid State Comm. 7 1785-1788.

Johnston, M.J.S. and Strens, R.G.J. (1973). Electrical conductivity of molten Fe-Ni-S-C core mix, Phys. Earth Planet. Int. 7 217-218.

Jones, L.E.A. and Liebermann, R.C. (1974). Elastic and thermal properties of fluoride and oxide analogues in the rocksalt, fluorite, rutile and perovskite structures, Phys. Earth Planet. Int. 9 101-107.

Jørgensen, C.K. (1962). The nephelanxetic series. Prog. Inorg. Chem. 4 73-124.

Katsura, T., Iwasaki, B., Kimura, S. and Akimoto, S. (1967). High-pressure synthesis of the stoichiometric compound FeO, J. Chem. Phys. 47 4559-4560.

Kim, K-T., Vaidya, S.N. and Kennedy, G.C. (1972). Effect of pressure on the temperature of the eutectic minimums in two binary systems: NaF-NaCl and CsCl-NaCl, J. Geophys. Res. 77 6984-6989.

King, H.E. (1979). Physical Properties of FeS at High Temperature and High Pressure: Crystal Structure, ^{57}Fe Mössbauer Resonance and Electrical Conductivity, Ph.D. thesis, State Univ. of New York at Stony Brook.

King, H.E. and Prewitt, C.T. (1982). High-pressure and high-temperature polymorphism of iron sulphide (FeS), Acta Cryst. B38 1877-1887.

King, H., Virgo, D. and Mao, H.K. (1978). High-pressure phase transitions in FeS, using ^{57}Fe Mössbauer Spectroscopy, Ann. Rept. Geophys. Lab. 78 830-835.

Koch, F. and Cohen, J.B. (1969). The defect structure of $Fe_{1-x}O$, Acta Cryst. B25 275-287.

Kraut, E.A. and Kennedy, G.C. (1966). New melting law at high pressures, Phys. Rev. 151 668-675.

Kullerud, G., Bell, P.M. and England, J.L. (1965). High-pressure differential thermal analysis, Ann. Rept. Geophys. Lab. 64 197-199.

Kundig, W. (1967). Evaluation of Mössbauer spectra for ^{57}Fe, Nucl. Instr. Meth. 48 219-228.

Kurash, V.V., Gol'danskii, V.I., Malysheva, T.V. and Urusov, V.S. (1972). Mössbauer spectrum of wüstite at low temperatures, Inorg. Mater. 8 1183-1184.

Kurash, V.V., Kulikov, G.A. and Makarov, E.C. (1973). Study of Mg and Fe isomorphism in "ninningerite" MgS, "troilite" FeS system (in Russian), Geokhimiya 8 1266-1267.

Kurepin, V.A. (1975). Component activities, thermodynamic characteristics of reactions, and phase equilibria in the Fe-O system at high temperatures and pressures, Geochem. Int. (trans. from Geokhimiya) 114-121.

Larionov, L.V. (1977). Phase transitions and differentiation of matter in the interior of the Earth during the Earth's evolution, Izvestia, Phys. Solid Earth 12 398-402.

Lay, T. and Helmberger, D.V. (1983). A shear velocity discontinuity in the lower mantle, Geophys. Res. Lett. 10 63-66.

Levin, R.L. and Wagner, J.B. (1966). Lattice-parameter measurements of undoped and chromium-doped wüstite, Trans. Amer. Inst. Min. (Metall.) Engrs. 236 516-519.

Liebermann, R.C. (1974). Elasticity of pyroxene-garnet and pyroxene-ilmenite phase transformations in germanates, Phys. Earth Planet. Int. 8 361-374.

Liebermann, R.C., Ringwood, A.E., Mayson, D.J. and Major, A. (1974). Hot-pressing of polycrystalline aggregates at very high pressure for ultrasonic measurements, Proc. 4th Int. Conf. High Pressure, Kyoto, Phys.-Chem. Soc. Japan, pp495-502.

Lindsley, D.H. (1966). Pressure-temperature relations in the system $FeO-SiO_2$, Ann. Rept. Geophys. Lab. 65 226-230.

Liu, L.G. (1976). The high-pressure phases of $FeSiO_3$ with implications for Fe_2SiO_4 and FeO, Earth Planet. Sci. Lett. 33 101-106.

Liu, L.G. (1978). A new high-pressure phase of $Ca_2Al_2SiO_7$ and implications for the Earth's interior, Earth Planet. Sci. Lett. 40 401-406.

Liu, L.G. (1979). Phase transformations and the constitution of the deep mantle in The Earth, its Origin, Structure and Evolution, edited by M.W. McElhinny, Academic Press, London, pp177-202.

Liu, L.G. (1981). Structural considerations in high-pressure phase transformations of simple crystals, High Temp.-High Pres. 13 387-398.

Liu, L.G. and Bassett, W.A. (1975). The melting of iron up to 200 kbar, J. Geophys. Res. 80 3777-3782.

Liu, L., Shen, P. and Bassett, W.A. (1982). High-pressure polymorphism of FeO? An alternative interpretation and its implications for the Earth's core, Geophys. J.R. astr. Soc., 70 57-66.

Loper, D.E. (1978). The gravitationally powered dynamo, Geophys. J.R. astr. Soc. 54 389-404.

Mann, G.S. and Van Vlack, L.H. (1976). FeS-MnS phase relationships in the presence of excess iron, Metallurgical Trans. 7B 469-475.

Mao, H.K. (1974). A discussion of the iron oxides at high pressure with implications for the chemical and thermal evolution of the Earth, Ann. Rept. Geophys. Lab. 73 510-518.

Mao, H.K. and Bell, P.M. (1971). High-pressure decomposition of spinel (Fe_2SiO_4), Ann. Rept. Geophys. Lab. 70 176-177.

Mao, H.K., Bell, P.M. and Yagi, T. (1979). Iron-magnesium fractionation model for the Earth, Ann. Rept. Geophys. Lab. 78 621-625.

Mao, H.K., Takahashi, T., Bassett, W.A., Kinsland, G.L. and Merrill, L. (1974). Isothermal compression of magnetite to 320 kbar and pressure-induced phase transformation, J. Geophys. Res. 79 1165-1170.

Mao, H.K., Takahashi, T., Bassett, W.A., Weaver, J.S. and Akimoto, S. (1969). Effect of pressure and temperature on the molar volumes of wüstite and of three $(Fe,Mg)_2SiO_4$ spinel solid solutions, J. Geophys. Res. 74 1061-1069.

Mao, H.K., Zou, G. and Bell, P.M. (1981). High-pressure experiments on FeS with bearing on the composition of the Earth's core, Ann. Rept. Geophys. Lab. 80 267-272.

Mao, N. (1974). Velocity-density systematics and its implications for the iron content of the mantle, J. Geophys. Res. 79 5447-5452.

McCammon, C.A., Ringwood, A.E. and Jackson, I. (1983). Thermodynamics of the system Fe-FeO-MgO at high pressure and temperature and a model for formation of the Earth's core, Geophys. J.R. astr. Soc. 72 577-595.

McQueen, R.G., Marsh, S.P., Taylor, J.W., Fritz, J.N. and Carter, W.J. (1970). The equation of state of solids from shock wave studies, in High-Velocity Impact Phenomena, ed. Kinslow, Academic Press, N.Y. pp293-417.

Mizutani, H., Hamano, Y., Akimoto, S. and Nishizawa, O. (1972). Elasticity of stishovite and wüstite (abstract), Trans. Am. Geophys. Union 53 527.

Montano, P.A. and Seehra, M.S. (1976). Magnetism of iron pyrite (FeS_2) - A Mössbauer study in an external magnetic field, Solid State Comm. 20 897-898.

Morosin, B. (1970). Exchange striction effects in MnO and MnS, Phys. Rev. B 1 236-243.

Muirhead, K.J. and Hales, A.L. (1980). Evidence for p wave velocity discontinuities at depths greater than 650 km in the mantle, Phys. Earth Planet. Int. 23 304-313.

Murnaghan, F.D. (1951). Finite Deformation of an Elastic Solid, John Wiley and Sons, Inc. New York, 1951, 140pp.

Murthy, V.R. and Hall, H.T. (1972). The origin and composition of the Earth's core, Phys. Earth Planet. Int. 6 123-130.

Navrotsky, A. and Davies, P.K. (1981). Cesium chloride vs. nickel arsenide as possible structures for (Mg,Fe)O in the lower mantle, J. Geophys. Res. 86 3689-3694.

Newton, R.C., Jayaraman, A. and Kennedy, G.C. (1962). The fusion curves of the alkali metals up to 50 kilobars, J. Geophys. Res. 67 2559-2566.

Nishikawa, M. and Akimoto, S. (1971). Bridgman anvil with an internal heating system for phase transformation studies, High Temp.-High Pressures 3 161-176.

Ohnishi, S. and Mizutani, H. (1978). Crystal field effect on bulk moduli of transition metal oxides, J. Geophys. Res. 83 1852-1856.

Ohtani, E. (1983). Melting temperature distribution and fractionation in the lower mantle, Phys. Earth Planet. Int., in press.

Okamoto, T., Fujii, H., Hidaka, Y. and Tatsumoto, E. (1967). Effect of hydrostatic pressure on the Néel temperature in FeO and CoO, J. Phys. Soc. Japan 23 1174.

Ono, K., Ito, A. and Hiraharo, E. (1962). Mössbauer study of hyperfine field, quadrupole interaction, and isomer shift of Fe^{57} in $FeS_{1.00}$, $FeS_{1.05}$ and $FeS_{1.07}$, J. Phys. Soc. Japan 17 1615-1620.

Ostapenko, G.T. (1971). Thermodynamics of first-order phase transitions under non-hydrostatic stress, Geochem. Int. (trans. from Geokhimiya) 771-778.

Ostapenko, G.T. (1973). Thermodynamics of second-order phase transitions under non-hydrostatic stress, Geochem. Int. (trans. from Geokhimiya) 148-155.

Oversby, V.M. and Ringwood, A.E. (1971). Time of formation of the Earth's core, Nature 234 463-465.

Pearson, W.B. (1967). A Handbook of Lattice Spacings and Structures of Metals and Alloys vol. 2, Pergamon Press, Oxford, 1446pp.

Perthel, R. (1960). Über den Ferrimagnetismus nicht stöchiometrischer Eisensulfide, Ann. Physik. 7 273-295.

Pidgeon, R.T. (1978). Big Stubby and the early history of the Earth, in Fourth Int. Conf., Geochronology, Cosmochronology, Isotope Geology, U.S. Geol. Surv. Open-File Rep. 78-701, pp334-335.

Pollard, R.J., McCann, V.H. and Ward, J.B. (1983). Magnetic structures of αMnS and MnSe from ^{57}Fe Mössbauer spectroscopy, J. Phys. C : Solid State Phys. 16 345-353.

Price, D.C. (1981). Empirical lineshape for computer fitting of spectral data, Aust. J. Phys. 34 51-56.

Price, D.C., Maartense, I. and Morrish, A.H. (1974). Hyperfine interactions at ^{57}Fe in Fe^{2+}-doped $MnCO_3$, Phys. Rev. B 9 281-293.

Ramdohr, P. (1980). The Ore Minerals and their Intergrowths Vol. 1, Pergamon Press, Berlin 440pp.

Reed, S.J.B. and Ware, N.G. (1973). Quantitative electron microprobe analysis using a lithium drifted silicon detector, X-ray Spectrometry 2 69-74.

Reed, S.J.B. and Ware, N.G. (1975). Quantitative electron microprobe analysis of silicates using energy-dispersive X-ray analysis, J. Petrology 16 499-519.

Ringwood, A.E. (1962a). Prediction and confirmation of olivine spinel transition in nickel orthosilicate, Geochim. Cosmochim. Acta 26 457-469.

Ringwood, A.E. (1962b). A model for the upper mantle, J. Geophys. Res. 67 857 - 867.

Ringwood, A.E. (1970). Phase transformations and the constitution of the mantle, Phys. Earth Planet. Int. 3 109-155.

Ringwood, A.E. (1975). Composition and Petrology of the Earth's Mantle, McGraw-Hill, N.Y. 618pp.

Ringwood, A.E. (1977). Composition of the core and implications for origin of the Earth, Geochem. J. 11 111-135.

Ringwood, A.E. (1979). Origin of the Earth and Moon, Springer-Verlag, New York, 295pp.

Ringwood, A.E. and Major, A. (1968). Apparatus for phase transformation studies at high pressures and temperatures, Phys. Earth Planet. Int. 1 164-168.

Romanov, V.P. and Checherskaya, L.F. (1972). Mössbauer spectra of non-stoichiometric and stoichiometric wüstites, Phys. Stat. Sol. 49B K183-K187.

Roth, W.L. (1960). Defects in the crystal and magnetic structures of ferrous oxide, Acta Cryst. 13 140-149.

Sawamoto, H., Ohtani, E. and Kumazawa, M. (1974). High pressure decomposition of γ-Fe_2SiO_4, Proc. 4th Int. Conf. High Press. Kyoto 1974, 194-201.

Schreinemakers, F.A.H. (1916). Invariant, monovariant and divariant equilibria, Proc. Acad. Sci. Amsterdam 19 514-527.

Schroeer, D. (1970). The Mössbauer effect in microcrystals, Mössbauer Effect Methodology, vol. 5, (ed. Gruverman), Proc. 5th Symp. Möss. Effect Method. New York, 1969. Plenum Press, pp141-162.

Schwartz, E.J. and Vaughn, D.J. (1972). Magnetic phase relations of pyrrhotite, J. Geomag. Geoelec. 24 441-458.

Seregin, P.P., Bondarevskii, S.I. and Efimov, A.A. (1970). Mössbauer effect at ^{57m}Fe atoms in CoS, Soviet Phys. Solid State 12 1462-1463.

Shannon, R.D. (1976). Revised effective ionic radii and systematic studies of interatomic distances in halides and chalcogenides, Acta Cryst. A32 751-767.

Shen, P., Bassett, W.A. and Liu, L. (1983). Experimental determination of the effects of pressure and temperature on the stoichiometry and phase relations of wüstite, Geochim. Cosmochim. Acta 47 773-778.

Simons, B. (1980). Composition-lattice parameter relationship of the magnesiowüstite solid solution series, Ann. Rept. Geophys. Lab. 79 376-380.

Simons, B. and Seifert, F. (1979). High-pressure wüstite : cell parameters and Mössbauer spectra, Ann. Rept. Geophys. Lab. 78 625-626.

Sinclair, W.J. (1982). Aspects of Crystal Chemistry, Ph.D. thesis, Australian National University, 110pp.

Skinner, B.J. and Luce, F.D. (1971). Solid solutions of the type (Ca,Mg, Mn,Fe)S and their use as geothermometers for the enstatite chondrites, Am. Mineral. 56 1269-1296.

Sorai, M., Ensling, J. and Gütlich, P. (1976). Mössbauer effect study on low-spin $^1A_1 \rightarrow$high-spin $^5T_2$ transition in tris(2-picolylamine) iron chloride I. Dilution effect in $[Fe_xZn_{1-x}(2\text{-pic})_3]Cl_2 \cdot C_2H_5OH$, Chem. Phys. 18 199-209.

Srivastava, C.M., Shringi, S.N. and Babu, M.V. (1981). Mössbauer study of the low-temperature phase of magnetite, Phys. Stat. Sol. 65A 731-735.

Stacey, F.D. (1977). Physics of the Earth 2nd ed. John Wiley and Sons, Inc., New York, 414pp.

Stacey, F.D. and Irvine, R.D. (1977). Theory of melting : thermodynamic basis of Lindemann's law, Aust. J. Phys. 30 631-640.

Stevenson, D.J. (1981). Models of the Earth's core, Science 214 611-619.

Sumino, Y. and Anderson, O.L. (1980). Elastic constants of single-crystal MgO at temperatures between 80°K and 1300°K (abstract), Trans. Am. Geophys. Union 61 1102.

Sumino, Y., Kumazawa, M., Nishizawa, O. and Pluschkell, W. (1980). The elastic constants of single crystal $Fe_{1-x}O$, MnO and CoO, and the elasticity of stoichiometric magnesiowüstite, J. Phys. Earth 28 475-495.

Suzuki, I., Okajima, S. and Seya, K. (1979). Thermal expansion of single-crystal manganosite, J. Phys. Earth 27 63-69.

Swanson, H.E., Fuyat, R.K. and Ugrinic, G.M. (1955). Standard X-ray diffraction powder patterns Vol. 4, Natl. Bur. Standards (US) Circ. No. 539, 75pp.

Taylor, C.R. and Chipman, J. (1943). Equilibria of liquid iron and simple basic and acid slags in a rotating oven furnace, AIME Trans. 154 228-245.

Temperly, A.A. and Lefevre, H.W. (1966). The Mössbauer effect in marcasite structure iron compounds, J. Phys. Chem. Solids 27 85-92.

Tossell, J.A. (1977). SCF-Xα scattered wave MO studies of the electronic structure of ferrous iron in octahedral coordination with sulphur, J. Chem. Phys. 66 5712-5719.

Touzelin, B. (1974). High-temperature X-ray determination of iron monoxide lattice parameters under controlled atmosphere. Decomposition of iron monoxide between 25 and 570°. Rev. Int. Hautes Temp. Refract. 11 219-229.

Townsend, M.G., Ripley, L.G. and Horwood, J.L. (1975). Absence of magnetic order in cobalt monosulphide, Phys. Stat. Solidi A 32 K29-K32.

Urey, H.C. (1952). The Planets, Yale Univ. Press, New Haven, Connecticut, 245pp.

Usselman, T.M. (1975a). Experimental approach to the state of the core: Part 1. The liquidus relations of the Fe-rich protion of the Fe-Ni-S system from 30 to 100 kb, Am. J. Sci. 275 278-290.

Usselman, T.M. (1975b). Experimental approach to the state of the core Part 2: Composition and thermal regime, Amer. J. Sci. 275 291-303.

Vallet, P. and Raccah, P. (1965). Thermodynamic properties of solid iron (II) oxide. Mem. Sci. Rev. Met. 62 1-29.

Van Zandt, L.L. and Honig, J.M. (1974). Theories pertaining to the semiconductor-metal transition in crystals, Ann. Rev. Mat. Sci. 4 191-220.

Vassiliou, M.S. and Ahrens, T.J. (1981). Hugoniot equation of state of periclase to 200 GPa, Geophys. Res. Lett. 8 729-732.

Vassiliou, M.S. and Ahrens, T.J. (1982). The equation of state of $Mg_{.6}Fe_{.4}O$ to 200 GPa, Geophys. Res. Lett. 9 127-130.

Vaughn, D.J. and Craig, J.R. (1978). Mineral Chemistry of Metal Sulphides, Cambridge Univ. Press, Cambridge 493pp.

Violet, C.E. and Pipkorn, D.N. (1971). Mössbauer line positions and hyperfine interactions in α iron, J. Appl. Phys. 11 4339-4342.

Vityazev, A.V. and Mayeva, S.V. (1976). Model of the Earth's early evolution, Izvestia, Phys. Solid Earth 12 79-85.

Vogel, R. and Hillner, G. (1953). Das Zustandsschaubild Eisen-Eisensulfid-Kobaltsulfid-Kobalt, Arch. Eisenhüttenwesen, 24 133-141.

Wakabayashi, I., Kobayashi, H., Nagasaki, H. and Minomura, S. (1968). The effect of pressure on the lattice parameters Part I. PbS and PbTe Part II. Gd, NiO and α-MnS, J. Phys. Soc. Japan 25 227-233.

Walker, D., Stolper, E.M. and Hays, J.F. (1978). A numerical treatment of melt/solid segregation: size of the eucrite parent body and stability of the terrestrial low-velocity zone, J. Geophys. Res. 83 6005-6013.

Wang, C-Y. (1970). Can mantle minerals have the NiAs structure? Phys. Earth Planet. Int. 3 213-217.

Watt, J.P. and Ahrens, T.J. (1982). The role of iron partitioning in mantle composition, evolution and scale of convection, J. Geophys. Res. 87 5631-5644.

Watt, J.P. and O'Connell, R. (1978). Mixed-oxide and perovskite-structure model mantles from 700-1200 km, Geophys. J.R. astr. Soc. 54 601-630.

Weaver, J.S., Takahashi, T. and Bassett, W.A. (1971). Calculation of the P-V relation for sodium chloride up to 300 kilobars at 25°C, in Accurate Characterization of the High Pressure Environment (ed. E.C. Lloyd) Natl. Bur. Std. (US) Spec.-Publ. No. 326, pp189-199.

Will, G., Hinze, E. and Nuding, W. (1980). The compressibility of FeO measured by energy dispersive X-ray diffraction in a diamond anvil squeezer up to 200 kbar, Phys. Chem. Minerals 6 157-167.

Willis, B.T.M. and Rooksby, H.P. (1953). Change of structure of ferrous oxide at low temperature, Acta Cryst. 6 827-831.

Wilson, J.A. (1972). Systematics of the breakdown of Mott insulation in binary transition metal compounds, Adv. Phys. 21 143-198.

Window, B., Dickson, B.L., Routcliffe, P. and Srivastava, K.K.P. (1974). A versatile multiple Mössbauer spectrometer, Jour. Physics E:Sci. Instru. 7 916-921.

Worthington, M.H. (1973). The Inversion of Seismic Data Using Monte Carlo and Linear Programming Techniques, Ph.D. thesis, Aust. Nat. Univ., Canberra, 168pp.

Wright, C. (1983). Anomalies in the p wave travel time curve at distances close to 44° and 50°, Geophys. J.R. astr. Soc., submitted.

Wright, C. and Lyons, J.A. (1981). Further evidence for radial velocity anomalies in the lower mantle, PAGEOPH 119 137-162.

Yagi, T. and Akimoto, S. (1981). Rapid X-ray measurements to megabar range - static compression of α-Fe_2O_3 (abstract), Program with Abstracts; U.S.-Japan Seminar on High Pressure Research: Applications in Geophysics, Hakone, Japan 12-15 Jan. 1981, p22.

Yagi, T. and Akimoto, S. (1983). Rapid X-ray measurements to 100 GPa range and static compression of α-Fe_2O_3 in High-Pressure Research in Geophysics, Adv. Earth Planet. Sci. vol. 12, eds. Akimoto and M. Manghnani, Centre for Academic Publications, Tokyo, pp81-92.

Yamamoto, A. (1982). Modulated structure of wüstite ($Fe_{1-x}O$) (three-dimensional modulation), Acta Cryst. B38 1451-1456.

Zou, G., Bell, P.M. and Mao, H.K. (1981). Application of the solid-helium pressure medium in a study of the α-ε Fe transition under hydrostatic pressure, Ann. Rept. Geophys. Lab. 80 272-274.

Zou, G.T., Mao, H.K., Bell, P.M. and Virgo, D. (1980). High pressure experiments on the iron oxide wüstite, ($Fe_{1-x}O$), Ann. Rept. Geophys. Lab. 79 374-376.